Durham E-Theses

Ultraluminous X-ray sources

SUTTON, ANDREW

How to cite:

SUTTON, ANDREW (2013) *Ultraluminous X-ray sources*, Durham theses, Durham University. Available at Durham E-Theses Online: http://etheses.dur.ac.uk/9431/

Ultraluminous X-ray sources

Andrew D. Sutton

A thesis presented for the degree of
Doctor of Philosophy

Durham
University

Department of Physics
University of Durham
United Kingdom

September 2013

Abstract

Ultraluminous X-ray sources (ULXs) are accreting black holes with X-ray luminosities in excess of the Eddington limit for a typical $\sim 10~M_\odot$ Galactic black hole. There is an emerging consensus that most ULXs are probably fairly typical stellar remnant black holes in a new super-Eddington 'ultraluminous' accretion state, characterised by a soft excess and high energy spectral curvature, which may be associated with a radiatively-driven wind and cool, optically thick Comptonisation respectively. However, this scenario may be insufficient to produce some of the most luminous ULXs. Here we present a sample of extreme luminosity ULXs, and show that their X-ray spectral and timing properties are consistent with most of them being in the sub-Eddington low/hard state. Given their luminosities, this suggests that these ULXs contain 10^3–$10^4~M_\odot$ black holes. But, in one of the extreme ULXs we find evidence of high energy spectral curvature, which is a key feature of the ultraluminous state. We explore this ULX further, and show that its X-ray spectrum is consistent with being in the ultraluminous state, but with any wind emission obscured from view by the high column density of material in the direction of the source. We also investigate the ultraluminous state further, and present an X-ray spectral and timing study of ULXs with some of the highest quality *XMM-Newton* data. We show that their spectral and timing properties are consistent with current models of super-Eddington accretion, where a massive, radiatively-driven wind forms a funnel-like geometry around the source. Then, the observed X-ray properties are dependant on both the accretion rate, and the inclination at which the ULX system is observed. Finally, we consider optical counterparts to a small sample of ULXs. We fit the X-ray and optical data of these with a new spectral model of an irradiated, colour-temperature-corrected accretion disc, finding that ~ 0.1 per cent of their bolometric luminosity is reprocessed in the outer disc. This may be due to the opposing effects of self-shielding in the accretion disc and reflection in a super-Eddington wind.

Contents

List of Figures

List of Tables

Declaration

The work described in this thesis was undertaken between 2009–2013 when the author was a postgraduate research student under the supervision of Dr. T. Roberts in the Department of Physics at the University of Durham. This work has not been submitted for any other degree at the University of Durham or any other University.

Portions of this thesis have appeared in the following papers:

- Sutton A.D., Roberts T.P., Walton D.J., 2011, AN, 332, 362

- Sutton A.D., Roberts T.P., Walton D.J., Gladstone J.C., Scott A.E., 2012, MNRAS, 423, 1154

- Sutton A.D., Roberts T.P., Gladstone J.C., Farrell S.F., Reilly E., Goad M.R., Gehrels N., 2013, MNRAS, 434, 1702

- Sutton A.D., Roberts T.P., Middleton M.J., 2013, MNRAS, 435, 1758

Acknowledgements

I would like to thank my supervisor, Dr. Tim Roberts, without whom this thesis would not have been possible. I am also grateful to Prof. Chris Done for her help and advice, particularly regarding Chapter 5; Dr. Matt Middleton, who took the time to answer many of my questions about ULXs; Dr. Jeanette Gladstone, who helped me to grasp the basics of X-ray data analysis, back when I had just started my PhD; and to the rest of the research group, who have helped to create a fun and interesting place to work. On a personal note, I would also like to thank the close friends that I have made in Durham, especially Martin; they have helped to keep me going, even when my work meant that I could not make much time for them; Naveena, for putting up with me when her situation was just as stressful as mine; and finally my family, as without their support and encouragement I could not have got this far.

Chapter 1

Introduction

The main body of this thesis describes research in the field of ultraluminous X-ray source (ULX) astronomy. ULXs are bright X-ray sources, which are thought to contain black holes. It is therefore appropriate to begin with a brief overview of some highlights from the history of X-ray astronomy, to provide some context around the discovery of ULXs, and further research in the field. It will become evident that one of the major drivers of progress throughout the brief history of X-ray astronomy has been the rapid advancements in instrumentation – Section 1.2 describes some instruments from the current generation of X-ray observatories that have provided much of the data used throughout this thesis. Following this, we summarise the various types of black hole phenomena that are seen throughout the Universe, before focussing in on a particular variety – the ULXs.

1.1   A brief history of X-ray astronomy

Although X-rays were discovered in the late 19th Century by W. Röntgen, the dawn of X-ray astronomy was not until much later – arguably in the late 1940s. Following the conclusion of World War II, parts of ~ 100 German V-2 rockets which had been captured by the US were shipped to White Sands, New Mexico, where they were constructed by the US army for use in research and experimentation. It was on the August 5, 1948, that as part of the V-2 rocket program, scientists from the US Naval Research Laboratory led by T. Burnight made the first detection of X-rays originating from the Sun (Keller, 1995). Prior to the advent of scientific rocketry, X-ray astronomy had not been possible; as X-rays are strongly absorbed

by the Earth's atmosphere, the detection of X-rays from extra-terrestrial sources requires detectors to be placed at much higher altitudes than can be achieved with mountain-top observatories. Following the first successful detection, the era of X-ray sounding rockets continued throughout the following decades. At first observations were focussed on the Sun, as it was expected to be the only bright source of X-ray emission; until, on June 18, 1962 an Aerobee sounding rocket carrying a payload of three Geiger counters was launched with the intention of studying solar X-rays reflected from the lunar surface. But the mission did not go as planned, instead Giacconi et al. (1962) not only discovered a diffuse background of X-ray emission, but also identified an X-ray source $\sim$ a million times brighter than the Sun in the constellation of Scorpius (Sco X-1). This marked the first detection of an X-ray source from outside of the Solar System. X-ray sounding rocket experiments continued throughout the 1960s, and from 1965 were joined by balloon-borne X-ray detectors – which, whilst they could not reach as high an altitude as rockets, so could not detect soft X-rays, were capable of observing more penetrating high energy X-rays. Further X-ray sources were discovered, many of which later turned out to be binary stars and black holes in the Galaxy, and by the end of the 1960s, 59 discrete X-ray sources had been reported from rocket and balloon-borne observations (Dolan, 1970).

The next major landmark in the history of X-ray astronomy came in 1970, with the launch from Kenya of the first dedicated X-ray astronomy satellite – *Uhuru* (Giacconi et al., 1971a; its name means 'freedom' in Swahili). Placing X-ray detectors in orbit allowed for major improvements in exposure times compared to the earlier sounding rockets; and, over the following $\sim$ 2 years *Uhuru* was able to scan the sky, culminating in the first all-sky X-ray source catalogue (Forman et al., 1978), containing 339 objects. It was soon found that many X-ray sources were variable, leading to the implication that they were in compact binary systems. Furthermore, the discovery of $\sim$ second and sub-second time-scale variability implied that some sources contained compact objects such as neutron stars or black holes (e.g. Cen

X-3 – Giacconi et al., 1971b; Cyg X-1 – Holt et al. 1971, Oda et al. 1971; Her X-1 – Tananbaum et al. 1972). Following the success of *Uhuru*, the 1970s saw the launch of numerous other satellites for X-ray astronomy, including: *Ariel V* (Smith & Courtier, 1976) in 1974, which was used to discover several bright transient sources, including A0620-00, which at its peak was the brightest recorded cosmic X-ray source (Elvis et al., 1975); *High Energy Astrophysics Observatory-1* (*HEAO-1*) in 1977, which resulted in an all-sky catalogue of 842 sources (Figure 1.1; Wood et al. 1984); and *HEAO-2* in 1979 (Giacconi et al., 1979). *HEAO-2* is much better known as the *Einstein* telescope, and was particularly notable as the first mission to carry an imaging X-ray telescope, which utilised grazing incidence reflection with a set of four Wolter type 1 nested mirrors, and represented a major leap forward in the capability of X-ray instrumentation. Furthermore, *Einstein* was of particular importance, at least in the context of this thesis, as it was responsible for the discovery of a new class of non-nuclear X-ray sources in external galaxies, with X-ray luminosities in excess of typical Galactic sources (Fabbiano, 1989). This new class of astrophysical phenomena was refered to by several names, including: extraluminous X-ray binaries (Colbert & Mushotzky, 1999), superluminous X-ray sources (Roberts & Warwick, 2000), and intermediate-luminosity X-ray objects (Colbert & Ptak, 2002); but, they eventually became known as ULXs (Okada et al., 1998).

The early nineties saw the launch of *Rosat* (short for *Röntgensatellit*; Trümper 1982) and *Advanced Satellite for Cosmology and Astrophysics* (*ASCA*; Tanaka et al. 1994). In the early phase of the mission, *Rosat* carried out an all-sky survey (Figure 1.1), producing a catalogue containing ~ 150000 X-ray sources; and, the latter phase was dedicated to pointed observations, resulting in the serendipitous detection of ~ 100000 objects. Using *Rosat* data many more candidate ULXs were identified (Colbert & Mushotzky 1999; Roberts & Warwick 2000; Colbert & Ptak 2002; Liu & Bregman 2005). *ASCA* was the first X-ray astronomy mission to use CCDs, and provided moderate spatial and spectral resolution. The advent of X-ray CCD
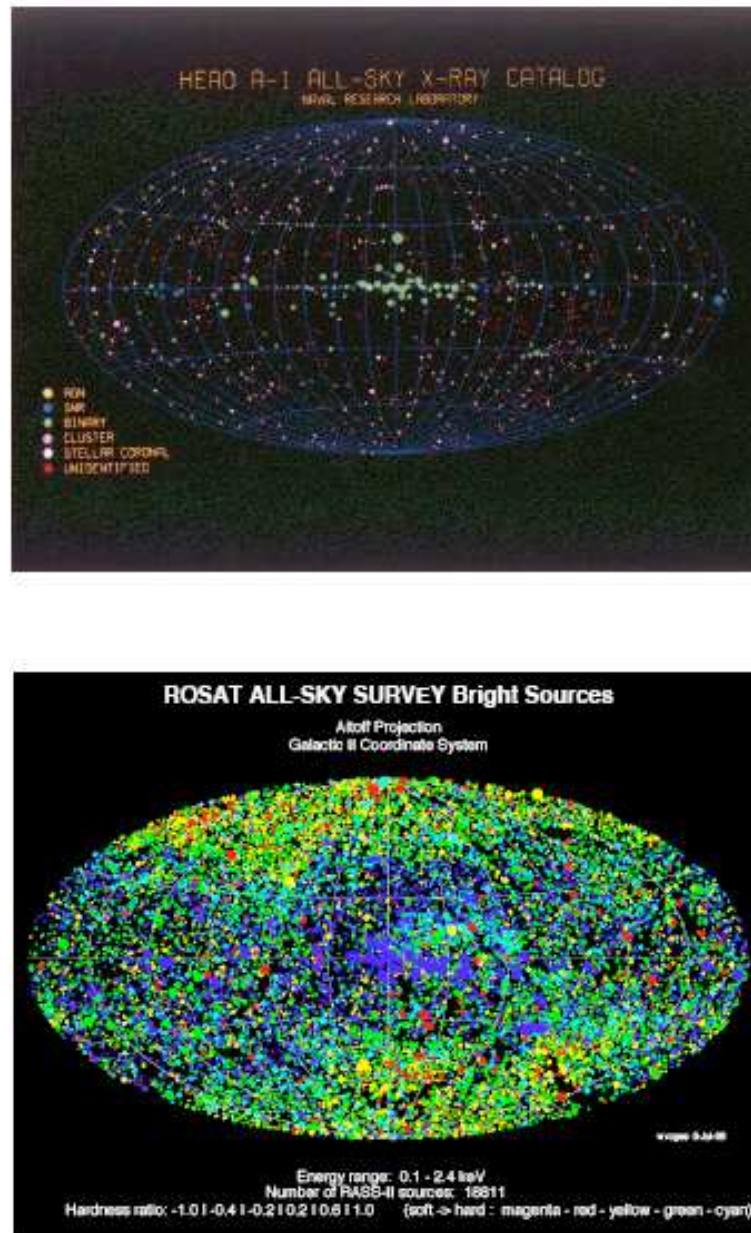
Figure 1.1: Projections showing sources detected in the (*top*) *HEAO-1* and (*bottom*) *Rosat* all-sky surveys (`http://heasarc.gsfc.nasa.gov/Images/heao1/heao1.gif` and `http://www.mpe.mpg.de/xray/wave/rosat/gallery/calendar/1997/jun.php`).

spectroscopy allowed scientists to obtain X-ray spectra of unprecedented quality, for many astrophysical objects – including the ULXs. Throughout this decade X-ray instrumentation improved still further, and towards the end of the twentieth century, some of the current generation of X-ray observatories were launched into orbit. We will discuss these in the following section.

In the 65 years since the first detection of Solar X-rays, X-ray astronomy has advanced from a rather esoteric pursuit to a major field in modern astronomical research. Indeed, in recent years ~ 20 per cent of papers submitted to the astro-ph repository on arXiv[1] have been in the field of high energy astronomy[2]. Currently, it provides a window on to a plethora of astrophysical phenomena which emit X-rays, including: the Sun and other stars; supernovae; white dwarf, neutron star and black hole binary systems; massive black holes thought to reside in the centres of most galaxies; galaxy clusters; and, the X-ray background. In this thesis we will focus on a small subset of these objects: the ULXs.

1.2 Current X-ray instrumentation

The current generation of X-ray telescopes includes *Chandra* (Holt, 1993), *Suzaku* (Mitsuda et al., 2007), the X-ray Telescope (XRT) on *Swift* (Burrows et al., 2004), *XMM-Newton* (Jansen et al., 2001), and recently *NuSTAR* (Harrison et al., 2010). Whilst all of these missions contribute to the study of ULXs, most of the X-ray data analysed for this thesis comes from *XMM-Newton* and *Chandra*, so these are particularly worthy of further mention here. Additionally, Chapter 3 includes some *Swift* XRT data; *Swift* is a multi-wavelength observatory, designed primarily for the detection and rapid follow up of gamma ray bursts. The instrument of interest here is the XRT, which is an imaging spectrometer with a single Metal Oxide Semi-conductor

---

[1]http://arxiv.org/archive/astro-ph
[2]http://arxiv.org/help/stats/2012_by_area/index

(MOS) CCD. A particular strength of *Swift* is its rapid slew time, which allows it to quickly move between targets, making it particularly suitable for monitoring campaigns with relatively short exposure times. This was the main motivation for the use of *Swift* here, where a monitoring campaign was used to provide a trigger for a deeper *XMM-Newton* observation.

1.2.1 *XMM-Newton*

XMM-Newton, or the *X-ray multi-mirror mission – Newton* was launched on December 10, 1999, as the second cornerstone mission in ESA's Horizon 2000 programme. *XMM-Newton* is in a 48 hour elliptical orbit, which allows for long, uninterrupted exposures using its suite of three co-aligned X-ray telescopes with focal lengths of 7.5 m, and a 30 cm optical/UV telescope. The satellite carries three main scientific instruments which are all operated simultaneously, these are: the European Photon Imaging Camera (EPIC); the reflection grating spectrometer (RGS); and, the Optical Monitor (OM). RGSs are fitted to two of the three X-ray telescopes, and they are intended for high resolution X-ray spectroscopy, and the OM provides simultaneous optical/UV coverage of the target field. However, the main instrument of interest for ULX astronomy is EPIC. EPIC consists of three CCD detectors, including two MOS arrays, each with seven CCDs, and one pn camera consisting of 12 CCDs; a sketch of the *XMM-Newton* payload is shown in Figure 1.2, and the chip geometries in Figure 1.3, both of which are taken from the Users' Handbook[3]. Each of the MOS detectors shares an X-ray telescope with one of the RGS instruments, whose gratings are mounted behind these telescopes to divert $\sim$ half of the incident flux to the RGS. The pn camera is mounted on the third X-ray telescope, where it has an unobstructed focal path. The EPIC detectors enable sensitive imaging spectroscopy observations to be made in the 0.15–15 keV energy band, with $\sim$ 6 arcsecond full-

---

[3]`http://heasarc.gsfc.nasa.gov/docs/xmm/uhb/`
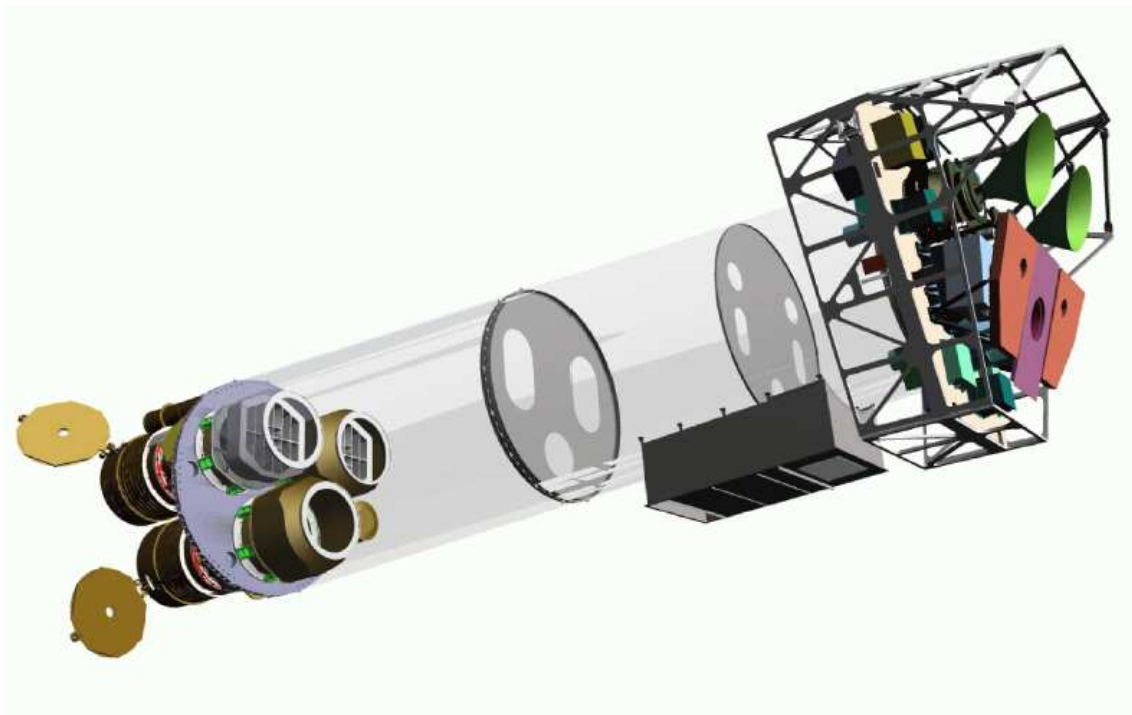
Figure 1.2: A sketch of the *XMM-Newton* payload taken from the Users' Handbook. The mirror modules are mounted to the left hand side, and the focal plane instruments to the right.

width half maximum (FWHM) spatial resolution across the ~ 30 arcminute field of view, and allow for moderate energy resolution (E/dE ~ 50 at 6.5 keV). When operating in the standard 'full frame' mode, the MOS and pn chips have 2.6 s and 73.4 ms time resolution respectively. The EPIC chips can also be operated in various 'partial window' modes, where only parts of the chip are read out; and 'timing' mode, where spatial information is only recorded in one dimension, as the second dimension is used as a measure of time.

As *XMM-Newton* has a relatively large field of view, pointed observations have also resulted in a large number of serendipitous detections of X-ray sources. This has allowed the production of serendipitous source catalogues (Watson et al. 2001; Watson et al. 2009), the latest of which – 3XMM-DR4[4] – was released on July 23,

---

[4]http://xmmssc-www.star.le.ac.uk/Catalogue/3XMM-DR4/

Comparison of focal plane organisation of EPIC MOS and pn cameras
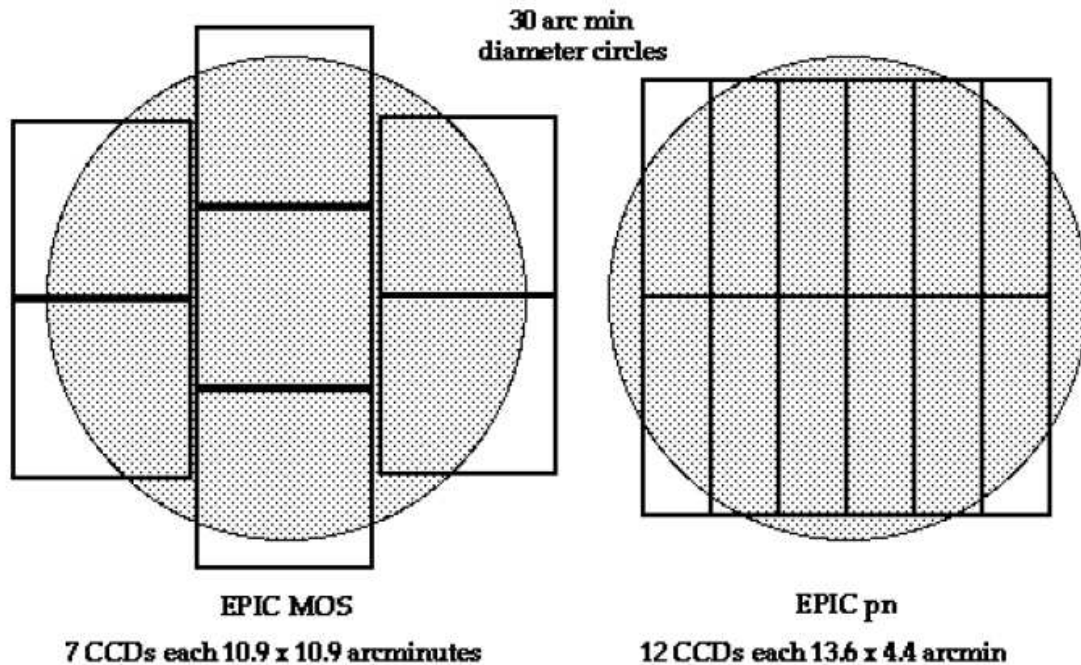
Figure 1.3: Sketch of the field of view of the *XMM-Newton* EPIC detectors, taken from the Users' Handbook. Two CCDs have been powered off due to hardware failure, possibly caused by micrometeorite impacts, these are CCDs 3 and 6 on MOS1 (centre top and centre bottom in the left hand sketch).

2013, and contains 531261 detections of 372728 unique sources.

1.2.2 *Chandra*

The *Chandra* X-ray observatory forms the X-ray section of NASA's 'Great Observatories' programme, which also includes visible and near UV coverage by the *Hubble Space Telescope* (*HST*); infrared capability, contributed by the *Spitzer Space Telescope*; and previously gamma ray and hard X-ray coverage from the now defunct *Compton Gamma Ray Observatory*. *Chandra* carries two focal plane instruments: the Advanced CCD Imaging Spectrometer (ACIS) and the High Resolution Camera (HRC); it also contains the High Energy Transmission Grating (HETG) and the Low

8.3'

8.3'

ACIS−I chips
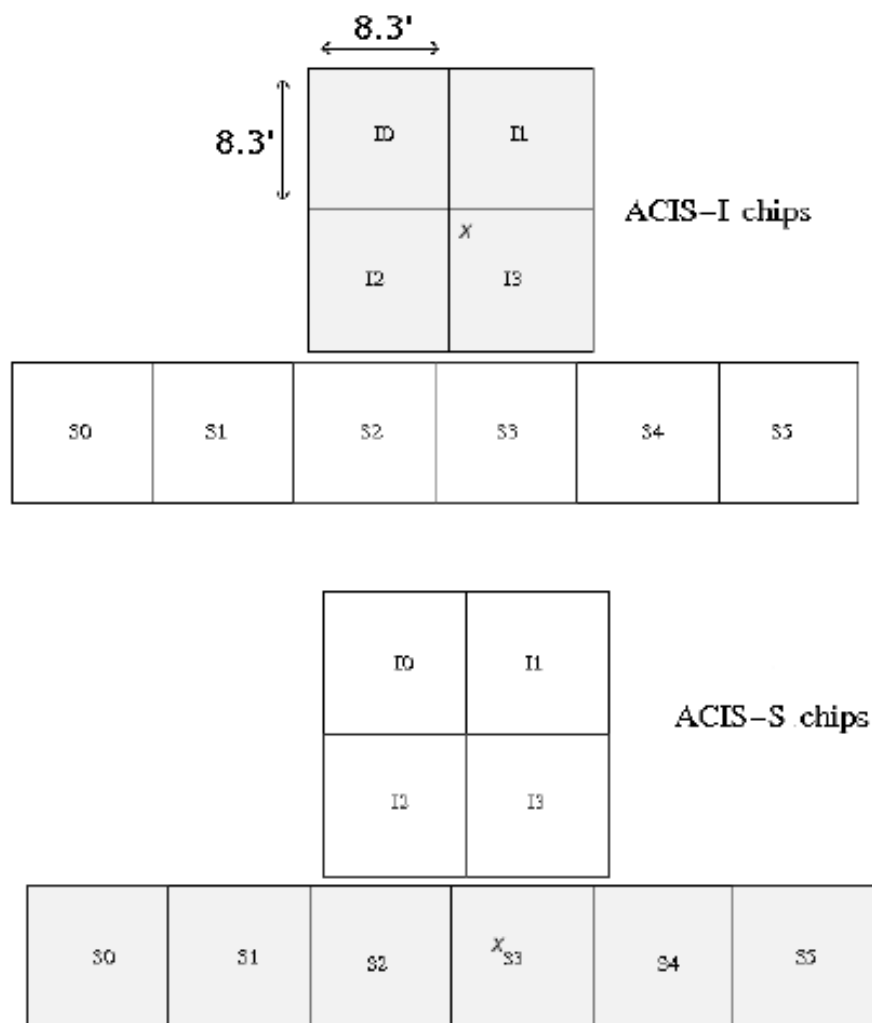
ACIS−S chips

Figure 1.4: Diagram showing the layout of the *Chandra* ACIS-I and ACIS-S chips, taken from the *Chandra* proposers' observatory guide. Both the ACIS-I and ACIS-S are used for imaging spectroscopy, whilst the ACIS-S chips can also be used in conjunction with the HETG or LETG for high resolution dispersive spectroscopy.

Energy Transmission Grating (LETG), which can be moved into place between the mirror assembly and the focal plane instruments, and are used with either focal plane instrument to carry out high resolution X-ray spectroscopy. Unlike *XMM-Newton*, the instruments aboard *Chandra* are not operated simultaneously, rather they must be alternated.
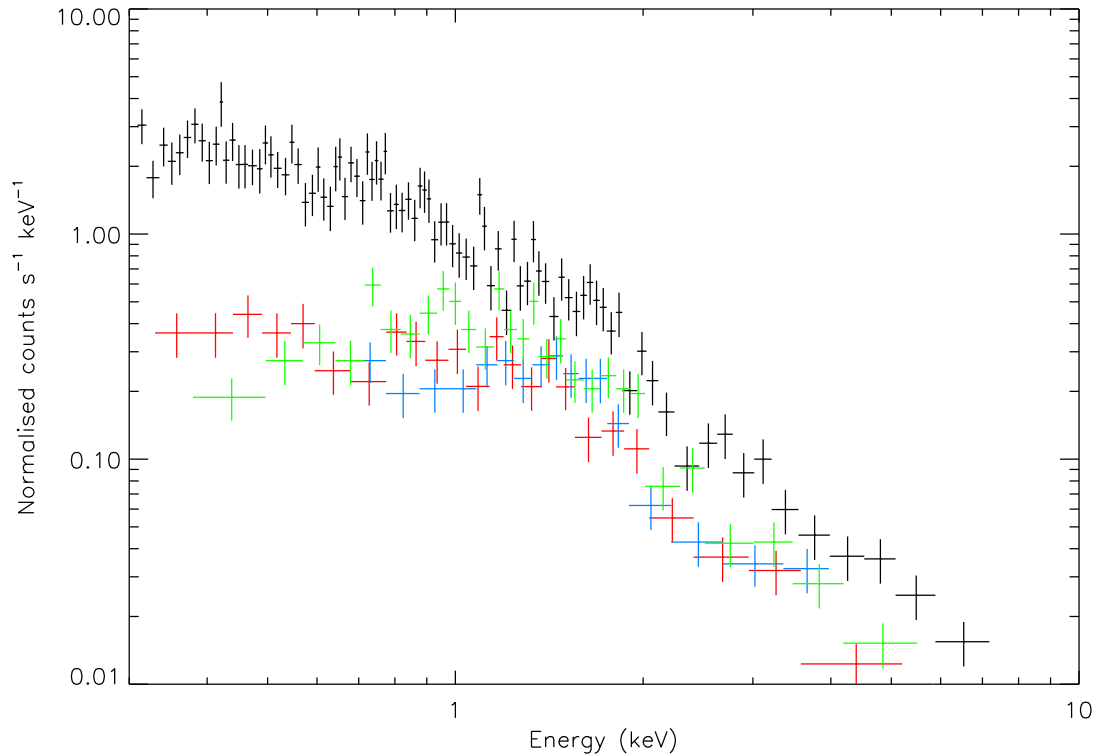
Figure 1.5: A comparison of X-ray count spectra for simulated *XMM-Newton* and *Chandra* observations of a power-law, which are shown to demonstrate the relative on-axis spectral responses of the EPIC and ACIS instruments. The spectra were created for an exposure time of 1 ks, and a power-law spectrum with $\Gamma = 2$ and a normalisation of 1×10^{-3} photons cm^{-2} s^{-1} keV^{-1} at 1 keV. The instruments shown are: *XMM-Newton* EPIC pn (black), MOS1 (red; a MOS2 spectrum is not shown, but it has a similar spectral response to MOS1), *Chandra* ACIS-I (blue), and ACIS-S (green). Although the ACIS-I and ACIS-S instruments have a similar response to MOS1 and MOS2 across much of the energy range, it should be noted that all of the *XMM-Newton* instruments are operated simultaneously, whilst the *Chandra* instruments can only be used independently. Thus, *XMM-Newton* EPIC collects $\sim$ 4 times as many photons per source as *Chandra* ACIS does.

All of the *Chandra* data sets analysed in this thesis are from the ACIS detector. ACIS, as the name suggests, is an imaging spectrometer; it has two arrays of chips, which operate in the 0.1–10 keV energy range. The ACIS-I array contains four CCDs in a 2×2 arrangement, and is used for imaging; whilst the ACIS-S array has six CCDs arranged in a line, which can be used as a read-out array for the HETG or LETG, or for imaging. Figure 1.4 shows a diagram of the arrangement of the ACIS-I and ACIS-S chips, taken from the *Chandra* proposers' observatory guide[5]. All of the ACIS-I CCDs and four of the ACIS-S CCDs are front illuminated, the other two ACIS-S CCDs (CCD 1 and 3) are back illuminated; the back illuminated CCDs have better low energy quantum efficiency, thus allow for more photons to be detected from soft sources. ACIS has excellent, sub-arcsecond spatial resolution, which is significantly better than the EPIC detector on *XMM-Newton*. However, *Chandra* has a much smaller photon collecting area than *XMM-Newton*, especially at high energies, making *XMM-Newton* more efficient for X-ray spectroscopy and timing; a comparison of *XMM-Newton* EPIC and *Chandra* ACIS spectroscopy is shown in Figure 1.5.

ACIS offers two main operating modes, these are 'timed exposure' mode where the CCDs collects data for a pre-set amount of time, and 'continuous clocking' mode, which is similar to the *XMM-Newton* EPIC timing mode. One potential issue with this instrument, given its long read out time and the fact that it focuses photons onto a small number of pixels, is pile-up. Pile-Up occurs when multiple photons are detected as a single event, and it can distort the energy spectrum and the measured count rate. However, most ULXs (and all of those observed by *Chandra* in this thesis) have relatively low count rates at X-ray energies, so the affects of pile-up are small, and in many cases can be neglected. Where pile-up could be an issue, it can be reduced by using lower frame times; this is usually achieved by using a subarray, which means that only a restricted region of the chip is used to collect data, as this

---

[5]http://cxc.harvard.edu/proposer/POG/html/

lowers the nominal frame time thus avoids loss of observing efficiency. The HRC has excellent spatial resolution, but unlike ACIS it has very poor energy resolution and is of limited use for non-dispersive spectroscopy; although, it can be used to gain useful spectral information at low X-ray energies when combined with the LETG.

1.3 Black holes

Most simply, black holes are regions of space-time so dense that not even light can escape from them. Although the idea of 'dark stars' with escape velocities in excess of the speed of light had been suggested by J. Michell and P.-S. Laplace in the 18th century, the modern theoretical concept of a black hole arose in 1916 as a consequence of the theory of general relativity (Einstein, 1916). Schwarzschild (1916) discovered a mathematical solution to Einstein's field equations which predicted a singularity on a spherical surface enclosing a mass M. Schwarzschild's solution corresponds to the surface around a non-spinning black hole (a Schwarzschild black hole), where the escape velocity equals the speed of light; it is termed the 'event horizon', and it occurs at a radius of $R_\mathrm{S} = 2R_\mathrm{g} = 2\mathrm{G}M/c^2$, where R_S is known as the Schwarzschild radius, and R_g the gravitational radius. The theory behind a Schwarzschild black hole was later generalised to a spinning black hole (Kerr black hole; Kerr 1963); indeed, the 'no-hair theorem' of black holes predicts that mass, spin and electrical charge are the only parameters that affect the how a black hole interacts with the Universe outside of the event horizon, and of these it is likely that only mass and spin are of importance in astrophysical black holes, as any electrical charge would quickly be neutralised. As they are effectively isolated from the external Universe by their event horizon, we cannot observe black holes directly; rather, we can only detect their effect on the external Universe. Due to their strong gravitational fields, some black holes attract matter from the inter-stellar medium, or a companion star if they are in a binary system; as the matter falls towards the black hole, conservation

of angular momentum causes it to spiral inwards forming an accretion disc. The disc extends inwards to the innermost stable circular orbit (ISCO; $6R_{\mathrm{g}}$ for a Schwarzschild black hole; $1R_{\mathrm{g}} < R_{\mathrm{ISCO}} < 6R_{\mathrm{g}}$ for a Kerr black hole), where material rapidly falls in to the event horizon. Viscous stresses thermalise the gravitational potential energy (Shakura & Sunyaev, 1973), which in the simplest case can be radiated locally, allowing black hole systems to be observed by astronomers.

Black holes occur on a variety of mass scales throughout the Universe, and according to the no hair theorem, the accretion flow should depend only on the mass and spin of the black hole. Furthermore, much of the dependence on mass can be removed by scaling the accretion rate to a characteristic value – the Eddington rate. The Eddington accretion rate, and the corresponding Eddington luminosity are defined as the rate and luminosity at which the outward radiation pressure and the inward gravitational pull are equal in magnitude. The Eddington luminosity for a black hole isotropically accreting pure neutral hydrogen is:

$$L_{\mathrm{Edd}} = \frac{4\pi \mathrm{G} M m_{\mathrm{p}} c}{\sigma_{\mathrm{T}}} \tag{1.1}$$

where m_{p} is the mass of a proton, and σ_{T} the Thompson cross section. In the following, we describe the various types of black hole phenomena that are observed, from the smallest stellar remnants in the local Galaxy to the largest black holes which reside in the centres of galaxies.

1.3.1   Stellar remnant black holes

As a star approaches the end point of its stellar evolution, if sufficiently massive, it will undergo core collapse when the energy it produces by nuclear fusion is no-longer sufficient to oppose its own gravity. The collapse can expel the outer layers of the star in a supernova, and if the remaining core is more massive than $\sim 1.4~M_{\odot}$, as is typically the case for a $\gtrsim~9~M_{\odot}$ star (Heger et al., 2003), then ultimately neutron

degeneracy may halt the collapse, resulting in a neutron star, as is the case in the first extra-solar X-ray source discovered – Sco X-1. For even more massive progenitor stars, neutron degeneracy in the remaining core can be insufficient to oppose further gravitational collapse, and a black hole results; this can occur through fall-back of the expelled material onto an initial neutron star, or direct collapse to a black hole in the largest stars. Typically, this can occur for stars of mass $\gtrsim$ 25 $M_\odot$ with $\sim$ solar metalicity (Heger et al., 2003); although in extreme cases stars as large as $\sim$ 50–80 $M_\odot$ may instead form neutron stars under favourable conditions in binary systems (Belczynski & Taam, 2008). It is predicted that black holes up to about $\sim$ 30 $M_\odot$ may be produced by stellar collapse at moderate metallicities; however, in low metallicity environments black holes up to $\sim$ 80 $M_\odot$ may form (Belczynski et al., 2010). Throughout this thesis we adapt the convention of Feng & Soria (2011) when discussing stellar remnant black holes, by referring to black holes of $\leq$ 20 $M_\odot$ as stellar mass black holes (sMBHs), and 20–100 $M_\odot$ objects as massive stellar black holes (MsBHs).

Although large stellar remnant black holes can theoretically be produced, this does not seem to be the case locally; all of the $\sim$ 20 confirmed Galactic black hole binaries (BHBs) are in the sMBH regime (Remillard & McClintock, 2006), and the highest known black hole mass for an extra-Galactic stellar remnant BHB is 15.65 ± 1.45 $M_\odot$ in M33 X-7 (Orosz et al., 2007)[6]. The observed sMBHs are powered by accretion from a binary companion, and these accretion systems are classed as high mass X-ray binaries (HMXBs) or low mass X-ray binaries (LMXBs) based on the relative mass of the companion star. LMXBs typically have companion stars of $\leq$ 1 $M_\odot$, and are generally type A stars or later (White et al., 1995). Accretion takes place through Roche lobe overflow; the Roche lobe is the region where material is gravitationally bound to the star, then as the star evolves, it can fill its Roche lobe

---

[6]There is evidence that IC 10 X-1 may contain a larger 24–33 $M_\odot$ black hole (Prestwich et al. 2007; Silverman & Filippenko 2008).

and material can be transferred through the L1 Lagrange point in to the accretion disc around the black hole. Black hole LMXBs are typically transient systems, they are usually very faint (quiescent), but undergo bright outbursts (e.g. King et al. 1996). During the quiescent phase material steadily builds up in the accretion disc from the companion, and an outburst is triggered when the material in the disc exceeds a critical value; this process is known as the hydrogen ionisation instability (see e.g. Done et al. 2007 for details). On the other hand, HMXBs generally contain massive O or B stars, and have accretion flows dominated by captured stellar winds, and so are persistent.

X-ray spectra from BHBs mainly show a composite of two components – a thermal component and a non-thermal (power-law) component (Remillard & McClintock, 2006); but some BHBs also require a contribution from reflection, where the X-ray power-law is reflected by the accretion disc, producing a broad feature at $\sim$ 10–30 keV (Done & Nayakshin, 2001). The thermal component originates from the disc, and is well represented by multi-colour-disc (MCD) models. MCDs consist of the sum of black bodies originating from different radii in the accretion disc; in a standard 'thin disc' (Shakura & Sunyaev, 1973) the disc temperature varies as $T(R) \propto R^{-3/4}$. So, the inner disc dominates the MCD spectrum, leading to a characteristic peak disc temperature corresponding to the inner disc, which in BHBs is in the X-ray band at $\sim$ 1 keV. The non-thermal component originates from Comptonisation of the soft disc photons in an optically thin medium (Sunyaev & Trümper 1979; Sunyaev & Titarchuk 1980), and is often modelled as a power-law with an exponential cut off at 30–100 keV (e.g. McClintock & Remillard 2006).

Variations in the balance of the two components of this composite spectrum give rise to four canonical sub-Eddington states in BHBs (Figure 1.6; see e.g. Remillard & McClintock 2006, Done et al. 2007): the quiescent state; the low/hard or hard state; the high/soft or thermal state; and the very high or steep power-law state. However, these states do not always exactly match the observed parameters in BHBs, and
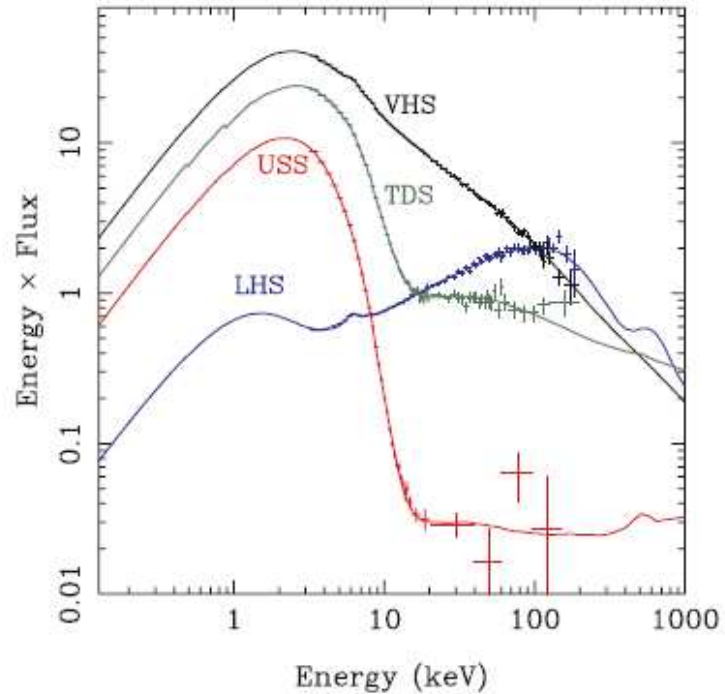
Figure 1.6: A range of X-ray spectra observed for the Galactic BHB GRO 1655−40, taken from Done et al. (2007). The states are: (LHS) low/hard state; (TDS) thermal dominant of high/soft state; (SPL) steep power-law or very high state; and (USS) ultra soft state, which can be considered part of the high/soft state.

this has given rise to the suggestion of additional intermediate states, which exhibit features from more than one of the canonical states (Mendez & van der Klis, 1997). The quiescent state occurs at the lowest Eddington ratios, when the X-ray spectrum of the BHB is both faint and non-thermal, being best represented by a hard power-law (Remillard & McClintock 2006; McClintock & Remillard 2006; 1–10 keV luminosity of $L_X \sim 10^{30.5}$–$10^{33.5}$ erg s^{-1}; power-law spectral index of $\Gamma \sim 1.5$–2.1). Next, the low/hard state is characterised by a non-thermal power-law spectrum with $\Gamma \sim 1.4$–2.1 (Remillard & McClintock, 2006), plus some contribution from a cool thermal component. Also, this state displays a persistent radio jet (Fender, 2006), and has high levels of variability, with fractional variability of ~ 30 per cent being typical (Belloni, 2010). Possibly, the low/hard state can be understood as a truncated disc

spectrum, with an inner optically thin flow coupled to an inner disc corona (Done et al., 2007). It has been suggested that the quiescent and low/hard states result from the same physical mechanism operating over several orders of magnitude in X-ray luminosity (Remillard & McClintock, 2006); but, this may be unlikely, as Corbel et al. (2006) demonstrate that the quiescent state spectrum of XTE J1550-564 is spectrally softer than the low/hard state.

The X-ray spectrum of BHBs in the high/soft state is dominated by a thermal component, which to the first order can be approximated as an MCD, and peaks around the temperature of the ISCO. The progression from the low/hard to the high/soft state may be consistent with the inner edge of the thin disc moving in towards the ISCO, and the hot inner-flow collapsing (Esin et al. 1997; Poutanen et al. 1997). This luminosity at which a source begins to exhibit the high/soft state varies, even within an individual source, from ~ 0.003–$0.2 L/L_{\rm Edd}$ (Done & Gierliński, 2003). Finally, the very high state tends to be observed in BHBs as their luminosity approaches the Eddington limit; it has significant contributions from both thermal and non-thermal components, where the non-thermal component is power-law like with typical soft spectral indexes of $\Gamma \sim 2.5$ (Remillard & McClintock, 2006). High frequency quasi-periodic oscillations (QPOs) are often associated with the very high state, and explosive jet formation and coronal mass ejection are seen in some sources (McClintock & Remillard, 2006).

1.3.2 Supermassive black holes

Supermassive black holes (SMBHs) with masses $\sim 10^5$–10^{10} $M_\odot$ occupy the opposite extreme of the black hole mass scale to sMBHs. Most galaxies are thought to contain SMBHs at their centres (e.g. Kormendy & Richstone 1995; Magorrian et al. 1998). Indeed, this is thought to be the case in the Galactic centre, where some of the best evidence comes from the inferred orbits of stars around the centre of the Galaxy
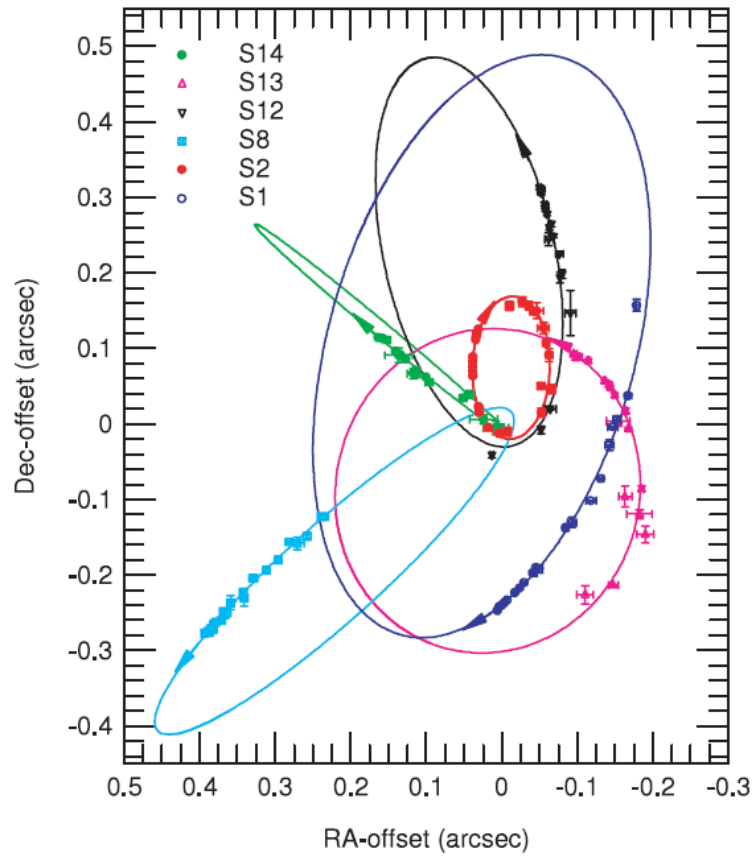
Figure 1.7: A projection of the inferred orbits of six stars around the Galactic centre, which implies the presence of a SMBH. The figure is taken from Eisenhauer et al. (2005).

(Schödel et al. 2002; see Figure 1.7); this implies that there must be an undetected $4.1 \pm 0.6 \times 10^6$ $M_\odot$ of mass (Ghez et al., 2008), and it is so dense that it can presumably only be a black hole. SMBHs may be produced by the direct collapse of massive population III stars, which can form with masses $\gtrsim 100$ $M_\odot$ in the low metallicity environment of the early Universe (Bromm et al., 2002). Such massive stars could undergo direct collapse to a black hole, and subsequently build up mass by accreting gas (e.g. Yu & Tremaine 2002), or through hierarchical black hole mergers (e.g. Schneider et al. 2002). Alternatively, the progenitors of the SMBHs may form via the gravitational collapse of gas in dark matter halos, without the need to form a massive star (Begelman et al. 2006; Regan & Haehnelt 2009). Although the SMBH in our Galaxy is currently relatively faint, it is thought that active galactic nuclei (AGNs) are powered by accretion on to SMBHs, and presently faint SMBHs must have previously been much more luminous (e.g. Rees 1984). AGNs are notable for their bright continuum spectra over many orders of magnitude in electromagnetic frequency; and, although all AGNs are thought to be powered by accretion onto SMBHs, it is clear from observations that this process must be able to produce several classes of sources with distinct properties. In the following paragraphs we provide a brief taxonomy of AGN, before describing unified models which attempt to explain all of the varying phenomena using a single class of object.

'Seyfert galaxies' are an eponymous class of galaxies containing AGN that were first identified by Seyfert (1943); Seyfert galaxies were originally split into 'Seyfert 1 galaxies' and 'Seyfert 2 galaxies' based on their observational properties, but later intermediate classes with properties of both were also used (e.g. Seyfert 1.9; Osterbrock 1977). Seyfert 1 galaxies have highly luminous continuum spectra, with very broad emission lines from allowed transitions, and narrower forbidden lines. These lines are Doppler broadened, with the allowed lines corresponding to speeds of ~ 1000–5000 km s^{-1} and the forbidden lines ~ 500 km s^{-1}. Seyfert 2 galaxies have much fainter continuum spectra, and less X-ray emission, indicating that they have

been absorbed by large hydrogen column densities of $\sim 10^{22}$–10^{24} cm^{-2}. Similarly to Seyfert 1 galaxies, they display emission lines, but both the forbidden and permitted lines are narrow. Notably, where they are spatially resolved, both Seyfert 1 and Seyfert 2 galaxies tend to be spiral galaxies. 'Broad-line radio galaxies' and 'narrow-line radio galaxies', as their names suggest, can to a certain extent be considered the radio loud analogues of Seyfert 1 and Seyfert 2 galaxies. However, breaking the analogy with Seyferts, both broad- and narrow-line radio galaxies can have extended radio lobes, which are thought to be inflated by jets from the central source (Blandford & Rees 1974; Scheuer 1974); and, they are typically found in large elliptical galaxies. An additional class of 'weak-line radio galaxies' has also been suggested, where the central source is probably relatively under-powered (e.g. Tadhunter et al. 1998).

Both radio loud and radio quiet 'quasars/QSOs'[7] have very bright continuum spectra, and similarly to the Seyfert 1 and broad-line radio galaxies, they display broad emission lines. Some QSOs also have broadened absorption lines, which are thought to originate in the source itself, whilst many narrower absorption features are thought to be due to intervening material along our line-of-sight to the source. QSOs vary in bolometric luminosity from $\sim 10^{45}$ to greater than 10^{48} erg s^{-1}, and observations of high redshift sources show that bright QSOs were much more common in earlier epochs. Due to their similar properties, it has been suggested that radio quiet quasars may be the high luminosity counterparts of Seyfert 1 galaxies, rather than a distinct class (Staubert & Maisack, 1996). Radio loud quasars are further split into sources with steep and flat radio spectra; sources with steep spectra tend to be lobe dominated, whilst flat spectra radio loud quasars tend to be dominated by emission from the core (Tadhunter, 2008). 'Blazars' are radio loud AGN that

---

[7]Quasars is short for quasi-stellar radio sources, but it was found that about 90 per cent of quasars are relatively radio quiet, so these objects are often referred to as quasi-stellar objects, or QSOs instead (Carroll & Ostlie, 2003).
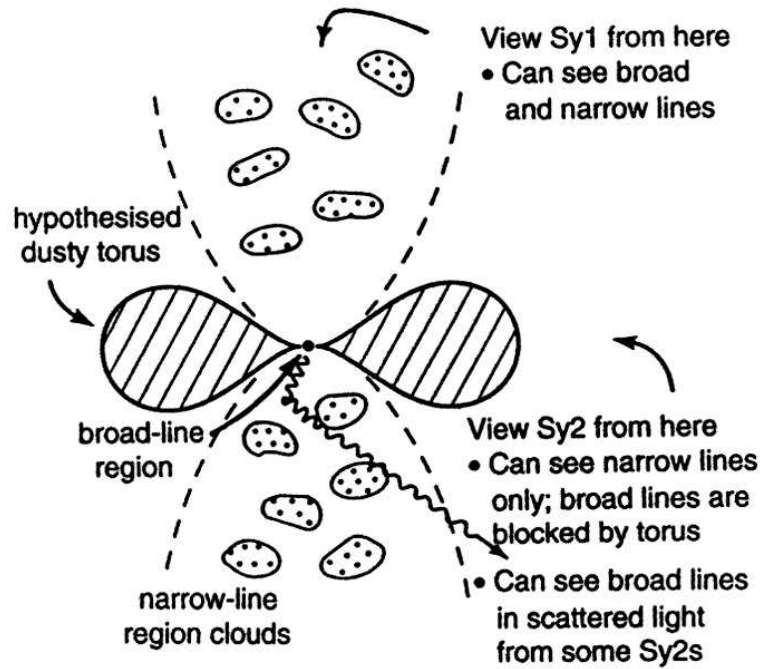
Figure 1.8: A sketch of a unification scheme for radio quiet AGN.

display rapid variability and a high degree of linear polarisation. Blazars are further split into 'BL Lac objects', which have only faint spectral lines, and 'optically violent variable quasars', which are more luminous and display broad emission lines. Flat spectrum radio loud quasars are often highly variable at optical wavelengths, and can also be classified as optically violent variable quasars (Tadhunter, 2008).

It has long been suggested that the different types of AGNs were in fact the same object, but observed under different conditions (Rowan-Robinson, 1977). Separate unification schemes exist for radio quiet and radio loud AGNs; in radio quiet sources, it is thought that the broad lines originate from close to the central SMBH, the narrow lines are produced in clouds much further above the accretion disc, and a dusty torus surrounds the broad line region, which can obscure it from view at certain inclinations (e.g. Veilleux 2003; Figure 1.8[8]). Then, if viewed close to edge on, the observer has a clear line-of-sight to the narrow line region but not the broad line

---

[8]http://ned.ipac.caltech.edu/level5/March02/Roy/Figures/figure2.jpg
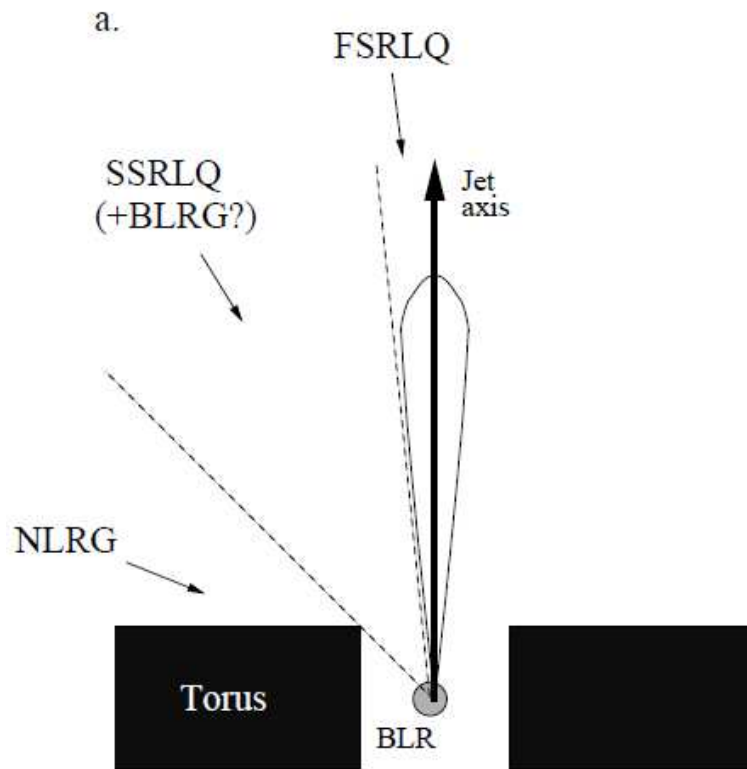
Figure 1.9: A sketch of a suggested unification scheme for radio loud AGN, taken from Tadhunter (2008). The abbreviations used are: FSRLQ – flat spectrum radio loud quasar; SSRLQ – steep spectrum radio loud quasar; BLRG – broad-line radio galaxy; NLRG – narrow-line radio galaxy; BLR – broad-line region.

region, so the source appears as a Seyfert 2 galaxy; else, if observed closer to face on, the observer sees both the broad and narrow line regions, and it appears as a Seyfert 1 galaxy, or a radio quiet Quasar if the AGN is more luminous. In this case, we might expect a class of 'QSO 2s' corresponding to Seyfert 2 galaxies in very luminous radio quiet AGNs, and indeed these sources may have been observed (Wolter et al., 2005). A similar unification scheme exists for radio loud AGN, but with the addition of a radio jet (e.g. Tadhunter 2008; Figure 1.9). In this case, a narrow-line radio galaxy is observed at angles where the torus blocks the broad line region from view, and if both the broad- and narrow-line regions can be observed, then a broad-line radio galaxy or a steep radio spectrum quasar is seen, depending on the luminosity of

the AGN. Finally, if the line-of-sight to the source is within the beaming angle of the jet, then a flat radio spectrum quasar or blazar may be observed (Barthel 1989; Tadhunter 2008).

1.3.3   The X-ray background

Finally, the largest scale on which we observe emission from black holes is in the X-ray background; as previously mentioned, the X-ray background was first discovered when it was accidentally observed by Giacconi et al. (1962), and it is thought that its cosmic component can be accounted for by discrete X-ray sources. Whilst the soft ($\lesssim 1$ keV) X-ray background was seen to be dominated by Galactic emission and absorption (McCammon & Sanders, 1990), the hard X-ray background was determined to be nearly isotropic on large scales, having only weak Galactic anisotropies (Warwick et al. 1980; Iwan et al. 1982), implying that it probably had an extra-Galactic origin. Subsequent observations have been able to resolve much of the X-ray back ground into discrete sources, e.g. Shanks et al. (1991) used a deep *Rosat* image to show that quasars can account for $\gtrsim 30$ per cent of the X-ray background at 1 keV; Mushotzky et al. (2000) used *Chandra* to resolve ~ 75 per cent of the 2–10 keV background into point sources; and Moretti et al. (2003) have used combined *Rosat*, *Chandra* and *XMM-Newton* data to show that $94.3^{+7.0}_{-6.7}$ and $88.8^{+7.8}_{-6.6}$ per cent of the soft (0.5–2 keV) and hard (2–10 keV) X-ray background respectively can be accounted for by known discrete sources. Furthermore, Moretti et al. (2003) claim that the entire soft band X-ray background can be accounted for by extrapolating the population of known sources to lower fluxes; however, in the hard band, this fails to account for ~ 7 per cent of the observed background. Current thinking is that much of the unresolved hard X-ray background can be accounted for by a population of heavily obscured Compton thick AGNs (e.g. Gilli et al. 2007; Moretti et al. 2012). Indeed, X-ray observations have been able to identify a number of candidate

Compton thick AGN (e.g. Georgantopoulos et al. 2013; Mateos et al. 2013).

1.4 Ultraluminous X-ray sources

There is excellent evidence for the existence of black holes with masses in the stellar mass and supermassive regimes; but, with the discovery of ULXs by *Einstein* (Fabbiano, 1989), astronomers had a new class of black hole phenomenon which did not seem to fit in to either class. ULXs are non-nuclear X-ray sources in external galaxies with $L_X \geq 10^{39}$ erg s^{-1} (e.g. Roberts 2007; here, and throughout the remainder of this work, unless stated otherwise, L_X and f_X refer to luminosities and fluxes in the 0.3–10 keV band). ULXs cannot be particularly faint, mis-placed AGNs; as, if they were SMBHs, they would be expected to fall to the centre of its galaxy due to dynamical friction within a Hubble time (Tremaine et al., 1975). However, the Eddington limit for a 10 $M_\odot$ sMBH is $\sim 1.3 \times 10^{39}$ erg s^{-1} (Makishima et al., 2000), and Galactic BHBs are not seen to regularly accrete at rates close to the Eddington limit, rather they are usually sub-Eddington (e.g. $\sim$ a few per cent of Eddington in the low/hard state; McClintock & Remillard 2006). So, if the accretion state in ULXs is analogous to the BHBs, then even the faintest ULXs would imply a population of black holes of ~ 100 $M_\odot$; whilst some of the brightest ULXs, including the hyperluminous X-ray sources (HLXs; $L_X \geq 10^{41}$ erg s^{-1}; e.g. Matsumoto et al. 2001; Farrell et al. 2009; Pizzolato et al. 2010) would be a factor of $\gtrsim$ 100 more massive still. This led to the suggestion that ULXs could represent a new population of black holes with masses between those of the stellar remnants and the supermassive objects – the so called 'intermediate-mass black holes' (IMBHs; 10^2–10^4 $M_\odot$; Colbert & Mushotzky 1999).

With the advent of *XMM-Newton* and *Chandra*, high quality ULX X-ray spectra could be obtained for the first time; and, at first the data seemed to support the IMBH hypothesis. When the X-ray spectra were fitted using phenomenological MCD

plus power-law models, as had been employed with much success in BHBs, they revealed the presence of characteristic MCD profiles; but, whilst MCDs in BHBs peak around ~ 1 keV, the discs in ULXs seemed to be cooler (~ 0.1 keV). In standard thin accretion discs, the inner disc temperature scales with the black hole mass as $T_{\mathrm{in}} \propto M^{-1/4}$; therefore the apparent cool discs in ULXs were used as evidence to argue in favour of IMBHs in ULXs (e.g. Kaaret et al. 2003; Miller et al. 2003; Miller et al. 2004). Furthermore, individual Galactic BHBs follow a well known X-ray luminosity-disc temperature relation – $L_{\mathrm{X}} \propto T_{\mathrm{in}}^4$; but ULXs occupy a completely separate region of the luminosity-temperature parameter space, as they are both cooler and more luminous. Thus, it seemed ULXs were not BHBs with very high accretion rates, rather it was suggested that they must contain a new type of primary; this was taken as further evidence that ULXs were IMBHs (Figure 1.10; Miller et al. 2004). More evidence for IMBHs came from the detection of BHB-like QPOs in a few ULXs, apparently at much lower frequencies than the corresponding QPOs in BHBs, which were used to argue that they were in the same sub-Eddington accretion states, but with scaled up masses (e.g. M82 X-1, Strohmayer & Mushotzky 2003; NGC 5408 X-1, Strohmayer et al. 2007, Strohmayer & Mushotzky 2009; and NGC 6946 X-1 Rao et al. 2010).

However, there were several inconsistencies with the interpretation of ULXs as sub-Eddington accreting IMBHs. Observational evidence against IMBHs came from the close spatial and temporal association of ULXs with ongoing star formation, as was most notably seen in the Cartwheel galaxy (Gao et al. 2003; King 2004; Mapelli et al. 2008), where an infeasibly high fraction of the galaxies mass would be contained in black holes if all of the ULXs were IMBHs (King, 2004). This suggested that they were a type of HMXB, which naturally provides them with the large mass reservoir required to sustain ULX luminosities (Rappaport et al., 2005). Also, it was noted that the power-law form of the X-ray luminosity function (XLF) for HMXBs in nearby star forming galaxies was smooth across the transition from
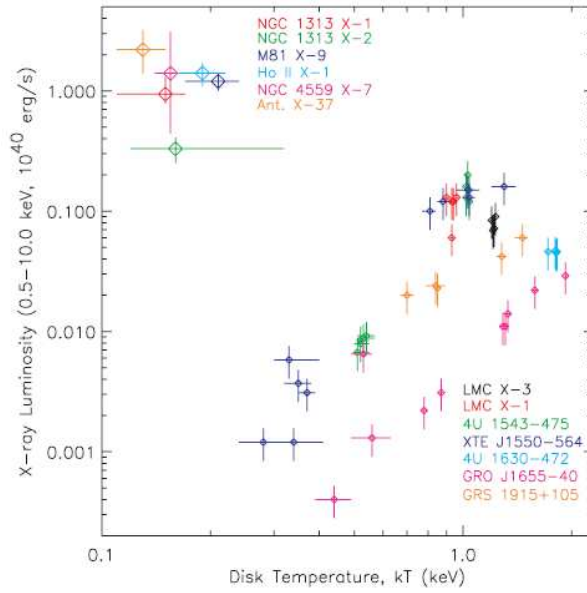
Figure 1.10: X-ray luminosities and inferred disc temperatures for a sample of ULXs (large diamonds), a number of BHBs (small diamonds) are also shown for comparison, taken from Miller et al. (2004). The fact that ULXs appeared to be both more luminous and cooler was taken as evidence that they contained IMBHs.

standard HMXBs to ULXs, but then breaks at $\sim 2 \times 10^{40}$ erg s^{-1} (Figure 1.11; Grimm et al. 2003; Swartz et al. 2004; Swartz et al. 2011; Mineo et al. 2012). This break is important, as its luminosity is only ~ 10 per cent of the Eddington luminosity for a $\sim 10^3$ $M_\odot$ IMBH; a similar turn-off at such a low Eddington fraction is not seen in other accretion-powered populations, and it made it difficult to reconcile the ULXs with a population of IMBHs. Clearly, the multiple lines of evidence were contradictory, and the nature of the primary black hole in ULXs remained a matter of some debate. However, subsequent reanalyses of some of the highest quality *XMM-Newton* X-ray spectra revealed features that were not consistent with sub-Eddington state identifications – ULXs have both a soft excess and high energy curvature at > 2 keV (Figure 1.12; Roberts et al. 2005; Stobbart et al. 2006; Gonçalves & Soria 2006; Gladstone et al. 2009; Miyawaki et al. 2009). Furthermore, Heil et al. (2009) examined the timing propeties of a sample of 16 ULXs, and found that variability in
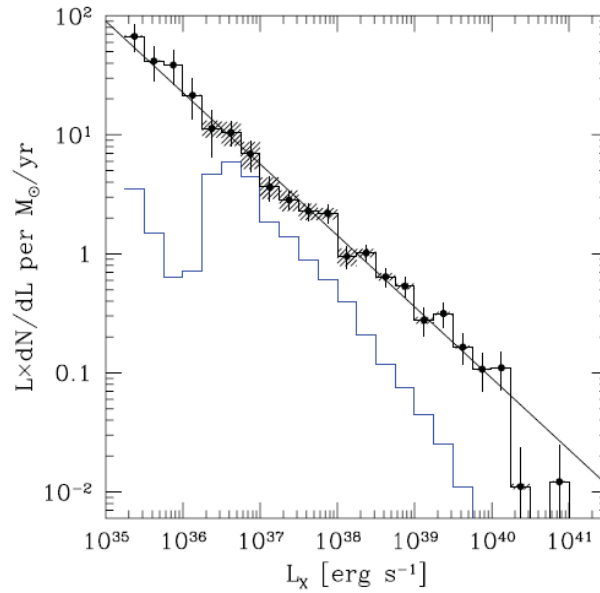
Figure 1.11: HMXB XLF normalised by star formation rate (Mineo et al., 2012), where the blue line shows the expected cosmic X-ray background contamination, and the black line a power-law fitted to the XLF. The power-law form of the HMXB XLF appears to break at $\sim 10^{40}$ erg s^{-1}, this behaviour is unlike the sub-Eddington BHBs, and was t aken as evidence that ULXs did not contain IMBHs.

some ULXs was supressed relative to that seen in BHBs and AGNs; and, Middleton et al. (2011a) disputed the sub-Eddington identification of the QPO in NGC 5408 X-1, as it was dissimilar to QPOs observed in very high state BHBs. Instead of IMBHs, it now seems that the majority of ULXs are likely powered by accretion onto fairly typical stellar remnant black holes. In this case, many may be classic sMBHs, which would need to be accreting at super-Eddington rates to produce the observed luminosities. However, this requirement could be relieved somewhat in some ULXs, if they instead contain slightly larger MsBHs, which may form in regions of low metallicity (Zampieri & Roberts 2009; Mapelli et al. 2010; Belczynski et al. 2010).

Stobbart et al. (2006) demonstrated that some of the highest quality *XMM-Newton* ULX spectra were well represented by a model consisting of two thermal (or
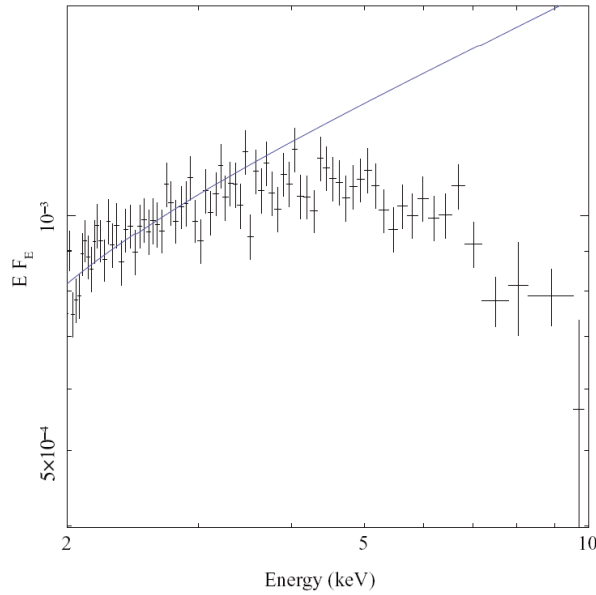
Figure 1.12: *XMM-Newton* EPIC pn data of NGC 1313 X-2 with clear high energy curvature, the data are over plotted with a low energy power-law, corresponding to the low energy component in a broken-power-law fit to the data (Gladstone et al., 2009).

thermal-like) components, different to the spectra shown by typical sub-Eddington black holes, suggestive of a new, super-Eddington 'ultraluminous' accretion state (Roberts, 2007). Gladstone et al. (2009) investigated this further, using some of the highest quality *XMM-Newton* ULX spectra. They identified three characteristic ULX spectral types, which they speculated could represent a sequence with accretion rate. In their interpretation, at around the Eddington limit ULXs appear with broad disc-like spectra; as the accretion rate becomes more super-Eddington a two-component spectrum emerges, initially peaking in the higher energy component; and, at the highest super-Eddington accretion rates the balance of the two components shifts, and the ULX appears instead with its peak at the softer end of the 0.3-10 keV spectrum. Throughout this thesis we refer to these three ultraluminous spectral regimes as the 'broadened disc', 'hard ultraluminous' and 'soft ultraluminous' states respectively (Figure 1.13). Initially Gladstone et al. (2009) interpreted the hard

spectral components as a Comptonising corona around the inner disc, which is cooler than the corona in BHBs and optically thick; and the soft component as the disc emission minus the inner regions which would be obscured by the corona. However, more recent work has refined this; the hard spectral component may indeed originate in a Comptonising corona around the inner regions of the accretion disc; similarly, the consistently super-Eddington Galactic black hole binary GRS 1915+105 (Done et al., 2004) also requires cool Comptonisation (Zdziarski et al. 2001; Middleton et al. 2009; Ueda et al. 2009). Alternatively, the hard emission could instead be coming directly from the hot inner disc (Middleton et al. 2011a), with its spectral shape plausibly due to a large colour correction (Kajava et al., 2012). The soft component likely originates in the photosphere at the base of a massive radiatively driven wind, as is expected to occur in black holes that are close to or exceeding Eddington-limited accretion (Poutanen et al., 2007); this is consistent with the apparent cooling of the soft component as its luminosity increases ($L \propto T^{-3.5}$; Kajava & Poutanen 2009).

However, the Gladstone et al. (2009) model does not offer a unique solution, and other models of ULX spectra include slim disc and reflection models. Super-critical slim discs (Abramowicz et al., 1988) are able to reproduce the observed spectra in some ULXs, and predict masses in the MsBH regime (Vierdayanti et al., 2006). However, a slim disc alone may not be a good physical model, as radiatively driven winds are expected to be driven from close to the inner disc, as the accretion rate becomes super-Eddington (Poutanen et al. 2007; Dotan & Shaviv 2011). Reflection models require that a power-law-like continuum can be produced at a few r_{g} above the accretion disc; then, they argue that all of the observed spectral features of ULXs can be produced by relativistically blurred reflection from the accretion disc (Caballero-García & Fabian, 2010). Proponents of this model suggest that the power can be magnetically extracted from the accretion disc to the emission region, thus avoiding the Eddington limit (Caballero-García & Fabian, 2010).

In the remainder of this thesis we present four studies which attempt to answer
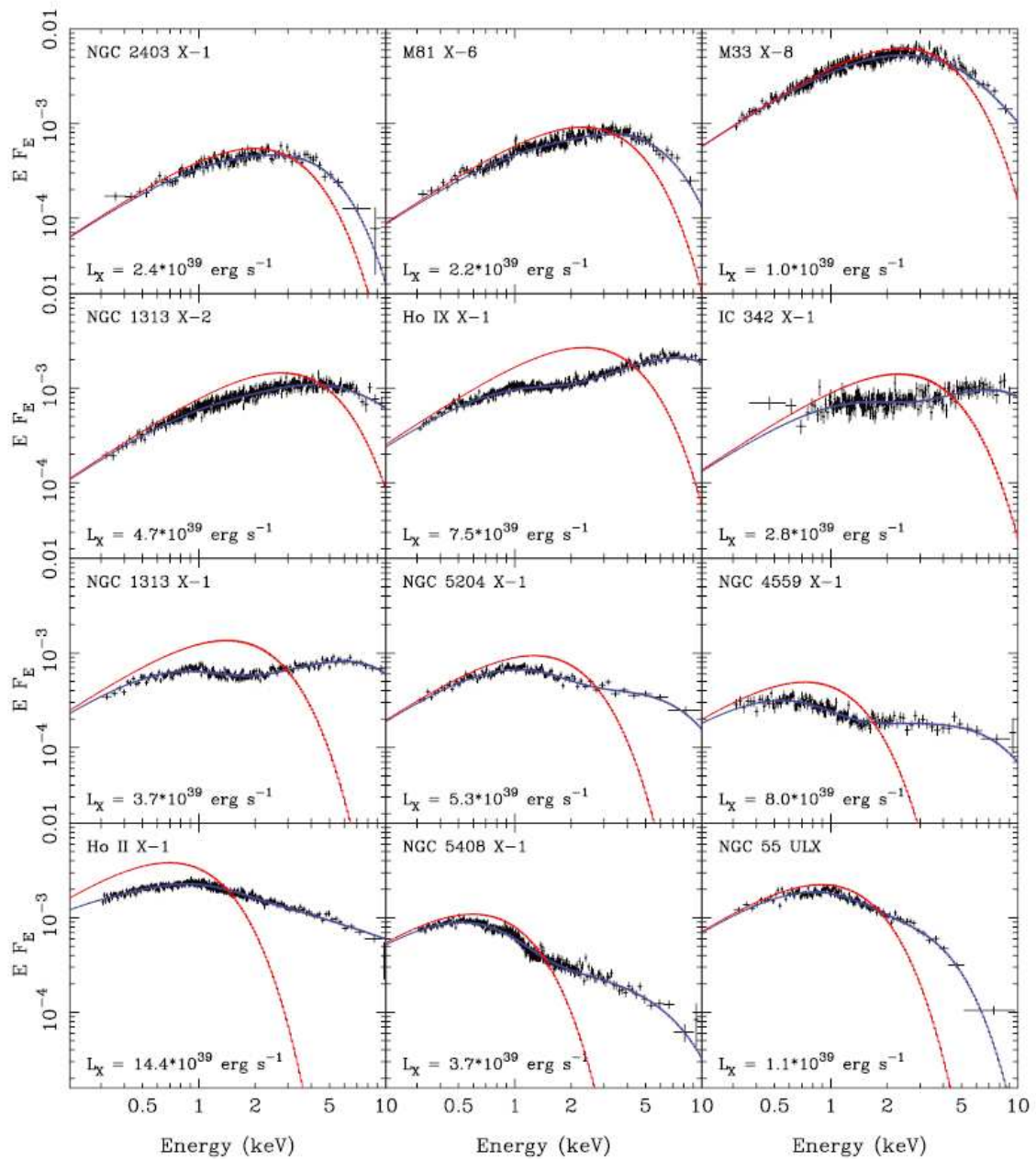
Figure 1.13: X-ray spectra from a sample of ULXs with high quality X-ray data, taken from Gladstone et al. (2009). The data shown in black are from the EPIC pn, and are unfolded through their ultraluminous state model, which includes an optically thick corona and emission from the outer disc. The model is shown in blue, and the recovered disc spectrum is shown in red. The first four objects (starting at the top left, and reading across each row) have broadened disc spectra, the next three objects have hard ultraluminous spectra, and the final five soft ultraluminous spectra.

a number of remaining pertinent questions in the field of ULX astronomy. Having here argued that most ULXs are sMBHs or MsBHs, in Chapter 2 we ask whether the brightest ULXs may still contain IMBHs. In one of the bright ULXs we find evidence of an ultraluminous state spectrum; so, in Chapter 3 we look at this source in more detail, and examine inter-observational changes in its X-ray properties. In Chapter 4, we present analysis of a sample of ULXs which mostly have more typical X-ray luminosities, and ask what their timing properties can tell us about their putative super-Eddington accretion states. In Chapter 5 we present a combined X-ray and optical analysis of a sample of broadened disc ULXs, using a new spectral model of emission from a colour-temperature corrected accretion disc. Finally, in Chapter 6 we draw conclusions from the previous four chapters, and outline some avenues for further progress in the field of ULX astronomy, that should be achievable in the near future.

Chapter 2

The most extreme ultraluminous X-ray sources: evidence for intermediate-mass black holes?

We present the results from an X-ray and optical study of a new sample of eight ULX candidates, which were selected as the brightest ULXs ($L_X > 5 \times 10^{40}$ erg s^{-1}) located within 100 Mpc identified in a cross correlation of the 2XMM-DR1 and RC3 catalogues. These objects are so luminous that they are difficult to describe with current models of super-Eddington accretion onto all but the most massive stellar remnants; hence they are amongst the most plausible candidates to host IMBHs. Two objects are luminous enough in at least one observation to be classed as HLX candidates, including one persistent HLX in an S0 galaxy that (at 3×10^{41} erg s^{-1}) is the second most luminous HLX yet detected. The remaining seven sources are located in spiral galaxies, and several appear to be closely associated with regions of star formation as is common for many less luminous ULXs. However, the X-ray characteristics of these extreme ULXs appear to diverge from the less luminous objects. They are typically harder and potentially more variable on short timescales, which is consistent with the sub-Eddington low/hard state, and given the observed luminosities of these objects suggests the presence of 10^3–10^4 $M_\odot$ IMBHs. This

strengthens the case for these brightest ULXs as good candidates for the eventual conclusive detection of IMBHs in the present-day Universe. However, we caution that a combination of the highest plausible super-Eddington accretion rates and the largest permitted stellar remnant black holes cannot yet be completely ruled out.

2.1 Introduction

Although the existence of a population of black holes with masses between those in Galactic BHBs and in AGNs has long been postulated, these IMBHs have remained observationally elusive, with dynamical evidence for such objects in large globular clusters still the subject of some dispute (e.g. Gebhardt et al. 2005; Anderson & van der Marel 2010). Yet such objects appear necessary to explain the initial seeding of the SMBHs now present in most galaxy nuclei (Volonteri, 2010), whose mass was subsequently built up either through the accretion of gas (e.g. Yu & Tremaine 2002), or through hierarchical black hole mergers (e.g. Schneider et al. 2002). It is likely that the processes forming these seeds – for example, the collapse of Population III stars, or dynamical interactions in dense stellar environments – would have left relic IMBHs in the halos of present-day galaxies (e.g. Ebisuzaki et al. 2001; Madau & Rees 2001; Islam et al. 2004). Indeed, the latter process may still be ongoing in some young, dense stellar clusters (Portegies Zwart et al. 2004), adding to the primordial IMBH population. Furthermore, the tidal stripping of merging satellite galaxies containing nuclear black holes may also add to this population in large galaxy haloes (e.g. Bellovary et al. 2010). It is therefore puzzling that the existence of such IMBHs remains to be confirmed.

Although ULXs were once touted as IMBH candidates, it now seems that most are probably stellar remnant black holes in a new super-Eddington accretion state (Chapter 1; Gladstone et al. 2009); however, there do remain some plausible IMBH candidates in the ULX population. Work by Swartz et al. (2011) has demonstrated

that an extrapolation of the local XLF out to 100 Mpc underpredicts the observed numbers of high luminosity ULXs, particularly those that possess luminosities greater than 10^{41} erg s^{-1}, suggesting that such objects originate in a separate physical population to the HMXBs that likely underlie most ULXs. Indeed, while a combination of massive stellar black holes, possibly formed in low metallicity regions (up to 80 $M_\odot$; Zampieri & Roberts 2009, Belczynski et al. 2010), and close to maximal radiation from super-Eddington accretion (~ 20 $L_{\rm Edd}$ from a face-on disc; Ohsuga & Mineshige 2011) could explain ULXs up to $\sim 10^{41}$ erg s^{-1}, objects exceeding this luminosity appear to require a different physical scenario. It is these HLXs that may present us with the best evidence for IMBHs to date.

Very few *bona fide* HLXs are known: the best candidates include M82 X-1 (e.g. Matsumoto et al. 2001), ESO 243-49 HLX-1 (Farrell et al., 2009), Cartwheel N10 (Pizzolato et al., 2010) and CXO J122518.6+144545 (Jonker et al., 2010). Most observations have focussed on the nearest HLX, M82 X-1 at $d \sim 4$ Mpc, and the most luminous, ESO 243-49 HLX-1 at $L_{\rm X,peak} \sim 10^{42}$ erg s^{-1}. M82 X-1 is notable for several reasons, including its co-location with a massive, young stellar cluster (Portegies Zwart et al., 2004), the detection of a $50 - 100$ mHz QPO in its power spectrum (Strohmayer & Mushotzky, 2003), a reported 62-day periodicity in its X-ray light curve (Kaaret & Feng, 2007) and plausible transitions between a low/hard state and a thermal dominant state (Feng & Kaaret, 2010), all of which contribute to the picture of this object as an excellent IMBH candidate. ESO 243-49 HLX-1 is most remarkable for its high peak luminosity and regular outbursts, which appear to possess a fast rise/exponential decay profile and to repeat on timescales of ~ 1 year (Lasota et al., 2011). This object also appears to mimic BHXRB behaviour in its hardness-intensity diagram as it transits through its outbursts, indicative of sub-Eddington state changes (Servillat et al., 2011).

It is evident that the most luminous ULXs are rare, and little is known about them as a class; yet from the arguments presented here, they appear to be potentially

important targets in the ongoing search for IMBHs. One way to learn more of this population is to extend the number of known objects using archival searches. As such, this chapter details a study of ten candidate extreme ULXs selected from the Walton et al. (2011b) catalogue of ULXs detected in the 2XMM-DR1 survey, that display observed luminosities well in excess of the break in the XLF, including two new HLXs.

This chapter is adapted from Sutton et al. (2012), early results of which were published in Sutton et al. (2011), and is laid out as follows. In Section 2.2 selection of the new sample, and the reduction of the optical and X-ray data is described. Section 2.3 details the imaging, spectral and timing results from all *XMM-Newton* and *Chandra* datasets for the sources available at the time of the study, and describes some optical follow up work. The characteristics of these objects are then compared to those of the less luminous bulk of the ULX population in Section 2.4, before the implications of the findings are discussed with respect to the nature of the objects in Section 2.5, and finally the chapter is summarised in Section 2.6.

2.2   Sample selection & data reduction

2.2.1   Sample selection

Walton et al. (2011b) present a catalogue of 470 candidate ULXs in 238 galaxies, detected in archival *XMM-Newton* observations, produced from a cross-correlation of the RC3 catalogue of galaxies (de Vaucouleurs et al., 1991) and the 2XMM-DR1 catalogue (Watson et al., 2009). This was reduced to a small sample of the most luminous, relatively nearby ULXs by filtering on luminosity ($L_{\rm X} > 5 \times 10^{40}$ erg s^{-1} in the 0.2–12 keV band) and distance ($d < 100$ Mpc). A sample of 12 sources were found to match these criteria. Additional quality checks of the *XMM-Newton* data for the selected sources were then performed, and 2 of the 12 sources were excluded from the

final sample. We excluded a ULX candidate detected near to the cD galaxy NGC 4889, in the galaxy cluster Abell 1656, where we could not separate sufficient source counts from the strong diffuse emission in which the candidate ULX was embedded to permit detailed study. The other excluded source was M82 X-1, as it has been extensively studied by other authors (e.g. Matsumoto et al. 2001; Kaaret et al. 2006; Feng & Kaaret 2010), and the *XMM-Newton* data is somewhat complicated by the presence of a strong ISM component around the position of the ULX, and bright and variable nearby objects[1].

The 10 remaining objects are listed in Table 2.1, along with some characteristics of their presumed host galaxies. The X-ray sources are assumed to be at the distance of the host galaxy, and for the majority of sources cosmology-corrected distances are used ($H_0 = 71$ km s^{-1} Mpc^{-1}, $\Omega_M = 0.27$, $\Omega_\Lambda = 0.73$, Komatsu et al. 2009), calculated using redshifts from de Vaucouleurs et al. (1991). An exception to this is Src. 8, whose host galaxy is sufficiently nearby that its peculiar motion could dominate its measured recession velocity, so we instead use the distance of 14.9 Mpc from Tully (1988). Table 2.1 also provides a luminosity for each object, calculated using this distance and the 2XMM 0.2–12 keV flux. It is immediately evident that the extreme luminosity sample presented here includes 3 candidate HLXs - Src. 1, Src. 4 and Src. 7 (additionally, Src. 3 had previously been identified as a HLX by Davis & Mushotzky 2004, see Section 2.3.1).

In addition to the data sets identified in the 2XMM catalogue, the *XMM-Newton* science archive[2] and *Chandra* data archive[3] were searched for further observations covering the objects. All the archived *XMM-Newton* EPIC and *Chandra* ACIS observations potentially covering the positions of the 10 candidate ULXs were extracted

---

[1]Of the other notable HLXs mentioned in the introduction, ESO 243-49 HLX-1 was not included in the sample as its host is not in the RC3 catalogue, and both Cartwheel N10 and CXO J122518.6+144545 lie beyond the 100 Mpc limit of this sample.

[2]http://xmm.esac.esa.int/xsa/

[3]http://cxc.harvard.edu/cda/

from the archives, and examined for further detections of the 10 objects. Details of all relevant observations are shown in Table 2.2, with the exceptions of the *XMM-Newton* observations 0300530401 and 0301651201 (plus several additional short observations of Src. 6, see caption for details). These were pointed in the proximity of Src. 6 and Src. 10 respectively, but were not used as they contained no useful data due to the presence of heavy background flaring throughout the duration of the EPIC exposures. In all cases, the ULX in question was detected. All but one of the sources (Src. 7) are present in multiple archived observations, including six with archival *Chandra* data. We were awarded additional *Chandra* time during cycle 12 to observe the other four sources (proposal ID 12620389, PI Sutton: results for Src. 2, Src. 4 and Src. 7 were obtained prior to the completion of this study, and are included here; however an observation of Src. 8 was scheduled at too late a date for inclusion here, but results from this are reported in the following chapter).

2.2.2 *XMM-Newton* data reduction

The *XMM-Newton* data were reduced and data products were extracted using the standard tools available in the *XMM-Newton* SAS[4] (version 9.0.0). Severe background flaring resulted in multiple exposures being obtained in a number of the observations[5]. However, in all cases only one of the exposures contained a significant length of good time. In each case we identified the sole exposure containing useful science data per observation and focused our analysis upon it. In two observations of Src. 6 the solar proton flaring was severe enough to render the data from whole instruments unusable, in particular the pn detector in observation 0300530301 and the MOS1 detector in 0300530601. However, background flaring was present to some significant level in almost all the *XMM-Newton* observations, with the only exceptions being

---

[4]http://xmm.esac.esa.int/sas/

[5]This affected both MOS and pn detectors during observation 0145190201 of Src. 8, and MOS detectors alone were affected during observations 0200780101, 0147610101 and 0145190101 of Src. 1, Src. 5 and Src. 8 respectively.

Table 2.1: The extremely luminous candidate ULX sample

Source ID	2XMM source	Host galaxy	Galaxy type[a]	d[b]	Sep.[c]	N_{H}[d]	$L_{\mathrm{X,max}}$[e]
Src. 1	2XMM J011942.7+032421	NGC 470	SA(rs)b	32.7	33	3.09	15.3 ± 0.8
Src. 2	2XMM J024025.6−082428	NGC 1042	SAB(rs)cd	18.9	96	2.61	5.1 ± 0.2
Src. 3	2XMM J072647.9+854550	NGC 2276	SAB(rs)c	33.3	45	5.52	6.4 ± 0.3
Src. 4	2XMM J120405.8+201345	NGC 4065	E	87.9	18	2.40	13.1 ± 1.7
Src. 5	2XMM J121856.1+142419	NGC 4254	SA(s)c	33.2	103	2.70	6.0 ± 0.3
Src. 6	2XMM J125939.8+275718	NGC 4874	cD0	99.8	57	0.89	5.8 ± 1.3
Src. 7	2XMM J134404.1−271410	IC 4320	S0?	95.1	18	5.04	28.2 ± 2.4
Src. 8	2XMM J151558.6+561810	NGC 5907[f]	SA(s)c: edge-on	14.9	102	1.38	5.6 ± 0.1
Src. 9	2XMM J163614.0+661410	MCG 11-20-19	Sa	96.2	16	3.14	6.5 ± 1.2
Src. 10	2XMM J230457.6+122028	NGC 7479	SB(s)c	32.8	68	5.08	7.1 ± 0.3

Notes: [a] Galaxy morphology from de Vaucouleurs et al. (1991). [b] Host galaxy distances in Mpc. These are cosmology-corrected distances using redshifts from de Vaucouleurs et al. (1991), with the exception of NGC 5907 where the distance from Tully (1988) was used. [c] Separation of the candidate ULX position from the nucleus of its host galaxy, in units of arcseconds. [d] Galactic column densities interpolated from Dickey & Lockman (1990), in units of 10^{20} cm^{-2}. [e] Maximum detected 0.2–12 keV luminosity of the ULX candidate, based on the 2XMM broad band fluxes and the quoted distance, in units of 10^{40} erg s^{-1}. [f] The part of NGC 5907 west of its dust lane, that hosts the ULX candidate, is also known as NGC 5906.

Table 2.2: Observation details

Source ID	Observatory	ObsID[a]	Date (yyyy/mm/dd)	$t_{\exp}$[b] (ks)	Total counts[c] (0.3–10.0 keV)	Off-axis angle[d] (arcmin)
Src. 1	*XMM-Newton*	0200780101	2004/01/24	4.0/3.8/3.6	850 ± 30	5.25
	Chandra	10562	2008/11/12	28.1	610 ± 20	0.29
	XMM-Newton	0601670101	2009/06/27	40.1/53.9/47.1	2550 ± 50	1.10
Src. 2	*XMM-Newton*	0093630101	2001/08/15	11.6/15.0/ -	920 ± 30	14.41
	XMM-Newton	0306230101	2006/01/12	- /53.1/52.1	2860 ± 60	12.18
	XMM-Newton	0553300401	2009/08/12	42.2/48.4/ -	4310 ± 70	14.38
	Chandra	12988	2010/10/09	29.0	2770 ± 50	0.32

Notes: [a] Observation identifiers. [b] The sum of the good time intervals for each detector. For *XMM-Newton* observations it is shown in the order pn/MOS1/MOS2, a dash indicates that the source was not detected. [c] Total background-subtracted source counts accumulated in the observation (sum of all 3 EPIC detectors for *XMM-Newton* observations). [d] Angular separation between the on-axis position of the observation and the 2XMM source position. [e] The *Chandra* observation of Src. 3 was able to resolve the candidate HLX into multiple sources (Figure 2.1). [f] NGC 4874 is the central galaxy in the Coma cluster, and the Coma cluster has been extensively observed by both *Chandra* and *XMM-Newton* (in many cases for calibration purposes). There are a number of similar observations from both observatories that are not included in this analysis, due to the short exposure time ($\lesssim$ 10 ks), but are available in the archives.

Table 2.2: continued

Source ID	Observatory	ObsID[a]	Date (yyyy/mm/dd)	$t_{\exp}$[b] (ks)	Total counts[c] (0.3–10.0 keV)	Off-axis angle[d] (arcmin)
Src. 3	*XMM-Newton*	0022340201	2001/03/16	- /52.3/52.3	2070 ± 50	6.08
Src. 3a[e]	*Chandra*	4968	2004/06/23	45.6	320 ± 20	1.13
Src. 3b[e]	*Chandra*	4968	2004/06/23	45.6	190 ± 10	1.10
Src. 3c[e]	*Chandra*	4968	2004/06/23	45.6	120 ± 10	1.06
Src. 4	*XMM-Newton*	0112270601	2003/01/02	- /6.5/6.5	75 ± 9	2.10
	XMM-Newton	0112271001	2003/06/09	- /6.9/6.9	140 ± 10	0.48
	XMM-Newton	0112271101	2003/06/30	3.1/3.6/3.6	210 ± 10	0.60
	Chandra	12990	2011/07/13	5.0	57 ± 8	0.30
Src. 5	*XMM-Newton*	0147610101	2003/06/29	13.1/17.3/19.4	1770 ± 40	2.75
	Chandra	7863	2007/11/21	5.1	270 ± 20	1.84
Src. 6[f]	*Chandra*	556	1999/11/04	9.6	60 ± 10	2.28
	XMM-Newton	0124711401	2000/05/29	11.0/16.8/16.8	350 ± 80	0.42
	XMM-Newton	0153750101	2001/12/04	17.0/21.0/21.0	580 ± 90	2.69
	XMM-Newton	0300530701	2005/06/06	16.0/23.6/24.3	430 ± 90	2.14
	XMM-Newton	0300530601	2005/06/07	14.3/ - /22.7	410 ± 80	2.21
	XMM-Newton	0300530501	2005/06/08	15.5/24.8/24.9	480 ± 90	2.31
	XMM-Newton	0300530301	2005/06/11	- /30.4/30.4	230 ± 70	1.60

Table 2.2: continued

Source ID	Observatory	ObsID[a]	Date (yyyy/mm/dd)	$t_{\exp}$[b] (ks)	Total counts[c] (0.3–10.0 keV)	Off-axis angle[d] (arcmin)
	XMM-Newton	0300530101	2005/06/18	15.7/18.0/18.0	480 ± 90	1.42
	Chandra	9714	2008/03/20	29.7	40 ± 10	1.86
	Chandra	10672	2009/03/15	28.5	110 ± 10	1.93
Src. 7	*XMM-Newton*	0092970801	2003/01/04	3.5/5.3/5.2	390 ± 20	1.10
	Chandra	12989	2011/03/21	49.4	1730 ± 40	0.31
Src. 8	*XMM-Newton*	0145190201	2003/02/20	10.6/24.5/25.2	7640 ± 90	2.40
	XMM-Newton	0145190101	2003/02/28	9.4/18.8/19.1	5460 ± 80	2.41
Src. 9	*Chandra*	553	1999/10/19	5.9	14 ± 4	4.83
	Chandra	1454	1999/10/19	11.4	29 ± 5	4.87
	Chandra	1666	2001/08/30	48.6	120 ± 10	2.29
	XMM-Newton	0112980101	2002/09/28	13.1/14.7/14.7	130 ± 20	4.11
	XMM-Newton	0112980401	2002/09/30	9.0/10.4/10.4	70 ± 10	4.15
	XMM-Newton	0112980501	2002/10/04	7.5/8.4/8.4	60 ± 10	4.12
	Chandra	7698	2007/06/13	5.1	8 ± 3	4.07
Src. 10	*XMM-Newton*	0025541001	2001/06/19	6.0/9.1/9.2	1270 ± 40	0.55
	Chandra	11230	2009/08/11	24.8	160 ± 10	2.30
	Chandra	10120	2009/10/24	10.0	56 ± 8	1.21

observations 0300530301 and 0112980101 of the ULX candidates Src. 6 and Src. 9 respectively. Good Time Interval (GTI) files were therefore created to allow high background epochs to be filtered out of the data, based on high energy (10–15 keV) full field light curves. The limiting count rate used to define the GTIs varied between observations, dependent on the best balance between minimising the source data loss whilst maximising the excision of background flares, with typical thresholds of 1.0–1.5 cts s^{-1} for pn fields and ~ 0.6 cts s^{-1} for MOS fields.

Source spectra and light curves were then extracted from circular apertures centred on the ULX candidate. Source extraction region radii were typically between ~ 15–40 arcseconds (which corresponds to an on axis fractional encircled energy of ~ 70–90 per cent at 1.5 keV), in order to maximise source counts whilst avoiding contamination from nearby sources. In three cases the source was positioned close to a chip gap, which would have severely restricted the radius of a circular aperture. In each of these cases elliptical source regions (with semi-major axes equivalent to the circular aperture radii) were used to extract the source data. In both the MOS1 data from Src. 3 in the 0022340201 dataset, and the pn data for Src. 5 in observation 0147610101, the ellipse was aligned with the nearby chip gap; however in the pn data for Src. 2 in 0093630101, the source was sufficiently far off-axis that the ellipse was aligned with the direction of maximum point spread function (PSF) extent. Larger circular apertures were used to provide source background data in all cases. These were positioned on the same chip, approximately the same distance from the readout nodes if possible, and were sized to include a minimum of ~ 50 per cent more area on the detector than source apertures. In cases where nearby sources placed limitations on the size of a background region, multiple circular apertures were used.

The final data products used in the analysis (i.e., spectra and light curves) were then extracted from the source apertures, using the GTI file and standard event patterns for the detectors (`PATTERN` ≤ 4 for the pn, `PATTERN` ≤ 12 for the MOS). Spectral extractions also used the conservative `FLAG` $= 0$ filter, although we alleviated

this somewhat for the light curve extractions by using the less restrictive `#xmmea_ep` or `#xmmea_em` filters for the pn or MOS detectors respectively instead. The appropriate response matrices for the spectral analysis were automatically generated during the spectral extraction in the SAS task XMMSELECT.

2.2.3 *Chandra* data reduction

Chandra data were reduced using CIAO[6] version 4.1.1, and calibration files from the *Chandra* CALDB version 4.1.0. Circular apertures with radii of 4 arcseconds (corresponding to an on axis fractional encircled energy of $\gtrsim$ 99 per cent at 1 keV) were used to extract the source data, with the only exception being in the case of Src. 3, as this ULX candidate was resolved by *Chandra* into multiple objects separated by less than the typical extraction region radius (see section 2.3.1). Instead, apertures of ~ 1 arcsecond radius (~ 90 per cent on axis fractional encircled energy at 1 keV) were used to avoid overlapping the source regions. Annular apertures, centred on the source, but with inner radii outside of the source region were used to characterise the background for each source. In the case of Src. 3, a single background annulus surrounding the resolved sources was used to avoid cross-contamination of the background regions by the neighbouring point sources. The data products were then extracted from the archived level 2 event files, to include all standard good event detections with energies between 0.3–10 keV, within the source data extraction apertures. The *Chandra* spectra were extracted using the CIAO script SPECEXTRACT, which also produces the appropriate response matrices for spectral analysis, and the light curves were extracted using DMEXTRACT.

---

[6]`http://cxc.harvard.edu/ciao/`

2.2.4 Optical data

This work also utilises optical data to further probe these extreme objects. As an initial step we retrieved Digitised Sky Survey version 2 (hereafter DSS2) data from the ESO archive[7], within a 5 arcminute square centred on the host galaxy of each ULX candidate. DSS2-blue images were used preferentially when available, but due to its limited coverage (only 45 per cent of the sky), the use of the alternative all-sky DSS2-red images was necessary for Src. 2 and Src. 7.

An examination of the Hubble Legacy Archive (HLA)[8] revealed that high resolution space-based optical imaging from *HST* was available for four of our objects. Enhanced *HLA* data products covering the source region were available for Src. 3, Src. 6 and Src. 8, and two data sets processed using the standard *HST* single image calibration pipeline were available for Src. 10. All this data was downloaded from the archive for further study; we tabulate the basic observation details in Table 2.3. As an initial step the astrometry of the images was improved using the IRAF tools CCFIND, CCMAP and CCSETWCS and objects common to the *HST* images and either the 2MASS (Src. 8) or USNO (Src. 3, Src. 6 and Src. 10) catalogues. Where individual counterparts to the X-ray sources were detected, aperture photometry was performed using GAIA and the appropriate Vega magnitude zero points from either Sirianni et al. (2005) for ACS/WFC observations, or the WFPC2 Data Handbook[9]. Corrections to a standard 0.5 arcsecond aperture were calculated using a mean magnitude correction from ten bright point sources in each field, and these were extrapolated to an infinite radius aperture, again using values from Sirianni et al. (2005) and the WFPC2 Data Handbook.

In addition to the study of archival imaging data for the sources, a low dispersion Gemini GMOS spectrum was obtained to further constrain the nature of an optical

---

[7]http://archive.eso.org/dss/dss
[8]http://hla.stsci.edu/
[9]http://www.stsci.edu/hst/wfpc2/documents/handbook/WFPC2_DHB.html

Table 2.3: Details of archival *HST* observations, and Galactic extinction in the direction of the targets

Source	$E(B-V)$	Prop. ID	Instrument	Filter
Src. 3	0.1	6355	WFPC2	F300W
		8597	WFPC2	F606W
		10877	WFPC2	F555W
				F814W
Src. 6	0.009	10861	ACS/WFC	F475W
				F814W
Src. 8	0.011	6092	WFPC2	F450W
				F814W
Src. 10	0.112	11575	ACS/WFC	F555W
				F814W

counterpart to Src. 6. The data were reduced using standard tools in the GMOS subpackage from the GEMINI package in IRAF. The specific tools used were: GSFLAT to extract the flat field; GSREDUCE to reduce both the target and calibration arc exposures; GSWAVELENGTH to establish the wavelength calibration, then GSTRANSFORM to apply it to the exposures; GSSKYSUB to subtract the sky background; GSCRREJ to reject cosmic ray events; GSEXTRACT to extract one dimensional spectra of the source, which were then combined using the tool GEMARITH. Gaussian line profiles were fitted where appropriate to the reduced optical spectrum of the counterpart using the CURVEFIT function in IDL version 6.2.

2.3 Data analysis & results

2.3.1 Spatial analyses

High resolution X-ray imaging

As an initial step, we investigated the spatial characteristics of the X-ray source detections. One particular issue for the *XMM-Newton* detections of these objects, especially given their relatively large distances, is whether we are seeing a single point-like object, or whether multiple objects and/or spatially extended components are present within the *XMM-Newton* beam. *Chandra* observations offer an excellent means of settling this issue, with the much smaller *Chandra* beam able to resolve objects that are confused by *XMM-Newton*, even in regions of high diffuse emission (e.g. in the centre of the starburst galaxies NGC 3256 & NGC 3310, Jenkins et al. 2004). We therefore began by examining the deepest *Chandra* detection for each object in our sample, in order to search for resolved structure.

Only one *XMM-Newton* detection was resolved to reveal finer structure by *Chandra*, namely Src. 3. This object had previously been identified as a HLX candidate in the spiral galaxy NGC 2276 by Davis & Mushotzky (2004) using the *XMM-Newton* data (Figure 2.1, *top*). However, their assumed distance for NGC 2276 of 45.7 Mpc is somewhat discrepant compared to more recent measurements and overestimates the distance to NGC 2276 (cf. Table 2.1). This in turn inflates the measured luminosity. The assumptions here, and the redshift from de Vaucouleurs et al. (1991), lead to a distance of 33.3 Mpc and hence a lower (although still extreme) 2XMM luminosity estimate of $\sim 6 \times 10^{40}$ erg s^{-1}. In the later *Chandra* observation of this source, the ULX candidate was shown to be resolved into three point sources (Figure 2.1, *bottom*; see also Wolter et al. 2011), although only the southern two lie coincident with the measured *XMM-Newton* source centroid position. Remarkably, each of the point sources is sufficiently luminous to be classified as a ULX, if at
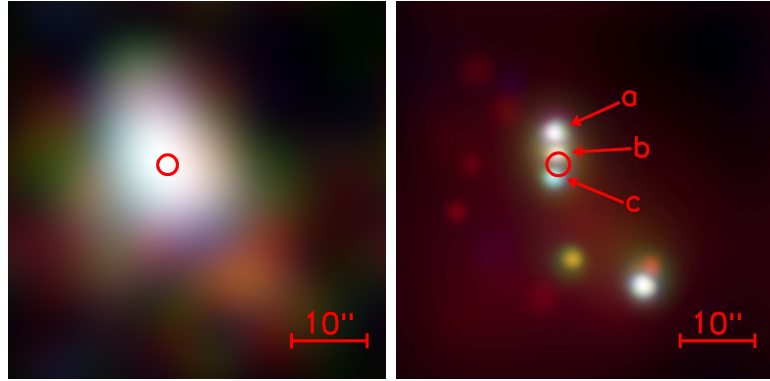
Figure 2.1: (*left*) True colour *XMM-Newton* image of Src. 3, where the rgb colours correspond to the 0.3–1.5, 1.5–2.5 & 2.5–10 keV energy bands respectively. The region circled is the effective 90 per cent uncertainty in the *XMM-Newton* position of the source. (*right*) Equivalent *Chandra* image. The *XMM-Newton* detection is resolved into three separate objects, two of which border on the 90 per cent *XMM-Newton* error region. They are referred to as labelled here throughout the rest of the chapter. These and all subsequent images are aligned such that north is up.

the distance of NGC 2276, with $L_X \gtrsim 5 \times 10^{39}$ erg s^{-1}. To find 3 such luminous ULXs within a small region of a galaxy – the projected separation of the 3 objects is < 150 pc – appears very remarkable, although this should be tempered by the realisation that the western regions of NGC 2276 have heightened star formation, with a galaxy-wide star formation rate estimated at $5 - 15 \ M_\odot$ yr^{-1} (Wolter et al. 2011 and references therein). This is plausibly the result of gravitational interaction with NGC 2300 and/or ram pressure interaction as NGC 2276 transits through the bright intra-group medium of the NGC 2300 group (e.g. Gruendl et al. 1993).

We then used an additional diagnostic test for extension on the other, apparently point-like objects. The CIAO SRCEXTENT script quantifies the size of each PSF, which it does by effectively calculating an average radius for the PSF using a Mexican Hat optimisation algorithm. We show the results of this in Table 2.4. These results are consistent with expectations for the *Chandra* PSF for both on-axis and slightly off-axis objects, where an extent of ~ 0.5 arcseconds is equivalent to

the 75 per cent encircled energy radius for 1.5 keV photons (see Figure 4.6 of the *Chandra* Proposer's Observatory Guide; also the *Chandra* High Resolution Mirror Array calibration documentation[10]). We have verified the off-axis extents are consistent with point-like objects by comparison to the population of point-like ULXs in the galaxy NGC 4490 (see Roberts et al. 2002; Fridriksson et al. 2008; Gladstone & Roberts 2009; Yoshida et al. 2010), eight objects that lie up to 3 arcminutes off-axis in three separate *Chandra* ACIS-S observations. Our extents are consistent with the SRCEXTENT-measured extents for these ULXs over the full range of off-axis angles seen. The only outlier is Src. 9, but even this is consistent at the 90 per cent confidence level. We conclude that there is no evidence for significant extended emission for any object, meaning that each ULX candidate remains consistent with a single, point-like object at the high X-ray spatial resolution of *Chandra*.

Source locations and optical counterparts

A second benefit of obtaining *Chandra* data for the objects in our sample is the accuracy of its astrometry, with sub-arcsecond positioning expected even without applying astrometric corrections. We were therefore able to derive accurate positions (shown in Table 2.4) and so examine multi-wavelength data in order to search for counterparts, and identify the environments hosting these objects. Initially we investigated the locations of the objects in our sample by overlaying their positions on DSS2 images, which we show here as Figure 2.2. Seven objects are associated with spiral galaxies; in the six cases where the galaxy is close to face-on, the ULX candidate appears to be located on or close to the spiral arms, in most cases in the outer regions of the disc. In the one edge-on case (NGC 5907, the galaxy containing Src. 8) the source is located in the plane of the disc, with a projected location coincident with a strong dust lane. We also searched for catalogued objects near to

---

[10]`http://cxc.harvard.edu/proposer/POG, http://cxc.harvard.edu/cal/Hrma/Index.html`
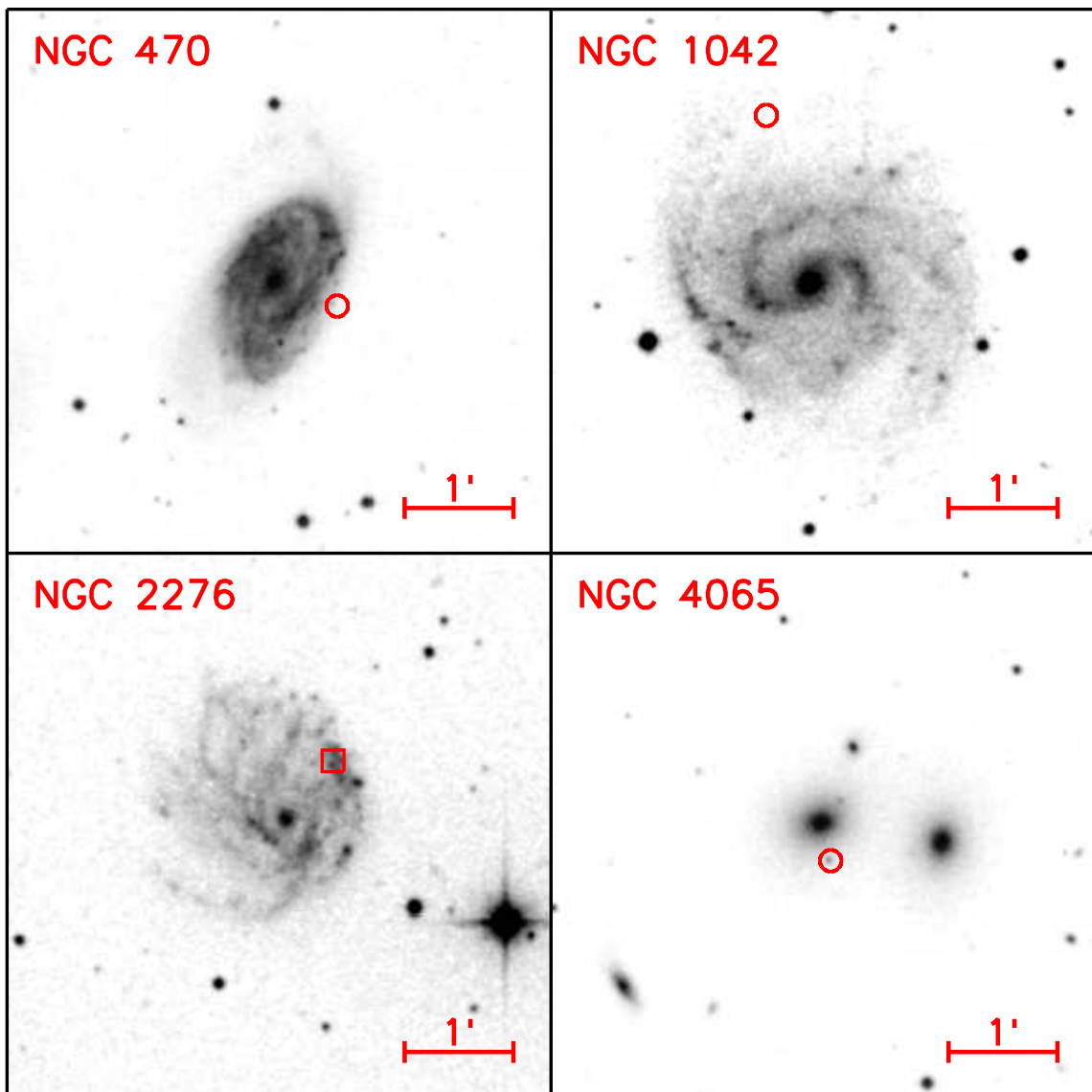
Figure 2.2: DSS2 images of the habitats of the 10 objects in the selected sample. The ordering of panels matches the numbering of the sources, starting at top left with Src. 1 and reading across each row. Data from the DSS2-blue survey is shown where available, but in the two cases this was not possible (Src. 2 & Src. 7). The DSS2-red filter data is shown instead. Each image is 5 arcminutes across, aligned such that North is up, and centred on the nucleus of the host galaxy. The greyscale is arbitrary in each panel, and displayed such that the internal structure of each galaxy can be seen. The position of each object is marked by a circle, except where *HST* data is available where instead a box is shown matching the size of the image in Figure 2.3. Note that the actual position errors are considerably smaller than the size of the circle shown.
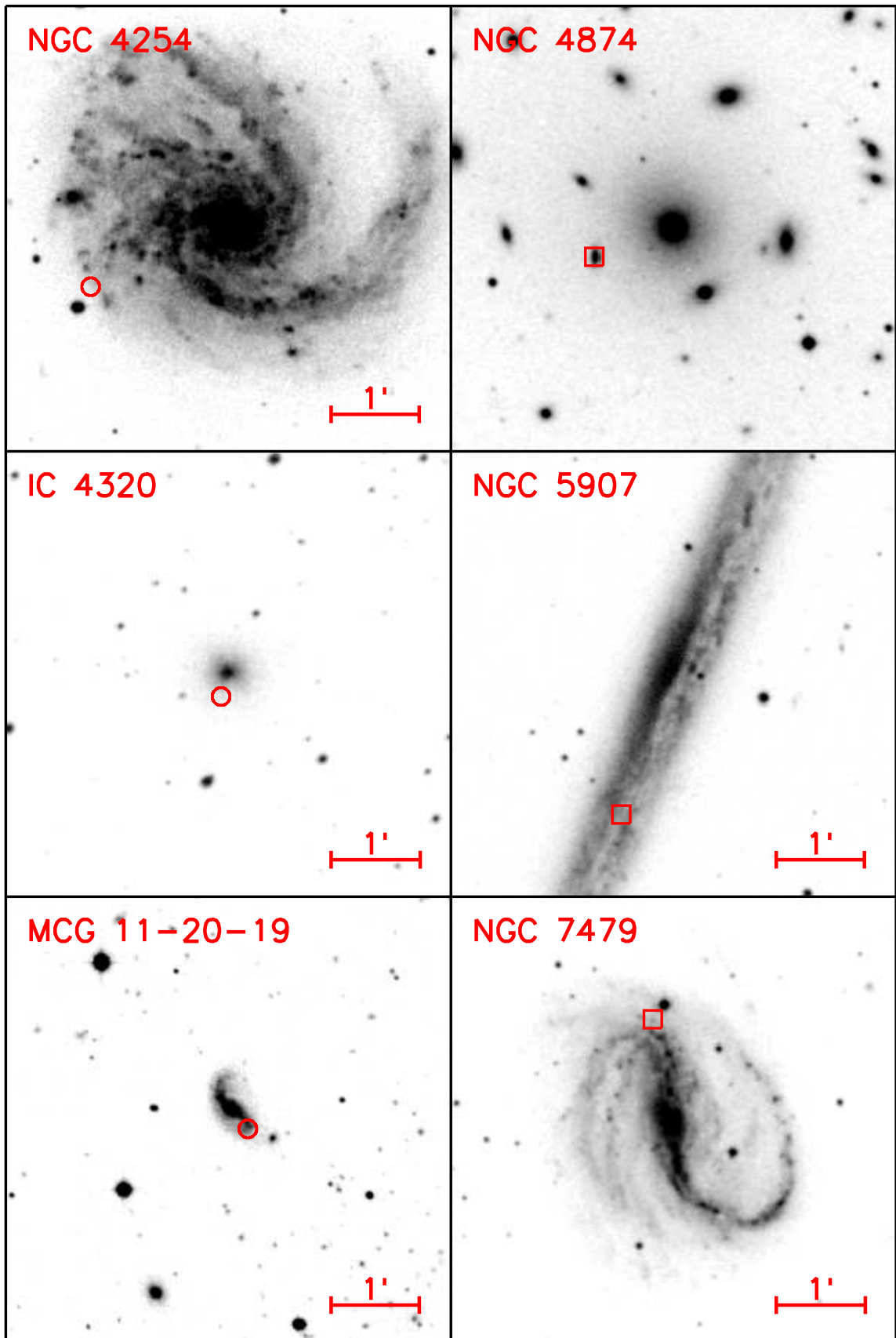
Figure 2.2: continued

Table 2.4: *Chandra* source characteristics

Source	Obs ID	RA, dec (J2000)	θ^a (arcmin)	Extent (arcsec)
Src. 1	10562	$011942.8 + 032422$	0.29	0.48 ± 0.03
Src. 2	12988	$024025.6 - 082430$	0.32	$0.49^{+0.02}_{-0.01}$
Src. 3a	4968	$072648.1 + 854554$	1.13	0.49 ± 0.04
Src. 3b	4968	$072647.9 + 854552$	1.10	$-^b$
Src. 3c	4968	$072648.3 + 854549$	1.06	$0.45^{+0.07}_{-0.06}$
Src. 4	12990	$120405.8 + 201345$	0.30	0.50 ± 0.1
Src. 5	7863	$121856.1 + 142419$	1.84	0.55 ± 0.05
Src. 6	10672	$125939.8 + 275716$	1.93	$0.62^{+0.1}_{-0.09}$
Src. 7	12989	$134404.2 - 271411$	0.31	0.50 ± 0.02
Src. 8^c	-	-	-	-
Src. 9	1666	$163614.1 + 661410$	2.29	0.7 ± 0.1
Src. 10	11230	$230457.7 + 122029$	2.30	0.54 ± 0.07

Notes: Source characteristics are measured from the *Chandra* observation with the greatest number of counts accumulated from the ULX candidate in question. ^{a} Off-axis angle of source. ^{b} SRCEXTENT was unable to constrain the size of this point-like object due to the proximity of the brighter Src. 3a. However, inspection shows its PSF appears very similar to its two verified point-like neighbours. ^{c} At the time of this study Src. 8 had not been observed with *Chandra*. However, a *Chandra* observation of the source since been taken, and is included in Chapter 3.

the positions of our objects using the NED and SIMBAD databases[11]. In the case of the spiral-hosted objects, three were in close proximity to catalogued HII regions: Src. 1 is ~ 2 arcseconds from HII region 46 of Hodge & Kennicutt (1983); Src. 3 is within ~ 6 arcseconds of regions 61 & 65 of Hodge & Kennicutt (1983); and Src. 10 is within ~ 2 arcseconds of regions 197 & 898 of Rozas et al. (1999). These associations imply a strong possibility that these objects are associated with ongoing star formation, as appears the case for many less luminous ULXs (e.g. Swartz et al. 2009).

The three objects associated with elliptical galaxies present a more diverse subsample. As Figure 2.2 shows, the object near to NGC 4065 (Src. 4) appears to

---

[11]http://ned.ipac.caltech.edu, http://simbad.u-strasbg.fr

have a faint, point-like counterpart. Subsequent to the selection of the sample this object was revealed to be a background QSO by SDSS spectroscopy (object SDSS J120405.83+201345.0). We therefore do not consider it further in this chapter, apart from briefly reporting its properties in Section 2.3.4. The second object associated with an elliptical, Src. 6, is actually found to be in the close proximity of a satellite galaxy (SDSS J125939.65+275714.0) of the central dominant galaxy of the Coma cluster, although it is displaced from the satellite galaxy nucleus by ~ 4 arcseconds. The final object, Src. 7, is the most X-ray luminous object in the sample, although also amongst the most distant. Its host is a peculiar S0 object that appears to be crossed by a dust lane (Lauberts, 1982). However, there is no obvious counterpart to this object in the DSS image.

A minority of the objects in the sample are also covered by *HST* imaging observations, as listed in Table 2.3. We show these four datasets in Fig 2.3, where we display the immediate region covering the candidate ULX position at the full *HST* spatial resolution. We overlay an X-ray position error circle on top of the image to indicate the likely position of each ULX candidate. This is calculated as the combination of position errors from the astrometric uncertainty of the *Chandra* data, the X-ray source centroid, and the astrometric registration of the *HST* data, as per Roberts et al. (2008). Possible point-like candidate counterparts are apparent within the X-ray position error circle for all of the objects. Aperture photometry was performed on the brightest identified counterpart in each case (which in most cases is the only counterpart, although there are possibly fainter objects within the crowded regions in NGC 2276), as described in Section 2.2.4, and we list the derived magnitudes of the counterparts in Table 2.5.

The brightest individual objects within the error circles for the ULXs in NGC 2276 (Src. 3a–c) display absolute magnitudes in the ranges $M_{F606W} \sim -8 \rightarrow -10$ and $M_{F814W} \sim -9 \rightarrow -11$, albeit with large uncertainties. Archival *HST* F300W and F555W observations covering the field of Src. 3a–c are also available, but the
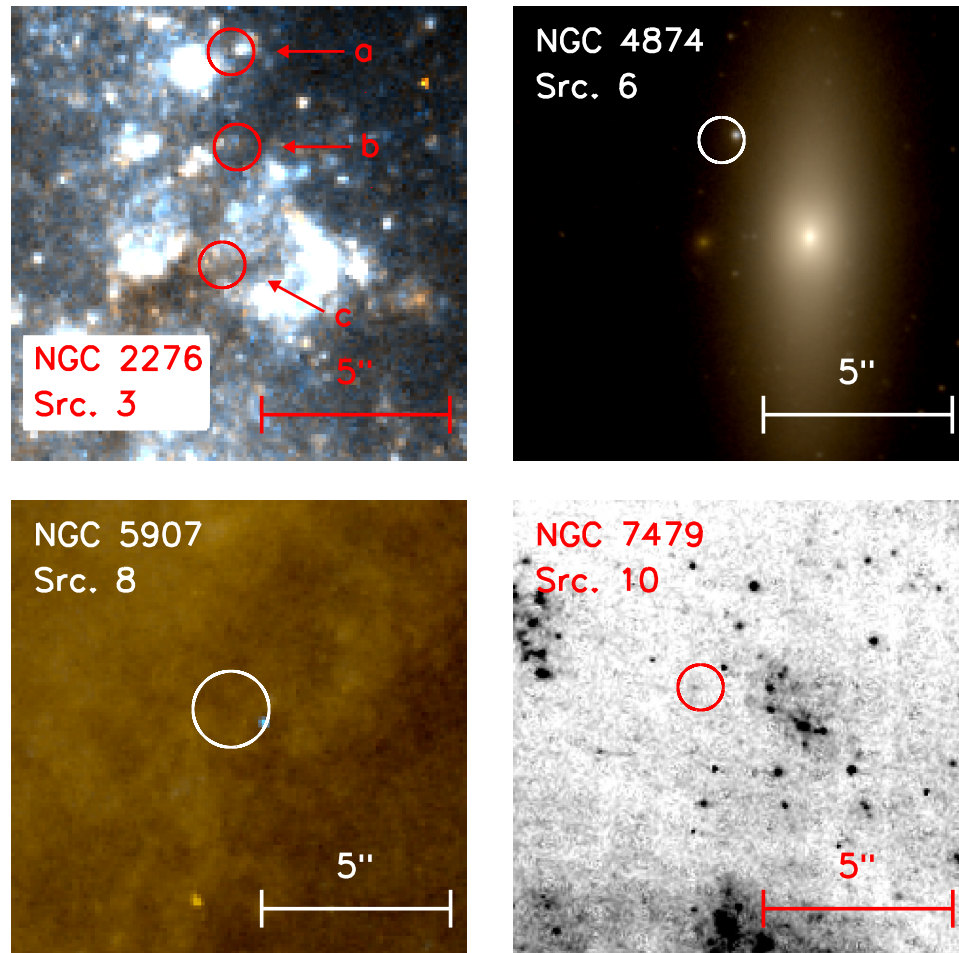
Figure 2.3: *HST* images of the regions containing four of the candidate ULXs. (*Top left*; Src. 3a, b & c) This *HST* data is displayed as a 3-colour image, with the F814W filter providing the red data, F555W the blue, and green taken as an average of the two. The data is displayed on a linear scale to aid the visualisation of the counterparts. (*Top right*; Src. 6) The image is 3-colour, with the F814W data in red, F475W in blue, and an average of the two filters in green. The image is displayed logarithmically to permit the separation of the counterpart from the galaxy to be seen. (*Bottom left*; Src. 8) A 3-colour image using F814W as red, F450W as blue, and an average of the two as green. This is scaled linearly for display purposes. (*Bottom right*; Src. 10) A single, linearly greyscaled image in the F555W band is presented to emphasize the faint counterpart.

Table 2.5: *HST* photometry for candidate counterparts

Source ID	Filter	m_f [a]	M_f [b]
Src. 3a	F300W	22 ± 4	-11.1
	F555W	23.1 ± 0.9	-9.8
	F606W	22.9 ± 0.8	-10.0
	F814W	21.8 ± 0.8	-11.0
Src. 3b	F300W	-	-
	F555W	25 ± 2	-7.9
	F606W	25 ± 3	-7.9
	F814W	23 ± 5	-9.8
Src. 3c	F300W	-	-
	F555W	-	-
	F606W	24 ± 3	-8.9
	F814W	24 ± 5	-8.8
Src. 6	F475W	22.0 ± 0.2	-13.0
	F814W	21.2 ± 0.2	-13.8
Src. 8	F450W	21.5 ± 0.4	-9.4
	F814W	-	-
Src. 10	F555W	26 ± 2	-6.9
	F814W	26 ± 5	-6.8

Notes: [a] Apparent magnitudes, for the filter f, in the Vega photometric system. [b] Absolute magnitudes, corrected for foreground extinction as per Table 2.3.

magnitude of the brightest optical source within the error circle of Src. 3c is not constrained by the F555W observation, and similarly for both Src. 3b and c in the F300W observation. Such magnitudes are more luminous than typical individual supergiant stars, although examples of luminous blue variable stars with similar magnitudes are known (e.g. Cyg OB2-304 with $M_V \sim -10.6$; Massey et al. 2001). However, these magnitudes are also reasonable for young massive star clusters, such as one might find in an intense star forming region, and even somewhat unremarkable – for example more than 50 young clusters in the Antennae have absolute magnitudes of $M_V < -11.3$ (Whitmore et al., 1999). Src. 6 is a very interesting case, as it is located in an early type galaxy. However, the possibility of a globular cluster host seems rather unlikely, as its absolute magnitude is larger than would be expected for such an object. A very interesting alternative is that it could be located in an Ultra-Compact Dwarf (UCD) galaxy, a number of which are also known to be located within the central regions of the Coma cluster (Madrid et al., 2010). Given that UCDs are thought to fill an evolutionary step between the largest globular clusters and dwarf spheroidal galaxies, such an environment might be an ideal place to look for IMBHs. However, the colour of the object is anomalously blue (F475W−F814W $\approx$ 0.8) compared to other UCDs in the same field, which typically have F475W−F814W colours of $\sim$ 1.5 to 2, and so is perhaps more indicative of a background QSO. The next object, Src. 8, is a very blue object, not being detected in the F814W filter, and hence must be located at the near side of the dust lane in its host galaxy (NGC 5907). Its absolute magnitude of ~ -9.5 in the F450W filter is too large for a single stellar object, but is potentially indicative of a young, blue stellar cluster (e.g. Whitmore et al. 1999). Finally, the counterpart to Src. 10 appears consistent with a single giant star, although again its magnitudes are poorly constrained by the data and so no further constraints from its colour information are forthcoming.

Optical spectroscopy of a counterpart

Given the interesting nature of the counterparts to these objects, further follow-up observations to identify their nature are critical. To this end, we have already obtained a follow-up low-dispersion optical spectrum of the possible UCD galaxy counterpart to Src. 6 using the GMOS long slit spectrometer on the Gemini-North telescope. Unfortunately, in this case the spectrum revealed emission lines consistent with a relatively high redshift QSO ($z \approx 3.25$), thus explaining its blue colours. We therefore identify this object as the second contaminant in our sample, and do not consider it further in the analysis (although, we breifly describe its properties in Section 2.3.4).

Background contamination estimate

Out of the ten objects in our initial sample we have therefore identified two background contaminants. But how many should we expect? To answer this question we have revisited the background contamination calculations presented for the parent 2XMM-DR1/RC3 sample in Walton et al. (2011b). We repeat the process presented in that paper, with appropriate changes for consistency with this sample. Firstly, we redefined the galaxy sample, such that we only considered galaxies within 100 Mpc, then calculated new flux limits at which sources would enter the sample. In general, this is different for each of the sample galaxies, and for regions of space where the 2XMM observations are of a sufficient depth to detect any extreme ULX, this is equal to the flux expected form a 5×10^{40} erg s^{-1} point source at the distance of the galaxy. Where the 2XMM observations were of insufficient depth to detect all potential extreme ULXs, the appropriate flux limit was the limiting sensitivity of the X-ray data, and this was used instead. These flux limits were combined with the expected number density of resolved background point sources as a function of flux sensitivity (N($>$S), per unit sky area) from Moretti et al. (2003) to estimate

the number of background contaminants expected per pixel. The total expected background contribution is then the sum of the pixel contributions within the d_{25} radius of each galaxy (excluding the galaxy nuclei, chip gaps, etc.). Background estimates were calculated in both the hard and soft energy bands used by Walton et al. (2011b; 0.5–2 and 2–12 keV) for each of the EPIC detectors; these were combined in a weighted average, from which we predict a false detection rate of ∼ three objects with apparent luminosities above 5×10^{40} erg s^{-1} across our entire sample, albeit with large uncertainties stemming from the small number statistics. As with Walton et al. (2011b), the background contamination is expected to be higher for elliptical galaxies, where we predict ∼ two contaminants, compared to ∼ one for spiral galaxies; this is due to elliptical galaxies typically being greater in size and distance than spiral galaxies, hence cover they a larger area on the sky, and lower flux sources can appear as ULXs. These estimates compare favourably to what we have detected; the two identified background sources are indeed located close to elliptical galaxies, matching the prediction. On the other hand, the low predicted background rate for spiral galaxies (one out of seven detections) provides further confidence that the majority of these objects are real luminous ULXs, associated with their parent galaxies.

A further check for background sources may be obtained by considering the distribution of source – galaxy centre separations. Background contaminants would be randomly distributed, so the number of sources within a given separation would increase as the separation squared, whilst the distribution of ULXs would be expected to peak towards the galaxy centres (Swartz et al., 2011). However, given the small number statistics in this sample, the spatial distribution of sources is not well constrained, and such a test is of limited use. Instead, a consideration of the X-ray – optical flux ratios of the sample sources may be a more fruitful avenue to pursue. Typically, background contaminants (i.e. QSOs) are seen with 2–7.5 keV X-ray – R-band optical flux ratios of ∼ 0.1–10 (Caccianiga et al., 2008). Here, we

extract 2–7.5 keV X-ray fluxes, and estimate expected optical magnitudes for the sources with *HST* data at their maximum observed X-ray fluxes, if they were indeed background sources. For an X-ray – optical flux ratio of ten, we estimate R-band magnitudes of ~ 22 for Src. 3 and Src. 10, and ~ 20 for Src. 8. For Src. 3a and Src. 8, the observed F606W and F450W magnitudes roughly correspond to magnitudes in the V and B bands respectively, and we use coefficients from Sirianni et al. (2005) to estimate a V band magnitude of ~ 26.0 for Src. 10. We use these along with an AGN spectral template from Assef et al. (2010) to approximate R-band magnitudes of ~ 23.3, 21.8 and 26.3 for Src. 3a, Src. 8 and Src. 10 respectively. In the case of Src. 3a, this is close to the expected magnitude for a background contaminant, but Src. 3a is outside of the 90 per cent *XMM-Newton* error region for the ULX, and the counterparts to Src. 3b and c are fainter, albeit with large errors. The observed counterparts to Src. 8[12] and Src. 10 are fainter than expected for background contaminants, even with a high X-ray to optical flux ratio of ~ 10. This argues that these sources are indeed ULXs in the identified galaxies, rather than background contaminants, although it should be noted that the X-ray and optical observations were not simultaneous.

2.3.2   X-ray spectral analysis

Where sufficient counts were available to enable X-ray spectral analysis, the spectra were fitted with basic spectral models using XSPEC v.12.6.0. Observations with ≥ 250 counts were grouped using the FTOOL GRPPHA to a minimum of twenty counts per energy bin, to produce bins with Gaussian errors and hence permit the use of χ^2 statistics in fitting the data. Where only $100 - 250$ counts were available, models were fitted to ungrouped X-ray spectra using Cash statistics (Cash, 1979). The data were not background subtracted for the Cash analyses; instead in each of these cases

---

[12]Although the counterpart to Src. 8 is shown to be a false detection in Chapter 3.

Table 2.6: X-ray spectral modelling

Source ID	Obs ID	Absorbed power-law			Absorbed MCD			
		$N_H{}^a$	Γ^b	χ^2/dof^c	$N_H{}^a$	$kT_{\mathrm{in}}{}^d$	χ^2/dof^c	$f_{\mathrm{X,PL}}{}^e$
Src. 1	0200780101	$0.26^{+0.1}_{-0.08}$	2.2 ± 0.2	$54.8/43$	< 0.09	1.0 ± 0.1	$\mathbf{34.5/43}$	$8.0^{+0.4}_{-0.8}$
	10562	$0.14^{+0.07}_{-0.08}$	1.8 ± 0.2	$\mathbf{27.9/25}$	< 0.03	$1.2^{+0.2}_{-0.1}$	$[39.9/25]$	$1.95^{+0.08}_{-0.2}$
	0601670101	0.10 ± 0.02	1.80 ± 0.08	$\mathbf{132.3/131}$	< 0.004	$1.22^{+0.1}_{-0.08}$	$[227.8/131]$	$1.49^{+0.05}_{-0.05}$
Src. 2	0093630101	$0.20^{+0.06}_{-0.05}$	2.2 ± 0.2	$\mathbf{43.3/41}$	< 0.04	0.9 ± 0.1	$[74.4/41]$	$6.6^{+0.5}_{-0.5}$
	0306230101	$0.18^{+0.04}_{-0.03}$	1.61 ± 0.09	$\mathbf{126.6/133}$	0.03 ± 0.02	1.6 ± 0.1	$154.7/133$	$8.4^{+0.2}_{-0.5}$
	0553300401	0.16 ± 0.03	$1.59^{+0.08}_{-0.07}$	$\mathbf{219.6/214}$	$0.02^{+0.02}_{-0.01}$	1.6 ± 0.1	$[281.6/214]$	$10.8^{+0.3}_{-0.4}$
	12988	0.26 ± 0.04	$1.9^{+0.1}_{-0.09}$	$\mathbf{122.4/132}$	0.04 ± 0.03	$1.3^{+0.1}_{-0.09}$	$152.6/132$	$8.0^{+0.2}_{-0.5}$

Notes: Errors shown for spectral parameters are 90 per cent confidence ranges. ^{a} Absorption column density external to our Galaxy ($\times 10^{22}$ cm^{-2}). ^{b} Power-law photon index. ^{c} Statistical goodness of the fit, in terms of the χ^2 statistic and number of degrees of freedom. Numbers in bold indicate which model provided the best fit to the data, whilst numbers in square brackets indicate a fit that is rejected at 2σ significance. ^{d} Inner-disc temperature (keV). ^{e} Observed 0.3–10 keV flux, in units of 10^{-13} erg cm^{-2} s^{-1}, based on the power-law fit. ^{f} Total counts from this observation were insufficient for χ^2 fitting, instead Cash statistics were used (Cash, 1979). Goodness of fit is shown instead of χ^2/dof.

Table 2.6: continued

Source ID	Obs ID	Absorbed power-law			Absorbed MCD			$f_{\mathrm{X,PL}}$ [e]
		N_H [a]	Γ [b]	χ^2/dof [c]	N_H [a]	kT_{in} [d]	χ^2/dof [c]	
Src. 3	0022340201	0.10 ± 0.04	$1.42^{+0.09}_{-0.08}$	$107.1/92$	< 0.01	$1.9^{+0.2}_{-0.1}$	$\mathbf{104.8/92}$	$4.6^{+0.2}_{-0.2}$
Src. 3a	4968	$0.5^{+0.4}_{-0.2}$	1.9 ± 0.3	$16.4/12$	< 0.4	$1.2^{+0.5}_{-0.2}$	$\mathbf{15.1/12}$	$0.76^{+0.06}_{-0.2}$
Src. 3b	4968	0.4 ± 0.2	$2.1^{+0.3}_{-0.4}$	$\mathbf{10.9\%}$ [f]	< 0.2	$1.3^{+0.4}_{-0.2}$	13.9% [f]	$0.35^{+0.05}_{-0.1}$
Src. 3c	4968	$1.5^{+1}_{-0.7}$	1.7 ± 0.6	$[100\%$ [f]$]$	$0.9^{+0.7}_{-0.4}$	$2.3^{+2}_{-0.8}$	$[100\%$ [f]$]$	$0.39^{+0.06}_{-0.3}$
Src. 5	0147610101	$0.26^{+0.06}_{-0.05}$	1.5 ± 0.1	$\mathbf{74.1/86}$	$0.08^{+0.03}_{-0.04}$	1.8 ± 0.2	$94.1/86$	$4.4^{+0.2}_{-0.2}$
	7863	< 0.5	$1.4^{+0.5}_{-0.4}$	$\mathbf{6.8/10}$	< 0.2	$1.7^{+0.9}_{-0.4}$	$8.7/10$	$6.8^{+0.8}_{-2}$
Src. 7	0092970801	< 0.2	1.7 ± 0.3	$\mathbf{15.0/16}$	< 0.05	1.2 ± 0.2	$16.7/16$	$2.8^{+0.2}_{-0.4}$
	12989	$0.08^{+0.05}_{-0.04}$	$1.63^{+0.09}_{-0.1}$	$\mathbf{78.8/69}$	< 0.007	$1.34^{+0.1}_{-0.09}$	$[103.0/69]$	$3.2^{+0.2}_{-0.3}$
Src. 8	0145190201	$0.97^{+0.07}_{-0.06}$	$1.88^{+0.07}_{-0.06}$	$\mathbf{409.5/366}$	0.54 ± 0.04	$1.66^{+0.08}_{-0.07}$	$[420.0/366]$	$15.8^{+0.3}_{-0.4}$
	0145190101	$0.84^{+0.07}_{-0.06}$	1.68 ± 0.07	$267.0/251$	0.49 ± 0.04	1.9 ± 0.1	$\mathbf{258.5/251}$	$14.7^{+0.4}_{-0.4}$
Src. 9	1666	< 0.2	$1.6^{+0.4}_{-0.3}$	$\mathbf{1.1\%}$ [f]	< 0.06	$1.4^{+0.5}_{-0.3}$	$[98.4\%$ [f]$]$	$0.34^{+0.06}_{-0.09}$
	0112980101	< 0.2	$1.8^{+0.4}_{-0.3}$	$\mathbf{83.3\%}$ [f]	< 0.03	$1.5^{+0.4}_{-0.3}$	$[97.8\%$ [f]$]$	$0.61^{+0.06}_{-0.09}$
Src. 10	0025541001	$0.27^{+0.08}_{-0.07}$	$1.9^{+0.2}_{-0.1}$	$\mathbf{61.3/62}$	< 0.07	$1.4^{+0.2}_{-0.1}$	$66.1/62$	$4.7^{+0.2}_{-0.2}$
	11230	0.6 ± 0.2	$4.2^{+0.9}_{-0.8}$	$[96.7\%$ [f]$]$	< 0.3	$0.40^{+0.1}_{-0.08}$	$\mathbf{57.3\%}$ [f]	$0.28^{+0.04}_{-0.2}$

the background spectrum was first constrained from the background aperture, and then added to the fit as a constant component, normalised for the relative sizes of the extraction regions. In all cases the fitting was limited to the 0.3-10 keV band.

The spectra were fitted with both an absorbed power-law continuum and an absorbed multi-colour disc blackbody (MCD; DISKBB in XSPEC) models, with the latter representative of the emission from a standard optically-thick, geometrically thin accretion disc (Mitsuda et al., 1984). Absorption was modelled by the TBABS model, using abundances from Wilms et al. (2000). Two absorption components were included, the first of which was fixed to the Galactic line-of-sight column to the object (Dickey & Lockman 1990, cf. Table 2.1), and the second left as a free parameter to model intrinsic absorption in the source and/or its host galaxy. Where multiple *XMM-Newton* EPIC detectors were operating, an additional multiplicative constant was included in the spectral model. This was fixed to 1.0 for the pn detector (or MOS1 where no pn data were available) and varied freely for the others, in order to account for the calibration uncertainties between the EPIC detectors. In all cases with equally sized extraction apertures the values of this parameter remained within a few percent of unity, and the values scaled appropriately where smaller extraction regions were necessary on individual detectors.

Table 2.6 shows the parameters resulting from fitting the two simple models to the source data. Plots of the absorbed power-law spectral fits, unfolded from the detector response, are displayed in Figure 2.4 for all observations with greater than 250 source counts. An absorbed power-law continuum spectrum provides a statistically acceptable fit (i.e., null hypothesis probability > 5 per cent, so rejection likelihood < 95 per cent) to data from all but two observations. These exceptions are the least luminous of the resolved source triplet, Src. 3c, which was not well characterised by either model; and a marginal rejection of the latter, much less luminous observation of Src. 10, which was the sole dataset acceptably fitted by the MCD model alone. In contrast, eight spectra were acceptably fitted by the absorbed
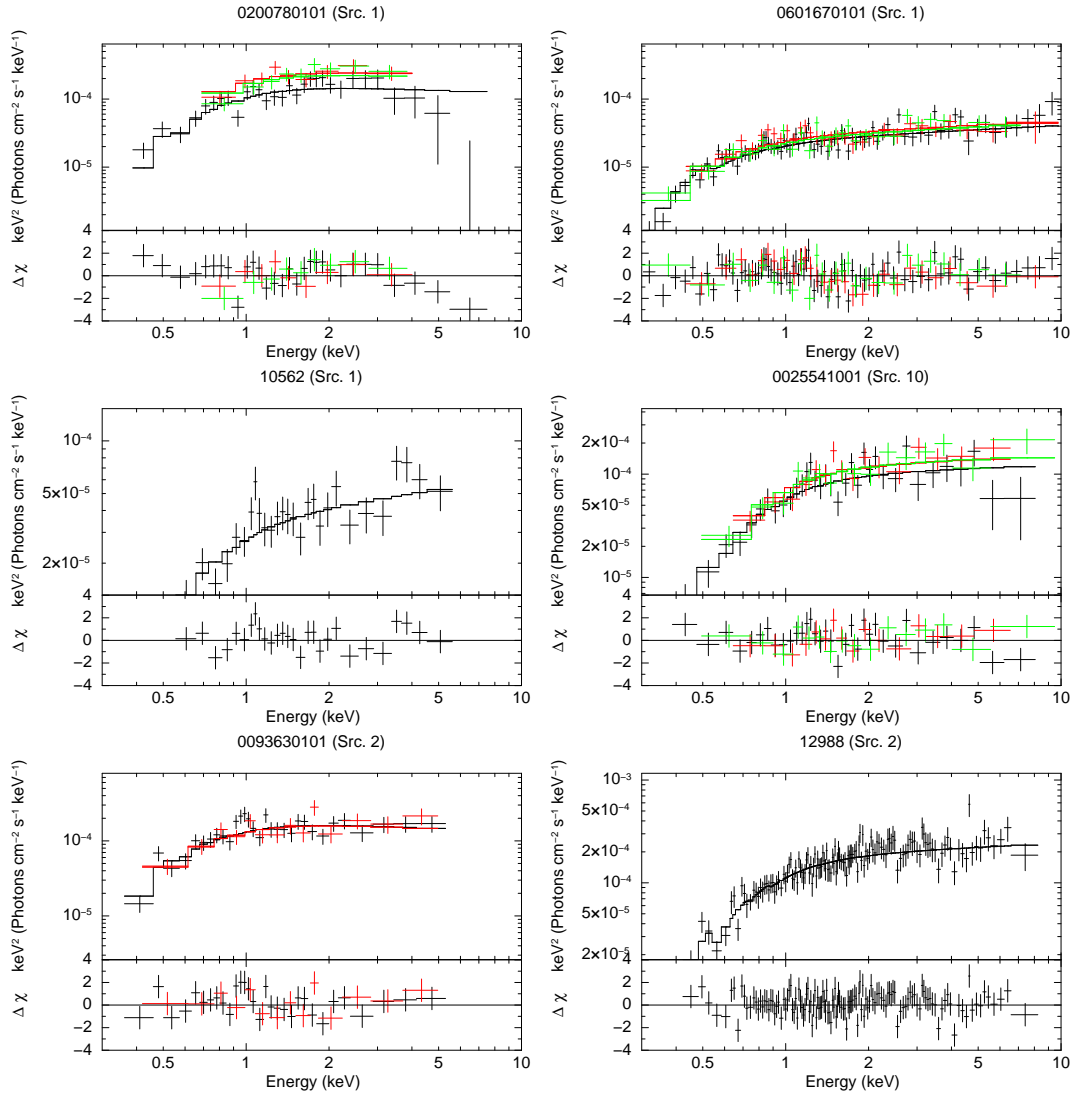
Figure 2.4: *XMM-Newton* EPIC pn (black), MOS1 (red), MOS2 (green) or *Chandra* spectra for observations with greater than 250 source counts, all of which are unfolded from the detector response. Multiple observations of sources are shown side-by-side where possible. Where there are two or more observations of a source with the same detector, plots are shown on the same scale for direct comparison. Over-plotted lines show the best fitting absorbed power-law spectra (Table 2.6), with one absorption component set to the Galactic value and another free to model intrinsic absorption in the ULX candidates. A range of photon indexes between 1.4-2.2 were obtained.
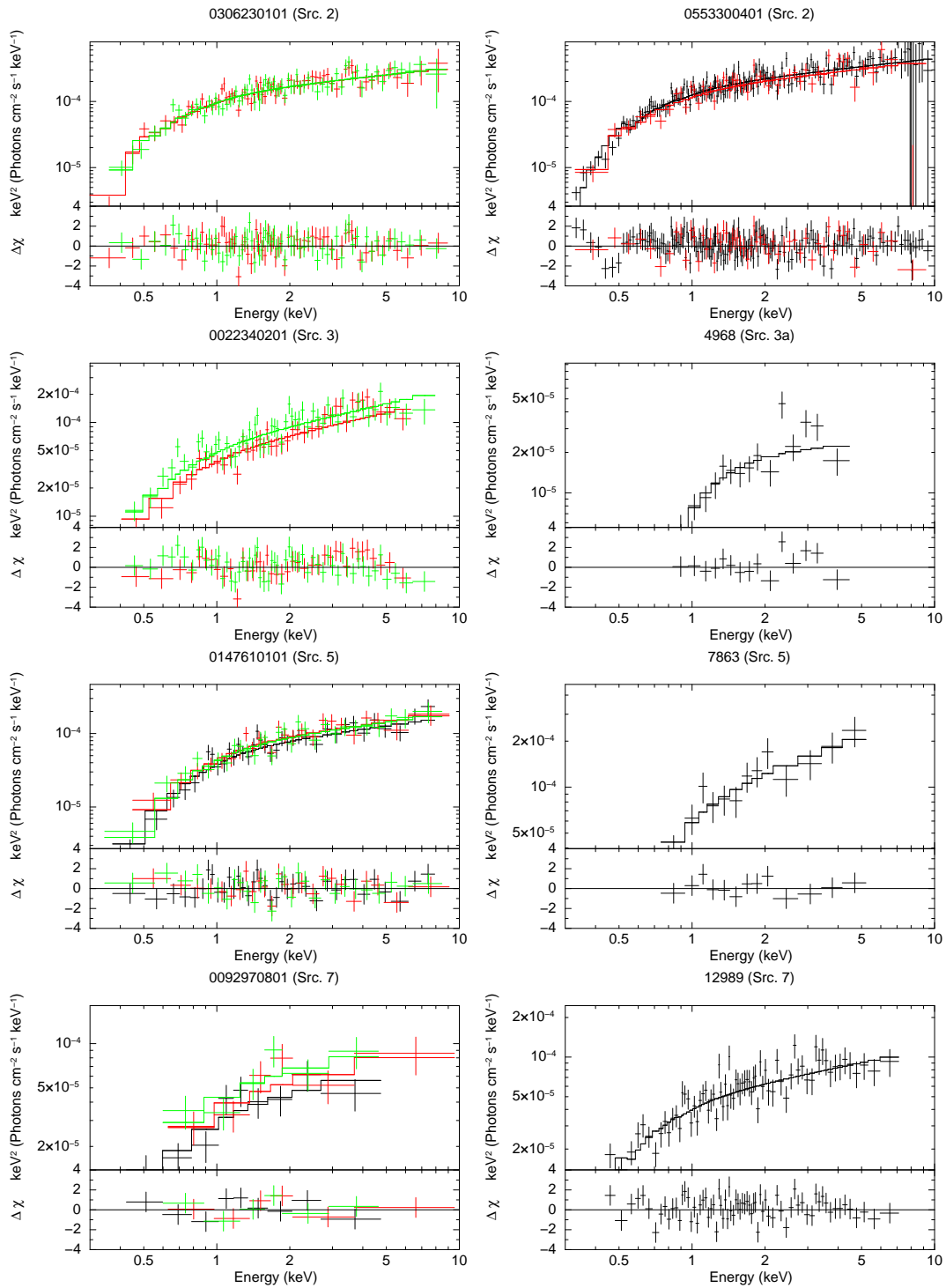
Figure 2.4: continued
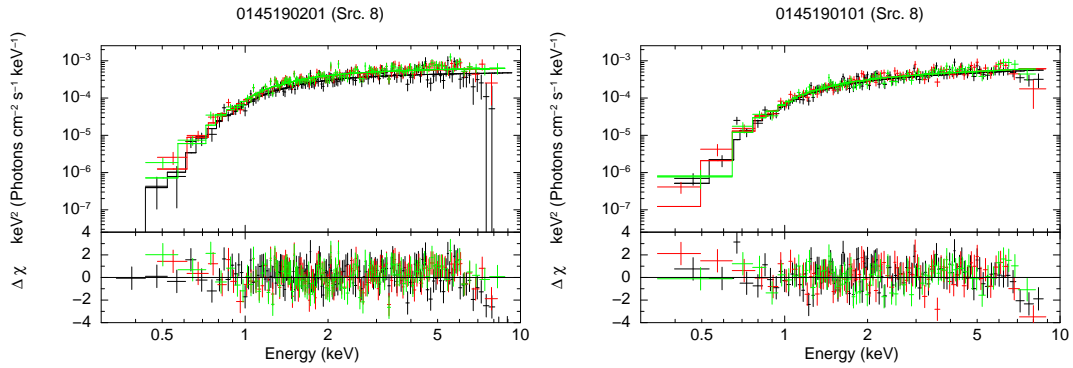
Figure 2.4: continued

power-law model, but rejected a MCD fit at greater than the 95 per cent level, and 11 spectra were acceptably fitted by both models. In all, the absorbed power-law fit was statistically preferred (i.e., provided the closer fit to the data) in 15/21 cases, compared to 5/21 for the MCD, although many of these preferences were marginal in nature.

The large majority of the spectra that were acceptably characterised as absorbed power-law continua all had rather hard photon indexes, with $\Gamma = 1.4$–2.2. The absorption column densities for these fits were mostly moderate (where well con-strained), with values in the range $\sim (1$–$3) \times 10^{21}$ cm^{-2}, although the column for Src. 8 was notably higher at $\sim 10^{22}$ cm^{-2}, which may be due to its location in an edge-on system. It should be noted however, that such an interpretation may bring into doubt any physical association with the particularly blue potential counterpart to this source. We discuss this further in Section 2.4.1. The spectra that were ac-ceptably fitted by the absorbed MCD model had – with one notable exception – inner disc temperatures of $kT_{\rm in} \sim 1.0$–1.9 keV, and rather low modelled absorption columns at $< 1 \times 10^{21}$ cm^{-2}, where well-constrained. The exception was the fainter observation of Src. 10, where the MCD model was the only acceptable fit, and the spectrum was remarkably soft with an inner disc temperature $kT_{\rm in} \sim 0.4$ keV.

An inner disc temperature in the range 1–2 keV is fairly typical for a sub-

Eddington stellar mass black hole in the thermal dominant state, with the accretion disc extending to the innermost stable circular orbit (McClintock & Remillard, 2006). However, for objects at close to $L_X \sim 10^{41}$ erg s^{-1} it would appear somewhat anomalous, and certainly not indicative of the presence of IMBHs, which should have much cooler disc-dominated spectra (e.g. Kaaret et al. 2003; Miller et al. 2003; Miller et al. 2004), as indeed does seem to be the case for the fainter dataset for Src. 10. We investigated whether there was any evidence for cool disc components in the other spectra by fitting a two-component, absorbed MCD plus power-law model to the best datasets (the 12 spectra with $\gtrsim$ 1000 counts), where we had the best opportunity of deconvolving the spectra into multiple components. In all but two cases there was no discernable improvement to the absorbed power-law spectral fit with the addition of a cool disc component. Two cases offered marginal improvements: the fit to the original *XMM-Newton* detection of Src. 3 (before being resolved by *Chandra*) improved by $\Delta\chi^2 = 10.9$ for two additional degrees of freedom with a ~ 0.1 keV disc; and the first, most luminous detection of Src. 1 improved by $\Delta\chi^2 = 13.1$ for two additional degrees of freedom with a ~ 0.07 keV disc. However, in the latter case the MCD model alone still offered the most acceptable fit to the data. This lack of strong cool disc components in the sample is perhaps unsurprising given the lack of strong soft residuals in the spectra presented in Figure 2.4.

However, one object stands out as possessing interesting residuals in Figure 2.4. Both observations of Src. 8, the highest quality data in the sample with > 5000 counts per dataset, appear to show a high energy spectral turnover beyond ~ 5 keV. Interestingly, this feature is the key diagnostic of the putative ultraluminous state, that is seen in many less-luminous ULX spectra (Gladstone et al., 2009). We note that the other main diagnostic of this putative state, a soft excess, is not seen; although this may be due to the object being buried in an edge-on galaxy, and hence its soft X-rays being relatively highly obscured, as is suggested by its spectral fits (cf. Table 2.6). Interestingly, this is very comparable to the object NGC 4517 ULX1

(Walton et al. 2011a), which is also located in an edge-on galaxy and has a highly absorbed soft spectrum, with a break at high energy. Confirmation was sought of the significance of the spectral break using the method of Stobbart et al. (2006), i.e., by fitting unabsorbed power-law and broken power-law models to the 2–10 keV X-ray spectra of both observations of Src. 8. A broken power-law model provided a better fit to both observations, with very significant F-test probabilities of 1×10^{-12} (0145190201) and 4×10^{-8} (0145190101), hence the spectrum is confirmed to be consistent with the ultraluminous state.

Both Figure 2.4 and Table 2.6 demonstrate that the individual objects also displayed both flux and spectral shape variations between different observing epochs. In some cases the spectral variability was quite subtle, for example a hardening of the absorbed power-law spectrum with flux in Src. 2. In other objects the contrasts were much starker, particularly in Src. 1 and Src. 10. In the former case the object transits from an absorbed disc-like spectrum at high flux to an absorbed power-law spectrum in the two subsequent spectra where the flux is a factor > 4 lower, and in the latter case the spectrum changes from hard and power-law-like at high flux to much softer and disc-like after a drop in flux of nearly a factor 20. We discuss these changes further in Section 2.5.

2.3.3   X-ray timing

Short term variability

In addition to extracting X-ray spectra, we also extracted background-subtracted light curves for each observation. A representative selection of these light curves is shown in Figure 2.5, covering the differing data qualities, exposure lengths and amounts of variability in the data (see below). The light curves are binned such that there are ~ 25 counts per element of temporal resolution.

The fractional variability amplitude, F_{var}, was used to determine whether statis-
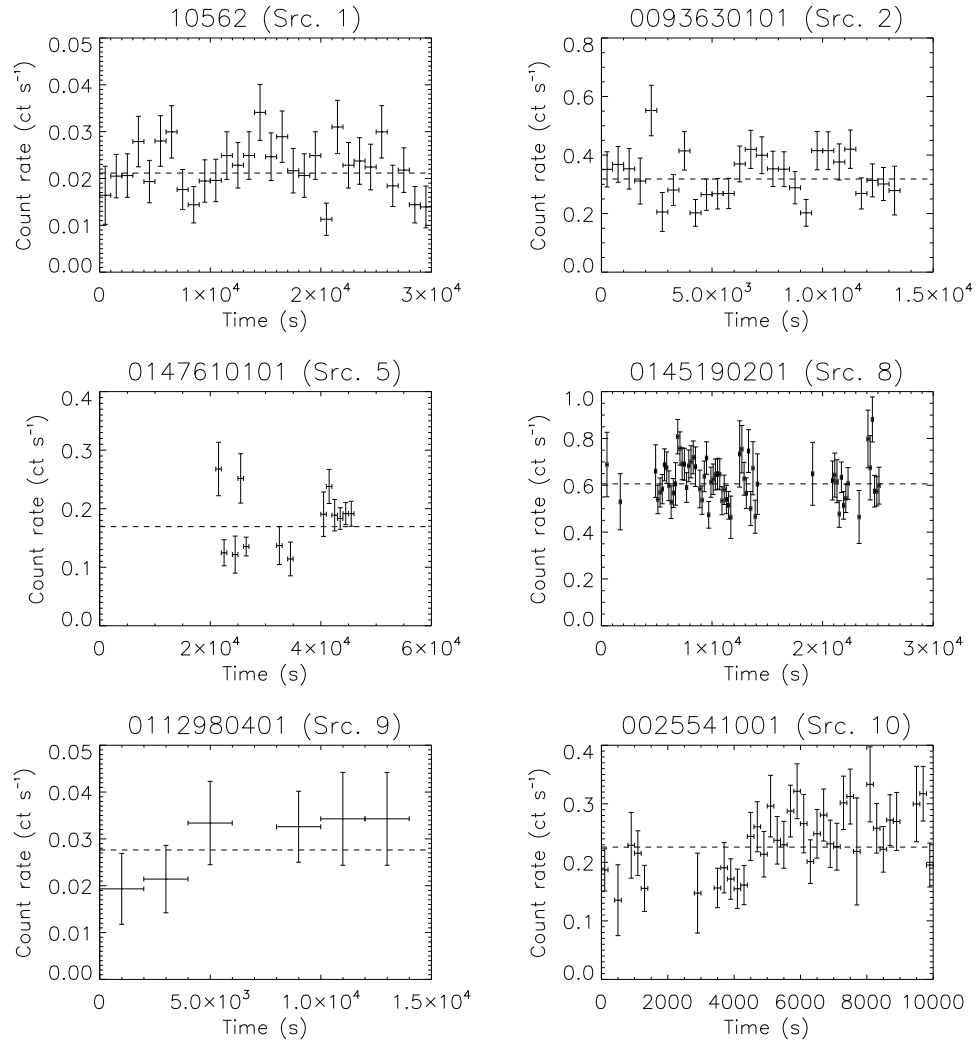
Figure 2.5: A selection of background-subtracted light curves of the ULX candidates, chosen to show a variety of behaviours and data quality: continuous, moderate count rate data (*top left & top right*); sparse data (*middle left & middle right*); low count rate data (*bottom left*); variability about a mean count rate (*top left & top right*) and an apparent maintained shift in the mean count rate (*bottom left & bottom right*). *XMM-Newton* light curves are summed over all EPIC detectors, except for 0093630101, where only pn and MOS2 detections were used. The dashed line shows the minimised χ^2 best fitting constant count rate for each observation.

Table 2.7: Luminosity and variability of the extreme luminosity ULXs

Obs ID	L_X [a]	$F_{\mathrm{var}}(200\ \mathrm{s})$ [b]	$F_{\mathrm{var}}(2\ \mathrm{ks})$ [b]
Src. 1			
0200780101	$10.2^{+0.5}_{-1}$	$< 0.2^c$	-
10562	$2.5^{+0.1}_{-0.3}$	-	0.11 ± 0.06
0601670101	$1.90^{+0.07}_{-0.06}$	-	$< 0.1^c$
Src. 2			
0093630101	2.8 ± 0.2	-	-
0306230101	$3.6^{+0.1}_{-0.2}$	-	0.05 ± 0.04
0553300401	$4.6^{+0.1}_{-0.2}$	0.09 ± 0.04	0.10 ± 0.02
12988	$3.4^{+0.1}_{-0.2}$	$< 0.1^c$	0.13 ± 0.02
Src. 3			
0022340201	6.1 ± 0.3	-	0.08 ± 0.04
4968 - a	$1.01^{+0.08}_{-0.2}$	-	-
4968 - b	$0.46^{+0.06}_{-0.1}$	-	-
4968 - c	$0.52^{+0.08}_{-0.4}$	-	-
Src. 5			
0147610101	$5.8^{+0.2}_{-0.3}$	0.13 ± 0.06	-
7863	9^{+1}_{-3}	$< 0.3^c$	-
Src. 7			
0092970801	30^{+2}_{-4}	$< 0.3^c$	-
12989	35^{+2}_{-3}	-	$< 0.1^c$
Src. 8			
0145190201	$4.19^{+0.09}_{-0.1}$	0.07 ± 0.02	-
0145190101	3.9 ± 0.1	0.11 ± 0.02	-
Src. 9			
553	2.9 ± 0.9	-	-
1454	3.2 ± 0.6	-	-
1666	$3.8^{+0.7}_{-1}$	-	-
0112980101	$6.8^{+0.7}_{-1}$	-	-
0112980401	5.9 ± 0.8	-	-
0112980501	5 ± 1	-	-
7698	1.9 ± 0.7	-	-
Src. 10			
0025541001	6.1 ± 0.3	0.10 ± 0.06	-
11230	$0.36^{+0.05}_{-0.2}$	-	-
10120	0.40 ± 0.05	-	-

Notes: [a]0.3–10 keV observed luminosity, in units of 10^{40} erg s^{-1}, calculated as per the text. The quoted errors are the 1σ confidence ranges on the luminosity. [b]Fractional variability amplitude. Values and errors are shown where variability is detected at $> 1\ \sigma$ significance (the quoted errors are the 1σ confidence ranges). Upper limits shown are 3σ limits, and are calculated where the variability was less than white noise. The FTOOL LCSTATS was used to provide this upper limit.

tically significant short term variability was present in the incident count rate of the sources. Here we define F_{var} as

$$F_{\mathrm{var}} = \sqrt{\frac{\frac{1}{N-1}\sum_{i=1}^{N}(x_i - \bar{x})^2 - \frac{1}{N}\sum_{i=1}^{N}\sigma_{\mathrm{err},i}^2}{\bar{x}^2}} \qquad (2.1)$$

as per Vaughan et al. (2003), where N is the number of temporal bins used, x_i are the individual count rates per bin, $\bar{x}$ is the mean count rate and $\sigma_{err,i}^2$ are the variances on the individual count rates. Variability was tested for on two separate fixed timescales, 200 s and 2 ks, and the results are shown in Table 2.7. Unfortunately, in most of the 24 observations the low count rates resulted in insufficient counts per temporal bin ($\lesssim$ 20), or short exposure times limited the available number of temporal bins (again, $\lesssim$ 20), which made such an analysis impractical. These datasets are shown as the blank spaces in Table 2.7. In fact, the data was only adequate for these analyses in nine observations at 200 s, and seven at 2 ks. In determining F_{var} temporally incomplete light curve bins (e.g. due to overlapping with the end points of GTIs, or the on/off times of instruments) were excluded so that the errors on the data points were normally distributed. Short term variability was detected at greater than 2σ significance in observations of four (and at greater than 3σ in two) of the eight sources in the sample, most notably from both observations of Src. 8 on 200 s timescales. The other marginally significant detections and upper limits were of sufficient quality to constrain values that were consistent with similar levels of variability, mainly at $\sim$ 10 per cent of the total count rate.

Long term variability

In order to study the long term variability of the sources, fluxes were obtained for each observation, that were converted to luminosities using the distances in Table 2.1. Where an observation contained sufficient counts to allow spectral fitting, fluxes were

determined using the absorbed power-law continuum spectral fit. For observations with insufficient counts for spectral fitting, light curves were χ^2 fitted with a constant count rate, and the resultant best fitting value was converted to a flux using PIMMS[13]. A characteristic spectral index of 2.0 and an intrinsic absorption column of 1.0×10^{21} cm^{-2} were assumed, except for observation 10120 of Src. 10, where the parameters of the much softer disc-like spectrum seen in observation 11230 were used instead. The observed luminosities are shown in Table 2.7, alongside the F_{var} values.

Most objects display long term luminosity variations at some level between the observations. In three objects the initial high luminosity that led to them being included in the sample is not maintained in subsequent observations, and appears to drop by factors > 4. Indeed, as a result of spectral fitting, two objects appear to be slightly under-luminous compared to the selection criteria of the sample (Src. 2 & Src. 8), although in both cases their peak luminosity is still considerable at $\sim 4 \times 10^{40}$ erg s^{-1}. In contrast, the most luminous object, Src. 7, remains persistently extremely luminous at $\sim 3 \times 10^{41}$ erg s^{-1} in both observations obtained to date.

2.3.4 An aside: the two identified background contaminants

In the course of this work two extreme ULX candidates were identified as background contaminants. These were Src. 4, initially associated with NGC 4065 by Walton et al. (2011) and identified as a background QSO on the basis of SDSS spectroscopy; and Src. 6, initially associated with NGC 4874 but later identified as a background QSO using Gemini GMOS spectroscopy. Table 2.8 shows the results of the simple X-ray spectral fits to the data for these objects, for comparison with the presumed *bona fide* extreme ULXs analysed in the rest of this chapter (see Section 2.5.3 for discussion related to this comparison). Also, the Gemini GMOS spectrum of the optical counterpart to Src. 6 is shown in Figure 2.6. The broad emission lines

---

[13]http://heasarc.nasa.gov/Tools/w3pimms.html
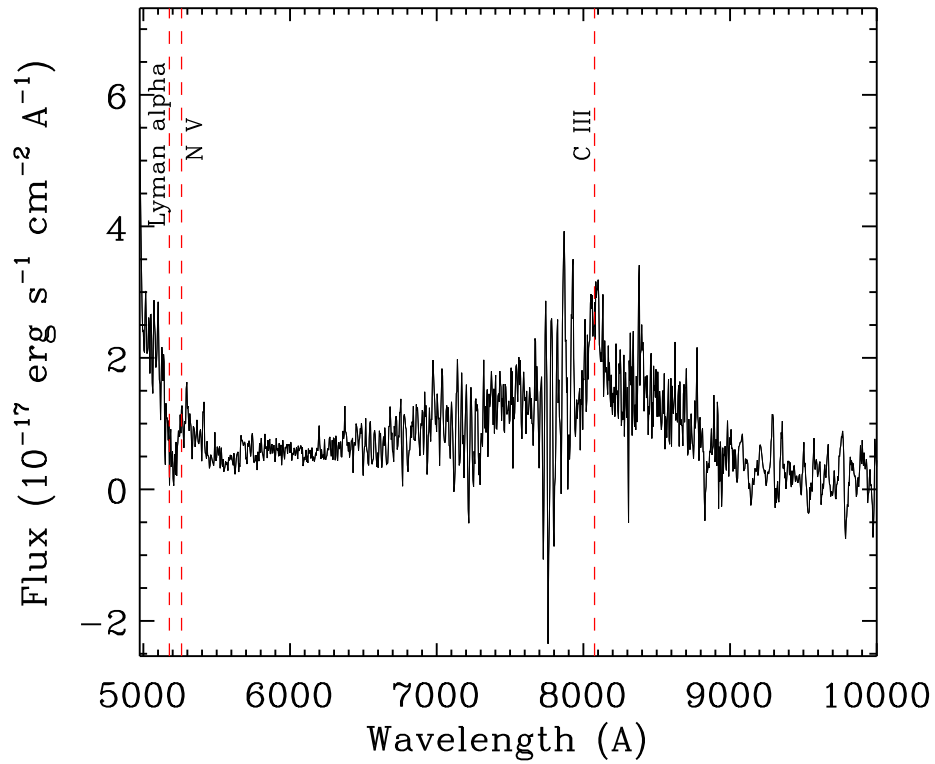
Figure 2.6: Gemini GMOS-N longslit spectrum of the optical counterpart to Src. 6, taken using the R150 grating and the 0.75 arcsecond slit. It was suggested that this source may be a bright ULX in a UCD in the Coma cluster, however lines identified in this spectrum (shown by dashed red lines; see text for details) instead identify it as a QSO at redshift ≈ 3.25.

present at ~ 5177, 5265 & 8076 Å are identifiable with the Lyman α 1216 Å, NV 1240 Å & CIII 1909 Å lines (respectively) at a redshift of $z \approx 3.25$, demonstrating this is very likely to be a high redshift QSO.

Table 2.8: X-ray spectral fitting results for the background contaminants

		Absorbed power-law			Absorbed multi-colour-disc				
Source ID	Obs ID	$N_H{}^a$	Γ^b	χ^2/dof	$N_H{}^a$	kT_{in}^c	χ^2/dof	$L_{\mathrm{ULX}}{}^d$	$L_{\mathrm{QSO}}{}^e$
Src. 4	0112270601	-	-	-	-	-	-	7.6 ± 0.9^f	1.2 ± 0.2
	0112271001	< 0.2	$2.4^{+0.6}_{-0.5}$	$41\%^g$	< 0.04	$0.6^{+0.2}_{-0.1}$	$88\%^g$	12 ± 3	1.9 ± 0.5
	0112271101	< 0.1	$2.5^{+0.5}_{-0.3}$	$62\%^g$	< 0.02	$0.43^{+0.09}_{-0.07}$	$88\%^g$	12^{+4}_{-2}	$1.9^{+0.6}_{-0.3}$
	12990	-	-	-	-	-	-	7 ± 1^f	1.1 ± 0.2
Src. 6	556	-	-	-	-	-	-	4.5 ± 0.8^h	37 ± 7
	0124711401	< 0.3	$2.3^{+3}_{-0.6}$	$23.9/32$	< 1	< 0.4	$27.4/32$	< 9	< 70
	0153750101	< 0.1	$1.4^{+0.4}_{-0.3}$	$41.3/42$	< 0.1	$1.3^{+0.8}_{-0.4}$	$39.9/42$	11^{+2}_{-4}	90^{+20}_{-30}
	0300530701	< 0.4	$1.7^{+1}_{-0.5}$	$42.0/45$	< 0.2	$1.1^{+0.8}_{-0.5}$	$41.3/45$	< 10	< 80
	0300530601	< 0.2	$1.6^{+0.6}_{-0.4}$	$36.6/31$	< 0.1	$1.1^{+0.8}_{-0.4}$	$36.6/31$	< 20	< 200
	0300530501	< 0.3	$2.3^{+2}_{-0.8}$	$45.7/44$	< 0.2	$0.5^{+0.3}_{-0.2}$	$45.6/44$	7^{+2}_{-3}	60 ± 20
	0300530301	< 4	$2.0^{+4}_{-0.7}$	$45\%^g$	< 1	$1.0^{+0.6}_{-0.5}$	$35\%^g$	< 120	< 1000
	0300530101	< 0.2	$1.5^{+0.8}_{-0.4}$	$33.7/41$	< 0.1	$1.3^{+2}_{-0.8}$	$36.4/41$	10^{+2}_{-5}	80^{+20}_{-40}
	9714	-	-	-	-	-	-	1.9 ± 0.4^h	15 ± 3
	10672	< 0.2	$2.2^{+0.9}_{-0.5}$	$46\%^g$	< 0.06	$0.6^{+0.3}_{-0.2}$	$75\%^g$	$2.9^{+0.6}_{-0.8}$	24^{+5}_{-7}

Notes: ^{a}Absorption column density external to our own Galaxy ($\times 10^{22}$ cm^{-2}). ^{b}Power-law photon index. ^{c}Inner-disc temperature (keV). ^{d}0.3–10 keV luminosity ($\times 10^{40}$ erg s^{-1}), estimated from a power-law spectral fit, and assuming the object is at the distance of the foreground galaxy. ^{e}0.3–10 keV luminosity ($\times 10^{44}$ erg s^{-1}), estimated from a power-law spectral fit, and assuming the object is at the distance derived from its optical spectral redshift measurement. ^{f}This observation had insufficient counts for spectral fitting, so a power-law spectrum with the same spectral index and absorption column as observation 0112271001 was assumed when estimating the flux. ^{g}Goodness of the minimised cash-statistic fit. ^{h}Again, insufficient counts were available for spectral fitting, so a power-law spectrum was assumed with a typical spectral index of 2 and an intrinsic absorption column of 1×10^{21} cm^{-2}.

2.4 Comparing the characteristics of the sample sources to other ULXs

In the previous sections we have examined the characteristics of a small sample of the most luminous ULXs. Here, we will attempt to place these results in the wider context of ULX and HLX studies.

2.4.1 Spatial properties

Similarly to other ULXs, all but one of the sample remain unresolved and point-like at the X-ray spatial resolution of the *Chandra* observatory, which is the highest currently available. In the one case where the original *XMM-Newton* source detection was resolved to reveal underlying structure, Src. 3, it resolved into three luminous ULXs, each of which is point-like. However, the sum of luminosities in the three resolved objects is substantially below the luminosity of the original *XMM-Newton* detection. Moreover, by virtue of the short-term variability in the original detection we can conclude that it is likely that just one of the three objects was substantially brighter in the first epoch, such that it was the dominant source of flux in the *XMM-Newton* detection. As it is unclear which of the three subsequently resolved objects was brightest in the original data, we retain all three in this work. However, for the purposes of constraining the relative changes within this object (e.g. its luminosity with time), we base the second epoch measurement on the brightest of the three resolved objects, Src. 3a, in the remainder of this chapter, which effectively provides a lower limit on the long term change in flux.

The locations of the candidate ULXs within their host galaxies may also be used as a comparator. The objects that lie coincident with face-on spiral galaxies all appear associated with the outer regions of their hosts, close to spiral arm structure. In three galaxies that have had their HII regions mapped, the ULXs all lie close to

known HII regions. This evidence would seem indicative of these objects being associated with recent star formation; and this appears in common with less luminous ULXs. Indeed, an association with star formation has long been qualitatively established by the discovery of populations of ULXs in star forming galaxies in the early years of the *Chandra* mission (e.g. Fabbiano et al. 2001; Roberts et al. 2002; Gao et al. 2003), with subsequent studies quantifying the relationship with the amount of ongoing star formation (e.g. Swartz et al. 2004; Gilfanov et al. 2004; Swartz et al. 2009). Furthermore, the quoted separation of the extreme ULXs from known HII regions is of the order ~ 200 pc in NGC 470 and NGC 7479, consistent with the separation of ULXs from stellar clusters in the Antennae (Zezas et al. 2002) and other nearby starforming galaxies (Kaaret et al., 2004). In the two face-on galaxies with *HST* imaging, NGC 2276 and NGC 7479 (both ~ 33 Mpc distant, where the ~ 1 arcsecond diameter error region equates to ≈ 160 pc), the objects appear near to likely star forming complexes in the spiral arms. All four of these ULXs possess candidate counterparts, consistent with stellar clusters in the three NGC 2276 ULXs (Src. 3a–c), and a possible supergiant stellar counterpart to the NGC 7479 object (Src. 10). Thus the objects remain at the very least associated with a star forming environment, even in *HST* imaging. This is also a characteristic in common with two of the three best studied HLXs; M82 X-1 is located in the centre of an archetypal starburst galaxy (e.g. Matsumoto et al. 2001; Kaaret et al. 2001), and object N10 is in the famous starforming ring of the Cartwheel galaxy (Gao et al., 2003).

Src. 8 presents an interesting case; it lies coincident with a dust lane in the edge-on galaxy NGC 5907, and is relatively highly absorbed in the X-rays, consistent with being embedded within the dust lane; yet has a very blue counterpart, that is also relatively luminous with $M_{F450W} = -9.4$. It is difficult to interpret this as a young stellar cluster or a single giant star as there is no evidence for further star formation in its vicinity; but this object cannot be a background object as the high extinction through the NGC 5907 dust lanes would not permit a background object with blue

colours to be visible. Given the X-ray characteristics of this object discussed later, it would seem to be a plausible ULX; therefore its blue colour and high absolute magnitude suggest its optical emission is dominated by reprocessed X-ray emission from the outer regions of the accretion disc, as suggested for some fainter ULX optical counterparts (e.g. Tao et al. 2011; Grisé et al. 2012) and ESO 243-49 HLX-1 (Farrell et al. 2012; Soria et al. 2012), although the high X-ray absorption column remains a problem for this interpretation.

After the exclusion of two of the sample near elliptical galaxies as background QSOs, we are left with Src. 7 alone in this type of habitat. It is somewhat surprising that we find any HLX in this type of environment, given their lack of star formation. Indeed, previous results show that the X-ray luminosity functions of elliptical galaxies are steep (e.g. complete sample of Walton et al. 2011b; also Kim & Fabbiano 2010), and Irwin et al. (2004) demonstrated that the numbers of ULX candidates with luminosities above 2×10^{39} erg s^{-1} found in and around elliptical galaxies were consistent with background expectations, with a couple of notable exceptions. Hence this detection is quite remarkable, particularly at a luminosity of $\sim 3 \times 10^{41}$ erg s^{-1} which makes it the second most luminous ULX candidate known after ESO 243-49 HLX-1 (Farrell et al., 2009). We caution that there is a non-negligible chance of it being an unidentified background object. However, we note that its location – close to a peculiar S0 galaxy that possesses a dust lane, somewhat like Cen A but with no indication of nuclear activity – is also interesting, particularly as ESO 243-49 HLX-1 shares a very similar environment (Farrell et al., 2012). This object therefore deserves further study to elucidate its nature.

2.4.2   X-ray characteristics

In Section 2.3.2 we investigated the X-ray spectra of the objects in this sample, finding a general preference for a power-law-like spectrum, which was intrinsically hard.
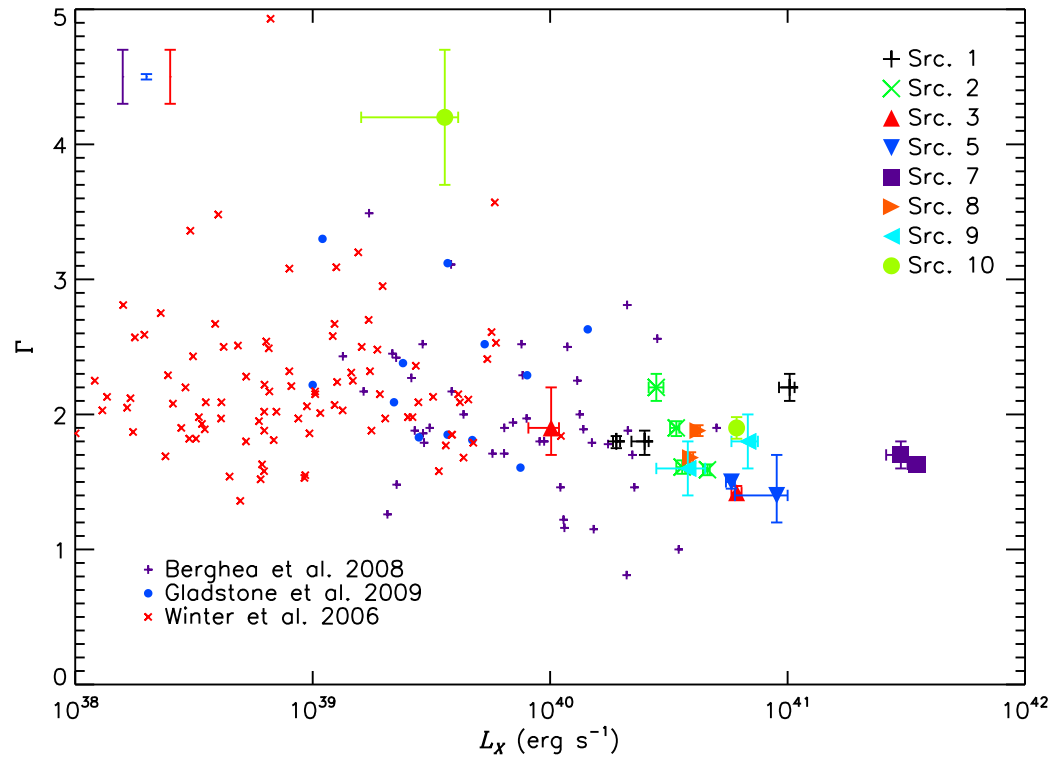
Figure 2.7: The relationship between power-law photon index Γ and observed luminosity for ULXs. Data points from our sample are plotted only where sufficient data was available for spectral fitting, and are plotted against the observed 0.3–10 keV luminosity, calculated using the power-law spectral fit and assuming that sources are at the distance of the identified host galaxy. All error bars are 1σ uncertainty regions. Different sources are identified by the symbols shown in the key (top right). Three samples of lower luminosity ULXs are included for comparison (smaller data points). Data are taken from: *purple plus sign* – Berghea et al. (2008), where luminosities were calculated from spectral parameters using a dummy response in XSPEC; *blue filled circles* – Gladstone et al. (2009), luminosities were obtained from a coupled disc-corona model (DKBBFTH, Done & Kubota 2006); *red crosses* – Winter et al. (2006), unabsorbed luminosities were converted to observed luminosities using PIMMS and assuming the power-law spectral fit. Typical error bars for each of the three comparison samples are shown in the same order from left to right in the top left corner.

We place these results in the context of other work on ULXs in Figure 2.7, where we compare the photon indexes of the power-law fits to the objects in our sample to three more samples of ULXs fitted with power-law continua, all as a function of luminosity. The three comparator samples are from: Gladstone et al. (2009), containing 12 of the best quality ULX datasets in the *XMM-Newton* archive, and covering the $10^{39} - 10^{40}$ erg s^{-1} luminosity regime; the larger sample of *Chandra* datasets analysed by Berghea et al. (2008), ranging from 10^{39} to 5×10^{40} erg s^{-1} in luminosity; and the large sample of ULXs with *XMM-Newton* data presented by Winter et al. (2006); although after removing their correction for absorption, we find the observed luminosities of many objects in the Winter et al. sample to lie significantly below 10^{39} erg s^{-1}.

Figure 2.7 suggests a hardening of the average photon index with increased observed luminosity; we investigate this further in Table 2.9, where we calculate the weighted mean value for the photon index for various samples shown in Figure 2.7. This clearly shows that the average spectrum of ULXs is harder at higher luminosities, as originally suggested by Berghea et al. (2008). Indeed, the effect appears quite pronounced; the two samples composed of sources below 10^{40} erg s^{-1} (Gladstone et al. 2009, and the less luminous Berghea et al. 2008 objects) have weighted mean photon indexes $\langle \Gamma \rangle > 2$, whereas the more luminous samples are significantly harder with $\langle \Gamma \rangle \sim 1.6$. This is clear evidence of a difference in the properties of the most luminous ULXs from the more ordinary ULX population. Interestingly, similarly hard spectral indexes have been seen in two well-studied HLXs: M82 X-1 with e.g. $\Gamma = 1.55 \pm 0.05$ (Kaaret et al., 2009), and Cartwheel N10 with $\Gamma = 1.75 \pm 0.25$ (Wolter et al., 2006). However the most luminous ULX, ESO 243-49 HLX-1, appears somewhat different; in its brightest phases it is distinctly soft, with e.g. $\Gamma = 3.4 \pm 0.2$ (Godet et al., 2009)[14], although it hardens significantly to $\Gamma \sim 2$ when at fainter

---

[14]The best quality X-ray spectral data currently available for ESO 243-49 HLX-1 at its peak luminosities show its spectrum to be dominated by a cool ($kT_\mathrm{in} \leq 0.26$ keV) disc component, see

Table 2.9: Mean photon index for various ULX samples

Sample	$\langle \Gamma \rangle$
Gladstone et al.	2.19 ± 0.01
Berghea et al., $< 10^{40}$ erg s^{-1}	2.10 ± 0.07
Berghea et al., $> 10^{40}$ erg s^{-1}	1.54 ± 0.06
This sample (all)	1.72 ± 0.07
This sample, $> 5 \times 10^{40}$ erg s^{-1}	1.61 ± 0.07

fluxes (Farrell et al. 2011; Servillat et al. 2011), such that it appears similar to the sources presented here (see Section 2.5.1).

We also previously examined evidence for intra-observation variability in our objects. Here, we compare the results to well-constrained variability measurements from less-luminous ULXs. Specifically, in Figures 2.8 & 2.9 we compare the fractional variability over the 0.3–10 keV range for our sample of luminous ULX candidates to the fractional variability of a selection of lower luminosity ULXs, on time scales of both 200 s and 2 ks. The comparison sample were selected for having both a well constrained power spectrum in Heil et al. (2009), and a well-constrained flux by Gladstone et al. (2009). Their fractional variabilities were calculated by integrating the power-law and broken power-law power spectra from Heil et al. (2009), and normalising by flux using the values from Gladstone et al. (2009). As Figures 2.8 & 2.9 demonstrates, the variability levels of the less luminous ULXs are low (typically 2 per cent fractional variability or less where well constrained), consistent with many reports of low short-term variability levels in ULXs (e.g. Swartz et al. 2004; Feng & Kaaret 2006a; Heil et al. 2009). In contrast, the measurements and constraints on the higher luminosity objects are consistent with higher levels of variability, ~ 10 per cent or more fractional variability in most cases, although most error bars are relatively large due to the poorer data quality in these objects. This, then, tentatively

Servillat et al. (2011).
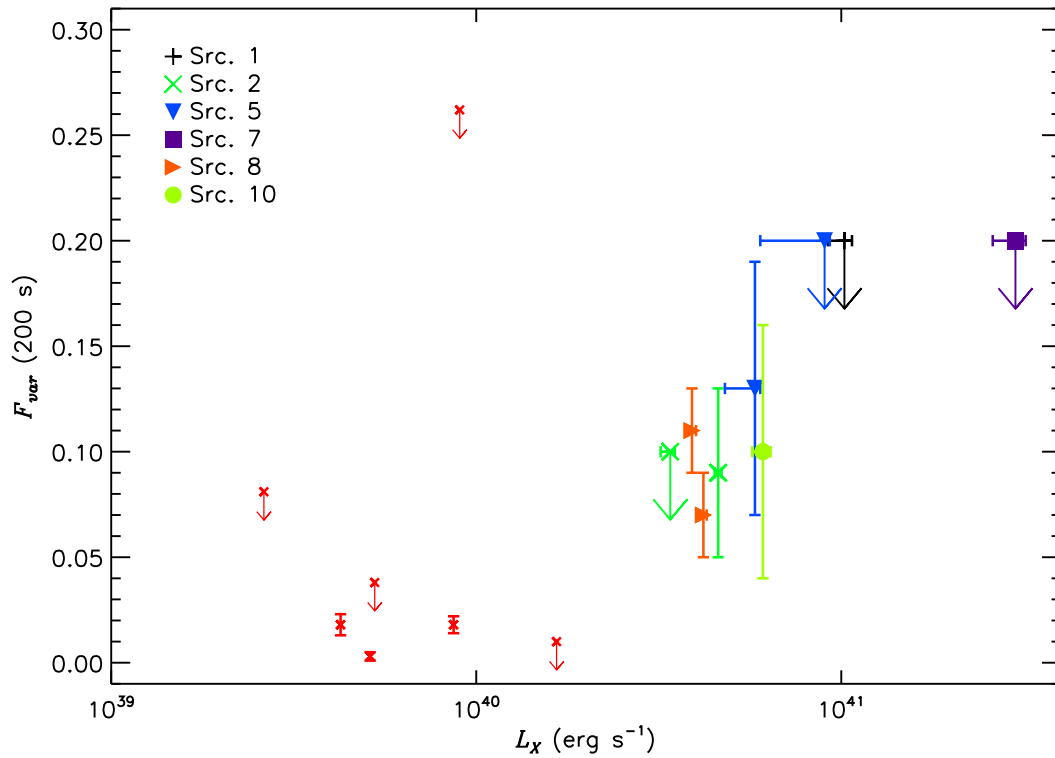
Figure 2.8: Fractional variability amplitude (F_{var}) for a time resolution of 200s, shown as a function of 0.3–10 keV luminosity. The upper limits shown are 2σ significance levels in all cases, and error bars are 1σ confidence regions. Each object from the luminous ULX sample is labelled by a different symbol; a key is provided at the top left. Lower luminosity ULXs (small crosses) are shown for comparison, these data points were obtained by the integration of fits to the power spectra for a selection of sources from Heil et al. (2009). Count rates from Gladstone et al. (2009) for the same observations were used to calculate F_{var}. The comparison sample includes (from left to right) - NGC 2403 X-1, NGC 1313 X-1, NGC 1313 X-2, NGC 5204 X-1, Ho IX X-1, NGC 4559 X-1 and Ho II X-1.

points to a second observational difference between 'normal' ULXs and their higher luminosity cousins; more short-term variability in the more luminous objects.

In Figure 2.10 we show the changes in the luminosity of the objects with time. It is immediately obvious the data is extremely sparse, with no more than $2-6$ measurements per object over a baseline of up to a decade; hence any conclusions
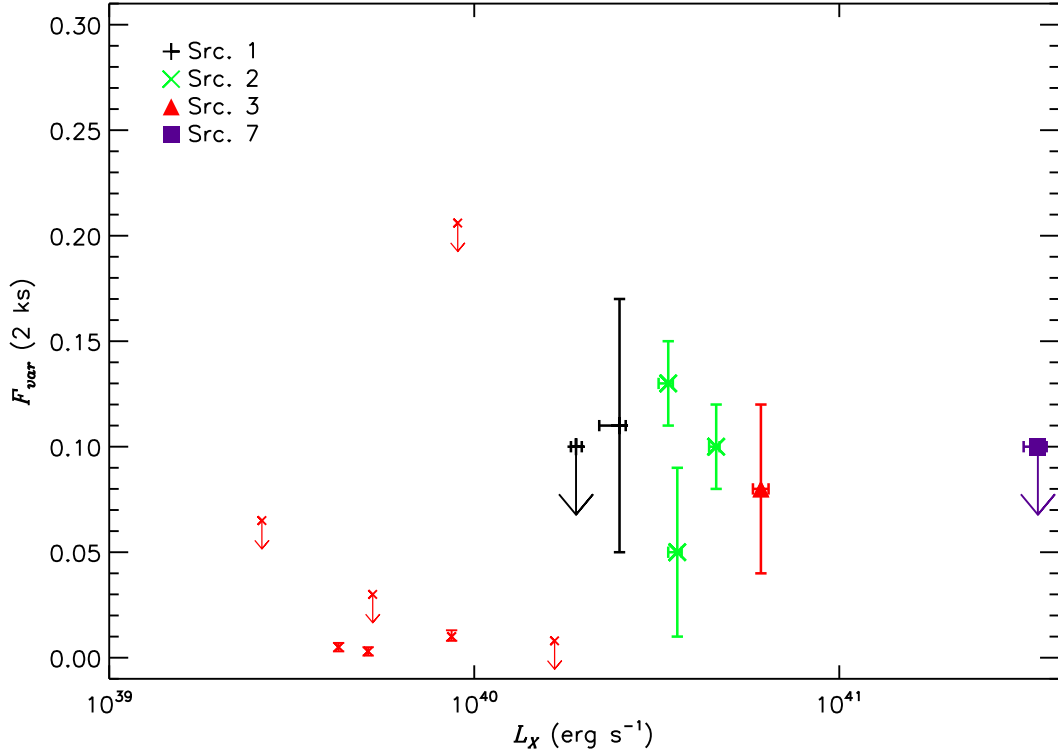
Figure 2.9: As Figure 2.8, but for a time resolution of 2ks.

made on their long-term behaviour must be very tentative as we simply cannot tell how the objects behaved when they were not being observed. With this caveat in mind, we can tentatively sort the objects into two groups: firstly three objects that appear to fade substantially from an initial peak in luminosity, down to more 'usual' ULX luminosities ($\lesssim 2 \times 10^{40}$ erg s^{-1}). This includes the only HLX candidate with a spiral host, Src. 1 in NGC 470, the *XMM-Newton* detection subsequently resolved by *Chandra*, Src. 3, and Src. 10 (which we discuss further below). The remaining five objects all sustain their extreme luminosities, within a factor ~ 2, most notably Src. 7 which is detected at a luminosity $\sim 3 \times 10^{41}$ erg s^{-1} in both epochs. Given the sparse data available from our sample, and the lack of extensive monitoring of less luminous ULXs, we are also able to do little to compare the long-term variability
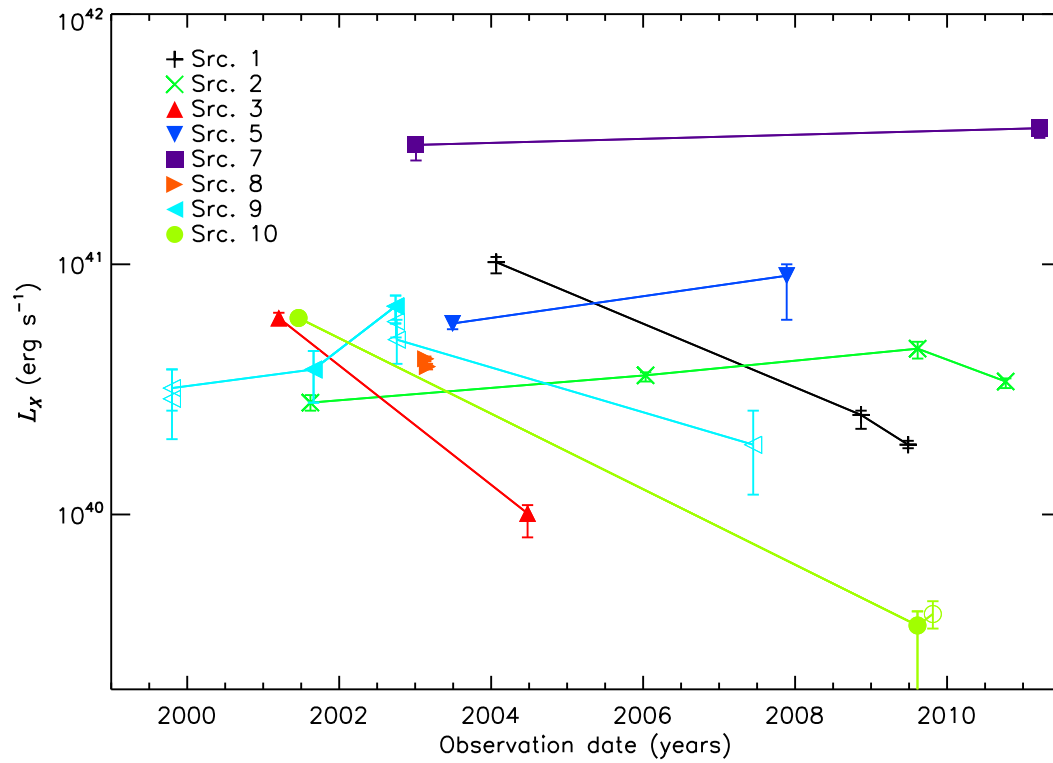
Figure 2.10: Long term light curves of the objects in our sample. We show the observed 0.3–10 keV luminosity, plotted against observation date. Filled symbols correspond to observations with greater than 100 counts, where the fitted absorbed power-law models were used to calculate luminosity. Unfilled symbols correspond to observations with insufficient counts for spectral fitting, where instead spectral parameters were assumed as per Section 2.3.3. The low luminosity data point for Src. 3 corresponds to the most luminous of the resolved sources (Src. 3a) in the *Chandra* observation.

properties of our objects to other ULXs. Recently *Swift* monitoring programmes have been undertaken for a small handful of objects, that appear persistently bright with typical flux variations of factors up to ~ 5 over the course of the monitoring campaigns (e.g. Kaaret & Feng 2009; Grisé et al. 2010). The HLX candidate M82 X-1 also appears to vary similarly in *RXTE* monitoring, although it also displays a periodic signal on 62 day timescales (Kaaret & Feng, 2007). The brightest HLX, ESO 243-49 HLX-1, again appears different – its variability resembles an outburst cycle in an ordinary X-ray binary, with a fast rise to peak luminosities followed by a slow decay in flux, and a 375 ± 13 day gap between two outburst peaks (Lasota et al. 2011; Servillat et al. 2011).

Further inspection of Figure 2.7 shows that several of the objects display significant X-ray spectral variability, in this case represented by a change in photon index at different flux levels (or, indeed, at different observation epochs with similar flux levels, as is the case for Src. 8). However, these changes are not consistent across the small sample, with some objects hardening with increased flux (e.g. Src. 2), and others softening (e.g. Src. 1). This at least is consistent with the varied picture seen across the population of lower luminosity ULXs, where many different behaviours are observed with changing luminosity (e.g. Feng & Kaaret 2009; Kajava & Poutanen 2009; Grisé et al. 2010; Vierdayanti et al. 2010; Servillat et al. 2011). Perhaps more revealing are the situations in which the preferred spectral model changes with luminosity, as they may indicate direct analogies with known spectral state transitions. We discuss this in the following section.

2.5 Discussion: on the nature of the most extreme ULXs

This work has highlighted that there are possible differences between the standard population of lower luminosity ULXs, and those most luminous objects that we study here. Most notably, the brightest objects are spectrally harder, well described by power-law continua with photon indexes $\Gamma \sim 1.7$, and there is tentative evidence they display higher amplitude flux variability, with typical F_{var} of ~ 10 per cent on timescales of 200 - 2000 seconds. But what does this mean physically for the objects in our sample?

2.5.1 Intermediate-mass black holes?

Perhaps the most interesting question we can ask is: do these objects finally offer evidence for a population of IMBHs underlying some ULXs? As discussed earlier, most super-Eddington models for stellar-mass black holes struggle to explain the high luminosities of this sample (e.g. Zampieri & Roberts 2009), and there are suggestions that a different class of objects is required to explain sources above the X-ray luminosity function break (Swartz et al., 2011). It is therefore quite a straightforward step to infer that we may be looking at IMBHs.

Crucially, this inference does appear to be supported by the observational characteristics of the sample. In particular, the X-ray spectra and timing properties are consistent with the low/hard state as described by McClintock & Remillard (2006), sharing both a power-law spectrum (with $\Gamma \sim 1.7$) and a fractional variability level consistent with ~ 10 per cent. Given that the low/hard state is typical only found at Eddington fractions of 10 per cent or less, this immediately constrains the masses of our black holes to be in the IMBH regime. We calculate individual lower limits for each object, based on the highest observed luminosity with a power-law-like spec-

trum and the 10 per cent L_{Edd} limit, in Table 2.10 as mass M_1. This implies black hole mass lower limits of $(1.9$–$27) \times 10^3 \ M_\odot$ across our sample.

One issue with the timing result is that McClintock & Remillard (2006) note that $10 - 30$ per cent fractional variability is expected in the 0.1 - 10 Hz range in the low/hard state, whereas we only probe frequencies as high as ~ 0.1 Hz in the best of our data. However, if we are dealing with large black holes we would expect their variability timescales to increase proportionally to their mass for the same accretion rate (McHardy et al., 2006); hence a 1000 $M_\odot$ black hole would vary on 100 times longer timescales than a 10 $M_\odot$ black hole. So, the $0.1 - 10$ Hz section of the PSD for a stellar mass black hole scales to the $10^{-3} - 0.1$ Hz regime, that we probe here, for a $\sim 1000 \ M_\odot$ IMBH.

An important test of whether these objects really are in the low/hard state would be to observe them transit into other states that are also seen at sub-Eddington luminosities in Galactic binaries. Such transitions have been suggested for ESO 243-49 HLX-1 (Servillat et al., 2011) and M82 X-1 (Feng & Kaaret, 2010), with in both cases the high luminosities at which these transitions occur providing a strong argument for IMBHs. Interestingly, ESO 243-49 HLX-1 appears to possess a hard power-law X-ray spectrum at similar luminosities to the objects in this sample. We potentially see a similar transition in one case: Src. 1 is far better described by a MCD, representative of the thermal dominant state, than a power-law at its highest luminosity ($\sim 10^{41}$ erg s^{-1}), and vice versa in subsequent lower luminosity datasets ($\leq 2.5 \times 10^{40}$ erg s^{-1}). Unfortunately, the timing data is of insufficient quality to confirm these states (with the little or no variability expected in the thermal dominant state potentially providing a distinction). However, the temperature of the disc appears highly anomalous for an IMBH, at ~ 1 keV, making the identification of a classical transition for an IMBH very dubious in this case.

One prediction that we can make is that if these are IMBHs in the low/hard state, then they should be emitting a steady radio jet. If so, the peak observed X-ray

luminosity can be used in conjunction with the radio luminosity to provide limits on the black hole mass via the so-called X-ray-radio fundamental plane (Merloni et al., 2003). We have attempted to do this using the currently available data. To this end, the *VLA* FIRST (Becker et al., 1995) and NVSS (Condon et al., 1998) 1.4 GHz radio surveys were searched at the source positions for any radio counterparts. However, none were detected, so the radio catalogue completeness limits were used as an upper-limit to the radio flux instead. A flat radio spectrum was assumed to extrapolate the radio flux from the observed band to 5 GHz, and 2-10 keV X-ray fluxes were extracted from the highest 0.3-10 keV flux of each source using PIMMS and spectral parameters from the appropriate power-law fit. Before presenting the limits we highlight two important caveats: firstly that the fundamental plane is not calibrated for IMBHs/ULXs, which may lead to some uncertainty; and secondly we are severely limited in what conclusions we can draw by the lack of simultaneous X-ray and radio observations.

Nevertheless, we present the upper limits on the IMBH masses in Table 2.10 as M_2. For a number of the sources the fundamental plane estimated limits on black hole mass are several orders of magnitude greater than the low/hard state mass limits, and in the SMBH mass regime. For these sources large improvements in radio detection limits would be necessary to use the X-ray-radio fundamental plane to test for IMBHs. However, for the closest source (Src. 8) the upper limit is already in the IMBH regime, and only $\sim$ an order of magnitude above the lower limit from the low/hard state identification. For two more objects (Src. 2 and Src. 5) a modest improvement of less than an order of magnitude would begin to constrain the mass within the IMBH regime.

However, there are problems with interpreting these objects as IMBHs. One such issue is the location of the objects, the majority of which are found in the same star forming environments as lower-luminosity ULXs. While the necessity to form only one such object in any galaxy neatly sidesteps the strong arguments for the bulk of

the populations of ULXs in these regions having to be predominantly stellar-mass objects (King 2004; Mapelli et al. 2008), one still has to both form these very massive objects, and then capture a high mass star, in order to appear as a ULX. Even so, processes such as the assembly and subsequent collapse of a very massive star at the centre of a young, massive star cluster have been suggested as viable IMBH formation channels in star forming regions (e.g. Portegies Zwart et al. 2004), and may provide a natural environment in which to capture a star to feed the IMBH (Hopman et al., 2004). However, in this case the lack of particularly bright and massive stellar clusters coincident with the ULXs may be an acute problem, even more so than the lack of such coincidences noted for less luminous ULXs (e.g. Zezas et al. 2002). Alternatively, if the IMBHs are not newly formed, the small number of such objects we observe may be commensurate with the predicted difficulties of capturing a young star into a close orbit by an IMBH (Madhusudhan et al., 2006), presuming such objects could find their way into a star forming region.

For the one object not readily related to star formation, Src. 7 in the S0 galaxy IC 4320, assuming the identification as a low/hard state binary is correct then an older IMBH must be required. In this case the possibilities include a primordial Population III star remnant (e.g. Madau & Rees 2001), or the stripped nucleus of an accreted dwarf galaxy (e.g. King & Dehnen 2005; Bellovary et al. 2010), although the requirement to accrete from a massive stellar reservoir likely remains. Again, we note the only established HLX with a luminosity in excess of Src. 7, ESO 243-49 HLX-1, is also associated with an S0 host (Farrell et al., 2012).

2.5.2 The most extreme super-Eddington objects?

While there are possible means of explaining the most luminous ULXs in star forming regions as IMBHs, as discussed above, it is incontrovertible that this is the same environment as that in which the majority of lower luminosity ULXs are found. We

Table 2.10: Limits on the black hole mass for an IMBH from low/hard state Eddington arguments and the X-ray - radio fundamental plane.

Source ID	$M_1/M_\odot{}^a$	$M_2/M_\odot{}^b$
Src. 1	$\gtrsim 1900$	$\lesssim 2 \times 10^6$
Src. 2	$\gtrsim 3500$	$\lesssim 2 \times 10^5$
Src. 3	$\gtrsim 4700$	$\lesssim 2 \times 10^6$
Src. 5	$\gtrsim 6900$	$\lesssim 5 \times 10^5$
Src. 7	$\gtrsim 2.7 \times 10^4$	$\lesssim 2 \times 10^8$
Src. 8	$\gtrsim 3200$	$\lesssim 3 \times 10^4$
Src. 9	$\gtrsim 5200$	$\lesssim 3 \times 10^7$
Src. 10	$\gtrsim 4700$	$\lesssim 4 \times 10^6$

Notes: [a]Black hole mass limit from Eddington arguments, assuming that the source is in the low/hard state and accreting at ≤ 10 per cent of the Eddington rate when at maximum luminosity with a power-law spectrum. For seven of eight objects this is the highest luminosity seen; for Src. 1 its highest luminosity spectrum is far better described by a MCD, so we use the second highest luminosity dataset for this object. [b]Black hole mass derived from the X-ray-radio fundamental plane.

should therefore explore whether it is possible that these most luminous objects are driven by a more extreme version of the super-Eddington processes now thought to power the majority of the lower luminosity ULXs.

There are possible scenarios in which we might explain most of these luminous objects by super-Eddington emission. Firstly, we note that Zampieri & Roberts (2009) argue that the black holes underlying some ULXs in low metallicity regions may be formed from the collapse of a single low-metallicity star which, by virtue of reduced wind-driven mass loss during its life time, can leave a black hole remnant as large as $\sim 90\ M_\odot$ (see also e.g. Belczynski et al. 2010 for mass transfer binaries). A combination of this high mass and similar maximal Eddington rates as are inferred in some stellar mass ULX models could raise the maximum luminosity for stellar remnant ULX models to $\sim 10^{41}$ erg s^{-1}. In support, we note that the apparent locations of many of the ULXs studied here, on the outskirts of their host galaxy (cf. Figure 2.2), may indeed be consistent with the lower metallicity regions required to

form such objects. Secondly, King (2009) suggests that the degree of beaming due to geometric collimation by the inflated inner disc and outflowing wind at high accretion rates, that constrains the escape path of the X-rays from the central region, scales directly proportionally to the accretion rate. Hence, extreme luminosities may be explained by a high beaming factor (which may also help explain the rarity of such objects, as significant numbers could be present, but would not be visible outside their narrow beam).

However, both these scenarios would still have to explain why the X-ray characteristics of these ULXs appear so similar to the very sub-Eddington low/hard state, and not akin to the ultraluminous state spectra described by Gladstone et al. (2009). One possibility is the low quality of the data in most cases masks both the soft excess and the subtler high energy break of the ultraluminous state, and the underlying spectra are similar to those observed in Ho IX X-1 or NGC 1313 X-1 by Gladstone et al., where the best fitting power-law continua have indexes $\sim 1.6 - 1.85$. However, these observations both have particularly low fractional variability (cf. Figures 2.8 & 2.9), unlike the objects in the higher luminosity sample, which appear variable on short timescales (albeit with large errors, or only upper limits in some cases). One way around this would be if the higher luminosity objects are more prone to displaying extrinsic variability. This is suggested by Middleton et al. (2011a) to explain the variability of NGC 5408 X-1, where it could originate in blobs of outflowing material driven off the surface of the accretion disc by the extreme radiation pressures from its central regions, that cross the line-of-sight to those regions. Better data is required to resolve these issues; but it is notable that in the one dataset within this sample with reasonably good data quality (Src. 8 in NGC 5907) an ultraluminous state spectrum is observed. However, we note that the distance to NGC 5907 is uncertain, and recent estimates (e.g. $d = 13.4$ Mpc by Tully et al. 2009a) place the host galaxy near enough that the luminosity of Src. 8 is reduced by a further 20 per cent, such that it is consistent with the top end of the 'normal' ULX population. It

is therefore questionable whether it should be included within this sample. Even so, its hard power-law-like spectrum and detected fractional variability provide important testimony that an ultraluminous state object can possess similar observational characteristics to the sub-Eddington low/hard state in moderate quality data.

One further mass limit could be placed assuming that the sample contains high accretion rate objects. Both Gladstone & Roberts (2009) and Yoshida et al. (2010) note that the low luminosity ULXs in NGC 4490 and (in the latter paper) M51 appear to transit between a power-law spectral state at $\sim 10^{39}$ erg s^{-1} to a MCD-like model at slightly higher luminosities. Gladstone & Roberts suggest this could be a transition from a sub-Eddington steep power-law state to a $\sim$ Eddington rate state; if so the highest luminosity in which a power-law spectrum is observed provides an estimate of the black hole mass from the requirement $L_{\mathrm{X}}/L_{\mathrm{Edd}} < 1$. However, without seeing the transition luminosity to a MCD spectrum itself this measurement does not provide strong constraints (as with further observations we might see the power-law at higher luminosities); for the sources in the sample this estimated upper limit is in the range $\sim 200\text{--}2700\ M_\odot$, with the only possible constrained limit (from Src. 1) as $\leq 800\ M_\odot$ from the observed luminosity of the observation where a MCD fit is much preferred.

2.5.3 Contaminants?

A final point to consider is whether any more of our objects could be background (or, plausibly, foreground) contaminants. A calculation based on that performed by Walton et al. (2011b) was used to establish the expected contamination of this sample by background objects; this found that three were expected out of the ten selected sources with luminosities above 5×10^{40} erg s^{-1} within 100 Mpc. In the analysis we were able to identify two background QSOs near elliptical galaxies, including one new $z = 3.25$ QSO near NGC 4874. The calculation predicts one more background

object, likely to be associated with a spiral galaxy, but no such object has been identified at present. We note that we would be unlikely to identify such an object from its X-ray properties alone. In Table 2.8 we present X-ray spectral fits to the QSO datasets, using the same models as for the ULXs (cf. Table 2.6). Although Src. 4 does appear somewhat softer than the luminous ULXs, errors on its spectral parameters are large. Large errors also dominate the measurements for Src. 6, and we were not able to derive short-term variability characteristics for either source due to the paucity of data. We would not, therefore, have been able to distinguish these objects from ULXs without the optical follow-up data. We therefore caution that without further optical follow-up (which, as the case of Src. 6 shows, must go several magnitudes deeper than the DSS) we cannot rule out a QSO nature for the several ULXs currently lacking follow-up data.

Further possible contaminants include foreground objects and other rare types of objects within the host galaxies. We can at least rule out foreground stars as none are evident in the DSS images in Fig 2.2. However, one possibility that should be mentioned is that of recent supernovae in the host galaxies, which are not accounted for in the contamination calculation of Walton et al. (2011b). Such supernovae have been seen with typical X-ray luminosities in the range of 10^{37}–10^{41} erg s^{-1} and fade over a variety of timescales, e.g. SN 1988Z decreased by ~ 5 over 2 years, whilst SN 1980K decreased by a similar factor between days 35 and 82 after outburst (Immler & Lewin, 2003). Interestingly, the X-ray spectra of some objects have been seen to soften as the flux decreases, for example in SN 1999em (Pooley et al., 2002), where the early X-rays are thought to originate in the circumstellar gas shocked by the initial blast wave, whereas the later soft emission comes from the lower temperature reverse shock region (see Fransson et al. 1996 for details). We do see several objects in the sample whose X-ray emission appears to fade in the years following their initial detection, including one object (Src. 10) that also softens dramatically. However, each of these objects shows some degree of fractional variability within at least one

observation, consistent with a compact object and rejecting the recent supernova hypothesis. This, and the lack of any identified optical supernovae associated with the ULXs in this sample, argues that we do not have any such objects amongst our sources.

A second rare class of objects that may be associated with the host galaxies are recoiling SMBHs, as has been suggested for the HLX candidate CXO J122518.6+144545 (Jonker et al., 2010). Such objects are predicted to form via the binary coalescence of SMBHs during galaxy mergers, where anisotropic gravitational wave emission imparts a kick of up to several thousand km s^{-1} on the new, single SMBH (see Komossa 2012 and references therein). This kick is sufficient to displace the SMBH from the centre of its host galaxy, and in some cases even expel it completely. Such objects might appear both X-ray and optically luminous, as they are predicted to retain a reservoir of gas and stars to accrete from; a key indicator of their SMBH nature would then be broad emission lines in their optical spectra. However, we again regard the chances of detecting such an object in our sample to be low; none of our spiral galaxies are undergoing (or appear to have recently undergone) the major merger necessary to create such an object. Interestingly, the only early-type galaxy in our sample, IC 4320, possesses a dust lane, a characteristic that has been linked to minor galaxy mergers in such systems (Shabala et al., 2012). It also hosts the most luminous ULX in our sample. The detection and characterisation of the optical counterpart to this object is therefore of great interest.

2.6   Conclusions

Even in the absence of definitive black hole mass measurements for ULXs, various arguments have resulted in the wide acknowledgement that the majority of these extraordinary objects are most probably powered by super-Eddington accretion onto stellar remnant black holes. However, the luminosities that can be produced in

this manner are limited by both a maximum Eddington ratio and maximum stellar remnant black hole mass, which complicates the unification of the brightest ULXs with the less luminous population. These particularly luminous, extreme ULXs may instead remain as potential IMBHs, with their rarity consistent with arguments as to the difficulties in producing stable high accretion rates in many such objects.

Here we have presented a study of 10 candidate extreme ULXs. We were able to identify 2 as background QSOs, resulting in a sample of 8 good candidates for further study. By examining the X-ray emission characteristics of this sample we note that these extreme sources do indeed appear to be distinctly different from the lower luminosity ULXs. Not only are they typically spectrally harder, they are also consistent with being more variable (albeit at low statistical significance in many objects). This combination of spectral and timing characteristics is highly suggestive of the sub-Eddington low/hard state, which given the luminosities involved would strongly argue for large (10^3–10^4 $M_\odot$) IMBHs. This is however not entirely conclusive, as accretion at the highest plausible super-Eddington ratios onto the most massive stellar remnant black holes could potentially produce ULXs up to $\sim 10^{41}$ erg s^{-1}. Further high quality X-ray observations are therefore required to test this, with the capability to detect ultraluminous state-like signatures, especially for the sources that lie in the transition zone between the brightest local ULXs ($\sim 3 \times 10^{40}$ erg s^{-1}) and the HLX luminosity range.

The sample of 8 candidate ULXs includes 2 candidate HLXs. One is a transient HLX, that subsequently fades to high ULX luminosities; but the other appears persistent between two snapshots separated by 8 years, at a luminosity that is second only to ESO 243-49 HLX-1 amongst the known HLXs. These join the very small number of HLXs identified in the literature. As they are particularly difficult to explain as stellar remnants, they must be regarded as some of the best known IMBH candidates. Given the cosmological and astrophysical importance of IMBHs, HLXs are highly compelling targets for further observations with current and future

missions, to both better constrain the presence of a massive black hole and better understand the astrophysics of these remarkable objects.

Chapter 3

A bright ultraluminous X-ray source in NGC 5907

We present a multi-mission X-ray analysis of a bright (peak observed 0.3–10 keV luminosity of $\sim 6 \times 10^{40}$ erg s^{-1}), but relatively highly absorbed ULX in the edge-on spiral galaxy NGC 5907. The ULX is spectrally hard in X-rays ($\Gamma \sim 1.2$–1.7, when fitted with an absorbed power-law), and has a previously-reported hard spectral break consistent with it being in the ultraluminous accretion state. It is also relatively highly absorbed for a ULX, with a column of $\sim (0.4$–$0.9) \times 10^{22}$ atom cm^{-2} in addition to the line-of-sight column in our Galaxy. Although its X-ray spectra are well represented by accretion disc models, its variability characteristics argue against this interpretation. The ULX spectra instead appear dominated by a cool, optically-thick Comptonising corona. We discuss how the measured 9 per cent rms variability and a hardening of the spectrum as its flux diminishes might be reconciled with the effects of a very massive, radiatively-driven wind, and subtle changes in the corona respectively. We speculate that the cool disc-like spectral component thought to be produced by the wind in other ULXs may be missing from the observed spectrum due to a combination of a low temperature (~ 0.1 keV), and the high column to the ULX. We find no evidence, other than its extreme X-ray luminosity, for the presence of an intermediate mass black hole ($\sim 10^2$–10^4 $M_\odot$) in this object. Rather, the observations can be consistently explained by a massive ($\gtrsim 20$ $M_\odot$) stellar remnant black hole in a super-Eddington accretion state.

3.1   Introduction

Even though it now seems increasingly likely that the majority of ULXs are super-Eddington sMBHs or MsBHs, the precise mechanisms of super-Eddington accretion are still far from well understood, although much theoretical progress has been made in recent years (see e.g. Dotan & Shaviv 2011 and references therein). Observationally, the high quality X-ray spectroscopy offered by the EPIC detectors aboard *XMM-Newton* has revealed common morphologies for the best quality ULX spectra: a very broad, disc-like continuum for some ULXs, possibly close to the Eddington threshold, and a two-component spectrum consisting of a soft excess and a harder component with a distinct turnover at energies of several keV, which it has been suggested could be associated with higher super-Eddington accretion rates (e.g Stobbart et al. 2006; Gonçalves & Soria 2006; Gladstone et al. 2009). Despite the high quality of the data, these spectra can be fitted with multiple physical models – for instance, the disc-like spectra are well-fitted by advection-dominated 'slim' disc models (e.g. Watarai et al. 2001; Isobe et al. 2012), but may be preferentially fit by a combination of an advection-dominated disc and a cold, optically-thick corona in some cases (Middleton et al. 2011b; Middleton et al. 2012). The combination of a disc and a cool, thick corona may also provide a good explanation for the two component spectra seen in more luminous ULXs (Gladstone et al., 2009), but the interpretation of these two components may not be completely straightforward – for instance a massive, radiatively-driven wind offers a very plausible explanation for the soft component (Kajava & Poutanen 2009; Middleton et al. 2011a). Other interpretations are also possible, for example a combination of X-ray reflection and extremely broadened emission lines offers a statistically-valid solution for many ULXs (Caballero-García & Fabian 2010; Walton et al. 2011a).

So despite the clear advances in understanding provided by X-ray spectroscopy of ULXs, it is clear that it does not currently offer unique solutions to the nature of

ULXs. More information is therefore required to break this degeneracy. One means of addressing this is to examine the variation of the X-ray spectra with source luminosity, and so rule out physically implausible behaviour. Spectral variations have long been reported for individual ULXs observed on multiple occasions, although the analyses of these data have generally been based on simple phenomenological spectral models due to the moderate quality of the data (e.g. Kubota et al. 2002; Dewangan et al. 2004; Feng & Kaaret 2006b; Soria et al. 2009). A more systematic search for variability patterns was undertaken by both Kajava & Poutanen (2009) and Feng & Kaaret (2009), on the basis of power-law continua and MCD models. They both found a number of ULXs with correlated luminosity and power-law photon index, although Feng & Kaaret (2009) found others in starburst galaxies appeared considerably less variable in spectral shape at different fluxes. Kajava & Poutanen (2009) also found several ULXs that were well-described by accretion disc spectra, and showed luminosity-temperature relationships consistent with this interpretation. Perhaps most crucially, they found that some ULXs display spectral pivoting, consistent with two-component spectra; and the luminosity-temperature evolution of the soft component is consistent with an outflowing wind, not an accretion disc.

Further insights have come from studies of individual objects using high quality *XMM-Newton* data and more physically-motivated models. However, these have posed more questions than they have answered. NGC 1313 X-2 has been well-fitted with a model comprised of a Comptonising corona and an accretion disc, with the corona appearing cooler and optically thicker at higher luminosities (Pintore & Zampieri, 2012). In contrast, Kajava et al. (2012) report that when modelled by the same disc plus corona model, Ho II X-1 shows an opposite behaviour: an increase in coronal temperature with luminosity. This is compounded by further, complex spectral variability in previous *Swift* monitoring campaigns (Grisé et al., 2010). NGC 1313 X-1 is different again; it shows a range of coronal temperatures and optical

depths that do not correlate with luminosity (Pintore & Zampieri, 2012)[1]. From this small sample it therefore appears that the ULX population displays a variety of behaviours, possibly indicating some additional parameters – such as accretion geometry and/or viewing angle and/or complex absorption – are influential in their spectra. Clearly further investigation is necessary to gain an understanding of the physics of the accretion states in ULXs.

In this chapter, which is adapted from Sutton et al. (2013a), we present a thorough analysis of available observations of a ULX in the edge on spiral galaxy NGC 5907[2]. This object (2XMM J151558.6+561810, henceforth NGC 5907 ULX) was first identified as a ULX by Walton et al. (2011b) in a cross correlation of the 2XMM-DR1 (Watson et al., 2009) and RC3 galaxy (de Vaucouleurs et al., 1991) catalogues. NGC 5907 ULX was sufficiently X-ray luminous in those observations (taken in 2003) to be included in the extreme ULX sample in Chapter 2; although unlike other ULXs in that sample, the identification of an X-ray spectral break indicated that this source is likely in a super-Eddington regime. However, in a 2010 *Swift* follow-up observation its flux was observed to have dropped substantially. This source therefore provided an excellent opportunity to investigate spectral variations with flux in the ultraluminous state, and further *Swift* monitoring observations in 2011/2012 and *XMM-Newton* triggered observations in early 2012 (triggered by a factor of three diminution in count rate below the 2003 levels) were obtained. In the remainder of this chapter we constrain the changes in spectral and timing properties of NGC 5907 ULX with flux using the above data. We then discuss these changes both in light of the various traits seen in other ULXs, and the physical models used to explain these

---

[1]ESO 243-49 HLX-1 is again different, showing spectral variability similar to Galactic sMBH binaries, albeit at higher X-ray luminosities and lower disc temperatures; and it has an inner disc temperature - X-ray luminosity relationship consistent with $L_X \propto T^4$ (Servillat et al. 2011; Godet et al. 2012). However, its unique behaviour marks ESO 243-49 HLX-1 as physically distinct from the bulk of the ULX population, and so it is arguably a poor comparator for most ULXs in which there is no longer a strong suspicion of the presence of an IMBH.

[2]NGC 5907 is an edge-on SA(s)c spiral galaxy with a prominent dust lane. The regions west of the dust lane were originally catalogued as NGC 5906.

objects. We adopt a distance of $d = 13.4$ Mpc to NGC 5907 (Tully et al., 2009a) throughout this chapter.

3.2 Data reduction

NGC 5907 ULX has been observed by a variety of X-ray observatories. In addition to the *XMM-Newton* EPIC and *Swift* XRT observations introduced above, we also (somewhat fortuitously) obtained two proprietary *Chandra* ACIS-S observations within a couple of days of the latter of the two new *XMM-Newton* observations. Further details of observations with all three observatories are provided in an X-ray observation log (Table 3.1). The source location was also observed during a series of *ROSAT* PSPC-B observations in 1992 (sequence ID RP600190N00), although the ULX was not detected.

The *XMM-Newton* data were reduced using *XMM-Newton* SAS version 11.0.0. Both observations 0145190201 and 0145190101 were subject to severe background flaring. This resulted in multiple exposures being obtained in all three EPIC detectors in 0145190201, and solely the MOS detectors in 0145190101. However only one exposure per detector contained a significant duration of good (i.e low background) time, so this was identified and utilised in the following analysis. To account for any background flares still present within these and the other datasets, we constructed good time interval (GTI) files from the high energy (10–15 keV) full field light curves, to exclude time intervals with count rates of typically $\gtrsim$ 1 ct s^{-1} in the pn data, and $\gtrsim$ 0.5 ct s^{-1} in the MOS. Source energy spectra and light curves were extracted from circular apertures, with radii 30–40 arcseconds, centred on the position of NGC 5907 ULX. Circular apertures of 40–50 arcsecond radius were used to extract background data, that were located a similar distance from the readout node on the neighbouring CCD to the one containing the source for the pn detector, and on the same CCD as the source for both of the MOS detectors.

Table 3.1: X-ray observation log

Date [a]	Obs. ID [b]	$t_{\exp}$ [c]	Off-axis angle [d]
ROSAT PSPC-B			
1992-01-05	RP600190N00[e]	18.1	1.14
XMM-Newton EPIC			
2003-02-20	0145190201	10.7/18.4/18.8	2.40
2003-02-28	0145190101	10.6/17.2/17.5	2.41
2012-02-05	0673920201	4.5/11.9/12.1	1.20
2012-02-09	0673920301	12.2/17.3/16.3	1.12
Swift XRT			
2010-08-12	00031785001	5.6	2.42
2010-08-13	00031785002	5.2	3.57
2010-08-15	00031785003	6.8	1.78
2011-05-04	00031785005	1.2	1.85
2011-05-15	00031785006	1.9	1.55
2011-05-29	00031785007	2.6	2.09
2011-06-13	00031785008	2.1	2.20
2011-11-20	00031785012	2.1	3.29
2011-12-04	00031785013	0.9	2.74
2011-12-18	00031785014	1.0	2.17
2011-12-21	00031785015	0.9	1.31
2012-01-01	00031785016	1.9	1.68
2012-01-15	00031785017	1.7	0.65
2012-01-29	00031785018	2.2	0.91
2012-02-12	00031785019	1.5	3.61
Chandra ACIS-S			
2012-02-11	12987	16.0	0.02
2012-02-11	14391	13.1	0.02

Notes: [a]Observation start date (yyyy-mm-dd). [b]Observation identifier. [c]Cleaned Chandra ACIS-S/Swift XRT/XMM-Newton EPIC (pn/MOS1/MOS2)/combined ROSAT PSPC-B exposure time (ks). [d]Angle between the boresight position and the 2XMM co-ordinates of NGC 5907 ULX, in arcminutes. [e]ROSAT observation sequence ID, observations were taken over several days between 1992-01-05 – 1992-01-12.

Energy spectra and light curves were extracted from the data using the SAS task EVSELECT, which used both the source and background regions and the GTI files. Standard event patterns (`PATTERN` $\leq$ 4 for the pn, `PATTERN` $\leq$ 12 for the MOS) were selected. When extracting spectra the filter `FLAG = 0` was imposed; `#xmmea_ep` or `#xmmea_em` were used instead for light curves. Spectra were corrected using BACKSCALE to calculate the areas of source and background extraction regions for subsequent normalisation; redistribution matrices and ancillary response files were extracted using RMFGEN and ARFGEN respectively; finally spectral files were rebinned to a minimum of 20 counts per bin using SPECGROUP.

Pipeline-reduced *Swift* data for observations of NGC 5907 ULX were obtained from the NASA HEASARC archive. Source events were extracted from circular apertures centred on the X-ray source, with radii of 20 pixels ($\sim$ 47 arcseconds); for background events annular apertures were used, again centred on the ULX, with inner and outer radii of 50 & 120 pixels around the source positions. Source and background spectra were extracted using XSELECT[3] v2.4. The response file `swxpc0to12s6_20070901v011.rmf` was used in spectral fitting, and ancillary response files were extracted using XRTMKARF. *Swift* spectra were not grouped, instead Cash statistics (Cash, 1979) were used for subsequent spectral fitting, as described below.

Chandra data were reduced using CIAO version 4.4 and calibration files from the *Chandra* CALDB version 4.4.8. Both of the *Chandra* observations were taken using the 1/4 subarray to mitigate against the effects of pile-up, and the pile-up fraction in the actual observations was estimated as $\sim$ 2 per cent using PIMMS. Background light curves were extracted from the ACIS-S3 chip, with all of the detected point sources removed; these were then checked for any flaring using the LC_SIGMA_CLIP routine[4]. No further filtering of background flares was necessary for either obser-

---

[3]`http://heasarc.gsfc.nasa.gov/docs/software/lheasoft/ftools/xselect/`
[4]`http://cxc.harvard.edu/ciao/ahelp/lc_sigma_clip.html`

vation. Circular apertures with radii of 5 arcseconds (corresponding to an on-axis fractional encircled energy of $\gtrsim$ 99 per cent at 1 keV) were used to extract the source data. Annular apertures, centred on the source, were used to characterise the background count rate for each observation. These had inner and outer radii of 13–17 and 16–18 pixels for observations 12987 and 14391 respectively, set to exclude faint point sources visible in the sensitive ACIS-S images. The data products were then extracted from the level 2 event files, to include all standard good event detections with energies between 0.3–10 keV, within the source data extraction apertures. The *Chandra* spectra were extracted, and grouped with $\gtrsim$ 20 counts per energy bin using the CIAO script SPECEXTRACT, which also produces the appropriate response matrices for spectral analysis.

3.3 Data analysis & results

3.3.1 Spatial analysis

In Chapter 2 we identified a bright, blue optical source within the *XMM-Newton* positional uncertainty region for NGC 5907 ULX in HLA images. Here we repeat this analysis using the superior astrometry and smaller uncertainty region provided by the *Chandra* data. We firstly attempted to improve the astrometry in the *Chandra* image, by matching other bright X-ray point sources detected in *Chandra* observation 12987 with an optical catalogue. The CIAO script WAVDETECT was used to produce a list of X-ray sources detected within 6 arcminutes of NGC 5907 ULX, and we checked for optical counterparts in SDSS-II DR7 to sources with greater than 15 net X-ray counts. The SDSS catalogue was chosen primarily because it had been used by the HLA pipeline to correct the astrometry of the *HST* data, and when checked was found to provide an acceptable solution. However, only a single *Chandra* source had a clear counterpart in the SDSS; we therefore carried out an astrometric correction using this

object, but stress that it is particularly tentative. We also extracted the *Chandra* position of NGC 5907 ULX using WAVDETECT, which combined with the raw astrometric precision of *Chandra* is 15:15:58.63(0.02)+56:18:10.4(0.4) (the RA and Dec errors shown in brackets are the 1σ uncertainties, based on a combination of the centroiding error and the error on the astrometric solution for the *Chandra* field); the 'tentatively-corrected' *Chandra* position of the ULX is 15:15:58.62(0.01)+56:18:10.3(0.1). We then combined the new astrometric uncertainty of the X-ray data and the X-ray source centroid with the *HST* astrometric precision (as per Roberts et al. 2008) to calculate a new 90 per cent uncertainty region for the source position. Even at the high astrometric precision of *Chandra*, NGC 5907 ULX at least marginally retains the bright blue optical counterpart in the HLA images (Chapter 2) - it lies within the uncorrected 90 per cent uncertainty region, and on the outer edge of the 90 per cent uncertainty region after the tentative correction.

The counterpart has previously been reported with $m_{\mathrm{F450W}} = 21.5$ (Chapter 2; corrected for Galactic extinction). Here we report an estimated magnitude limit in the F814W band, which was calculated by subtracting an estimate of the background flux in an annulus centred on the target position from the upper limit of flux at the location of the optical source. We then converted this to a magnitude and corrected for Galactic extinction, obtaining a 3σ limit of $m_{\mathrm{F814W}} > 24$. If the *HST* magnitudes are used as an approximation of Johnson magnitudes, this implies an unphysical colour of $B - I \lesssim -2.5$. This therefore questions the veracity of the HLA detection, so as a check we obtained the individual flat-field calibrated distorted images corresponding to each exposure from the Barbara A. Mikulski Archive for Space Telescopes[5] (MAST), and aligned the images in each filter using TWEAKREG in the *HST* DRIZZLEPAC software package[6]. When we combined the individual images using ASTRODRIZZLE we were able to reproduce the detection of a bright source in the

---

[5]`http://archive.stsci.edu/`
[6]`http://www.stsci.edu/hst/HST_overview/drizzlepac`

Table 3.2: X-ray spectral analysis: power-law

Obs. ID	$\chi^2/$dof [a]	N_H [b]	Γ [c]	Norm. [d]
0145190201	268.4/335	0.85 ± 0.06	1.65 ± 0.06	3.5 ± 0.3
0145190101	272.5/256	0.82 ± 0.07	1.65 ± 0.07	2.8 ± 0.3
0673920201	63.5/77	0.5 ± 0.1	1.2 ± 0.1	$0.8^{+0.2}_{-0.1}$
0673920301	169.5/139	0.7 ± 0.1	$1.34^{+0.09}_{-0.08}$	$0.9^{+0.2}_{-0.1}$
12987	29.9/32	0.8 ± 0.3	1.2 ± 0.2	$0.8^{+0.3}_{-0.2}$
14391	34.1/26	$0.9^{+0.4}_{-0.3}$	1.2 ± 0.3	$0.9^{+0.4}_{-0.3}$

Notes: [a]Statistical goodness of the fit, in-terms of the χ^2 statistic and number of degrees of freedom. [b]Absorption column density external to our Galaxy ($\times 10^{22}$ cm^{-2}). [c]Power-law photon index. [d]Normalisation of the power-law spectral model ($\times 10^{-4}$ photons keV^{-1} cm^{-2} s^{-1}).

F450W band, as seen in the HLA images. However, upon examining the 3 individual F450W exposures we found detections close to the position of the counterpart in only 2 of the 3 images. Given the small temporal separation of the 3 exposures (which were all taken between 1996-03-01 21:44:16 and 22:08:36), it seems unlikely that a variable counterpart could be the cause of the non-detection. Instead, we suggest that the counterpart previously identified in the HLA images was a spurious detection, probably caused by the presence of overlapping cosmic rays in 2 of the 3 exposures. This suggests a potential issue with the cosmic ray rejection during the HLA processing.

3.3.2 X-ray spectral analysis

There were sufficient counts available to enable X-ray spectral analysis in all of the *XMM-Newton* and *Chandra* observations, so these were fitted with spectral models using XSPEC v.12.6.0. Firstly, the spectra were modelled using a simple, unphysical single component model – a doubly absorbed power-law (TBABS $\times$ TBABS $\times$ POWERLAW in XSPEC), with the abundances set to the values of Wilms et al. (2000). The first absorption component was frozen to the Galactic column in the direction of

NGC 5907 ULX (1.38×10^{20} cm^{-2}, Dickey & Lockman 1990), and the second was left free to model absorption intrinsic to the source and/or its host galaxy. An additional multiplicative constant was included when fitting the *XMM-Newton* spectra, which was frozen to unity for the pn channel, and free to vary for the two MOS channels to account for uncertainties in the calibration between the EPIC detectors. The parameters resulting from this spectral fitting are shown in Table 3.2. Given that a power-law is an empirical representation of the data, rather than a physical model, its uses are limited. Indeed, its use for this data is inherently questionable given the previous demonstration in Chapter 2[7] of the subtle but statistically significant presence of a high energy turnover[8], indicative of ultraluminous state spectra, in the data from the 2003 *XMM-Newton* observations. However, a power-law still provides a reasonable approximation to the 0.3–10 keV X-ray spectra in all cases (cf. Table 2), and proves useful in two ways. Firstly, as the data from the individual *Swift* monitoring observations had insufficient statistics for spectral fitting, we used these fits to provide an estimate of the source flux in those epochs (see below). Secondly, it provides a strong indication of spectral variability in the ULX. Although the absorption column remains roughly constant throughout the six spectral datasets, the slope shows a marked change between the 2003 and 2012 data, hardening as the normalisation (and so the flux) decreases.

So, in order to investigate the reasons for this spectral hardening, we attempted to fit some more physically motivated spectral models to the *XMM-Newton* and *Chandra* data. To get the best possible constraints on the model parameters, and motivated

---

[7]We note that further examination of this previous analysis indicated that the background emission was over-subtracted from the spectrum of NGC 5907 ULX. However, we repeated the analysis for the newly processed data, and found that the break was still detected in the 2–10 keV spectrum extracted from both of the high flux *XMM-Newton* observations, at greater than 3σ significance.

[8]Although it appears contradictory that a power-law model can provide a reasonable fit to the full band data when a break is present at high energies, this is also the case in 3/12 objects looked at by Gladstone et al. (2009), where the data quality was similar to that presented here. In each of those cases inspection of the data above 2 keV showed a statistically robust detection of a break.
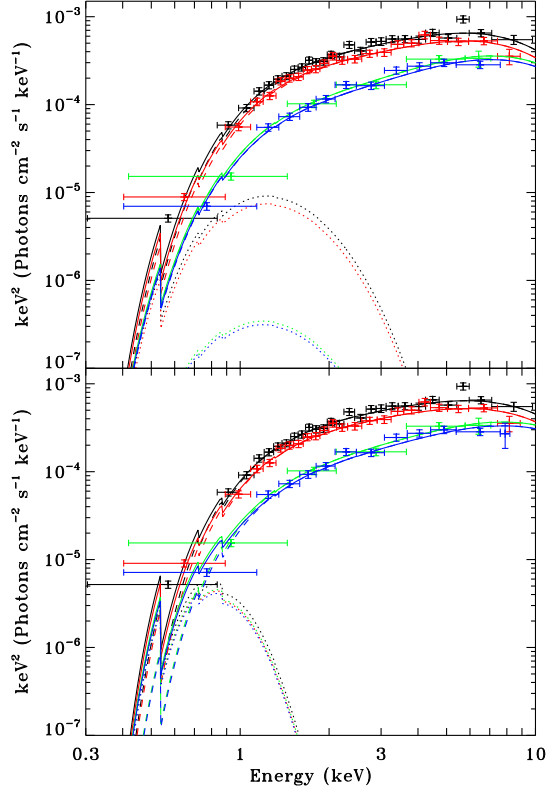
Figure 3.1: The best fitting absorbed MCD (dotted lines) plus Comptonisation (dashed lines) models. These models (TBABS × TBABS × (DISKBB+COMPTT) in XSPEC) are fitted to the bright (0145190201 in black and 0145190101 in red) and faint (0673920201 in green and 0673920301 in blue; although used in the fitting, the *Chandra* spectra are not shown for clarity) flux binned *XMM-Newton* energy spectra. Only EPIC pn data are shown, and data have been rebinned to 10σ significance per data point. The top panel shows the fit with the inner disc temperature and coronal seed temperature fixed to 0.3 keV; the bottom panel shows it fixed to 0.1 keV. The other model parameters of these fits are shown in Table 3.3.

Table 3.3: X-ray spectral analysis: physical models

			TBABS $\times$ TBABS $\times$ DISKBB		
Group ID	χ^2/dof [a]	$N_{\rm H}$ [b]	$kT_{\rm in}$ [c]	Norm [d]	
High flux	550.8/593	0.48 ± 0.03	2.03 ± 0.08	$5.7^{+0.8}_{-0.7} \times 10^{-3}$	
Low flux	311.0/280	$0.46^{+0.05}_{-0.06}$	$2.9^{+0.3}_{-0.2}$	$8 \pm 2 \times 10^{-4}$	
			TBABS $\times$ TBABS $\times$ DISKBB		
Group ID	χ^2/dof [a]	$N_{\rm H}$ [b]	$kT_{\rm in}$ [c]	p [e]	Norm [d]
High flux	511.9/592	$0.68^{+0.07}_{-0.05}$	$2.9^{+0.8}_{-0.3}$	0.61 ± 0.02	< 0.001
Low flux	308.7/279	0.6 ± 0.1	$3.7^{+3.6}_{-0.9}$	$0.68^{+0.07}_{-0.05}$	$< 7 \times 10^{-4}$
			TBABS $\times$ TBABS $\times$ COMPTT		
Group ID	χ^2/dof [a]	$N_{\rm H}$ [b]	kT_0 [f]	kT [g]	τ [h]	Norm [d]
High flux	503.5/591	$0.47^{+0.12}_{-0.09}$	$0.31^{+0.05}_{-0.06}$	1.9 ± 0.2	9.8 ± 0.9	$3.0^{+0.5}_{-0.4} \times 10^{-4}$
Low flux	306.0/278	$0.2^{+0.2}_{-0.1}$	$0.45^{+0.09}_{-0.12}$	$2.6^{+3.1}_{-0.6}$	9^{+2}_{-4}	$< 1 \times 10^{-4}$

Notes: Results from fitting various spectral models to the flux-binned *XMM-Newton* and *Chandra* spectra: the bright flux bin includes observations 0145190201 and 0145190101; the faint flux bin includes observations 0673920201, 0673920301, 12987 and 14391. The errors and limits shown are the 90 per cent confidence ranges. [a]Statistical goodness of the fit, in terms of the χ^2 statistic and number of degrees of freedom. [b]Absorption column density external to our Galaxy ($\times 10^{22}$ cm^{-2}). [c]Inner-disc temperature (keV). [d]Normalisation of the spectral component. For the disc models this is $(R_{\rm in}/D)^2 \cos(\theta)$ for a disc with inner radius $R_{\rm in}$ (in km) at a distance D (in units of 10 kpc) and at an inclination θ. [e]Exponent of the radial dependence of temperature in the p-free disc model. [f]Input soft photon temperature (keV) of the Comptonising corona. [g]Plasma temperature (keV) of the Comptonised component. [h]Optical depth of the Comptonised component. [i]In the MCD plus Comptonising corona model the input soft photon temperature of the corona was set equal to the inner disc temperature. [j]The inner disc temperatures were fixed in value, as per the text.

Table 3.3: continued

Group ID	χ^2/dof [a]	$N_{\rm H}$ [b]	$kT_{\rm in}$ [c,j]	Norm [d]	kT [g]	τ [h]	Norm [d]
		TBABS $\times$ TBABS $\times$ (DISKBB+COMPTT) [i]					
High flux	503.2/591	$0.55^{+0.17}_{-0.09}$	0.3	< 2	1.9 ± 0.2	9.9 ± 0.8	$3.1^{+0.2}_{-0.3} \times 10^{-4}$
Low flux	310.4/278	$0.44^{+0.20}_{-0.09}$	0.3	< 0.2	$2.1^{+0.5}_{-0.3}$	11 ± 2	$1.1 \pm 0.1 \times 10^{-4}$
High flux	504.9/591	$0.84^{+0.09}_{-0.08}$	0.1	1000^{+1400}_{-900}	$2.1^{+0.3}_{-0.2}$	8.6 ± 0.9	$6.3 \pm 0.6 \times 10^{-4}$
Low flux	306.2/278	$0.8^{+0.2}_{-0.1}$	0.1	800^{+1500}_{-700}	$2.5^{+1.5}_{-0.5}$	9^{+2}_{-3}	$1.8^{+0.3}_{-0.5} \times 10^{-4}$

by the apparent consistency in power-law spectra within the two separate periods of observations, we separated the spectra into a high flux group from the February 2003 observations (*XMM-Newton* observations 0145190201 and 0145190101), and a low flux group from February 2012 (*XMM-Newton* observations 0673920201 and 0673920301, plus *Chandra* observations 12987 and 14391). Each group of spectra was fitted simultaneously, with all model parameters held fixed between the observations. Similarly to the power-law, in each spectral model we included two absorption components (TBABS in XSPEC), one fixed to the Galactic column density in the direction of NGC 5907, the other free to model intrinsic absorption in the source/host galaxy. We also included a multiplicative constant to allow for calibration uncertainties between the detectors and differences between observations; this was fixed to 1 for the *XMM-Newton* EPIC pn detector in one observation per flux group (0145190201 and 0673920201), and was left free to vary for other observations/detectors. For the high flux bin, the constants for observation 0145190101 were ~ 20 per cent lower than for 0145190201, but the constants of detectors within individual observations were all within 10 per cent. For the faint flux bin, the constants of the *XMM-Newton* EPIC and *Chandra* ACIS-S detectors in each observation were within 10 per cent of each other.

Given the shape of the high flux spectra shown in Figure 4 of Chapter 2 – smooth, absorbed continua, with a turnover above 5 keV – we began by fitting accretion disc models to the data. An MCD (DISKBB in XSPEC) model was initially employed, and resulted in statistically acceptable fits, but with rather unrealistically high inner disc temperatures ($kT_{\rm in} > 2$ keV, Table 3.3, first model). We also attempted to fit the spectral data with a p-free disc model (Table 3.3, second model), which allows different values for the exponent of the radial dependence of temperature in the accretion disc p, with $p = 0.75$ indicating a standard Shakura-Sunyaev disc, and $p \approx 0.5$ indicating the presence of a slim (advection-dominated) disc (cf. Vierdayanti et al. 2006). This resulted in $\Delta\chi^2 = 38.9$ and 2.3 compared to the MCD fits, for one

additional degree of freedom for the high and low flux grouped observations respectively, i.e. indicating a significantly improved fit for the high flux group. However, in both cases the p-value was intermediate between the slim and standard disc solutions (with a standard disc acceptable within errors for the low flux group), and the disc remained anomalously hot, with $kT_{in} \sim 3 - 4$ keV. Furthermore, the normalisations of the p-free disc model were relatively unconstrained, with only upper limits present at the 90% level.

We also attempted to fit the X-ray spectra with a Comptonising corona (COMPTT in XSPEC), as an optically thick, cool corona could provide the high energy spectral break identified in Chapter 2. Such a corona provided acceptable fits to both of the observation groups (Table 3.3, third model), with slightly improved statistics compared to the p-free disc model ($\Delta\chi^2 = 2-8$ for one additional degree of freedom). The physical parameters derived from the model are consistent with those observed in many other ULXs (cf. Gladstone et al. 2009), implying a cool, optically-thick corona ($kT \sim 2-3$ keV; $\tau \sim 9-10$), with a cool medium providing the seed photons ($kT_0 \sim 0.31 - 0.45$).

Clearly, a spectrum consisting of a Comptonising corona with no accompanying emission from the input photon source is physically challenging (although scenarios in which a corona completely envelopes the X-ray emitting disc are certainly not impossible). We therefore attempted to fit the spectra with a two component model consisting of a MCD plus a Comptonising corona (DISKBB+COMPTT in XSPEC), with the disc assumed to provide the seed photons for the corona and hence the input soft photon temperature of the corona fixed to the inner disc temperature[9]. However, this resulted in very poor constraints on the model parameters, and no improvement to the fit statistics.

Despite this model not being a statistical requirement of fits to the X-ray data

---

[9]This is a common approximation for the moderate quality spectra obtained from ULXs, although see Pintore & Zampieri (2012) for a discussion on the limitations of this approach.

of NGC 5907 ULX, cool disc-like spectral components are a very common feature in other similarly luminous ULXs with high quality spectral data, so we consider the constraints on whether such a feature is present here. As a start point we note that the high absorption column to this object might act to mask the emission of an intrinsically soft spectral component; hence we attempted to estimate the amount of disc-like emission that could be intrinsically present, but obscured by the high column density, by fixing the disc temperature to a characteristic value. While a free fit does not constrain this temperature, and fixing the temperatures reveals similar χ^2 values for a range of disc temperatures between 0.1 and 1 keV, we choose to use 0.1 and 0.3 keV. This is motivated by the range of cool disc temperatures seen in other, similar ULX fits e.g. Gladstone et al. (2009, their Table 8; they model the disc using the DISKPN model in XSPEC, but state that this differs from DISKBB by less than 5 per cent for the same disc temperature); the low input photon temperature required by the Comptonisation-only model; and the hypothesis that a softer disc might more easily be hidden behind the high absorption column. The results for these fits are shown in Table 3.3 (fourth model). Clearly, the physical parameters of the coronal component are consistent within errors for both assumed cool disc temperatures; the main difference between the models for each disc temperature is that the cooler (0.1 keV) disc requires a substantially higher absorption column ($\sim 8 \times 10^{21}$ cm^{-2}, nearly twice that required for the 0.3 keV disc), which has the added implication that the model normalisations are all substantially larger for the cooler disc case.

We show the best-fitting disc plus corona models for the *XMM-Newton* data, unfolded from the instrument response, for both fixed disc temperatures in Figure 3.1. The plots clearly show why the soft disc is not required statistically; in both cases it contributes minimally to the observed spectrum. Indeed, in 3 of 4 cases the disc components only produce $\lesssim$ 0.5 per cent of the observed 0.3-10 keV flux, and the other case (high flux, 0.3 keV disc) has only $\sim$ 2.5 per cent of its observed flux in the disc component. However, the fraction of intrinsic (i.e. deabsorbed) flux in the

Table 3.4: Intrinsic luminosities for the components of the MCD plus corona model

Group ID	$kT_{\rm in}$	$L_{\rm X,diskbb}$ [a]	$L_{\rm X,comptt}$ [b]
High flux	0.3	< 0.5	5.1 ± 0.1
Low flux	0.3	< 0.06	2.3 ± 0.1
High flux	0.1	$1.4^{+1.1}_{-0.8}$	6.3 ± 0.2
Low flux	0.1	$1.2^{+1.1}_{-0.7}$	2.7 ± 0.2

Notes: Errors and limits shown on fluxes are 1σ confidence ranges. [a]0.3–10 keV intrinsic (i.e. deabsorbed) luminosity ($\times 10^{40}$ erg s^{-1}) of the 0.3 keV MCD component of the spectral model. [b]Same as [a], but for the Comptonising corona.

disc-like component could be substantially higher for both disc temperatures. We illustrate this in Table 3.4, where we provide the intrinsic luminosities for the two components for both flux groups, and both assumed disc temperatures. The deabsorbed luminosities were calculated using the CFLUX convolution model in XSPEC, over the 0.3–10 keV energy range, with the appropriate normalisation frozen as required by the model. Although the errors on the 0.1 keV disc are very substantial due to the large extrapolation necessary to correct for the high absorption column, it is apparent that such a disc might have a very substantial contribution to the 0.3-10 keV flux (at least ~ 10 per cent, and plausibly much higher), that is hidden from our view due to the high column. The contribution is less for the 0.3 keV disc, but even then up to a few per cent of the intrinsic flux may be in such a component.

Interestingly, these fits also provide a suggestion for the origin of the spectral changes. In the case of the 0.3 keV disc, it appears that the hardening of the spectrum is a result of the flux in the disc diminishing at a faster rate than the flux from the corona as the overall flux drops. However, in the case of a 0.1 keV disc this component appears to be consistent between the two observations, and the change in spectrum is originating in a slight (although not statistically distinctive given the quality of data) heating of the corona as the overall flux drops.

3.3.3   Long-term X-ray timing

In order to constrain the long-term variability of NGC 5907 ULX, we extracted a flux from each observation of the source. However, the exact method used differed for data from each observatory. There were insufficient counts per observation in the *Swift* spectra for statistically valid spectral model fitting, so parameters from the absorbed power-law models fitted to the *XMM-Newton* data were used instead. A typical value of intrinsic absorption of 8×10^{21} cm^{-2} was assumed. Even though the power-law fit parameters in Table 3.2 indicated that the source became spectrally harder at fainter fluxes in the small number of high quality X-ray observations, such behaviour was not assumed to be universally present in the source. Instead two values of Γ were used, $\Gamma = 1.0$ and 1.7, that approximate the upper and lower limits of the range observed by *XMM-Newton* and *Chandra*. Fluxes were obtained by fitting both absorbed power-law continua to the *Swift* data in XSPEC, using the C-statistic, with only the normalisations free to vary. The resulting fluxes are shown in Table 3.5. As higher quality spectral data were available for the *XMM-Newton* and *Chandra* observations, fluxes and errors were obtained from the absorbed Comptonisation model, using the best fit parameters for each flux group but with the normalisation of each observation allowed to vary. These values are also shown in Table 3.5, and were calculated using the XSPEC CFLUX convolution model component.

We also searched for any earlier detections of NGC 5907 ULX in archival *ROSAT* data. The source location fell within the field of view of a series of *ROSAT* PSPC-B exposures, taken between 1992-01-05 and 1992-01-12, with the source position at an off-axis angle of 1.14 arcminutes, and with a total exposure time of 18.1 ks. However, there was no significant detection of an X-ray source at the location of the ULX. Instead, we estimate an upper limit by counting the number of photons in a 1 arcminute circular region centred on the 2XMM position of the ULX, and we estimate the background using 3 such circles placed close to the source region.
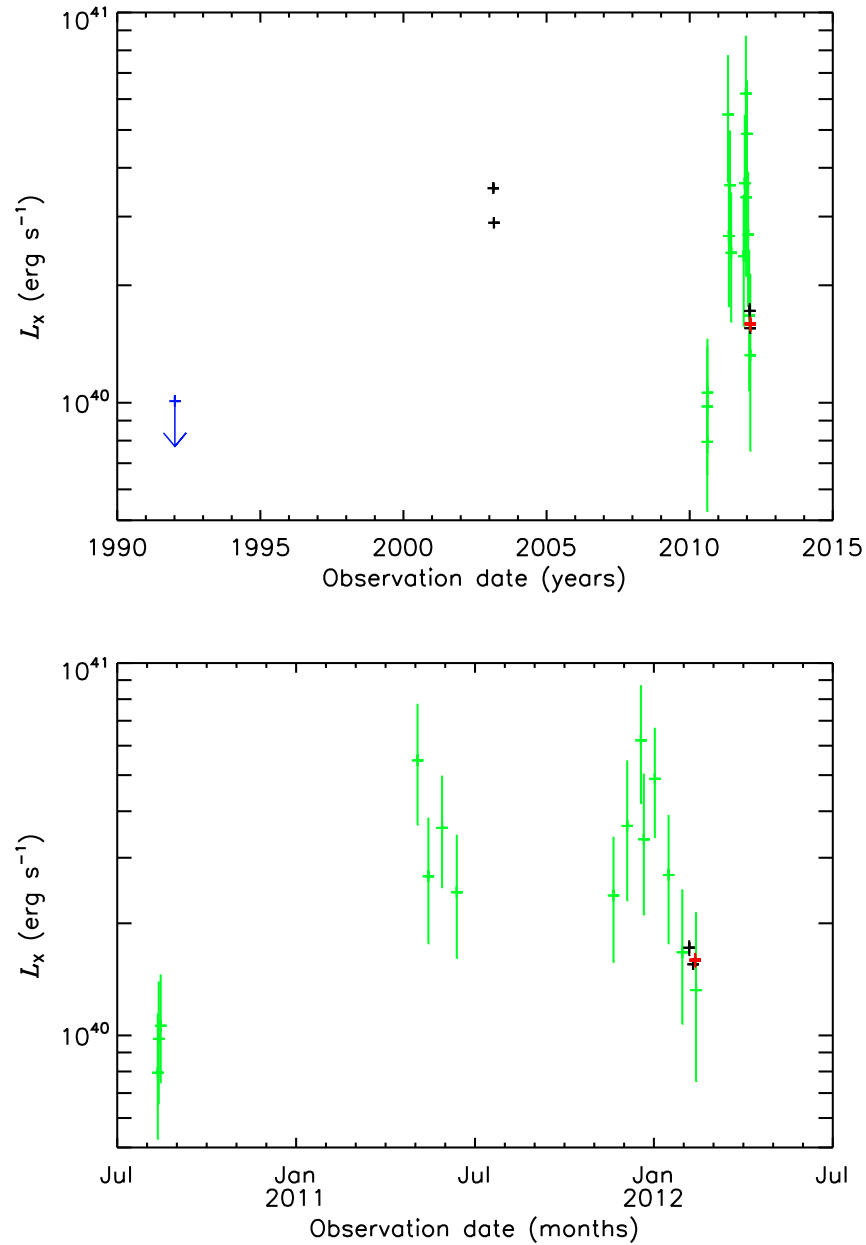
Figure 3.2: Multi-mission long-term X-ray light curves of NGC 5907 ULX showing the observed 0.3–10 keV fluxes and their associated 1σ error bars. Both the full range (*top*), and an enlargement displaying data from 2010 to present (*bottom*), are shown. *XMM-Newton* fluxes are shown in black and *Chandra* in red; these were calculated using the best fitting absorbed Comptonisation spectral model for each group, with the normalisations for the individual observations free to vary. *Swift* fluxes are shown in green; these are a mean of the two fluxes calculated using both the Γ = 1.7 and Γ = 1.0 spectral models, and the errors show the full 1σ uncertainty range for both models (see Table 3.5). A 1σ upper limit from an earlier series of *ROSAT* observations is shown in blue.

Table 3.5: Observed 0.3–10 keV X-ray fluxes

Obs. ID	$f_{\rm X}$ [a]	
XMM-Newton [b]		
0145190201	16.5 ± 0.3	
0145190101	13.5 ± 0.3	
0673920201	8.0 ± 0.4	
0673920301	7.2 ± 0.2	
Swift [c]		
	$\Gamma = 1.7$	$\Gamma = 1.0$
00031785001	$3.0^{+0.7}_{-0.6}$	$4.4^{+1.0}_{-0.9}$
00031785002	$3.7^{+0.8}_{-0.7}$	5 ± 1
00031785003	4.1 ± 0.7	$5.8^{+1.0}_{-0.9}$
00031785005	21 ± 4	30^{+6}_{-5}
00031785006	10 ± 2	15 ± 3
00031785007	14 ± 2	20 ± 3
00031785008	9 ± 2	14^{+3}_{-2}
00031785012	9 ± 2	13^{+3}_{-2}
00031785013	14^{+4}_{-3}	20^{+5}_{-4}
00031785014	23 ± 4	35 ± 6
00031785015	13 ± 3	19^{+5}_{-4}
00031785016	18^{+3}_{-2}	27 ± 4
00031785017	10 ± 2	15 ± 3
00031785018	6 ± 1	9 ± 2
00031785019	5^{+2}_{-1}	7^{+3}_{-2}
Chandra [d]		
12987	7.4 ± 0.3	
14391	7.4 ± 0.3	

Notes: [a]Observed 0.3–10 keV flux ($\times 10^{-13}$ erg cm^{-2} s^{-1}), calculated for each mission as described below. Errors shown for fluxes are the 1σ confidence ranges. [b]*XMM-Newton* EPIC fluxes are calculated using the absorbed MCD plus Comptonisation spectral model, and the CFLUX convolution model in XSPEC. [c]*Swift* XRT fluxes were calculated for two different absorbed power-law spectral models, with an extra-Galactic absorption column of $N_{\rm H} = 8 \times 10^{21}$ cm^{-2} and photon indexes of $\Gamma = 1.7$ (the upper limit of the range seen in the brighter/softer *XMM-Newton* observations) and $\Gamma = 1.0$ (the lower limit of the range seen in the fainter/harder *XMM-Newton* observations). All model components were frozen, except for the normalisation. [d]*Chandra* ACIS-S fluxes were calculated as per the *XMM-Newton* data.

The upper limit on count rate was converted to a flux limit and extrapolated to the 0.3–10 keV band using PIMMS v4.5 and two absorbed power-law spectral models, as with the *Swift* data. The higher of the two fluxes was used as an upper limit.

The 0.3–10 keV fluxes from all four observatories are displayed in Figure 3.2, in the form of a long-term light curve spanning $\sim$ two decades (*top*), and an expanded version covering the time range of the *Swift* monitoring data for clarity (*bottom*). Clearly NGC 5907 ULX is somewhat variable, as the flux is seen to change by factors of $\lesssim$ 10 on timescales of months to years. Multiple epochs of both high and low luminosity are seen, with the *Swift* data indicative of the luminosity varying between $\sim 8 \times 10^{39}$ and $\sim 6 \times 10^{40}$ erg s^{-1}, and a possible gradual decay over most of this range is observed at the start of 2012.

3.3.4   Short-term X-ray timing

An additional diagnostic tool, which can break some of the degeneracy inherent in the X-ray spectral fitting, is fractional variability. It can be used both to test for consistency with assumed accretion modes, or to confirm the identification of multiple spectral components by their differing variability properties. Three of the *XMM-Newton* observations (0145190201, 0145190101 and 0673920301) contained sufficient good time (a minimum of 20 temporal bins), and were at high enough count rates (resulting in at least 20 counts per temporal bin) to allow us to extract their fractional variability. We did this with 200 s temporal binning, across all of the available good time, using the definition of fractional variability given by Vaughan et al. (2003), and excluding bins that contained less than the full 200 s exposure. Firstly we extracted the broad band (0.3–10 keV) fractional variability from the light curve of each observation to test for changes in timing properties with spectral hardness (Figure 3.3, *top*), which we define here as the ratio between the fluxes in the 0.3–2 and 2–10 keV bands. These fluxes are taken from the disc plus Comptonisation model,
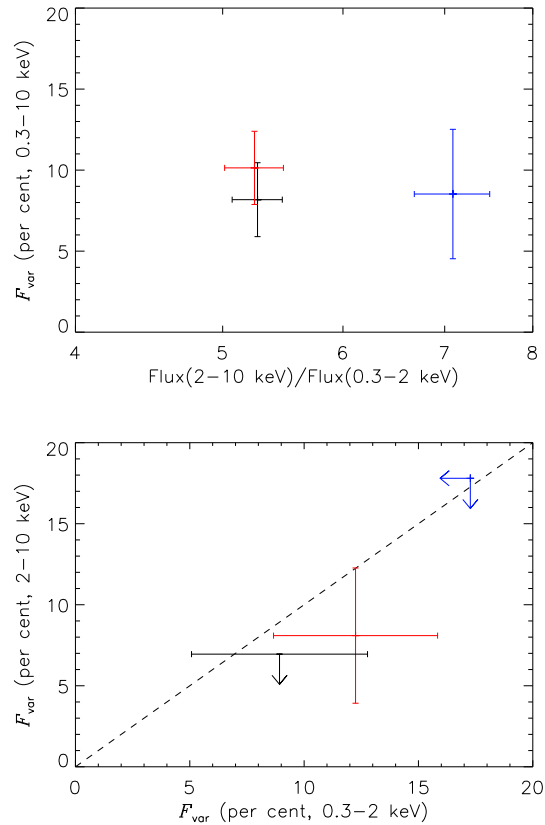
Figure 3.3: The fractional variability of NGC 5907 ULX on a time scale of 200 s, extracted from the *XMM-Newton* observations. *Top:* fractional variability across the whole energy band (0.3–10 keV) plotted against spectral hardness (see text). *Bottom:* soft band (0.3–2 keV) and hard band (2–10 keV) fractional variabilities plotted against each other, where the dashed line shows $F_{\mathrm{var}}(\mathrm{hard}) = F_{\mathrm{var}}(\mathrm{soft})$. Observations are identified using colour – 0145190201 in black, 0145190101 in red and 0673920301 in blue (observation 0673920201 has fewer than twenty continuous 200s temporal bins, so its fractional variability was not calculated). Errors and upper limits show the 1σ uncertainty levels. The fractional variability of NGC 5907 ULX is consistent (at the 1σ level) with remaining constant at the ~ 9 per cent level between observations, and in the hard and soft bands.

and corrected for the known foreground absorption (further corrections are highly uncertain, given the model-dependence of the measured absorption column). The broad band variability over the time scales probed is consistent with being unchanged between observations, despite the changes in spectral hardness. As a further step we extracted the fractional variability from the soft (0.3–2 keV) and hard (2–10 keV) *XMM-Newton* light curves, to test for different behaviour in the soft and hard spectral components (Figure 3.3, *bottom*). However, there was no strong evidence of this, with the fractional variability inconsistent between the energy bands at no more than the 1σ level, although this was not entirely surprising – the data quality was such that fractional variability was rather poorly constrained when split between two energy bands, and so in three cases it was only possible to place upper limits on it.

3.4 Discussion

We have presented an analysis of the various recent observations of NGC 5907 ULX, examining both its spectral and temporal behaviour as observed by *Swift*, *XMM-Newton* and *Chandra*. Here, we will attempt to interpret these observations in terms of the underlying physics of the source, primarily using the behaviours seen in other ULXs as a framework for our interpretation. However, we should start by summarising what was known before we obtained our recent observations. NGC 5907 ULX was included in the extreme ULX sample of Chapter 2, where it was deduced that these rare ULXs possessed observational characteristics that were consistent with IMBHs accreting below the Eddington limit. However, NGC 5907 ULX stood out from the other objects in that sample due to the identification of a high energy break in its *XMM-Newton* spectra. This is not a feature of the known sub-Eddington accretion states, rather it is a key diagnostic of the ultraluminous state, indicative of super-Eddington accretion onto stellar-mass black holes (Roberts 2007; Gladstone

et al. 2009), although in the case of NGC 5907 ULX the extreme luminosities reached may still require a massive stellar black hole (up to 100 $M_{\odot}$, as suggested by e.g. Zampieri & Roberts 2009) as its central engine.

The relatively high absorption column ($\gtrsim 5 \times 10^{21}$ cm^{-2} in almost all models) to NGC 5907 ULX creates problems in constraining and interpreting its X-ray spectrum, as it leads to a deficit of counts below 1 keV and so poor statistics at soft energies, even in the high quality *XMM-Newton* X-ray spectra (Figure 3.1). This dearth of soft counts may also have contributed to the non-detection by *ROSAT*. The practical effect of the high column is that it reduces the effective bandwidth that we can examine the source spectrum over, and so limits our ability to constrain the soft end of its spectrum. This is particularly unfortunate for ULXs, many of which are known to have strong soft excesses in their spectra (e.g. Stobbart et al. 2006), that are both a signature of ultraluminous state spectra and a key part of understanding the physics of their super-Eddington emission (Gladstone et al., 2009). In this chapter this problem is very evident in our inability to statistically differentiate between a pure Comptonisation spectrum, and a MCD plus Comptonisation model, and to place firm constraints on the cooler component in the latter model.

However, the data were still very revealing. We detected significant long-term flux variability, with possible peaks and troughs in the inter-observation light curve of NGC 5907 ULX (Figure 3.2; Table 3.5), with accompanying X-ray spectral variability also evident between the high quality *XMM-Newton* and *Chandra* detections. The light curve, although sparsely sampled, seems consistent with the variation seen in other ULXs that *Swift* has monitored on timescales of months to years (e.g. Kaaret & Feng 2009; Strohmayer 2009; although ESO 243-49 HLX-1 shows a different, regular outburst cycle behaviour, Lasota et al. 2011). One obvious difference is that this variation is at higher luminosities than most other ULXs at between $\sim 8 \times 10^{39}$ and 6×10^{40} erg s^{-1}. Similar variability patterns are also seen in a number of ULXs with either a mixture of *Swift* and *XMM-Newton* monitoring data, or campaigns

conducted on *XMM-Newton* and *Chandra* alone (e.g. Feng & Kaaret 2006b; Roberts et al. 2006; Grisé et al. 2010), but these data offer a crucial extra dimension – detailed spectral variability data. This has led to the realisation that ULXs can show spectral variability that is degenerate with X-ray luminosity, with this having been demonstrated for NGC 1313 X-1 and Ho II X-1 (Kajava et al. 2012; Pintore & Zampieri 2012). NGC 1313 X-2, on the other hand, has spectral parameters that correlate well with X-ray luminosity (Pintore & Zampieri, 2012).

Unfortunately, the clustering of our *XMM-Newton* and *Chandra* spectra means we only have effectively two measurements of the source spectrum, hence we are unable to draw conclusions on whether it also displays degenerate spectral variability. What we can conclude is that in the data we do have NGC 5907 ULX exhibits spectral hardening as its flux decreases (e.g. Table 3.2). Such a trend has also been reported for the $L_X – \Gamma$ correlated ULXs of Kajava & Poutanen (2009; for the objects NGC 253 X-4, IC 342 X-1, NGC 1313 X-1, Ho II X-1, Ho IX X-1, NGC 5204 X-1 and NGC 5408 X-1) and Feng & Kaaret (2009; NGC 1313 X-1, Ho II X-1 and NGC 5204 X-1, but not IC 342 X-1), although the spectral index of NGC 5907 ULX in its low flux state was unusually hard compared to these other ULXs. Interestingly, a number of the $L_X – \Gamma$ correlated ULXs also showed spectral pivoting, with three reported to have appeared in low/soft states (NGC 1313 X-1, Ho II X-1, NGC 5204 X-1; Kajava & Poutanen 2009; Kajava et al. 2012). Such spectral evolution is strongly suggestive of a two component spectrum, as is indeed seen for all three of these objects (e.g. Gladstone et al. 2009). All three are in the ultraluminous state, and a detailed inspection of their spectra indicates the pivoting originates in a change in the balance between the soft and hard spectral components (see Chapter 4). However, no such pivoting is seen in NGC 5907 ULX – it remains hard throughout all the observations. Indeed, an inspection of Table 3.3 shows there is no strong statistical necessity for a two-component spectrum for either the high or low flux groups. This is supported by the absence of a significant difference between the fractional variability

in the soft and hard bands in any observation. Together, they argue that this ULX is dominated by a single spectral component over the observed energy range.

Accretion disc models supplied a statistically acceptable single-component solution to both groups of spectra, with the high flux spectra preferring a non-standard radial emission profile ($p \sim 0.6$) consistent with some degree of advection. As the normalisation of both the MCD blackbody model and the p-free disc model provide a measure of the inner disc radius, we can use equation 8 of Makishima et al. (2000) to obtain an 'X-ray estimated' mass of the black hole in this ULX. Taking the upper limit on the high flux group from the p-free model (this is consistent with both low flux models, and a superior fit to the standard disc for the high flux data), we find that $M_{\mathrm{BH}}\alpha\sqrt{\cos(\theta)} < 5M_{\odot}$, where M_{BH} is the black hole mass, α is a positive parameter that equals unity for a Schwarzschild black hole, and is less than unity for a Kerr (i.e. spinning) black hole, and θ is the inclination angle of the accretion disc to our line-of-sight. Clearly this is a remarkably low mass estimate for a ULX that exceeds 5×10^{40} erg s^{-1} in luminosity, although we note that this limit will rise in the case of either the accretion disc not being face-on, or the black hole having significant spin. The latter may in part be a solution to the anomalously high disc temperatures we observe (~ 3 keV), as the disc would move deeper into the gravitational potential for a Kerr metric and hence heat up (Makishima et al., 2000), although an additional contribution to the high temperatures may also come from a large colour correction factor due to the hot underlying accretion disc (Kajava et al., 2012). However, even if the high disc temperature can be explained, two problems remain for the disc interpretation. Firstly, the temperature increases (very significantly, for a standard disc) as the flux diminishes; this is not the expected behaviour of an accretion disc, that classically follows an $L \propto T^4$ relationship (Done et al., 2007). Secondly, we do not expect to see variability from an accretion disc on anything other than the longest timescales (Wilkinson & Uttley, 2009); yet we see ~ 9 per cent fractional variability across all observations that are well constrained for NGC 5907 ULX. Thus, we

conclude a disc interpretation is unlikely for this object.

We therefore return to the Comptonisation models. An absorbed Comptonisation model provides a good single-component fit to both of the sets of grouped spectra. The fit parameters are similar to those seen in the coronae of other ULXs (e.g. Gladstone et al. 2009), being both cool and optically thick. Additionally, the temperature of the corona in NGC 5907 ULX appears to be cooler at higher luminosity. Although at first seemingly unphysical, such a single component spectrum may be physically understood in the context of the ultraluminous state model of ULXs. The key to understanding this lies in the physical interpretation, and the geometry of the two components. Although Gladstone et al. (2009) originally interpreted the two components rather literally as a thick corona above the inner disc, and the direct emission from the cooler outer disc, more recent work has provided evidence to revise this picture. In particular, it now seems likely the cool component originates in a massive outflowing funnel-shaped wind, as would be expected from a super-Eddington flow, e.g. Poutanen et al. (2007; see also Kajava & Poutanen 2009, Middleton et al. 2011a). The warmer component may then still be a thick corona above the central regions of the accretion disc, but alternatively it may be the direct emission from the inner regions of the disc itself, where the high temperatures and accretion rates distort the disc spectrum (e.g. Middleton et al. 2011a; Kajava et al. 2012). In this case, if we are viewing NGC 5907 ULX at an inclination close to face on, then we are looking directly down the opening angle of the wind, so observe the central emission with a high degree of geometrical beaming (King, 2009). It then remains to explain the observed spectral variability, possibly this could be interpreted by the corona cooling as more material is raised above the inner disc, so sharing the coronal power across more particles (cf. Vierdayanti et al. 2010; for Ho IX X-1; although see Kong et al. 2010 for an alternate view of the same data).

There is, however a possible flaw with the above interpretation: we detect ~ 9 per cent fractional variability in NGC 5907 ULX. Because, in the Comptonisation-

only model, we are essentially looking at an accretion disc that we expect to be invariant, we then again struggle to explain the variability. However, variability can be produced in this updated ultraluminous state model, where it is understood as originating from variable obscuration of the stable central emission by clumps of material from the wind intercepting the line-of-sight (Middleton et al. 2011a). But, critically, this can only occur at lines-of-sight close to the wind's edge, which appears at odds with the interpretation from the spectral data that we are viewing NGC 5907 ULX close to face-on. Here, we speculate that this apparent inconsistency can be circumvented if there is an intrinsic disc-like spectral component from the wind, which we are unable to observe due to its intrinsically cool temperature and the unusually high absorption column in the direction of the source. As such, we use the results of the two component MCD plus Comptonisation model, in an attempt to constrain the limits of a possible contribution from the wind. As the soft spectral data were of insufficient quality to properly constrain a disc component, we instead used characteristic values for ULX disc-like component temperatures of 0.1 and 0.3 keV. For the warmer of the two disc-like components, the spectral variability appeared mainly to originate in a far greater diminution of the disc component than the corona as the total flux faded; for the cooler disc the spectral hardening plausibly originated in subtle changes in the corona itself.

In this picture the warmer disc would seem to be the less likely scenario for NGC 5907 ULX, as to have the wind vary significantly more than the inner disc region would require at least a contrived geometry, that could extinguish our view of the outer X-ray emitting regions while retaining most of our view to the inner regions. However, a cooler disc fit might provide a more physically consistent explanation if we consider that, in order to reach the extreme luminosities seen in this object, an extreme super-Eddington flux is required, even for a MsBH. At high super-Eddington rates one would expect to see a very massive radiatively-driven wind; as this is effectively a blackbody emitter, its temperature is proportional to surface area, and

so will reduce as the material in the wind increases (King & Pounds, 2003), favouring a very cool component. Such a wind would not only increase the beaming factor, aiding in reaching the extreme luminosities (King, 2009); but also have a narrower opening angle for the collimated region created by the inner disc and wind, potentially leading to a higher probability of any line-of-sight to the central regions crossing the edge of the wind, thus imprinting variability (Middleton et al. 2011a). This scenario, while speculative, is consistent with the picture emerging from other ULXs, and so we favour it as the best current explanation for the properties of this ULX.

One final issue to deal with is the mass of the black hole powering this system. Other than the high luminosity, there is no evidence in support of an IMBH being harboured by NGC 5907 ULX. As we have discussed, its characteristics can be plausibly explained by a highly super-Eddington black hole. The maximal radiative emission by a super-Eddington system has been estimated as $\approx 20L_{\rm Edd}$ for a face-on system by Ohsuga & Mineshige (2011); hence, given the peak luminosity for NGC 5907 ULX of $\sim 6 \times 10^{40}$ erg s^{-1}, we are likely to be dealing with a black hole with mass $> 20M_{\odot}$, i.e. in the MsBH regime.

3.5   Conclusions

Here we have presented a thorough X-ray analysis of NGC 5907 ULX - a highly absorbed, luminous ULX in an edge-on spiral galaxy. This study has utilised a combination of *XMM-Newton*, *Chandra*, *Swift* and *ROSAT* observations. The *XMM-Newton* and *Chandra* X-ray spectral data were well fitted by a variety of spectral models, consistent with both sub- and super-Eddington solutions. These included accretion disc spectra, possibly with a degree of advection at the highest X-ray luminosities. However, low estimates of black hole mass based on the warm inner disc temperatures were particularly difficult to reconcile with the extreme X-ray luminosity, which peaks in excess of 5×10^{40} erg s^{-1}. These inconsistencies are compounded

by the failure of the source to follow a classical $L_{\mathrm{X}} \propto T^4$ relationship, and the seemingly ubiquitous ~ 9 per cent variability in its *XMM-Newton* light curves. Rather, spectra dominated by Comptonised emission from a cool, optically thick medium, provide a good fit to the X-ray spectral data, but again offer no explanation to the variability properties. We therefore speculate that a substantial radiatively-driven wind could be present, in the form of a cool (0.1 keV) disc-like spectral component, that is hidden from our view by a combination of its cool temperature and the high column to this source. In this scenario, an extreme (highly super-Eddington) accretion rate produces a massive, radiatively driven wind that both emits as a cool blackbody, and constricts the opening angle of the central regions of the disc. This narrower collimation may boost the perceived luminosity of the system, and would also mean any line-of-sight to the central regions could be crossed by the clumpy outflowing wind material, imprinting the observed short-term variability onto the stable emission from the inner regions. The long-term spectral variations then originate in subtle changes of the physical state of the optically-thick coronal component over time.

The X-ray spectral and timing evidence therefore could indicate that NGC 5907 ULX was observed at highly super-Eddington luminosities. As such, NGC 5907 ULX would not require an IMBH to produce the observed X-ray luminosities, rather the compact accretor is most likely in the MsBH regime.

Chapter 4

The ultraluminous state revisited: fractional variability and spectral shape as diagnostics of super-Eddington accretion

Although we are nearing a consensus that most ULXs below 10^{41} erg s^{-1} represent stellar remnant black holes accreting in a super-Eddington 'ultraluminous' accretion state, little is yet established of the physics of this extreme accretion mode. Here, we use a combined X-ray spectral and timing analysis of an *XMM-Newton* sample of ULXs to investigate this new accretion regime. We start by suggesting an empirical classification scheme that separates ULXs into three classes based on the spectral morphologies observed by Gladstone et al. (2009): a singly-peaked *broadened disc* class, and two-component *hard ultraluminous* and *soft ultraluminous* regimes, with the spectra of the latter two classes dominated by the harder and softer component respectively. We find that at the lowest luminosities ($L_{\mathrm{X}} < 3 \times 10^{39}$ erg s^{-1}) the ULX population is dominated by sources with broadened disc spectra, whilst ULXs with two component spectra are seen almost exclusively at higher luminosities, suggestive of a distinction between $\sim$ Eddington and super-Eddington accretion modes. We

find high levels of fractional variability are limited to ULXs with soft ultraluminous spectra, and a couple of the broadened disc sources. Furthermore, the variability in these sources is strongest at high energies, suggesting it originates in the harder of the two spectral components. We argue that these properties are consistent with current models of super-Eddington emission, where a massive radiatively-driven wind forms a funnel-like geometry around the central regions of the accretion flow. As the wind provides the soft spectral component this suggests that inclination is the key determinant in the observed two-component X-ray spectra, which is very strongly supported by the variability results if this originates due to clumpy material at the edge of the wind intermittently obscuring our line-of-sight to the spectrally hard central regions of the ULX. The pattern of spectral variability with luminosity in two ULXs that straddle the hard/soft ultraluminous regime boundary is consistent with the wind increasing at higher accretion rates, and thus narrowing the opening angle of the funnel. Hence, this chapter suggests that most ULXs can be explained as stellar remnant black holes accreting at and above the Eddington limit, with their observed characteristics dominated by two variables: accretion rate and inclination.

4.1 Introduction

Based on the ultraluminous state model of Gladstone et al. (2009), in Chapter 1 we argue that there are three spectral types of ULXs: broadened discs, hard ultraluminous and soft ultraluminous. Gladstone et al. (2009) suggested that these may represent a spectral sequence with increasing accretion rate: at around the Eddington limit ULXs have broadened disc-spectra; as the accretion rate increases a two component spectrum emerges, initially peaking in the high energy component with a hard ultraluminous spectrum; and, at the highest super-Eddington accretion rates, the balance of the two components shifts, and ULX appears with soft ultraluminous spectrum (see Fig. 4.2 for an illustration of these spectra). Currently it is

thought that the hard component may originate in a Comptonising corona around the inner accretion disc, or it could instead be emission from the hot inner disc (Middleton et al. 2011a), modified by a large colour correction (Kajava et al., 2012). The soft component likely originates in the photosphere at the base of a massive radiatively driven wind, as is expected to occur in black holes that are close to or exceeding Eddington-limited accretion (Poutanen et al., 2007). In this Chapter, we ask whether the different regimes really are a function of accretion rate alone, or whether they might instead depend on other characteristics of the ULX.

One way to make progress in this regard is to consider the question: how do the observed short-term variability properties of ULXs relate to the spectral regimes seen in the ultraluminous state? The extended thermal emission from the radiatively driven wind should be intrinsically stable over short time periods, given it originates in an optically-thick region. However, the smaller scale of the inner emission region means that it could vary, although this is not the case in many ULXs which instead are observed to have suppressed variability (Heil et al., 2009), possibly due to the stabilising effect of advection on the disc structure (Abramowicz et al. 1988). Despite this, a few ULXs have been reported as displaying short time-scale variability, including reported quasi-periodic variability in M82 X-1 (Strohmayer & Mushotzky, 2003), NGC 5408 X-1 (Strohmayer et al. 2007; Strohmayer & Mushotzky 2009; Middleton et al. 2011a) and NGC 6946 X-1 (Rao et al., 2010). While the timescales of these QPOs have been cited as evidence of the presence of IMBHs (Strohmayer & Mushotzky 2003; Strohmayer et al. 2007; Strohmayer & Mushotzky 2009; Rao et al. 2010), Middleton et al. (2011a) have suggested a way in which such variability could be produced in the ultraluminous state. If the material in the wind is clumpy in nature (Takeuchi et al., 2013), then if the line of sight to the central regions intersects the edge of the wind the clumps will imprint stochastic variability onto the hard component by intermittently obscuring it. As the soft emission originates in the wind itself, it is not adversely affected by this mechanism (Middleton et al.

2011a; Middleton et al. 2013). We show a schematic of the ultraluminous state model and example X-ray spectra in Figure 4.1, in which we illustrate how a single class of object can produce a hard dominated ultraluminous spectrum at viewing angles close to face on, a soft dominated ultraluminous spectrum at inclinations closer to the out-flowing wind, and the observed variability when viewed through the clumpy edge of the wind.

In the wind model, super-critical accretion discs have an extended photosphere, from which the outflow is driven. The outflow has a soft spectrum, which peaks at the temperature at the spherization radius (T_{Sp}). The spherization radius is the point where the optical depth normal to the accretion disc is maximum, and it is dependent on the mass accretion rate, and the amount of energy used in driving the wind, which results in an approximate relation between the peak colour-temperature of the wind and the mass accretion rate of $T_{SP} \propto \dot{M}^{-1/2}$ (Poutanen et al., 2007). Hydrodynamical simulations of such super-Eddington disc winds suggest that they emerge at angles of 10°–50° from the axis of the accretion disc, and become clumpy at heights of $\sim 250 R_S$ (Takeuchi et al., 2013). The clumps have a typical size of $\sim 10 R_S$, which corresponds to one optical depth, so they are marginally optically thick (Takeuchi et al., 2013) and can produce the required obscuration. Furthermore, Middleton et al. (2013) have recently claimed to have detected residuals in the X-ray spectra of NGC 5408 X-1 and NGC 6946 X-1, which they suggest are consistent with absorption by a partially ionised optically thick plasma. Such a plasma may occur at large distances above the disc ($\gtrsim 500 R_S$), where the optically thick wind disperses and becomes optically thin, if a combination of distance from the central source and self shielding by the inner wind allow the ionisation of the material to drop (Middleton et al., 2013).

However, this model of super-Eddington emission is not universally accepted, and other ULX models may explain the current data. Reflection models (Caballero-García & Fabian, 2010) give one alternative interpretation of the energy spectrum
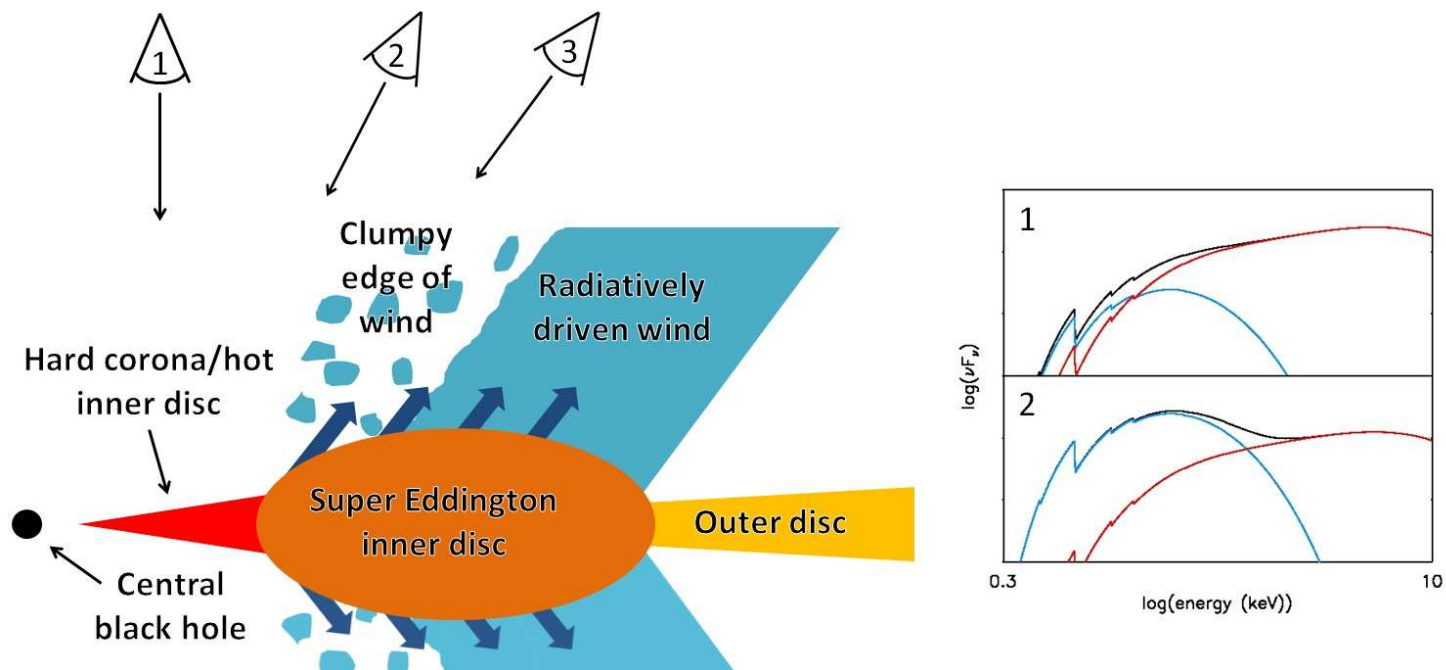
Figure 4.1: (*left*) Schematic of the ultraluminous state model of super-Eddington accretion and (*right*) example X-ray spectra. At large distances from the central black hole the accretion rate is locally sub-Eddington and the accretion disc takes the form of a standard thin disc (yellow). Closer to the centre of disc, within the photospheric radius the accretion disc inflates and becomes radiation-pressure dominated (orange), and a radiatively driven wind with a soft X-ray spectrum arises (blue), the edge of which is clumpy in nature. At the centre of the accretion disc a hard X-ray spectrum is produced, either in a cool, optically thick corona, or in the hot inner-disc itself with a large colour correction. This results in a two-component X-ray spectrum, with the balance of the components dependant on the angle at which the system is observed. Close to face on (spectrum 1, as seen at observing angle 1) the hard component from the central source (shown in red in the schematic and the spectra) dominates the spectrum, whilst at higher inclinations (spectrum 2, as seen at observing angle 2) the balance of the components shifts to the soft wind (blue). At lines of sight through the clumpy edge of the wind (observing angle 3), stochastic variability is imprinted on to the hard spectrum from the inner accretion disc, whilst the soft emission remains invariable.

from ULXs. These require a radiation source with a power-law-like continuum to be produced above a high spin black hole; the proponents of such models have suggested that power could be magnetically extracted from the disc and released in the emission region, thus avoiding the Eddington limit (Caballero-García & Fabian, 2010). The observed ULX spectral features, including the soft excess and high energy break, are then produced by relativistically-blurred reflection from the disc. Investigating the variability characteristics of ULXs provides a good test of such models – the detection of multiple spectral components, each with different variability properties, would be difficult to explain in terms of reflection. A further proposed model of ULX emission is that of slim (super-critical) discs (Abramowicz et al., 1988); these can reproduce the flat power-law spectra seen in many ULXs, and predict black hole masses in the massive stellar regime (Vierdayanti et al., 2006). However, it is not clear how variability could be produced in a slim disc alone, again providing a potential diagnostic test of such models; an additional physical issue is that slim disc spectral models neglect the wind that would be expected to arise as the accretion rate exceeds the Eddington limit (Poutanen et al. 2007; Dotan & Shaviv 2011), although later slim disc simulations do self-consistently include winds (e.g. Ohsuga & Mineshige 2011).

In this chapter, which is adapted from Sutton et al. (2013b), we present results from a combined X-ray spectral and timing analysis using multiple *XMM-Newton* detections of a sample of 20 ULXs with moderate to high quality X-ray data. We suggest a new empirical scheme to classify the ULXs by X-ray spectrum into three ultraluminous spectral types: broadened disc, hard ultraluminous and soft ultraluminous. Then, we characterise the spectral hardness and timing properties of ULXs in each class in order to further explore and constrain models of accretion in ULXs.

Table 4.1: The ULX sample

Source name	Reference[a]	2XMM ID	N_{H}[b]	Distance[c]	Reference[d]
NGC 55 ULX	1, 2, 3	2XMM J001528.8−391318	1.73	2.11	i
M31 ULX1	4, 5, 6	CXOM31 J004253.1+411422[e]	6.68	0.79	i
NGC 253 XMM2	3, 7	2XMM J004722.6−252050	1.38	3.68	i
NGC 253 ULX2	2, 7, 3	2XMM J004732.9−251749	1.38	3.68	i
M33 X-8	1	2XMM J013350.8+303937	5.69	0.92	i
NGC 1313 X-1	1, 2, 3, 7, 8	2XMM J031819.8−662911	3.95	4.39	ii
NGC 1313 X-2	1, 2, 8	2XMM J031822.1−663603	3.95	4.39	ii
IC 342 X-1	1, 3, 7, 8	2XMM J034555.6+680455	28.75	3.50	iii
IC 342 X-2	3	2XMM J034606.5+680705	28.75	3.50	iii
NGC 2403 X-1	1, 2, 3, 7, 8, 9	2XMM J073625.5+653540	4.17	3.50	i
Ho II X-1	1, 2, 3, 7, 8, 9	2XMM J081928.9+704219	3.41	3.42	ii
M81 X-6	1, 3, 8, 9	2XMM J095532.9+690034	4.22	4.27	i
Ho IX X-1	1, 2, 8	2XMM J095753.2+690348	4.26	3.61	iv
NGC 4190 ULX1	8	CXO J121345.2+363754[e]	1.62	3.47	v
NGC 4559 ULX2	1, 2, 3, 7, 8, 9	2XMM J123551.7+275604	0.80	6.98	i
NGC 4736 ULX1	3	2XMM J125048.6+410743	1.44	4.66	ii
NGC 5204 X-1	1, 2, 3, 7, 8, 9	2XMM J132938.6+582506	1.38	4.65	vi
NGC 5408 X-1	1, 2, 3 , 7	2XMM J140319.6−412258	5.93	4.80	vii
NGC 5907 ULX	3, 7	2XMM J151558.6+561810	1.38	13.4	i
NGC 6946 X-1	3, 8, 9	2XMM J203500.0+601130	20.05	6.80	viii

[a]The sample sources are selected from: 1 - Gladstone et al. (2009); 2 - Heil et al. (2009); 3 - Middleton et al. (in prep.); 4 - Henze et al. (2009); 5 - Kaur et al. (2012); 6 - Middleton et al. (2012); 7 - Walton et al. (011b); 8 - Liu & Bregman (2005); 9 - Swartz et al. (2004). [b]Galactic column density in the direction of the source ($\times 10^{20}$ cm^{-2}), taken from Dickey & Lockman (1990). [c]Distance to the ULX host galaxy in units of Mpc. [d]Distances to the ULX host galaxies are taken from: i - Tully et al. (2009b); ii - Jacobs et al. (2009); iii - Herrmann et al. (2008); iv - Dalcanton et al. (2009); v - Tikhonov & Karachentsev (1998); vi - Karachentsev et al. (2003); vii - Karachentsev et al. (2002); viii - Karachentsev et al. (2000). [e]All *XMM-Newton* detections of M31 ULX1 and NGC 4190 ULX1 were obtained too late for these two sources to be included in the 2XMM-DR3 catalogue, so do not have a 2XMM source designation, in these cases *Chandra* source IDs are shown instead.

Table 4.2: Observation log

Obs. ID[a]	Date[b]	t_{exp}[c] (ks)	Count rate[d] (ct s^{-1})	θ[e] (arcmin)	Obs. ID[a]	Date[b]	t_{exp}[c] (ks)	Count rate[d] (ct s^{-1})	θ[e] (arcmin)
				NGC 55 ULX					
0028740201	2001-11-14	30.4	2.0	4.40	0028740101	2001-11-15	21.4	1.1	11.25
0655050101	2010-05-24	83.0	1.1	1.13					
				M31 ULX1					
0600660201[f]	2009-12-28	16.2	5.2	2.66	0600660301[f]	2010-01-07	15.4	5.2	2.53
0600660401	2010-01-15	6.8	5.1	2.47	0600660501	2010-01-25	11.4	4.1	2.38
0600660601	2010-02-02	10.8	3.4	2.27					
				NGC 253 XMM2					
0125960101[g]	2000-06-03	34.2	0.1	5.37	0110900101	2000-12-13	7.4	0.1	4.55
0152020101	2003-06-19	38.0	0.4	5.29	0304850901	2006-01-02	9.8	0.2	3.12
0304851001	2006-01-06	9.8	0.2	3.15	0304851201	2006-01-09	18.0	0.2	3.17
				NGC 253 ULX2					
0125960101	2000-06-03	34.2	0.4	1.67	0110900101	2000-12-13	7.4	0.5	3.11
0152020101	2003-06-19	38.0	0.4	1.61	0304850901	2006-01-02	9.8	0.4	0.80
0304851001	2006-01-06	9.8	0.4	0.79	0304851201	2006-01-09	18.0	0.4	0.77
0304851301[g]	2006-01-11	6.4	0.2	0.80					

[a] *XMM-Newton* observation identifiers. [b] Observation start date, in yyyy-mm-dd format. [c] The amount of simultaneous good time in 200s bins, in all of the EPIC detectors used in the analysis. [d] Combined *XMM-Newton* EPIC count rate of the ULX. [e] Angular separation between the on-axis position of the observation and the 2XMM source position. [f] No MOS2 detection was included in the analysis of this observation. [g] No pn detection was included in the analysis of this observation. [h] No MOS1 or MOS2 detections were included in the analysis of this observation. [i] No MOS1 detection was included in the analysis of this observation.

Table 4.2: continued

Obs. ID[a]	Date[b]	$t_{\exp}$[c] (ks)	Count rate[d] (ct s^{-1})	θ[e] (arcmin)	Obs. ID[a]	Date[b]	$t_{\exp}$[c] (ks)	Count rate[d] (ct s^{-1})	θ[e] (arcmin)
				M33 X-8					
0102640401[g]	2000-08-02	11.6	1.2	12.29	0102640101	2000-08-04	5.6	8.4	1.16
0102640701[g]	2001-07-05	10.0	1.3	12.92	0102641001[g]	2001-07-08	6.0	1.6	10.50
0102642001	2001-08-15	8.4	2.2	14.08	0102642101	2002-01-25	9.8	4.2	10.65
0102642301	2002-01-27	10.0	4.5	8.67	0141980601	2003-01-23	10.0	2.6	14.05
0141980801	2003-02-12	6.6	6.9	1.10	0141980101[g]	2003-07-11	6.2	1.6	10.62
0141980301[h]	2003-07-25	6.4	2.9	8.56	0650510101	2010-07-09	60.6	3.0	9.53
0650510201	2010-07-11	53.6	7.1	4.06					
				NGC 1313 X-1					
0106860101	2000-10-17	10.4	1.1	1.45	0150280301[h]	2003-12-21	6.8	0.9	7.87
0150280601	2004-01-08	6.0	1.2	7.76	0205230301	2004-06-05	8.2	1.7	5.63
0205230501[g]	2004-11-23	15.4	0.4	7.83	0205230601	2005-02-07	4.4	0.9	7.38
0405090101	2006-10-15	77.4	1.0	1.51					
				NGC 1313 X-2					
0106860101	2000-10-17	10.4	0.4	5.44	0150280301	2003-12-21	6.8	1.4	1.02
0150280601	2004-01-08	6.0	0.6	1.04	0205230301	2004-06-05	8.2	1.5	1.26
0205230501	2004-11-23	12.6	0.5	0.99	0205230601	2005-02-07	4.4	1.5	1.10
0301860101	2006-03-06	18.2	1.0	6.17	0405090101	2006-10-15	77.4	0.9	5.40
				IC 342 X-1					
0093640901	2001-02-11	5.6	0.5	5.07	0206890201	2004-08-17	18.0	0.6	4.26

Table 4.2: continued

Obs. ID[a]	Date[b]	$t_{\exp}$[c] (ks)	Count rate[d] (ct s^{-1})	θ[e] (arcmin)	Obs. ID[a]	Date[b]	$t_{\exp}$[c] (ks)	Count rate[d] (ct s^{-1})	θ[e] (arcmin)
				IC 342 X-2					
0093640901[h]	2001-02-11	5.6	0.2	4.25	0206890201	2004-08-17	18.0	0.4	1.86
				NGC 2403 X-1					
0164560901	2004-09-12	56.0	0.2	5.36					
				Ho II X-1					
0112520601	2002-04-10	5.0	4.4	1.12	0200470101	2004-04-15	21.0	4.5	1.13
0561580401	2010-03-26	24.0	1.7	1.13					
				M81 X-6					
0111800101[i]	2001-04-22	77.2	0.6	3.35	0112521001	2002-04-10	7.0	0.5	11.93
0112521101	2002-04-16	8.0	0.5	11.88	0200980101[g]	2004-09-26	61.0	0.2	13.85
				Ho IX X-1					
0111800101[g]	2001-04-22	77.2	0.7	12.534	0112521001	2002-04-10	7.0	2.9	1.11
0112521101	2002-04-16	8.0	3.3	1.13	0200980101	2004-09-26	25.0	2.3	1.13
				NGC 4190 ULX1					
0654650201	2010-06-08	6.0	1.5	1.09	0654650301	2010-11-25	8.8	2.3	1.18
				NGC 4559 ULX2					
0152170501	2003-05-27	21.0	0.5	1.08					

Table 4.2 continued

Obs. ID[a]	Date[b]	t_{exp}[c] (ks)	Count rate[d] (ct s^{-1})	θ[e] (arcmin)	Obs. ID[a]	Date[b]	t_{exp}[c] (ks)	Count rate[d] (ct s^{-1})	θ[e] (arcmin)
				NGC 4736 ULX1					
0404980101	2006-11-27	37.0	0.4	2.05					
				NGC 5204 X-1					
0142770101	2003-01-06	12.0	0.8	1.13	0405690101	2006-11-15	7.6	1.7	1.10
0405690201	2006-11-19	22.0	1.5	1.08	0405690501	2006-11-25	17.0	1.0	1.13
				NGC 5408 X-1					
0112290601	2001-08-08	4.8	1.7	1.27	0112290701[g]	2001-08-24	5.6	0.7	1.23
0302900101	2006-01-13	88.0	1.2	1.09	0500750101	2008-01-13	27.3	1.1	1.06
0653380201	2010-07-17	64.2	1.5	1.12	0653380301	2010-07-19	106.2	1.5	1.12
0653380401	2011-01-26	83.4	1.4	1.11	0653380501	2011-01-28	86.2	1.4	1.07
				NGC 5907 ULX					
0145190201	2003-02-20	8.2	0.5	2.40	0145190101	2003-02-28	9.8	0.4	2.41
0673920301	2012-02-09	13.0	0.2	1.12					
				NGC 6946 X-1					
0200670101[g]	2004-06-09	4.0	0.2	1.38	0200670301	2004-06-13	8.0	0.5	1.41
0200670401[g]	2004-06-25	6.0	0.2	1.37	0500730201	2007-11-02	28.4	0.4	3.54
0500730101	2007-11-08	18.0	0.4	3.53					

4.2 Sample selection and data reduction

4.2.1 Sample selection

The primary driver of our ULX sample selection was the requirement for the data to be of high enough quality to allow us to conduct a statistically significant short-term timing analysis; as such, we defined the criteria for selecting observations based on combined EPIC count rates and the available good time. As a starting point, we used the ULXs previously identified as those with the highest quality *XMM-Newton* data, which were subject to an in-depth spectral analysis by Gladstone et al. (2009), and power spectral density analysis by Heil et al. (2009). In addition to these, we also considered ULXs with fluxes in excess of 5×10^{-13} erg cm^{-2} s^{-1} in the *ROSAT* HRI observed sample of Liu & Bregman (2005), and the *Chandra* archival sample of Swartz et al. (2004) as these are likely candidates for having reasonable quality *XMM-Newton* data, if they have been detected in previous observations. To these we added M31 ULX1 (CXOM31 J004253.1+411422; Henze et al. 2009; Kaur et al. 2012; Middleton et al. 2012), and all ULXs with a 0.3–10 keV count rate of $\gtrsim$ 0.3 ct s^{-1} in at least one observation in a cross correlation of the 2XMM-DR3 (Watson et al., 2009) and the RC3 (de Vaucouleurs et al., 1991) catalogues (Middleton et al. in prep.; which is an updated version of Walton et al. 2011b).

We then obtained and examined all of the archival *XMM-Newton* observations of these ULXs. Firstly we extracted their combined EPIC count rates. Motivated by the available ULX data, it was decided to extract fractional variability from light curves with 200 s temporal binning, as a compromise between having $\gtrsim$ 20 counts per bin and at least 20 temporal bins in a large sample of observations. When extracting the fractional variability we use a combined light curve from all of the available EPIC detections of the source, so we define the available good time in an observation as the sum of the 200 s bins in which all of the available detectors were on and free

from high levels of background flaring. We then rejected all of the sources which did not meet the selection criteria of a minimum average 0.3–10 keV combined EPIC count rate of 0.3 ct s^{-1}, in at least one *XMM-Newton* observation, and sufficient good time to extract light curves with at least twenty 200 s bins (i.e. a total of 4 ks good time), to ensure Gaussian statistics. The ULXs remaining in the sample are listed in Table 4.1, along with the Galactic column densities and distances to the assumed host galaxy. For the ULXs which met the sample criteria in at least one observation, we included all observations that had the same minimum good time, but met a less stringent count rate limit of at least 0.1 ct s^{-1}, corresponding to an average of 20 counts per bin. In addition to full-band (0.3–10 keV) timing analysis, we also examine the properties in two other bands (0.3-1 and 1-10 keV); for this we use sub-sets of the observations which meet the count rate limit of $\geq$ 0.1 ct s^{-1} in the appropriate energy band.

4.2.2 Data reduction

All archival *XMM-Newton* EPIC detections of the ULXs shown in Table 4.1 were downloaded from the NASA HEASARC archive, and those which met the criteria described in Section 4.2.1 were included in the subsequent work. We summarise all the data used in our analyses in Table 4.2.1.

The data were reduced, and products extracted using standard tools in *XMM-Newton* SAS (version 10.0.0). Firstly, we extracted high energy (10–15 keV) full field light curves using EVSELECT, from which we filtered out periods subject to high background flaring, using TABGTIGEN to generate good time interval (GTI) files. When creating GTIs, we ensured that only temporally complete bins were used (i.e. no drop-outs were left in the data that could affect the subsequent timing analysis). The exact filtering count rate varied between observations, to maximise the utilised data whilst avoiding flaring, but typical values were $\sim$ 1–1.5 and $\sim$ 0.6 ct s^{-1} for the

pn and MOS detectors respectively. When later calculating fractional variability we required that all of the available detectors were simultaneously on, so defined a GTI using the detector with the latest start time and earliest stop time. Generally this was the pn detector, except for observations with no pn detection of the ULX; here either MOS1 or MOS2 light curves were used to define the GTI.

Source spectra and light curves were mainly extracted from circular source regions with radii between 20–50 arcseconds, with apertures at the lower end of the range being used when other sources were in close proximity to the object of interest. One exception, where neighbouring sources necessitated a very small source region radius of 12.5 arcseconds, was NGC 253 ULX2. Also, in a few cases elliptical source regions were used, which were mainly necessary when the object neighboured a detector chip gap[1]. An elliptical region was also used for the MOS1 detection of M81 X-6 in observation 0112521001, where it was aligned with the direction of maximum point spread function as the source image was particularly elongated due to its large off-axis angle. One further exception was observation 0600660201 of M31 ULX1, here we followed Middleton et al. (2012), and used an annular source region to account for pile-up in the pn detection. Again following Middleton et al. (2012), we excluded the MOS2 data from the analysis of observations 0600660201 and 0600660301, as significant pile-up in these observations would have required the removal of large centroids. Count rates were low enough that pile-up was not an issue in other observations. Background spectra/light curves were extracted from circular regions; these were set equal in area to the source regions when extracting light curves, but larger regions were used when extracting spectra. Background regions were located at a similar distance from the read out node as the source, on the same or a neighbouring

---

[1]The affected observations were: NGC 55 ULX - 0028740101 (pn); M33 X-8 - 0102642301 (pn, MOS1 & MOS2) and 0650510101 (pn, MOS1 & MOS2); NGC 1313 X-1 - 0150280601 (MOS1 & MOS2); NGC 1313 X-2 - 0106860101 (MOS1 & MOS2), 0301860101 (MOS1 & MOS2) and 0405090101 (MOS1 & MOS2); NGC 2403 X-1 - 0164560901 (pn); M81 X-6 - 0111800101 (pn & MOS2); NGC 6946 X-1 - 0200670301 (pn), 0500730201 (pn) and 0500730101 (pn).

chip for pn detections, or on the same chip as the source for MOS detections.

Final data products were extracted using the appropriate GTI file, standard event patterns (`PATTERN` $\leq$ 4 for the pn detector, `PATTERN` $\leq$ 12 for the MOS detectors) and filters (`FLAG` = 0 for spectra; `#xmmea_ep` or `#xmmea_em` respectively for the pn and MOS light curves). Spectra, and appropriate response matrices were extracted using XMMSELECT, then grouped using the FTOOL GRPPHA; light curves were obtained using EVSELECT.

4.3   Analysis and Results

4.3.1   An empirical spectral classification scheme for ULXs

The first step was to attempt to classify each of the 89 ULX observations into one of the three proposed super-Eddington spectral regimes outlined above and shown in Figure 4.2. We chose to do this using a simple empirical model fit to the data, specifically a doubly-absorbed multi-colour-disc (MCD) plus power-law model (CONSTANT $\times$ TBABS $\times$ TBABS $\times$ (DISKBB + POWERLAW) in XSPEC). This is motivated by the work of Gladstone et al. (2009): in their work the disc-like spectra had relatively warm discs in this model ($kT_{\mathrm{in}} > 0.5$ keV), whereas the hard and soft ultraluminous spectra had cool discs and were themselves differentiated by their value of photon index Γ. This was > 2 for the soft ultraluminous spectra, and < 2 for the hard ultraluminous sources. We therefore base our classification scheme on these simple distinctions; we show the whole scheme in the form of a decision tree in Figure 4.3, and discuss it further below.

In order to perform the classification, the energy spectra were grouped to a minimum of 20 counts per energy bin, to allow the spectral fitting to be carried out using χ^2 statistics in XSPEC v12.6.0. The results of this fitting are shown in Appendix A (Table A.1). The first absorption component was set equal to the Galactic value in
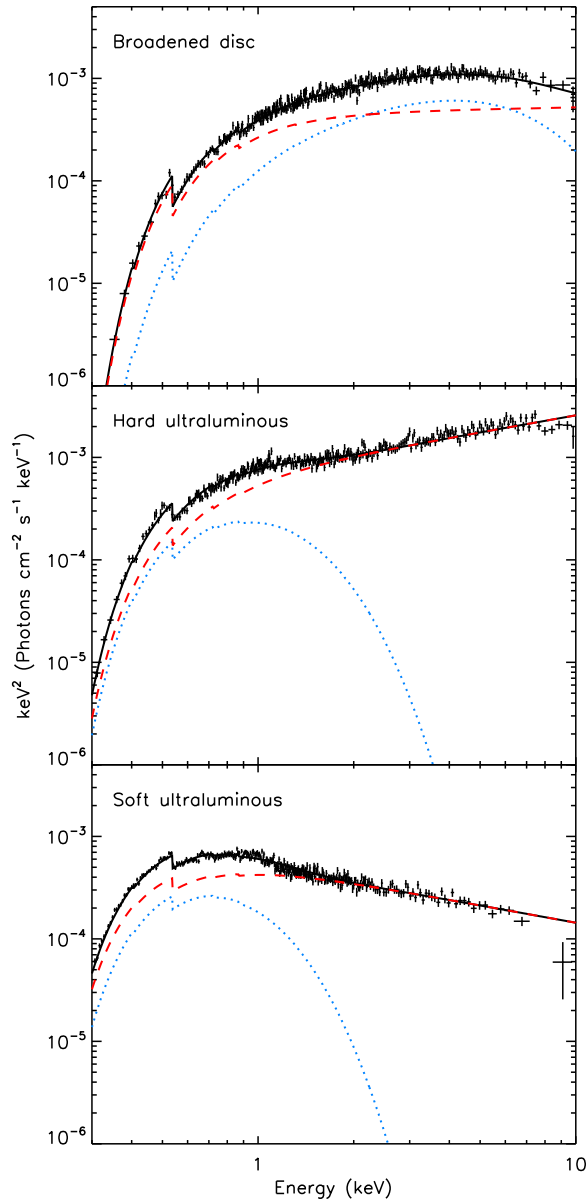
Figure 4.2: Example spectra from observations of different ULXs exhibiting each of the three spectral types. From top to bottom they are: broadened disc - observation 0405090101 of NGC 1313 X-2; hard ultraluminous - observation 0200980101 of Ho IX X-1 and soft ultraluminous - observation 0653380301 of NGC 5408 X-1. For clarity, data are rebinned to 10σ significance and only EPIC pn detections are shown. The contributions from each of the components in the best fitting absorbed MCD (blue dotted line) plus power-law (red dashed line) model are shown. The subtle spectral turnover indicative of ultraluminous state spectra is clearly seen in the data in the lower two panels, falling below the power-law tail whose slope is predominantly set by the data between ~ 2 and 6 keV.
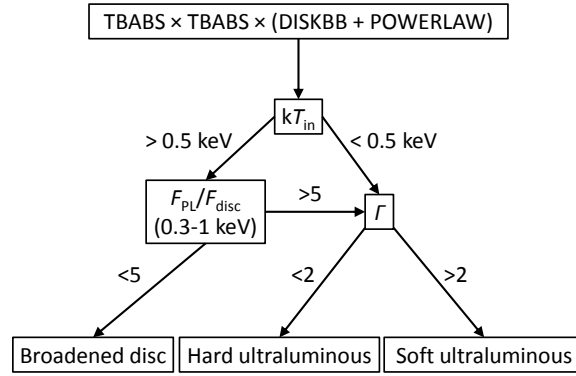
Figure 4.3: Decision tree showing the procedure by which observations were assigned into the three spectral types based on the resulting parameters from the doubly-absorbed MCD plus power-law spectral model.

the direction of the galaxy hosting the ULX (as per Table 4.1), and the latter was left free to model absorption intrinsic to the host galaxy and/or the source itself. Both components used the interstellar abundance tables of Wilms et al. (2000). Additionally, a multiplicative constant was included to account for calibration uncertainties between the detectors, which was fixed to 1 for the pn data (or MOS1 where no pn data was available), and left free to vary for the other detectors. The constant differed by no more than 10 per cent between detectors in most cases, with the small number of exceptions being attributable to different extraction regions and/or proximity to the edge of a chip. We also extracted the 0.3–1 keV absorbed flux contributed by each of the two model components, using the CFLUX convolution model in XSPEC[2]. The ratio of these fluxes, plus the best fitting disc temperature and the photon index from the MCD plus power-law model were then used as the basis of the empirical classification scheme to diagnose the spectral state, as shown in Figure 4.3.

While the classification scheme is attractive due to its simplicity, it does have

---

[2]To do this it was necessary to rearrange the spectral model such that absorption components were included separately for both the MCD and power-law, which were set to be equal, i.e. CONSTANT × (TBABS × TBABS × DISKBB + TBABS × TBABS × COMPTT), with the CFLUX model component inserted before either the first or third absorption component.

limitations. One of the key diagnostics of the hard and soft ultraluminous spectra is their high energy turnover. In most cases this feature is rather subtle, so is well-approximated by the power-law component in the MCD plus power-law model (cf. Figure 4.2). However, in ULXs with a stronger break the simple classification scheme can break down, which notably occurs in NGC 55 ULX in the sample of Gladstone et al. (2009). In this case the power-law cannot adequately approximate the strong high energy curvature, but a disc spectrum can; the two components switch places as the MCD is forced to the hard end of the spectrum, and the resulting hot disc temperature could then be naively associated with a broadened disc ULX. However, the strong soft excess in this source is then dominated by a very soft power-law component, so we can break the model degeneracy using the 0.3–1 keV flux ratio of the MCD and power-law by rejecting a broadened disc interpretation where a dominant fraction of the soft emission is in the power-law. The precise values chosen are motivated by NGC 55 ULX, and we include this modification in the complete classification scheme in Figure 4.3. This solution seems to be sufficient to identify soft ultraluminous spectra with pronounced hard curvature, however it is far from clear how to distinguish hard ultraluminous ULXs with pronounced curvature and little soft excess from broadened discs. A good example in this work occurs for observation 0145190101 of NGC 5907 ULX, where the best fitting MCD plus power-law model indicates a broadened disc spectrum; however, we reject this interpretation based on a detailed multi-mission study of this source (Chapter 3) and use the parameters from a secondary minimum in χ^2 space to instead classify it as a hard ultraluminous spectrum. We return to this point later in Section 4.4.1.

The example of NGC 5907 ULX leads to another potential source for ambiguity: in Chapter 3, we find that the high absorption column in the host galaxy likely suppresses the soft excess emission, such that it is not visible in the spectrum. Such degeneracy between absorption and the intrinsic spectral shape could again be a limitation of our empirical classification scheme; for example both IC 342 X-1 and

X-2 both sit behind a large Galactic absorption column, and in three out of four observations their spectral state is not constrained. As such, we further identify all highly absorbed ULX observations, and caution that the state identification in these sources is less certain. All sources with a combined column density consistent with $\gtrsim 0.5 \times 10^{22}$ cm^{-2} in the absorbed MCD plus Comptonisation model (see below) were classed as highly absorbed; this model was used for this purpose in preference to the MCD plus power-law, as a power-law representation of a Comptonised spectrum can become unphysical at low energies and can result in the absorption being over-estimated. On this basis, high absorption was seen in all observations of IC 342 X-1, IC 342 X-2 and NGC 5907 ULX, plus observation 0200670101 of NGC 6946 X-1.

One further complication arose when fitting the MCD plus power-law to the spectra from NGC 253 ULX2. This source is embedded in extended emission from the galaxy's disc and an outflow of hot gas from the starburst nucleus (Pietsch et al. 2001; Bauer et al. 2008), and initially the spectral fits were rather poor. However, the inclusion of an additional MEKAL component (with abundances frozen to solar values) to model the extended diffuse emission was able to improve this. As the MEKAL model represents emission from the hot collisionally-ionised gas in the region surrounding the source, it would not be expected to vary between observations. So, we were able to constrain the spectral parameters of the hot gas by simultaneously fitting all of the observations of NGC 253 ULX2 with an invariable hot gas, plus a variable ULX model. To constrain the hot gas parameters we again used the more physically motivated ULX model, namely an MCD, plus emission from a Comptonising corona and in this case the diffuse emission from the hot gas (CONSTANT × TBABS × (MEKAL + TBABS × (DISKBB + COMPTT)) in XSPEC). The model parameters of the MEKAL component were set to be equal in each detector for all of the observations, whilst the other model variables[3] were allowed to vary between observations, but were set

---

[3]These were the extra-Galactic absorption column; both the temperature and normalisation of the accretion disc; and the plasma temperature, optical depth and normalisation of the corona (the

to be identical for all of the detectors in a particular observation. The multiplicative constant was fixed to 1 for the pn detector, and free to vary for the MOS detector in all of the observations. The resulting best fitting temperature of the hot gas was $kT = 0.67^{+0.10}_{-0.05}$ keV, with a normalisation of $1.5 \pm 0.3 \times 10^{-5}$ cm^{-5}, which is consistent with the models of the hotter of two plasmas identified in the central region by Bauer et al. (2008). Subsequently, we included the MEKAL emission as a fixed additive component in the spectral model for NGC 253 ULX2, both when repeating the empirical state classification and in the following spectral analysis.

The resulting spectral classifications of the ULX sample are shown in Appendix A (Table A.1). Out of a total of 89 observations, 43 were uniquely classified as broadened discs, 15 as hard ultraluminous and 21 as soft ultraluminous. The classification of the remaining 10 observations was ambiguous, as the 1σ error bounds of the parameters were consistent with multiple spectral state identifications.

4.3.2 Characterising the ULX observations using X-ray luminosity and spectral hardness

As noted above, the use of an MCD plus power-law model can create problems when extracting fluxes that are corrected for absorption given the unphysical behaviour of a power-law at low energies. Therefore, in order to extract band-limited fluxes from the data, the X-ray spectra of the sample ULXs were also fitted using a second two component spectral model - a more physical absorbed MCD plus a Comptonising corona (CONSTANT × TBABS × TBABS × (DISKBB + COMPTT) in XSPEC). The additional advantage of this model is that cool, optically thick Comptonisation can better fit the hard spectral curvature seen in many ULXs (cf. Gladstone et al. 2009). As above, a multiplicative constant and two absorption components were included in the spectral model. The coronal input soft photon temperature was

---

input soft photon temperature was set equal to the inner disc temperature).
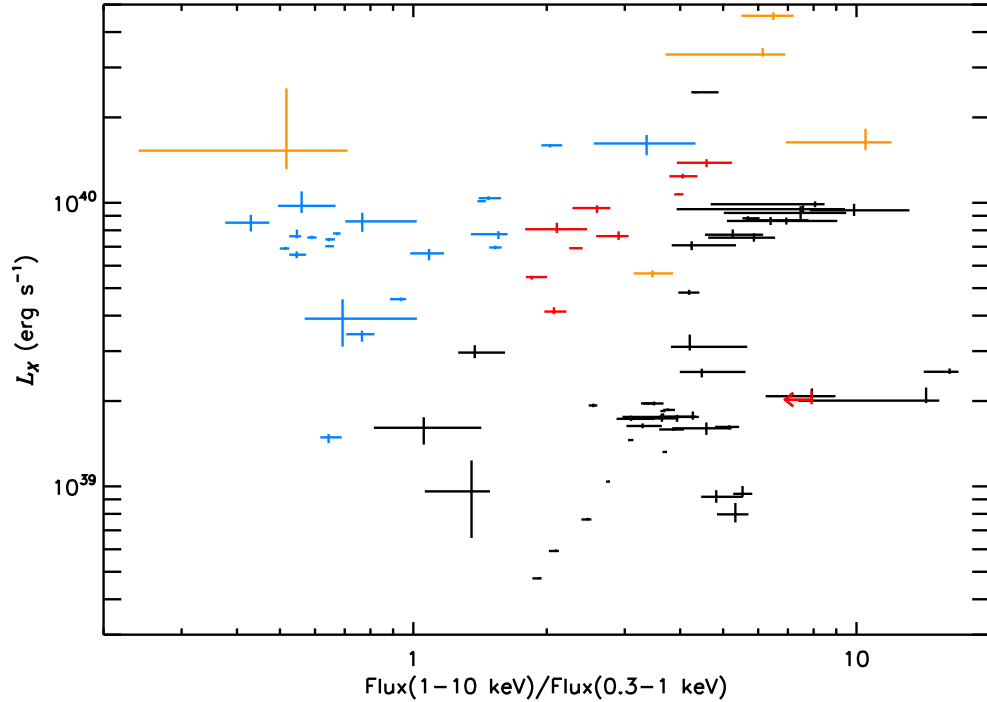
Figure 4.4: Hardness - luminosity diagram for the ULX sample. Spectral hardness is approximated as the ratio of the unabsorbed 0.3–1 and 1–10 keV fluxes extracted from the absorbed disc plus Comptonising corona model, and is plotted against the 0.3–10 keV unabsorbed luminosity. The sample is split into different ULX spectral regimes, which are identified by colour: broadened discs in black, hard ultraluminous in red and soft ultraluminous in blue. Only observations with a firm spectral classification are shown. Also, any highly absorbed observations (with 1σ upper limits of $N_{\mathrm{H}} \geq 0.5 \times 10^{22}$ cm^{-2}) are shown in orange, as the classification scheme is less reliable in highly absorbed sources. The different spectral types of ULXs tend to occupy different regions of the diagram: few hard ultraluminous or soft ultraluminous sources are seen below $\sim 3 \times 10^{39}$ erg s^{-1}, instead below this luminosity we see mostly modified disc ULXs; the hard and soft ultraluminous sources tend to be brighter, and are generally split by spectral hardness, as would be expected given the method by which we differentiate between them.

set equal to the inner disc temperature; whilst this is not entirely physical, as we are not necessarily observing the intrinsic inner disc temperature, it does provide a reasonable first approximation (cf. Pintore & Zampieri 2012 and the discussion therein). This model typically resulted in acceptable fits to the majority of the ULX data. However, the limitations of the model were apparent in a small number of high quality data sets, and it was rejected at 3σ significance in 9 of the 89 observations, which notably included the 5 highest data quality observations of NGC 5408 X-1. A physical interpretation of the best fitting spectral parameters is beyond the scope of the work presented here, and we just used the model to extract X-ray fluxes; we will return to this data, and in particular the features causing the poor fits in future work (Middleton et al. in prep.). Two observations of IC 342 X-2 had unconstrained disc components and were well fitted by the Comptonisation model alone, so a single-component absorbed Comptonisation model was used for the subsequent analysis of these data.

To characterise the X-ray spectrum seen in each of the observations, we extracted intrinsic (i.e. deabsorbed) fluxes in the full, soft and hard energy bands (0.3–10, 0.3–1 and 1–10 keV), using the CFLUX model component in XSPEC and the MCD plus Comptonising corona model. Spectral hardness was approximated as the ratio of the hard and soft band intrinsic fluxes, and 0.3–10 keV luminosities were also calculated using the full-band flux and the distances to the host galaxies from Table 4.1; these are shown in the form of a hardness-luminosity diagram in Figure 4.4, with the observations split into the three proposed spectral types using our empirical classification method. Few hard ultraluminous and soft ultraluminous ULXs are seen below $\sim 3 \times 10^{39}$ erg s^{-1}, and the ULXs less luminous than this tend to show broadened discs. However, a few broadened discs are seen at luminosities greater than $\sim 3 \times 10^{39}$ erg s^{-1}. As expected, given that the two states are differentiated by the spectral index of the power-law tail, the hard ultraluminous sources tend to be spectrally harder than the soft ultraluminous sources, although they both

seem to occupy a similar range of X-ray luminosities, with 12 out of 15 of the hard ultraluminous observations and 20 out of 21 of the soft ultraluminous observations being seen at 0.3–10 keV luminosities between $\sim (0.3\text{--}2) \times 10^{40}$ erg s^{-1}.

4.3.3 State changes in individual ULXs: ambiguous classifications or real spectral progression?

Of the 20 ULXs in the sample, 15 retained the same spectral classification throughout all of the observations included in this study when observations with an ambiguous spectral state are excluded; although 4 of these ULXs only had a single observation with a firm state identification, and the spectral state of IC 342 X-2 was not well constrained in any observation. However, NGC 253 ULX2, NGC 1313 X-1, Ho IX X-1, NGC 5204 X-1 and NGC 6946 ULX3 were all classified as being in two different spectral states.

NGC 253 ULX2 was observed with a disc-like spectrum in all but one observation, where it appeared with a hard ultraluminous spectrum at a similar deabsorbed 0.3–10 keV luminosity (estimated using an absorbed MCD plus Comptonisation model; see section 4.3.2). In this particular case, it seems likely that it may be a case of mistaken identity, possibly due to the relatively low data quality (~ 1000 counts). When fitting the MCD plus power-law model to observation 0304851001 of NGC 253 ULX2 the best fitting hard ultraluminous state solution had a fit statistic of $\chi^2/\text{dof} = 181.4/168$, but there was a second local minima in χ^2 space, with a fit statistic of $\chi^2/\text{dof} = 184.4/168$, which was instead consistent with this observation having a broadened disc spectrum.

Ho IX X-1 was observed with a hard ultraluminous spectrum in three observations, and a broadened disc in one. Unusually, the broadened disc observation occurred at the highest X-ray luminosity. In this case, the data quality is not particularly poor, and we suggest that this observation may be misclassified due to
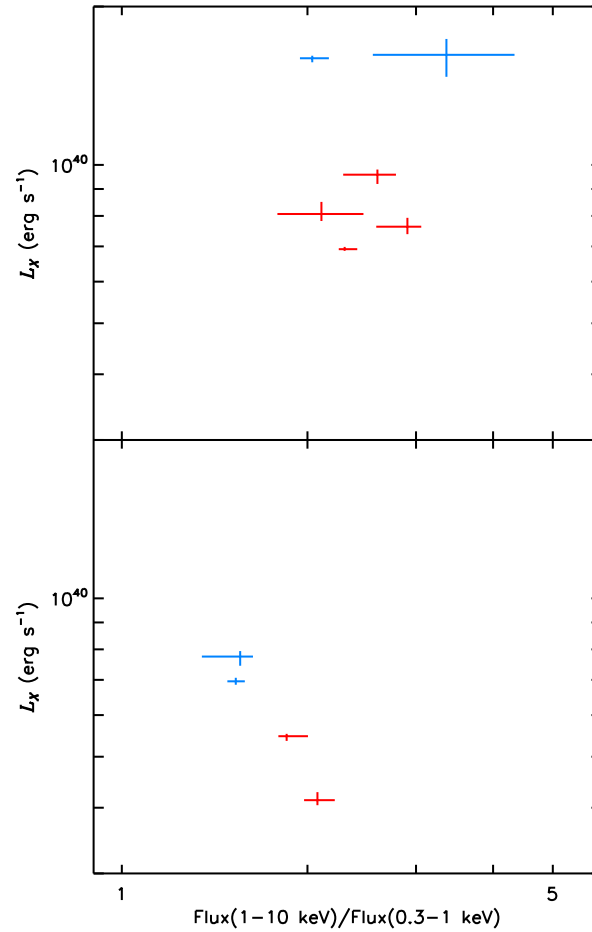
Figure 4.5: Hardness - luminosity diagrams, showing a sub-sample of the data from Figure 4.4 for two individual ULXs that are seen as both hard and soft ultraluminous sources; the sources are: (*top*) NGC 1313 X-1 and (*bottom*) NGC 5204 X-1. Again, colours represent the different ultraluminous state spectral regimes: red - hard ultraluminous and blue - soft ultraluminous.

the disc-like appearance of the strong spectral curvature in a highly optically-thick Comptonised spectrum (cf. the 'very thick' spectral interpretation of NGC 1313 X-1 and X-2 by Pintore & Zampieri 2012). Again, this highlights the issue in disentangling broadened discs and strongly Comptonised hard ultraluminous regime spectra.

Both hard and soft ultraluminous spectra were identified in observations of NGC 1313 X-1, NGC 5204 X-1 and NGC 6946 X-1. In the case of NGC 6946 X-1, the location of the two spectral types on the hardness - luminosity diagram appeared to be rather degenerate. In this case, we suggest that this was unlikely to be due to a real change in the spectral regime, as the spectral indices in the MCD plus power-law fits to NGC 6946 X-1 were all very close to the value of 2 used to separate the states. However, the hard ultraluminous and soft ultraluminous states in NGC 1313 X-1 and NGC 5204 X-1 do appear to clearly occupy distinct regions of hardness-luminosity space (Figure 4.5); and, the soft ultraluminous spectra were only seen to occur at greater X-ray luminosities than the hard ultraluminous spectra. Such spectral behaviour as observed in these two ULXs would seem to be consistent with the X-ray luminosity - spectral regime progression as originally suggested by Gladstone et al. (2009).

4.3.4   Short-term X-ray timing analysis

In addition to the spectral analysis detailed above, we also carried out some basic timing analysis using the diagnostic of fractional variability. Fractional variability and the associated errors were calculated following the prescription of Vaughan et al. (2003); it should be noted that this does not account for the effects of intrinsic scattering in the red noise, although Vaughan et al. state that differences in a fractional variability spectrum that are significantly larger than the estimated uncertainty would indicate achromatic variability. The main motivation behind this analysis was to provide an additional diagnostic of the spectral state, by e.g. checking

for multiple variability components, and to test for consistency with the ultraluminous spectral progression suggested by Gladstone et al. (2009). In addition to the full-band (0.3–10 keV) fractional variability, we also calculated values using the energy resolved light curves in a soft (0.3–1 keV) and hard (1–10 keV) energy band. Ideally we wanted to approximate the relative variability contributions from each of the components in the two component spectrum, but it is not possible to do this precisely, as the components overlap in energy and do not occur over the same energy range in all observations; however, whilst the detection of significantly different hard and soft fractional variabilities would not completely rule out single component spectral models (see e.g., Gierliński & Zdziarski 2005), it could provide a flag for a likely two component spectrum with different levels of variability in each component.

To calculate fractional variability, we extracted light curves in each of the three energy bands; these were extracted with 200s temporal binning, allowing us to probe variability on time scales from the corresponding Nyquist frequency up to the full available good time in each observation. The resulting values of fractional variability are shown in Appendix A (Table A.2), and similarly to the hardness-luminosity diagram (Figure 4.4) above, we show the full-band fractional variabilities of ULX observations of each spectral type, plotted against spectral hardness (Figure 4.6; *top*).

A range of variability behaviours were detected, and whilst many were consistent with upper limits of only a few per cent fractional variability (cf. Heil et al. 2009), this was not the case for all observations. Variability was detected in all three spectral classes of ULXs, although it was rather weak in the hard ultraluminous observations, where it was limited to at most ~ 10 per cent. However, some soft ultraluminous observations were much more variable, having full-band fractional variabilities of up to ~ 30 per cent; there were also a few highly variable detections (up to ~ 40 per cent) of disc-like ULXs: observations 0125960101 and 0152020101 of NGC 253 XMM2, plus observation 0404980101 of NGC 4736 ULX1 were all inconsistent (at

greater than 3σ significance) with having less than 10 per cent 0.3–10 keV fractional variability.

The high levels of variability in some of the soft ultraluminous observations were even more pronounced in the hard-band (Figure 4.6; *bottom*). Indeed, when we compare the fractional variabilities in the hard and soft energy bands (Figure 4.7), it was evident that most of the variability detected in these soft ULXs was actually seen in the emission from the hard component. Intriguingly, the high levels of variability in the hard emission were not always present in the soft ultraluminous observations, rather they seem to be transient. For example, of the 3 observations of Ho II X-1, all of which were classified as having soft ultraluminous spectra, only 1 showed strong hard variability (F_{var}(1–10 keV)$= 21.2 \pm 0.8$ per cent; compared to < 3 and 3.1 ± 0.7 per cent). There were a few ULXs with soft ultraluminous observations in which we did not detect strong variability, these were NGC 1313 X-1, NGC 4559 ULX2 and NGC 5204 X-1 (plus IC 342 X-2; although the identification of a soft ultraluminous spectrum in this source is highly questionable). However, each of these sources was only observed with a soft ultraluminous spectrum in at most 2 epochs, and so had only limited opportunities for the possibly transient variability to be detected.

4.4 Discussion

We have presented results from an X-ray spectral and timing analysis of a ULX sample, based on the highest quality available archival *XMM-Newton* data. Now we attempt to interpret these results, with particular reference to the framework of suggested spectral progression in the super-Eddington ultraluminous state. We begin by discussing the X-ray properties seen in the sample, before attempting to interpret them in terms of models of super-Eddington accretion.
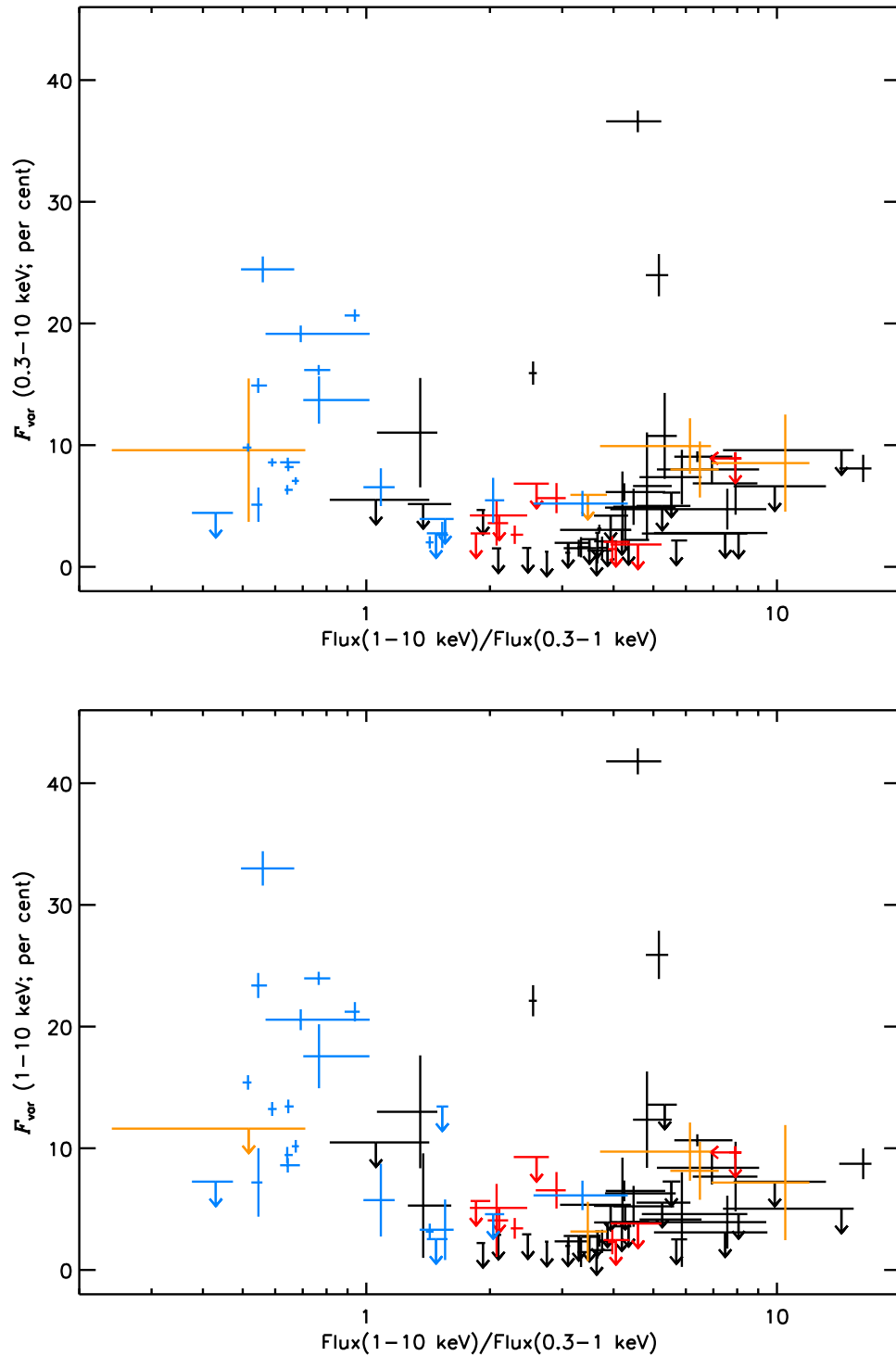
Figure 4.6: Full-band (*top*; 0.3–10 keV) and hard-band (*bottom*; 1–10 keV) fractional variability of the ULX sample plotted against spectral hardness. Fractional variability was calculated from light curves binned to 200s. Errors and limits shown are at the 1σ level. The colours correspond to the three ultraluminous spectral regimes, as per previous figures: broadened discs in black, hard ultraluminous in red and soft ultraluminous in blue. Only observations with a firm spectral classification are shown. Also, any highly absorbed observations (with 1σ upper limits of $N_{\mathrm{H}} \geq 0.5 \times 10^{22}$ cm^{-2}) are shown in orange, as the classification scheme is less reliable in highly absorbed sources.
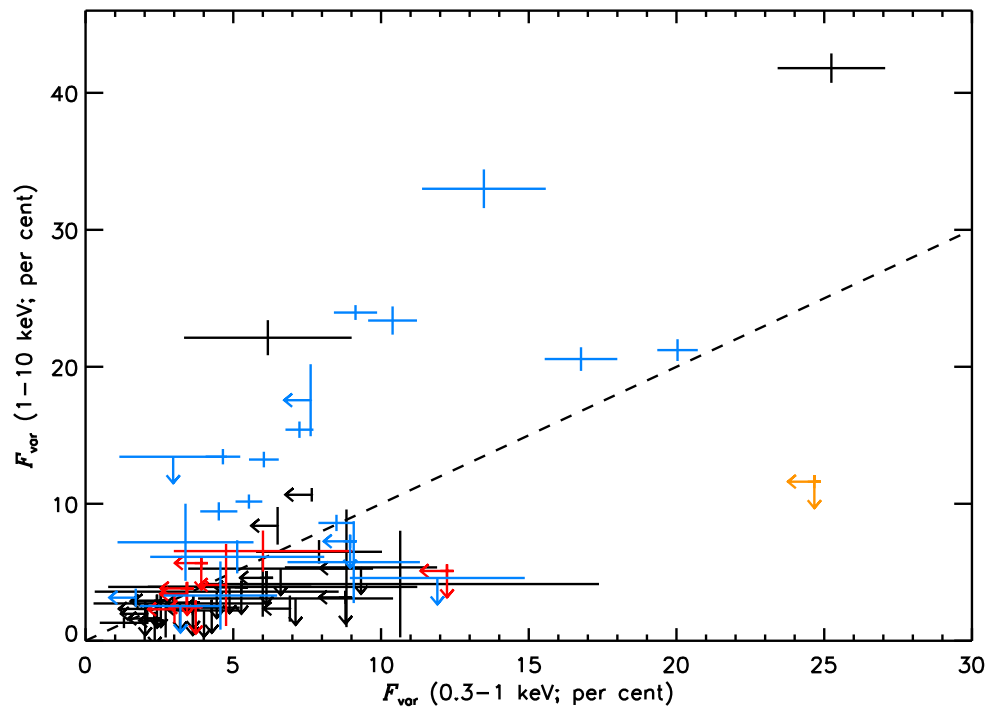
Figure 4.7: Hard-band (1–10 keV) fractional variability plotted against soft-band (0.3–1 keV) fractional variability for the ULX sample. The dashed line corresponds to equal values of fractional variability in each of the energy bands. Fractional variabilities were calculated from light curves with 200s temporal binning in both energy bands. The errors and limits shown are the 1σ uncertainty limits, and the colours correspond to the spectral regimes, as per the previous figures.

4.4.1 Interpreting the X-ray spectral and timing properties of the ULX sample

Below $\sim 3 \times 10^{39}$ erg s^{-1} the ULX population is dominated by observations with broadened disc-like spectra. Critically, this dominant population is consistent with the suggestion from the Gladstone et al. (2009) that these sources represent accretion rates at around the Eddington limit, with the luminosity limit strongly suggestive of accretion onto sMBHs of $\lesssim 20~M_\odot$. However, disc-like spectra are also observed at higher X-ray luminosities in three objects (NGC 1313 X-2, M81 X-6 and NGC 4190 ULX1), up to $\sim 10^{40}$ erg s^{-1}. If these sources are indeed powered by $\sim$ Eddington rate accretion, as the population of less-luminous disc-like ULXs implies, then we are either overestimating the distance to these brighter sources, they have a higher degree of beaming than the fainter disc-like sources, or – most interestingly – we may be observing the effects of $\sim$ Eddington rate accretion onto the larger MsBHs. However, it is pertinent here to again note the difficulty in distinguishing between hard ultraluminous spectra with pronounced curvature and broadened disc spectra. Given the position of these objects at the harder end of the ultraluminous regime objects in the hardness-intensity diagram, and that other ULXs observed at these luminosities appear in the super-Eddington hard ultraluminous or soft ultraluminous regimes, then the mis-identification of strongly Comptonised spectra with little or no soft excess as a broadened disc should be seriously considered. So, if the apparently disc-like ULXs above $\sim 3 \times 10^{39}$ erg s^{-1} intrinsically have hard ultraluminous spectra then MsBHs are not required in ULXs below $\sim 2 \times 10^{40}$ erg s^{-1}, and most of at least this sample of ULXs can then be produced solely by $\sim$ Eddington and super-Eddington accretion on to sMBHs. Clearly, future work to break this degeneracy in the classification scheme is of particular importance.

There are a number of issues in interpreting the broadened-disc ULXs as standard accretion discs. Not only are they broadened, such that it can be demonstrated that

they are not well fit by standard models of disc emission (c.f. Gladstone et al. 2009; Middleton et al. 2011b; Middleton et al. 2012), a few were also highly variable. This was the case in two observations of NGC 253 XMM2 and one of NGC 4736 ULX1. There were sufficient statistics in one observation of each source to extract a value of fractional variability in both the soft and hard energy bands; and, in each of these cases the light curve of the hard-band was significantly more variable than the soft-band, as is the case in the soft ultraluminous sources. If these are indeed disc spectra, then the possible origin of the variability is unclear; and it would seemingly rule out slim disc models. Rather, the variability properties would suggest that these spectra require a two component solution, in which case the broadened disc ULXs may actually be an emerging hard/soft ultraluminous spectrum. Indeed, it has been shown that M31 ULX1 (Kaur et al. 2012; Middleton et al. 2012) and M33 X-8 (Middleton et al. 2011b), whilst both disc-like in appearance, are instead better explained as emerging two component hard/soft ultraluminous-like spectra.

The hard and soft ultraluminous regime detections are almost exclusively brighter than $\sim 3 \times 10^{39}$ erg s^{-1}. In the absence of a highly contrived distribution of black hole masses with these spectral types only occurring around more massive black holes, the lack of fainter sources in either state implies that they must be occurring at luminosities well in excess of the Eddington limit. Although both the hard and soft ultraluminous regimes are seen to occur over a similar range of X-ray luminosities, the similarities end there. The hard ultraluminous spectra tend to be spectrally harder than the soft ultraluminous spectra, although this is not particularly surprising given that we differentiate between the two states based on the hardness of a power-law tail. Less trivial to explain is the difference in variability properties between the two states: variability in the hard ultraluminous state is rather weak and does not appear to exceed ~ 10 per cent in any individual object (and is much lower in most), whilst much stronger variability is seen in a number of the soft ultraluminous observations. The differing variability properties support the distinctions made by our spectral

classification system, but more importantly the nature of the variability can give us vital clues to the processes involved. Whilst Gladstone et al. (2009) argue that the progression to a soft ultraluminous state is characterised by the onset of a dominant spectral contribution from a soft wind, the emergent variability was observed to peak instead in the hard band. Such energy dependent variability seems to confirm that the spectral solution must also be at least two component in nature; but it is not obvious how this could be produced using reflection models, or the accretion rate driven spectral progression originally suggested by Gladstone et al. (2009). In the latter case, the optically-thick corona covering the inner disc would have to conspire to become variable in some (but not all) epochs, at around the same accretion rate that a strong wind begins to dominate the energy spectrum. This does not appear plausible. Instead, a mechanism by which ULXs with a soft ultraluminous spectrum display intermittent, strong variability of the hard component is required.

4.4.2   A unified model of ULX accretion

From the available evidence presented above, it seems clear that the X-ray spectral and timing characteristics of ULXs in the hard ultraluminous and soft ultraluminous regimes cannot be uniquely determined by accretion rate alone. Rather, we suggest that the key implication of this study is that it favours a model in which both regimes are produced in a single type of system, with the observed characteristics of the source being dependent on both accretion rate and – critically – the inclination of the ULX system (cf. Poutanen et al. 2007). The required angular dependence can naturally be introduced into the ULX system by the presence of a massive outflowing, radiatively driven wind. Such a wind is expected to occur at super-Eddington accretion rates (Poutanen et al. 2007; Dotan & Shaviv 2011; Ohsuga & Mineshige 2011), indeed the super-critical accretion flow simulations of Kawashima et al. (2012) produce such a wind, and find that it takes the form of a funnel. Then, when we

observe the ULX system face-on, we see down the funnel and observe emission from the innermost regions (that have a hard, cool corona/hot disc spectrum); however, at inclinations closer to the funnel opening angle, a much softer spectrum from the wind's photosphere is observed. So, at inclination angles between these, the ULX would appear with a shifting balance in the relative flux contributed from either component. In this model, the observed association between a soft spectrum and potential variability can also be achieved, if the variability can only occur at particular observation angles where the balance of component fluxes has shifted towards the wind. This is the case if the edge of the wind is clumpy in nature (cf. Middleton et al. 2011a; Takeuchi et al. 2013); then, at angles where the wind's edge intersects the line-of-sight to the central source, the clumpiness can result in variable obscuration of the hard emission region, thus extrinsically imprinting the observed, predominantly hard variability.

We argue that a unified ultraluminous state model can produce the spectral timing and properties seen in a large sample of ULXs, but for this model to be believable it is also essential that it can predict the spectral progression within individual sources. It has been predicted that an increase in the accretion rate onto a ULX would result in a narrowing of the wind's opening angle (King, 2008), thus shifting the emission from the various components relative to a fixed line-of-sight. Then, a ULX could potentially transit from the hard ultraluminous state to the soft ultraluminous state with increasing accretion rate, as the wind shifts towards the observer's line-of-sight. Indeed, we observe such a spectral change in both NGC 1313 X-1 and NGC 5204 X-1. Further, we would expect to see the onset of the characteristic hard variability as the accretion rate increases still further, and the clumpy edge of the wind enters the line-of-sight; future observations of a ULX progressing through the hard ultraluminous, invariable soft ultraluminous and variable soft ultraluminous regimes could provide a strong test of this model.

The wind itself is expected to be highly ionised; we might expect to see signatures

of this in the form of absorption features in ULX spectra. Walton et al. (2012) attempted to detect these using the stacked *XMM-Newton* spectra of NGC 1313 X-1 and Ho IX X-1, but found no evidence of absorption lines. However, both of these ULXs have been predominantly observed with hard ultraluminous spectra, which this work argues are likely to have clear lines-of-sight to the central emission regions, so no absorption from material in the wind is expected. Instead, the model favoured here would predict the detection of the imprint of wind absorption in soft ultraluminous ULXs; this may occur in the higher energy spectrum from the central region, or possibly across the full *XMM-Newton* band-pass if the emission from the wind is self-absorbed by the outflowing turbulent material as it becomes more diffuse and optically thin further from the source. Thus, these ULXs may display some observational similarities to high mass X-ray binaries, that are seen through columns of $> 10^{23}$ cm^{-2} of ionised stellar wind (e.g. Torrejón et al. 2010). We will revisit this in future work (Middleton et al. in prep.).

It is also interesting to consider the multi-wavelength properties of ULXs in each regime. Radio nebulae have been identified around two ULXs in the soft ultraluminous state - Ho II X-1 and NGC 5408 X-1 (Kaaret et al. 2003; Miller et al. 2005; Soria et al. 2006; Lang et al. 2007). However, radio nebulae are not a unique feature of the soft ultraluminous state, one is also observed around IC 342 X-1 (Cseh et al., 2012), which is in the hard ultraluminous state; if these nebulae are inflated by disc winds, then it may further support the argument that the distinction between hard and soft ultraluminous spectra is largely due to inclination.

4.5 Conclusions

We have presented results from an *XMM-Newton* spectral and timing study of a sample of 20 ULXs with some of the highest quality X-ray data available. Using a new classification scheme, we separated the ULXs into three spectral types based

on the results of Gladstone et al. (2009). A number of trends were identified in the spectral and timing properties of the sample, which we interpret in terms of a physical model.

• Below $\sim 3 \times 10^{39}$ erg s^{-1} the ULX population is dominated by broadened disc spectra. This is consistent with a population of sMBHs ($M \lesssim 20 M_\odot$) accreting at close to, and just above, the Eddington limit. We therefore suggest that the broadened disc ULXs bridge the luminosity gap between the standard sub-Eddington black hole binaries, and the super-Eddington ULXs with more extreme spectra. Hence, the brighter ULXs that display mainly hard ultraluminous and soft ultraluminous spectra must be at super-Eddington luminosities.

• A few broadened disc ULXs were seen at higher X-ray luminosities. Rather excitingly, these could be powered by accretion onto larger black hole primaries (MsBHs). However, more mundane explanations such as higher beaming factors cannot be discounted. Alternatively, they may be misclassified objects; a hard ultraluminous spectrum with little soft excess could readily be confused with a broadened disc, in which case typical sMBHs may be sufficient to produce the entire population of ULXs up to $\sim 2 \times 10^{40}$ erg s^{-1}.

• Interestingly, a few broadened disc ULXs display strong variability. Instead of being intrinsically disc-like, this suggests that broadened discs may in fact be emerging two-component hard/soft ultraluminous spectra.

• The brighter hard ultraluminous and soft ultraluminous ULXs differ by definition in spectral hardness, but crucially also differ in their variability properties. Low levels of variability are seen in the hard ultraluminous state (fractional variability $\ll 10$ per cent), whilst some soft ultraluminous observations are highly variable (10–30 percent fractional variability), with the variability being strongest in the higher energy part of the spectrum (> 1 keV).

• The observed X-ray properties can be achieved in a model with a funnel shaped wind, as is expected to emerge in super-Eddington sources. Viewed down the open-

ing angle of the wind we observe hard emission from the central source, and so a geometrically-beamed hard ultraluminous spectrum. At higher inclinations to our line-of-sight a wind-dominated soft ultraluminous spectrum is seen.

• In this model, the observed hard variability in spectrally soft sources originates from the changing obscuration of the hard central emission when observed through the clumpy edge of the out-flowing wind.

• If, as predicted, the opening angle of the wind narrows with increasing accretion rate, the observed spectrum can change from hard ultraluminous to soft ultraluminous at higher X-ray luminosities. This is the behaviour we see in NGC 1313 X-1 and NGC 5204 X-1.

This model is predicated on both theory and observation, and goes a long way towards unifying and explaining the X-ray characteristics of ULXs known to us from the best quality data available. But, as with any model, it requires further testing to confirm our current understanding, and develop deeper knowledge. We suggest that the key to this will be obtaining more high quality ULX observations that constrain the spectral and timing properties of ULXs to high precision, particularly in objects that are seen to transit between different spectral regimes. However, until such observations are taken, the data presented in this paper is suggesting to us that the properties of ULXs may be explained solely by a population of sMBHs, with their different observational characteristics dependent upon two variables: their accretion rate, and their inclination angle to our line-of-sight.

Chapter 5

Irradiated, colour-temperature-corrected discs in ultraluminous X-ray sources

We report results from a combined X-ray and optical spectral study of a sample of ULXs, which were selected for having broadened disc-like X-ray spectra, and known optical counterparts. Whilst attempts have been made to constrain the stellar types of optical counterparts to ULXs, the detection of optical variability instead suggests that they may be dominated by reprocessed emission from X-rays which irradiate the outer accretion disc. Here, we simultaneously fit optical and X-ray data from ULXs with a new spectral model of emission from an irradiated, colour-temperature-corrected accretion disc around a black hole, with a central Comptonising corona. We find that the ULXs require reprocessing fractions of $\sim 10^{-3}$, which is similar to sub-Eddington high/soft state BHBs, but less than has been reported for ULXs with soft ultraluminous X-ray spectra. We suggest that the reprocessing fraction may be due to the opposing affects of self-shielding in a convex super-critical accretion disc, and reflection from far above the central black hole by optically thin material ejected in a natal super-Eddington wind. Then, the higher reprocessing fractions reported for ULXs with wind-dominated X-ray spectra may be due to the stronger wind.

5.1 Introduction

In order to produce their observed X-ray luminosities, black holes in ULXs must have a large reservoir of mass to accrete from. If they are stellar remnant black holes in binary systems, then they must have companion stars with initial masses of $\gtrsim$ 10 $M_\odot$ (Rappaport et al., 2005). Previously, attempts have been made to constrain the spectral-type of the companion star to ULXs using the surrounding stellar population, or the colours of the companion itself, where one is detected. Indeed, young (OB) stellar clusters appear to be associated with a number of ULXs, e.g. stellar clusters with ages $\sim$ 5 Myr for NGC 5408 X-1 (Grisé et al., 2012) and $\leq$ 6 Myr for ULXs in the Antennae galaxies (Poutanen et al., 2013), which implies the presence of massive stellar companions in ULXs. However, this is not always the case, for example Feng & Kaaret (2008) found that the region around IC 342 X-1 lacked O stars, and was slightly older (at least $\sim$ 10 Myr); and, Yang et al. (2011) found that the stellar population around NGC 1313 X-1 was at least 30 Myr old, and lacked blue stars or young clusters. Point-like optical counterparts have been identified for a number of ULXs (Goad et al. 2002; Liu et al. 2002; Kaaret et al. 2004; Liu et al. 2004; Soria et al. 2005; Kuntz et al. 2005; Mucciarelli et al. 2005; Liu et al. 2007; Grisé et al. 2008; Rosado et al. 2008; Grisé et al. 2011; Gladstone et al. 2013), many of which are blue in colour, and appear to be consistent with large early-type companions; although many of the potential counterparts to ULXs in the sample of Gladstone et al. (2013) have colours which are not consistent with O-type identifications. However, Rappaport et al. (2005) caution that the outer regions of the accretion disc may also contribute optical flux, and that the optical light from the donor star in a ULX may be considerably less than would usually be expected for a non-donor star of the same initial mass, especially if mass transfer began early in its life.

In Galactic BHBs the X-ray flux from the inner source irradiates, and is repro-

cessed in the outer regions of the accretion disc, which can dominate the spectrum at optical wavelengths (Gierliński et al., 2009). The detection of stochastic variability superimposed onto the optical light curves of ULXs, most notably NGC 1313 X-2 (Grisé et al. 2008; Liu et al. 2009; Impiombato et al. 2011), indicates that this process may be occurring in ULXs, and if so, it is evidence that emission from an irradiated disc can strongly contribute to, and may even dominate the optical flux in some ULXs. However, one caveat is that the optical emission from the outer accretion disc in a ULX would be blue in colour, thus making it difficult to differentiate between it and flux from a young star based on optical colours. Further evidence that the optical flux may be dominated by disc reprocessing comes from the optical colours, variability and X-ray to optical flux ratios of some ULXs in the sample of Tao et al. (2011); and variable broad optical lines in NGC 1313 X-2 and Ho IX X-1, where the breadth of the lines indicate that the accretion discs must be close to face on (Roberts et al., 2011). Searches for associated X-ray and optical variability could be used as a test for disc irradiation, as fluctuations in X-ray emission would be expected to affect the flux which irradiates the disc; although no current studies do this, and the required multiple epochs of simultaneous optical and X-ray observations would be difficult to schedule, and would require a large amount of total observing time. Despite this, irradiated discs (DISKIR; Gierliński et al. 2008; Gierliński et al. 2009) have been successfully used to model the broadband X-ray and optical spectra of a number of ULXs, and these predict that a few per cent of the bolometric luminosity irradiates, and is reprocessed in the outer accretion disc; e.g. 0.03 and 0.015 of the bolometric luminosity is reprocessed in the outer disc in NGC 5408 X-1 and NGC 6946 X-1 respectively (Grisé et al. 2012; Berghea & Dudik 2012)[1]. These values are much higher than the irradiating fractions of $\sim 10^{-3}$ seen in high/soft

---

[1]An irradiated fraction of $\sim 2 \times 10^{-3}$ is reported in ESO 243-49 HLX-1 (Soria et al., 2012), although this source is arguably poor comparator to the bulk of the ULX population, as it remains a good IMBH candidate.

state Galactic BHBs (Gierliński et al., 2009). Kaaret & Corbel (2009) argue that such high reprocessing fractions rule out super-Eddington solutions in ULXs: slim discs are thought to have a convex shape, which would result in self shielding in the disc; and in models invoking winds, they argue that the outer regions of the ULX do not see the central hard emission, rather they are only irradiated by soft photons from the outflow, which would not thermalise in the disc. However, if a fraction of hard inner disc/coronal emission can be scattered by optically thin material in the wind much further from the ULX, then it may irradiate and thermalise in the outer regions of the accretion disc.

One limitation of the DISKIR model is that it does not include a colour-temperature-correction (Done et al., 2012). In this chapter we use a new spectral model of emission from an irradiated, colour-temperature-corrected disc, with a central corona, to model the X-ray and optical data from several ULXs which were classified as broadened discs in Chapter 4.

5.2 A new spectral model of an irradiated accretion disc with a colour-temperature-correction

Here, we use a new model of emission from black hole accretion to fit the X-ray and optical data from a ULX sample. The new model - OPTXAGNIR - combines the colour-temperature-corrected accretion disc and energetically coupled corona of OPTXAGNF (Done et al., 2012) with an irradiated disc, as in DISKIR (Gierliński et al., 2008). DISKIR models illumination of the outer disc by emission from the central disc and Compton tail. A fraction of the bolometric luminosity from the disc is thermalised to the local black body temperature at each radius, and contributes strongly to the UV and optical flux. However, DISKIR uses a multi-colour-disc prescription for the illuminating spectrum, and it neglects any colour-temperature-correction in the

intrinsic disc emission. OPTXAGNF (Done et al., 2012) is intended to model AGN spectra, it approximates a colour temperature corrected accretion disc spectrum, and energetically self-consistently includes both a soft excess and high energy tail. This is calculated by assuming that radiation within a given radius does not thermalise, but is distributed between a power-law and Comptonised component.

OPTXAGNIR modifies the OPTXAGNF model to include irradiation of the outer disc by assuming that the disc is illuminated by a flux of $L_{\mathrm{bol}}/4\pi r^2$, a fraction of which ($f_{\mathrm{out}}$) is reprocessed by the disc. The value of f_{out} depends on the geometry of the system, the albedo of the disc and the fraction of the non-reflected emission that is thermalised in the disc (Gierliński et al., 2008). In addition to f_{out}, OPTXAGNIR has all of the parameters of OPTXAGNF: black hole mass, distance from the observer, Eddington ratio, black hole spin, the radius of the corona, the outer disc radius, the electron temperature and optical depth of the soft Comptonisation component, the spectral index of the power-law, the fraction of the emission below the coronal radius that is in the power-law, the redshift and normalisation. A number of these parameters are not relevant to ULXs, and when fitting the model to ULX spectra we make a number of approximations: given the proximity of these sources, we set the redshift to 0; we fix the distance to that of the ULX host galaxy; and, we set the flux in the hard power-law to zero, as such a component has not been detected in ULX spectra, instead all of the power below the coronal radius is in a cool Comptonised corona. The model results in degeneracies in black hole spin, so we approximate the ULXs as having zero spin. Finally, we fix the model normalisation to 2 instead of 1, as is typically used for the OPTXAGNF model (Done et al., 2012); this is appropriate for a face-on accretion disc, and differs by a factor ~ 2 from an inclination of 60 degrees. We show examples of spectra from the OPTXAGNIR model for 10 and 30 $M_\odot$ black holes in Figure 5.1.
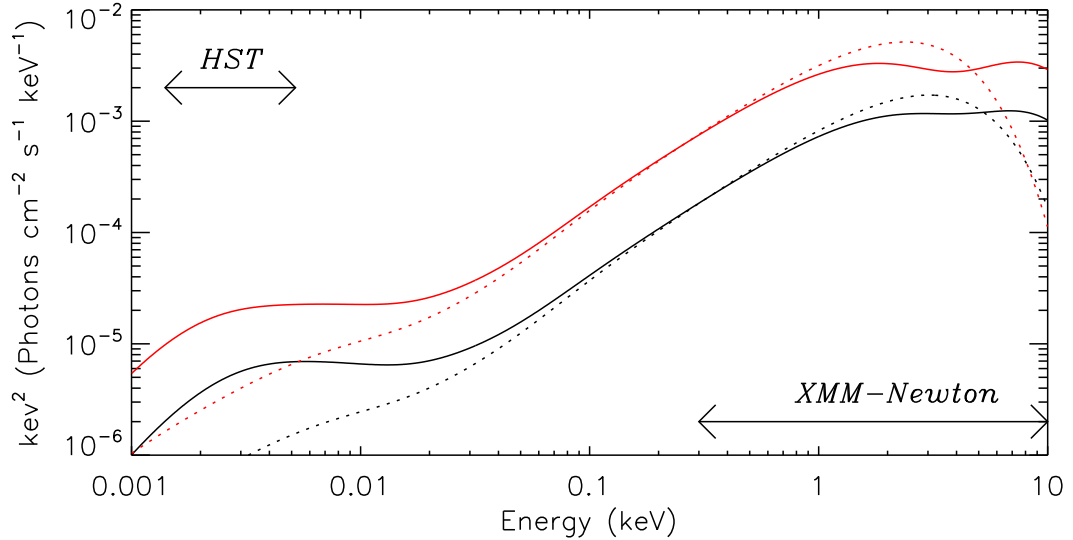
Figure 5.1: Examples of model broad-band unabsorbed ULX spectra from the OP-TXAGNIR spectral model, for a 10 (black) and 30 (red) $M_\odot$ black hole at 3 Mpc distance from the observer, with log $L/L_{\mathrm{Edd}} = 0.3$ and log $r_{\mathrm{out}} = 6$. The solid lines show spectra for ULXs with an optically-thick corona ($r_{\mathrm{cor}} = 25$, $\tau = 20$, $kT_{\mathrm{e}} = 2$), and a reprocessing fraction of $f_{\mathrm{out}} = 10^{-3}$; the dashed lines show the intrinsic colour-temperature-corrected disc spectra, with no corona or reprocessing in the outer disc; and, the two double sided arrows show the approximate energy ranges of the *HST* and *XMM-Newton* data analysed in this chapter.

5.3 Sample selection & data reduction

5.3.1 Sample selection

For this study, our principle requirement was for a sample of ULXs that had been observed at both X-ray and optical/ultraviolet wavelengths. Also, since the modified OPTXAGNF spectral model does not include any contribution to the X-ray emission from a radiatively driven wind, such as is expected to arise at super-Eddington accretion rates (Poutanen et al., 2007), we further restricted the selection of ULXs to those with disc-like X-ray spectra, which we expect to be accreting at $\sim$ the Eddington limit. To meet these criteria, we selected all of the ULXs identified with 'broadened

Table 5.1: ULX sample

Source name	2XMM/CXO ID	N_{H}[a]	Distance[b]
NGC 253 ULX2	2XMM J004732.9-251749	1.38	3.68^{i}
NGC 1313 X-2	2XMM J031822.1-663603	3.95	4.39^{ii}
NGC 2403 X-1	2XMM J073625.5+653540	4.17	3.50^{i}
M81 X-6	2XMM J095532.9+690034	4.22	4.27^{i}
NGC 4190 ULX1	CXO J121345.2+363754	1.62	3.47^{iii}

[a]Galactic column density in the direction of the ULX ($\times 10^{20}$ cm^{-2}), from Dickey & Lockman (1990). [b]Distance to the ULX host galaxy in Mpc, taken from: [i]Tully et al. (2009a); [ii]Jacobs et al. (2009); [iii]Tikhonov & Karachentsev (1998).

disc' spectra in Chapter 4 that also had optical counterparts identified by Gladstone et al. (2013) in *HST* HLA data. This resulted in a sample of 5 ULXs, details of which are shown in Table 5.1. For 4 of the 5 sources in the sample, Gladstone et al. (2013) identified only a single potential optical counterpart in the HLA images; the exception to this was NGC 1313 X-2, which had 2 potential counterparts. Here, we use only the counterpart to NGC 1313 X-2 previously identified by Liu et al. (2007), and confirmed by Grisé et al. (2008).

5.3.2 *XMM-Newton* data reduction

Having defined the sample, we then obtained all of the available *XMM-Newton* EPIC data from observations of the regions containing the 5 ULXs from the HEASARC data archive. All of the *XMM-Newton* observations included in this study are summarised in Table 5.3. The data were then reduced, and standard products extracted using *XMM-Newton* SAS(11.0.0). Firstly, high energy (10-15 keV) fullfield light curves were extracted using XMMSELECT with FLAG = 0 and PATTERN $\leq$ 4 or 12 for pn and MOS detections respectively. Several observations were excluded from further analysis as they contained high levels of solar flaring throughout the high energy light curves, these were: 0150280201 (NGC 1313 X-2), 0150280701 (NGC 1313 X-2), 0657801601 (M81 X-6). Of the remaining observations, the majority contained

Table 5.2: *HST* observation log

Date[a]	Instrument	Filter	Exposure time[b]	Magnitude[c]
NGC 253 ULX2				
2006-09-13	ACS-WFC	F475W	1482	21.7 ± 0.3
2006-09-13	ACS WFC	F606W	1508	20.8 ± 0.2
2006-09-13	ACS-WFC	F814W	1534	19.6 ± 0.2
NGC 1313 X-2				
2003-11-22	ACS-HRC	F330W	2760	21.6 ± 0.8
2003-11-22	ACS-WFC	F435W	2520	23.2 ± 0.4
2003-11-22	ACS-WFC	F555W	1160	23.4 ± 0.5
2003-11-22	ACS-WFC	F814W	1160	23.5 ± 0.6
NGC 2403 X-1				
2005-10-17	ACS-HRC	F330W	2912	23 ± 2
2005-10-17	ACS-WFC	F435W	1248	25 ± 1
2005-10-17	ACS-WFC	F606W	1248	24.5 ± 0.6
M81 X-6				
1995-01-31	WFPC2	F336W	1160	22 ± 2
2006-03-22	ACS-WFC	F435W	1200	23.7 ± 0.6
2001-06-04	WFPC2	F555W	8000	24 ± 2
2006-03-22	ACS-WFC	F606W	1200	23.8 ± 0.6
2001-06-04	WFPC2	F814W	8000	23 ± 2
NGC 4190 ULX1				
2008-01-07	WFPC2	F300W	4400	23.0 ± 0.3
2008-01-07	WFPC2	F450W	4400	24 ± 2
2008-01-08	WFPC2	F606W	1600	24 ± 2
2008-03-21	WFPC2	F814W	4400	25 ± 3

[a]Data of the *HST* observation (yyyy-mm-dd). [b]Exposure time of the *HST* observation in units of s. [c]Apparent Vega magnitude of the source corrected for Galactic reddening, taken from Gladstone et al. (2013).

periods of high background flaring[2], which were filtered out using GTI files created using TABGTIGEN. The exact filtering count rate varied between observations, to maximise the utilised data whilst avoiding flaring, but typical values were ~ 1.5 and ~ 0.6 ct s^{-1} for the pn and MOS detectors respectively.

For 4 of the 5 ULXs, source spectra were typically extracted from circular apertures with radii 30–50 arcseconds; however, for observations of NGC 253 ULX2 a neighbouring source necessitated a very small source region of 12.5 arcseconds. Also, in a few cases elliptical source regions were used when the source neighboured a detector chip gap. Background spectra were extracted from larger circular regions located at a similar distance from the read-out node as the source, on the same or a neighbouring chip in the same quadrant for pn detections, or on the same chip as the source for MOS detections. Source and background spectra were created using OGIP SPECTRAL PRODUCTS in XMMSELECT, with `FLAG` $= 0$ and `PATTERN` ≤ 4 or 12 for pn and MOS data respectively. Finally, the data were binned to a minimum of 20 counts per bin using the FTOOL GRPPHA.

5.3.3   *HST* magnitudes

HST magnitudes for the sample ULXs were taken from Gladstone et al. (2013). These were derived from an assortment of ACS-HRC, ACS-WFC and WFPC2 observations over a range of dates (see Table 5.2 for details). The Galactic-extinction-corrected Vega magnitudes (Table 4 of Gladstone et al. 2013) were converted into units of photons cm^{-2} s^{-1}. When converting the WFPC2 magnitudes we used values of zeropoints and `photflam` from the WFPC2 data handbook, along with filter wavelengths and bandwidths from the WFPC2 filters archive[3]. For the ACS data, we used zeropoints from Sirianni et al. (2005), as used by Gladstone et al. (2013), appropriate

---

[2]Exceptions to this were: all EPIC detectors in observations 0304850901, 0304851001, 0205230501 and 0112521001; the MOS1 and MOS2 detectors in observations 0304851201, 0205230301 and 0301860101; plus the pn detector in observation 0112521101.

[3]`http://www.stsci.edu/hst/wfpc2/documents/wfpc2_filters_archive.html`

Table 5.3: *XMM-Newton* observation log

Obs. ID[a]	Date[b]	Exposure time[c]	θ^d	$f_X{}^e$	flux group[f]
NGC 253 ULX2					
0125960101	2000-06-03	31.6/36.3/35.7	1.7	1.5	-
0125960201	2000-06-04	5.6/9.1/9.0	1.6	2.1	-
0110900101	2000-12-13	8.2/26.7/29.1	3.1	1.9	-
0152020101	2003-06-19	61.9/79.5/80.4	1.6	1.5	-
0304851101	2005-12-16	7.4/19.9/19.8	0.7	1.1	-
0304850901	2006-01-02	8.8/11.4/11.4	0.8	1.2	-
0304851001	2006-01-06	8.8/11.4/11.4	0.8	1.2	-
0304851201	2006-01-09	15.3/19.4/19.4	0.8	1.2	-
0304851301	2006-01-11	4.0/6.8/6.8/	0.8	1.2	-
NGC 1313 X-2					
0106860101	2000-10-17	18.8/27.1/26.9	5.4	0.8	low
0150280101	2003-11-25	1.3/2.5/2.5	1.0	2.0	high
0150280301	2003-12-21	7.5/10.1/10.2	1.0	3.4	high
0150280401	2003-12-23	3.2/5.4/5.7	1.0	3.9	high
0150280501	2003-12-25	2.3/8.5/8.7	1.0	1.7	low
0150280601	2004-01-08	7.2/11.2/11.4	1.0	1.1	low
0150281101	2004-01-16	3.3/7.2/7.3	1.1	1.0	low
0205230201	2004-05-01	-/7.7/8.0	1.3	0.8	low
0205230301	2004-06-05	8.8/11.5/11.5	1.3	4.0	high
0205230401	2004-08-23	4.4/10.6/10.7	1.1	0.8	low
0205230501	2004-11-23	12.5/15./15.5	1.0	0.9	low
0205230601	2005-02-07	8.7/11.9/11.9	1.1	3.9	high
0301860101	2006-03-06	17.4/21.3/21.3	6.2	3.6	high
0405090101	2006-10-15	80.0/105.3/105.4	5.4	3.4	high
NGC 2403 X-1					
0150651101	2003-04-30	-/5.6/5.7	1.7	1.2	-
0150651201	2003-09-11	-/5.1/5.4	3.8	1.3	-
0164560901	2004-09-12	51.2/70.6/72.6	5.4	1.2	-

[a]*XMM-Newton* observation identification number. [b]Date of the *XMM-Newton* observation (yyyy-mm-dd). [c]The amount of good time for each EPIC detector (pn/MOS1/MOS2) in units of ks. [d]Off-axis angle of the source in arcminutes. [e]Approximate observed 0.3-10 keV flux in units of $\times 10^{-12}$ erg cm^{-2} s^{-1}, calculated from an absorbed *p*-free disc model in XSPEC. The luminosity is calculated from the pn data were available, or the MOS1 data in observations with no pn detection. [f]The X-ray flux bin in which the observation was included for subsequent spectral fitting. Dashes are shown for sources in which flux binning was not used.

Table 5.3: continued

Obs. ID[a]	Date[b]	Exposure time[c]	θ[d]	f_X[e]	flux group[f]
		M81 X-6			
0111800101	2001-04-22	74.5/-/96.3	3.4	2.8	high
0112521001	2002-04-10	7.0/10.0/10.0	11.9	2.8	high
0112521101	2002-04-16	7.6/9.9/10.0	11.9	2.8	high
0200980101	2004-09-26	-/99.4/101.0	13.9	4.0	high
0657802001	2011-03-24	3.3/-/7.1	6.5	1.1	low
0657801801	2011-09-26	6.0/14.9/14.0	7.8	3.0	high
0657802201	2011-11-23	13.0/16.0/16.1	8.2	1.2	low
		NGC 4190 ULX1			
0654650101	2010-06-06	0.9/7.7/7.5	1.1	2.9	low
0654650201	2010-06-08	8.2/17.2/18.8	1.1	3.0	low
0654650301	2010-11-25	9.3/14.8/14.8	1.2	5.6	high

photflam and photplam values for the observation dates calculated with the *HST* ACS zeropoint calculator[4], and photbw from the *HST* ACS data analysis web page[5]. Having been converted into units of photons cm^{-2} s^{-1}, XSPEC readable spectra were created for each *HST* observation using the FTOOL FLX2XSP.

5.4 Data analysis

Having extracted the *XMM-Newton* EPIC spectra, and converted the *HST* magnitudes to an XSPEC readable format, the goal of the analysis was to simultaneously fit the X-ray and optical/infrared data with the new OPTXAGNIR spectral model. As several of the ULXs display some degree of X-ray flux variability, it was decided to flux bin the X-ray observations. However, the ULXs were not observed contemporaneously in each of the bands, so we do not know which X-ray flux corresponds to the *HST* epochs; so as a compromise, the *HST* data were simultaneously fitted with each flux bin of *XMM-Newton* data, and each possibility was assessed.

---

[4] http://www.stsci.edu/hst/acs/analysis/zeropoints/zpt.py
[5] http://www.stsci.edu/hst/acs/analysis/bandwidths

To flux bin the X-ray data an approximate flux was extracted from each observation using an absorbed p-free disc model – CONSTANT $\times$ TBABS $\times$ TBABS $\times$ DISKPBB in XSPEC 12.6.0. The p-free disc model allows a range of values for the exponent of the radial dependence of temperature p, with $p = 0.75$ being a standard multi-colour-disc, and $p < 0.75$ indicating advection; this allows for a broader spectrum, so is appropriate for approximating the flux in this ULX sample. A multiplicative constant was included in the spectral model, this was frozen to unity for the pn detector (or the MOS1 detector when no pn data was available), and free to vary for the other EPIC detectors to allow for calibration uncertainties between the detectors. TBABS and the Wilms et al. (2000) abundance table were used to model absorption in the X-ray spectrum; two such components were included, the first was fixed to account for the foreground Galactic column in the direction of the ULX, and the other left free to model any intrinsic absorption in the source and its host galaxy. $0.3 - 10$ keV fluxes were estimated for the pn data (or MOS1 when no pn data was available) using the FLUX command in XSPEC and are shown in Table 5.3. The *XMM-Newton* observations of each ULX were then grouped according to these fluxes: NGC 253 ULX2 and NGC 2403 X-1 varied by $\lesssim 1 \times 10^{-12}$ erg cm^{-2} s^{-1}, so a single flux group was used. Two flux groups were used for NGC 1313 X-2, M81 X-6 and NGC 4190 ULX1, these were: $\sim$ 1–2 and $\sim$ (2–4) $\times 10^{-12}$ erg cm^{-2} s^{-1} for NGC 1313 X-2 (which agrees with the classification by Pintore & Zampieri 2012, based on spectral parameters); $\sim$ 1 and $\sim$ (3–4) $\times 10^{-12}$ erg cm^{-2} s^{-1} for M81 X-6; $\sim$ 3 and $\sim$ 6 $\times 10^{-12}$ erg cm^{-2} s^{-1} for NGC 4190 ULX1.

The flux-grouped X-ray spectra were then fitted simultaneously with the *HST* data using XSPEC and an absorbed, irradiated, colour-temperature-corrected disc – CONSTANT $\times$ TBABS $\times$ TBABS $\times$ REDDEN $\times$ OPTXAGNIR. Again, a multiplicative constant was included to allow for calibration uncertainties between the EPIC detectors, and for slight variation in flux between the observations. The constant was set equal to unity for the channel corresponding to the pn detector in the earliest

observation in each flux group, and free for each of the other *XMM-Newton* data sets; whilst for the *HST* data, it was set to unity. The first absorption component was fixed to the Galactic column in the direction of the source, whilst the second was left free to model any intrinsic absorption in the ULX or host galaxy. The infrared/optical extinction (REDDEN) was linked to the extra-galactic X-ray absorption assuming $E(B - V) \approx 1.7 \times 10^{-22} N_H$ (Spitzer, 2004); Galactic extinction had already been corrected for in the magnitudes taken from Gladstone et al. (2013).

The initial spectral fits with all variables free (except for the assumptions described in section 5.2) were unable to place constraints on the fit parameters, so it was repeated with combinations of fixed black hole masses, outer disc radii, and ranges of the coronal radii. Two characteristic black hole masses were used, these corresponded both to a typical 10 $M_\odot$ sMBH and a 30 $M_\odot$ MsBH (Feng & Soria, 2011), and are consistent with the range of black hole masses thought to power the majority of ULXs (e.g. Chapter 3 & 4; Stobbart et al. 2006; Gladstone et al. 2009). The data were fitted with both an irradiated colour-temperature-corrected disc alone (i.e., with the coronal radius fixed to 6 r_g, and the electron temperature/optical depth frozen to arbitrary values, as the choice of coronal radius is such that there is no corona), and a disc plus Comptonising corona. An outer disc radius of 10^5 r_g (i.e. 1.5–4.5 $\times 10^{11}$ cm for a 10–30 $M_\odot$ black hole) is consistent with limits on the size of the disc implied by broad emission lines in the ULX NGC 5408 X-1 (Cseh et al., 2011). However, larger outer disc radii of $\sim 10^{12}$ cm have been implied for a number of ULXs based on irradiated disc models (NGC 1313 X-1, Yang et al. 2011; Ho II X-1, Tao et al. 2012; Ho IX X-1, Tao et al. 2011; NGC 5408, Grisé et al. 2012). In this case, an outer disc radius of $\sim 10^6$ r_g is appropriate (10^6 $r_g \approx (1.5$–$4.5)$ $\times 10^{12}$ cm for a 10–30 $M_\odot$ black hole). So, the ULX spectra were fitted using both fixed outer disc radii of 10^5 and 10^6 r_g.

5.5   Results

The results of the spectral fitting are shown in Tables 5.4 and 5.5, plus examples of the spectral models are shown in Figure 5.2 for the optical and low X-ray flux data from M81 X-6. Formally acceptable spectral fits (not rejected at 3σ significance) were found for each of the 5 ULXs, although it should be noted that the best fit to the NGC 253 ULX2 data would be rejected at greater than the 99 per cent significance level. For the 3 ULXs with 2 flux bins of X-ray data, the best fitting model was found for the high flux data in NGC 1313 X-2, and the low flux data in M81 X-6 and NGC 4190 ULX1. However, acceptable models were found for both sets of flux binned X-ray datasets in NGC 1313 X-2 and NGC 4190 ULX1, and we cannot distinguish which (or indeed, if any) of the flux binned X-ray data corresponds to each epoch of optical data, so we continue to consider both possibilities. Also, it should be noted that due to the relative amounts of *XMM-Newton* and *HST* data, the χ^2 statistic is heavily dominated by the X-ray data; so, the lack of an acceptable fit for the optical and high flux M81 X-6 X-ray data does not allow us to make conclusions about the unobserved X-ray spectrum during the optical observations, rather it simply indicates that the model was unable to reproduce the high flux X-ray spectrum.

In general, the inclusion of a Comptonised corona resulted in an improved fit to the data over a disc alone; further, in three of the ULXs (NGC 253 ULX2, NGC 1313 X-2 and M81 X-6) all spectral models without a corona are rejected at $> 3\sigma$ significance. Perhaps unsurprisingly given that these sources were identified as having broadened disc-like spectra in Chapter 4, a standard disc alone (i.e. no relativistic broadening and spin set to zero) is insufficient to reproduce the observed X-ray data. Similarly to other ULX X-ray spectral studies (e.g. Chapter 3; Dewangan et al. 2006; Goad et al. 2006; Stobbart et al. 2006; Gladstone et al. 2009), we found that the Comptonised coronae were generally cool and optically thick: the coronal parameters

Table 5.4: OPTXAGNIR fits with outer disc radius fixed at $10^5\ r_{\rm g}$

$N_{\rm H}{}^{a}$	Mass^{b}	$\log(L/L_{\rm Edd})^{c}$	$r_{\rm cor}{}^{d}$	$kT_{\rm e}{}^{e}$	τ^{f}	$f_{\rm out}{}^{g}$	$\chi^2/$d.o.f.^{h}
			NGC 253 ULX2				
0.236 ± 0.003	10	0.297 ± 0.006	6	-	-	$[3 \times 10^{-3}]$	$[4865.6/3092]$
0.206 ± 0.004	10	$0.200^{+0.008}_{-0.009}$	62 ± 8	1.26 ± 0.02	$14.9^{+0.5}_{-0.4}$	$[3 \times 10^{-3}]$	**3307.7/3089**
$[0.4]$	30	$[-0.1]$	6	-	-	$[2 \times 10^{-2}]$	$[13593.2/3092]$
$0.296^{+0.004}_{-0.002}$	30	$-0.241^{+0.008}_{-0.009}$	≥ 100	1.19 ± 0.01	14.7 ± 0.2	$\geq 1 \times 10^{-5}$	$[3394.8/3089]$
			NGC 1313 X-2				
			high X-ray flux				
0.122 ± 0.002	10	0.512 ± 0.007	6	-	-	$1.1^{+0.8}_{-0.5} \times 10^{-2}$	$[6009.4/4504]$
0.158 ± 0.003	10	0.30 ± 0.02	27 ± 2	1.49 ± 0.04	20^{+7}_{-3}	$[4 \times 10^{-3}]$	**4534.3/4501**
$[0.2]$	30	$[0.2]$	6	-	-	$[1 \times 10^{-2}]$	$[16307.6/4504]$
$0.246^{+0.002}_{-0.003}$	30	$-0.11^{+0.01}_{-0.02}$	≥ 100	$1.39^{+0.02}_{-0.01}$	12.0 ± 0.1	$3^{+12}_{-2} \times 10^{-2}$	$4666.7/4501$
			low X-ray flux				
$9 \pm 2 \times 10^{-3}$	10	-0.163 ± 0.007	6	-	-	$[9 \times 10^{3}]$	$[2544.2/1457]$
$8.5^{+0.4}_{-0.3} \times 10^{-2}$	10	0.29 ± 0.02	73 ± 3	≥ 7	4.3 ± 0.1	$[3 \times 10^{-3}]$	$[1790.7/1454]$
$[0.1]$	30	$[-0.6]$	6	-	-	$[7 \times 10^{-2}]$	$[3303.4/1457]$
$0.130^{+0.002}_{-0.004}$	30	$-0.46^{+0.02}_{-0.01}$	≥ 100	$2.6^{+0.6}_{-0.4}$	$5.3^{+0.6}_{-0.8}$	$6^{+13}_{-4} \times 10^{-2}$	$1602.4/1454$

Spectral parameters from TBABS $\times$ TBABS $\times$ REDDEN $\times$ OPTXAGNIR, with an outer radius of $10^5\ r_{\rm g}$. Errors and limits indicate the 1σ confidence regions. Parameters in square brackets are not constrained at the 1σ level by the model. ^{a}Extragalactic absorption column ($\times 10^{22}$ cm^{-2}). ^{b}Black hole mass ($M_\odot$), this was fixed to 2 characteristic values - 10 and 30 $M_\odot$. ^{c}Logarithm of the Eddington ratio. ^{d}Outer coronal radius ($r_{\rm g}$), this is fixed to 6 $r_{\rm g}$ in models with no corona. ^{e}Electron temperature of the Comptonised corona (keV). ^{f}Optical depth of the Comptonised corona. ^{g}Fraction of the flux from the central regions of the source that is reprocessed in the outer disc. ^{h}Goodness of fit in terms of $\chi^2/$degrees of freedom, values in bold indicate the statistical best fit for each source, whilst values in square brackets indicate fits which are rejected at 3σ signficance.

Table 5.4: continued

$N_H{}^a$	Mass^b	$\log(L/L_{Edd})^c$	$r_{cor}{}^d$	$kT_e{}^e$	τ^f	$f_{out}{}^g$	χ^2/d.o.f.^{h}
			NGC 2403 X-1				
$0.155^{+0.004}_{-0.005}$	10	-0.12 ± 0.01	6	-	-	$[8 \times 10^{-3}]$	1136.1/1009
0.161 ± 0.004	10	-0.16 ± 0.02	11.6 ± 0.6	$1.08^{+0.09}_{-0.06}$	≥ 30	$[1 \times 10^{-2}]$	1102.9/1006
[0.3]	30	[-0.4]	6	-	-	$[5 \times 10^{-2}]$	[2762.9/1009]
0.252 ± 0.007	30	-0.56 ± 0.02	40 ± 10	0.90 ± 0.02	16^{+3}_{-1}	$7^{+51}_{-6} \times 10^{-2}$	**1071.6/1006**
			M81 X-6				
			high X-ray flux				
$4.2 \pm 0.2 \times 10^{-2}$	10	0.401 ± 0.003	6	-	-	$[2 \times 10^{-3}]$	[2969.1/2436]
0.111 ± 0.002	10	0.417 ± 0.005	$10.6^{+0.4}_{-0.1}$	1.8 ± 0.1	≥ 30	$[2 \times 10^{-3}]$	[2905.8/2433]
[0.3]	30	[-0.8]	6	-	-	$[5 \times 10^{-2}]$	[8825.2/2436]
0.200 ± 0.003	30	$-4.5^{+0.3}_{-0.5} \times 10^{-2}$	62^{+8}_{-25}	1.11 ± 0.01	$15.0^{+0.7}_{-0.6}$	≤ 0.2	[2801.1/2433]
			low X-ray flux				
$4.0 \pm 0.6 \times 10^{-2}$	10	-0.12 ± 0.02	6	-	-	$[1 \times 10^{-2}]$	[485.1/279]
0.14 ± 0.01	10	0.35 ± 0.03	≥ 100	≥ 9	$4.1^{+0.5}_{-0.2}$	$[2 \times 10^{-3}]$	281.6/276
[0.1]	30	[-0.6]	6	-	-	$[7 \times 10^{-2}]$	[680.2/279]
$0.164^{+0.009}_{-0.008}$	30	-0.43 ± 0.02	25^{+10}_{-3}	$1.4^{+0.3}_{-0.1}$	≥ 10	≤ 0.4	**262.1/276**

Table 5.4: continued

$N_{\mathrm{H}}{}^a$	Mass^b	$\log(L/L_{\mathrm{Edd}})^c$	$r_{\mathrm{cor}}{}^d$	$kT_{\mathrm{e}}{}^e$	τ^f	$f_{\mathrm{out}}{}^g$	$\chi^2/\mathrm{d.o.f.}{}^h$
			NGC 4190 ULX1				
			high X-ray flux				
$5.8 \pm 0.3 \times 10^{-2}$	10	0.446 ± 0.003	6	-	-	$3^{+15}_{-2} \times 10^{-3}$	$[1163.6/920]$
$6.5 \pm 0.3 \times 10^{-2}$	10	0.494 ± 0.005	$19.1^{+2.8}_{-0.5}$	$1.56^{+0.08}_{-0.03}$	≥ 40	$3^{+14}_{-2} \times 10^{-3}$	$924.3/917$
$[0.2]$	30	$[-8 \times 10^{-2}]$	6	-	-	$[4 \times 10^{-2}]$	$[3548.4/920]$
0.140 ± 0.005	30	$2.5 \pm 0.5 \times 10^{-2}$	≥ 90	1.35 ± 0.03	$12.8^{+0.6}_{-0.2}$	$8^{+13}_{-4} \times 10^{-3}$	$963.6/917$
			low X-ray flux				
$4.9 \pm 0.3 \times 10^{-2}$	10	0.23 ± 0.01	6	-	-	$6^{+23}_{-4} \times 10^{-3}$	$863.8/845$
$5.2 \pm 0.3 \times 10^{-2}$	10	$0.190^{+0.003}_{-0.014}$	$13.9^{+0.9}_{-0.6}$	$1.15^{+0.03}_{-0.04}$	≥ 40	$6^{+25}_{-4} \times 10^{-3}$	**803.8/842**
$[0.2]$	30	$[-0.1]$	6	-	-	$[3 \times 10^{-2}]$	$[2488.6/845]$
$0.121^{+0.006}_{-0.005}$	30	-0.25 ± 0.02	≥ 60	1.03 ± 0.03	16 ± 1	$1.0^{+0.9}_{-0.5} \times 10^{-2}$	$806.1/842$

Table 5.5: OPTXAGNIR fits with outer disc radius fixed at 10^6 r_g

$N_H{}^a$	Mass^b	$\log(L/L_{Edd})^c$	$r_{cor}{}^d$	$kT_e{}^e$	τ^f	$f_{out}{}^g$	$\chi^2/$d.o.f.^{h}
			NGC 253 ULX2				
0.236 ± 0.003	10	0.297 ± 0.006	6	-	-	0.3 ± 0.2	[4848.4/3092]
0.206 ± 0.004	10	0.199 ± 0.007	62^{+10}_{-3}	$1.26^{+0.02}_{-0.01}$	$15.0^{+0.5}_{-0.4}$	$0.4^{+0.3}_{-0.2}$	**3288.7/3089**
[0.4]	30	[-0.1]	6	-	-	[1]	[13545.4/3092]
0.296 ± 0.004	30	-0.241 ± 0.009	≥ 100	1.19 ± 0.01	14.7 ± 0.2	≥ 0.6	[3340.3/3089]
			NGC 1313 X-2				
			high X-ray flux				
0.122 ± 0.002	10	0.512 ± 0.007	6	-	-	$1.1^{+0.8}_{-0.5} \times 10^{-2}$	[6009.4/4504]
0.158 ± 0.003	10	0.31 ± 0.02	27^{+3}_{-2}	1.48 ± 0.04	20^{+8}_{-3}	$3^{+2}_{-1} \times 10^{-2}$	**4518.8/4501**
[0.2]	30	[0.2]	6	-	-	$[2 \times 10^{-3}]$	[16300.3/4504]
0.246 ± 0.003	30	$-0.11^{+0.01}_{-0.02}$	≥ 100	$1.39^{+0.02}_{-0.01}$	12.0 ± 0.1	$4 \pm 2 \times 10^{-3}$	4660.0/4501
			low X-ray flux				
$9 \pm 2 \times 10^{-3}$	10	-0.163 ± 0.007	6	-	-	$1.9^{+1.0}_{-0.7} \times 10^{-2}$	[2528.7/1457]
$3.8 \pm 0.3 \times 10^{-2}$	10	-0.08 ± 0.02	≥ 100	$3.1^{+0.6}_{-0.8}$	$4.7^{+0.6}_{-0.8}$	$2.0^{+1.1}_{-0.8} \times 10^{-2}$	[1774.9/1454]
[0.1]	30	[-0.6]	6	-	-	$[7 \times 10^{-3}]$	[3297.6/1457]
0.129 ± 0.003	30	$-0.46^{+0.02}_{-0.01}$	≥ 100	$2.6^{+0.7}_{-0.4}$	$5.3^{+0.6}_{-0.7}$	$6^{+3}_{-2} \times 10^{-3}$	1595.9/1454

Spectral parameters from TBABS × TBABS × REDDEN × OPTXAGNIR, with an outer radius of 10^6 r_g. Errors and limits indicate the 1σ confidence regions. Parameters in square brackets are not constrained at the 1σ level by the model. ^{a}Extra-galactic absorption column ($\times 10^{22}$ cm^{-2}). ^{b}Black hole mass ($M_\odot$), this was fixed to 2 characteristic values - 10 and 30 $M_\odot$. ^{c}Logarithm of the Eddington ratio. ^{d}Outer coronal radius (r_g), this is fixed to 6 r_g in models with no corona. ^{e}Electron temperature of the Comptonised corona (keV). ^{f}Optical depth of the Comptonised corona. ^{g}Fraction of the flux from the central regions of the source that is reprocessed in the outer disc. ^{h}Goodness of fit in terms of $\chi^2/$degrees of freedom, values in bold indicate the statistical best fit for each source, whilst values in square brackets indicate fits which are rejected at 3σ signficance. ^{i}No fit parameters corresponding to a 10 $M_\odot$ black hole and a free corona are shown for the high flux X-ray data of M81 X-6, as this did not result in any improvement over a disc alone.

Table 5.5: continued

$N_{\mathrm{H}}{}^a$	Mass^b	$\log(L/L_{\mathrm{Edd}})^c$	$r_{\mathrm{cor}}{}^d$	$kT_{\mathrm{e}}{}^e$	τ^f	$f_{\mathrm{out}}{}^g$	$\chi^2/\mathrm{d.o.f.}^h$
NGC 2403 X-1							
$0.155^{+0.005}_{-0.004}$	10	-0.11 ± 0.01	6	-	-	$3 \pm 2 \times 10^{-3}$	1132.3/1009
0.161 ± 0.005	10	-0.16 ± 0.02	$10.9^{+0.7}_{-0.6}$	$1.09^{+0.08}_{-0.07}$	≥ 30	$4^{+3}_{-2} \times 10^{-3}$	1099.1/1006
$[0.3]$	30	$[-0.4]$	6	-	-	$[2 \times 10^{-3}]$	$[2761.9/1009]$
$0.253^{+0.008}_{-0.007}$	30	-0.56 ± 0.02	40 ± 10	0.90 ± 0.02	16^{+3}_{-2}	$3^{+2}_{-1} \times 10^{-3}$	**1071.1/1006**
M81 X-6							
high X-ray flux							
0.107 ± 0.002	10	0.401 ± 0.003	6	-	-	$5^{+4}_{-3} \times 10^{-3}$	$[2962.4/2436]^i$
$[0.3]$	30	$[-8 \times 10^{-2}]$	6	-	-	$[4 \times 10^{-3}]$	$[8820.1/2436]$
0.200 ± 0.003	30	$-4.5 \pm 0.3 \times 10^{-2}$	62^{+8}_{-7}	$1.11^{+0.03}_{-0.01}$	$15.0^{+0.7}_{-0.6}$	$3 \pm 1 \times 10^{-3}$	$[2797.5/2433]$
low X-ray flux							
$4.0 \pm 0.6 \times 10^{-2}$	10	-0.12 ± 0.02	6	-	-	$1.0^{+0.7}_{-0.5} \times 10^{-2}$	$[478.6/279]$
0.14 ± 0.01	10	0.36 ± 0.04	≥ 100	≥ 9	$4.1^{+0.4}_{-0.3}$	$7^{+7}_{-4} \times 10^{-3}$	274.9/276
$[0.1]$	30	$[-0.6]$	6	-	-	$[6 \times 10^{-3}]$	$[677.2/279]$
$0.165^{+0.010}_{-0.009}$	30	-0.43 ± 0.02	25^{+10}_{-4}	$1.4^{+0.4}_{-0.1}$	≥ 11	$5^{+3}_{-2} \times 10^{-3}$	**258.7/276**

Table 5.5: continued

$N_{\mathrm{H}}{}^a$	Mass^b	$\log(L/L_{\mathrm{Edd}})^c$	$r_{\mathrm{cor}}{}^d$	$kT_{\mathrm{e}}{}^e$	τ^f	$f_{\mathrm{out}}{}^g$	$\chi^2/\mathrm{d.o.f.}^h$
			NGC 4190 ULX1				
			high X-ray flux				
$5.8 \pm 0.3 \times 10^{-2}$	10	0.446 ± 0.005	6	-	-	$8 \pm 3 \times 10^{-4}$	$[1157.5/920]$
$6.5 \pm 0.4 \times 10^{-2}$	10	$0.494^{+0.004}_{-0.007}$	$19.0^{+4.0}_{-0.6}$	$1.56^{+0.13}_{-0.05}$	≥ 17	$8 \pm 3 \times 10^{-4}$	$917.9/917$
$[0.2]$	30	$[-8 \times 10^{-2}]$	6	-	-	$[1 \times 10^{-3}]$	$[3555.6/920]$
0.139 ± 0.005	30	$2.5^{+0.6}_{-0.5} \times 10^{-2}$	≥ 90	$1.3^{+0.6}_{-0.2}$	$12.9^{+0.6}_{-0.2}$	$7 \pm 4 \times 10^{-4}$	$969.1/917$
			low X-ray flux				
$4.9 \pm 0.4 \times 10^{-2}$	10	0.23 ± 0.01	6	-	-	$1.3^{+0.5}_{-0.4} \times 10^{-3}$	$858.2/845$
$5.2 \pm 0.4 \times 10^{-2}$	10	0.19 ± 0.02	$14.0^{+1.6}_{-0.7}$	$1.15^{+0.06}_{-0.05}$	≥ 20	$1.5 \pm 0.5 \times 10^{-3}$	**798.1/842**
$[0.2]$	30	$[-0.1]$	6	-	-	$[1 \times 10^{-3}]$	$[2495.4/845]$
$0.121^{+0.006}_{-0.005}$	30	-0.25 ± 0.02	≥ 60	1.03 ± 0.03	16 ± 1	$1.3^{+0.7}_{-0.6} \times 10^{-3}$	$811.2/842$

are typically constrained to $kT_e \sim 1 - 3$ keV and $\tau \gtrsim 10$. There is no consistently favoured black hole mass - a 10 $M_\odot$ black hole provides the best fit for NGC 253 ULX2, NGC 1313 X-2 and NGC 4190 ULX1, whilst a 30 $M_\odot$ black hole is preferred for NGC 2403 X-1 and M81 X-6; although the only source where either of the black hole masses is formally rejected for all combinations of outer disc radius and coronal radius is NGC 253 ULX2, where a 30 $M_\odot$ black hole cannot adequately describe the observed spectra.

Spectral fitting was carried out for two fixed characteristic outer disc radii of 10^5 and 10^6 r_g. Typically, the absorption, Eddington ratio, corona radius, electron temperature and optical depth vary little between models with the same black hole mass but different outer disc radii; there are however slight reductions in the value of χ^2 as the outer disc radius is increased, e.g. for the best fitting models of NGC 253 ULX2, NGC 1313 X-1, $\Delta\chi^2 = 19$, 15.5 respectively. The effect of varying the outer disc radius is clear from inspecting the spectral shape at optical wavelengths (Figure 5.2 *top* and *centre*), or the difference in the residuals to the spectral fit for each outer disc radius (Figures 5.3 and 5.4). The outer disc radius has little effect on the X-ray spectrum, but in combination with the fraction of emission reprocessed in the outer disc, it determines the contribution of the accretion disc to the optical spectrum. From the residual plots, it is clear that none of the spectral models can adequately reproduce the observed optical counterpart in NGC 253 ULX2; in NGC 1313 X-2 the 10^6 r_g outer disc radius is an improvement over 10^5 r_g, which under-predicts each of the optical magnitudes by greater than the 1σ confidence ranges. In the other ULXs the difference between the models is more subtle, but the 1σ confidence regions of the F435W and F606W fluxes in M81 X-6, and the F300W magnitude in NGC 4190 ULX1 lie outside of the model predictions for $r_{out} = 10^5$ r_g, and for these sources the optical data points which do lie within the 1σ error regions of the model are particularly unconstrained, having 1σ uncertainties of $\pm$ 2 - 3 magnitudes.

Finally, we consider the fraction of emission reprocessed in the outer disc. For

the models with $r_{\rm out} = 10^5 \ r_{\rm g}$, $f_{\rm out}$ is very poorly constrained. Where errors could be estimated, they were large, or only provided unphysically high upper limits. For the models with $r_{\rm out} = 10^6 \ r_{\rm g}$, which the model residuals would argue provides a superior fit to the optical data, we were able to place better constraints on $f_{\rm out}$. For NGC 253 ULX2, $f_{\rm out} \sim 0.4$, which seems unphysically large, however in this source it is clear from the fit residuals (Figures 5.3 and 5.4) that the model is unable to reproduce the observed optical data. For the other 4 ULXs, estimates of $f_{\rm out}$ range from $\sim 0.1 - 3$ per cent. Where there is both high and low flux X-ray data, as expected, the low flux X-ray data requires a larger fraction to be reprocessed. If we consider only the statistically best fitting model for each ULX, then we estimate $f_{\rm out} = 3^{+2}_{-1} \times 10^{-2}$, $3^{+2}_{-1} \times 10^{-3}$, $5^{+3}_{-2} \times 10^{-3}$ and $1.5 \pm 0.5 \times 10^{-3}$ for NGC 1313 X-2, NGC 2403 X-1, M81 X-6 and NGC 4190 ULX respectively. With the exception of NGC 1313 X-2, these are all in the range of a few $\times 10^{-3}$; furthermore, the reprocessed fraction quoted for NGC 1313 X-2 corresponds to a 10 $M_\odot$ black hole, and it could be a factor of ~ 10 lower if it instead contains a larger MsBH: $f_{\rm out} \sim (4\text{--}6) \times 10^{-3}$ for a 30 $M_\odot$ black hole.

5.6 Discussion

In this chapter we have used a new model of black hole accretion, which includes both a colour-temperature-correction and irradiation of the outer accretion disc to model the X-ray and optical spectra of a sample of ULXs. These have both *HST* and *XMM-Newton* archival data, show broadened disc-like X-ray spectra in Chapter 4 and have optical counterparts identified by Gladstone et al. (2013).

Using the OPTXAGNIR model, we were able to reproduce the observed spectra in 4 of the 5 sample ULXs; for NGC 253 ULX2 it is evident from the fit residuals that the model is unable to produce the observed optical flux. It is noteworthy that the *HST* counterpart to NGC 253 ULX2 is significantly brighter than most other known ULX
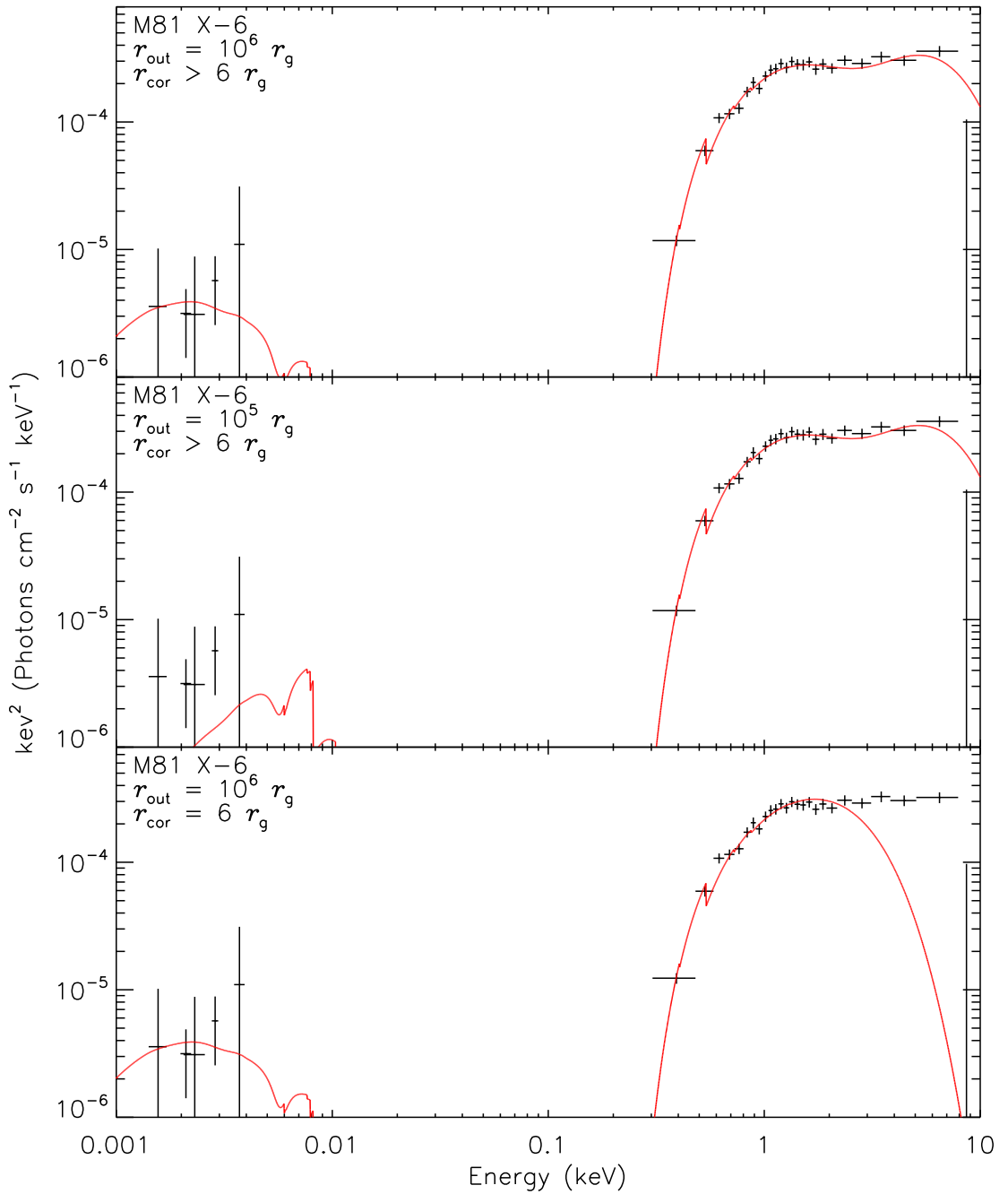
Figure 5.2: Combined optical and X-ray spectrum of M81 X-6, showing both the *HST* and low flux *XMM-Newton* data. For clarity, only the pn data from observation 0657802201 is shown, and it is rebinned to 10 σ significance. Several variants of the irradiated colour-corrected disc model are overplotted in red, these correspond to: (*top*) the statistically best fitting model, consisting of a 30 $M_\odot$ black hole with an outer disc radius of 10^6 r_g and the X-ray emission from the inner disc being reprocessed in a corona; (*centre*) a 30 $M_\odot$ black hole with an outer disc radius of 10^5 r_g and a corona; (*bottom*) a 30 $M_\odot$ black hole with an outer disc radius of 10^6 r_g, but no corona.
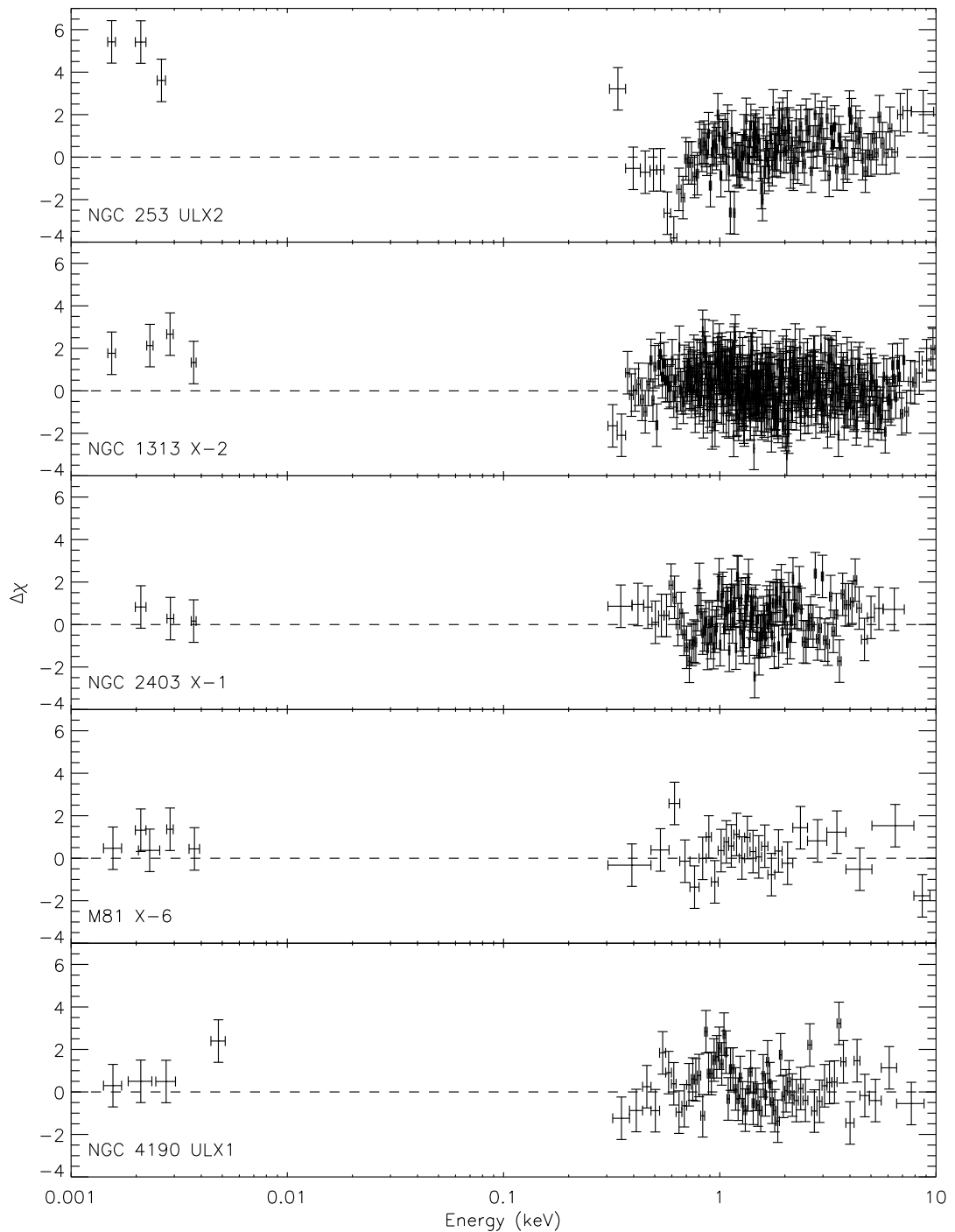
Figure 5.3: Residuals from the statistically best-fitting spectral model to each of the sample ULXs, with an outer disc radius of $10^5\ r_{\rm g}$ shown in Table 5.4. The residuals are plotted in terms of $\Delta\chi$, and the dashed line corresponds to $\Delta\chi = 0$. Only X-ray data from the longest *XMM-Newton* EPIC pn exposure of the target in the appropriate X-ray flux state is shown, and these are rebinned to 10 σ significance for clarity.
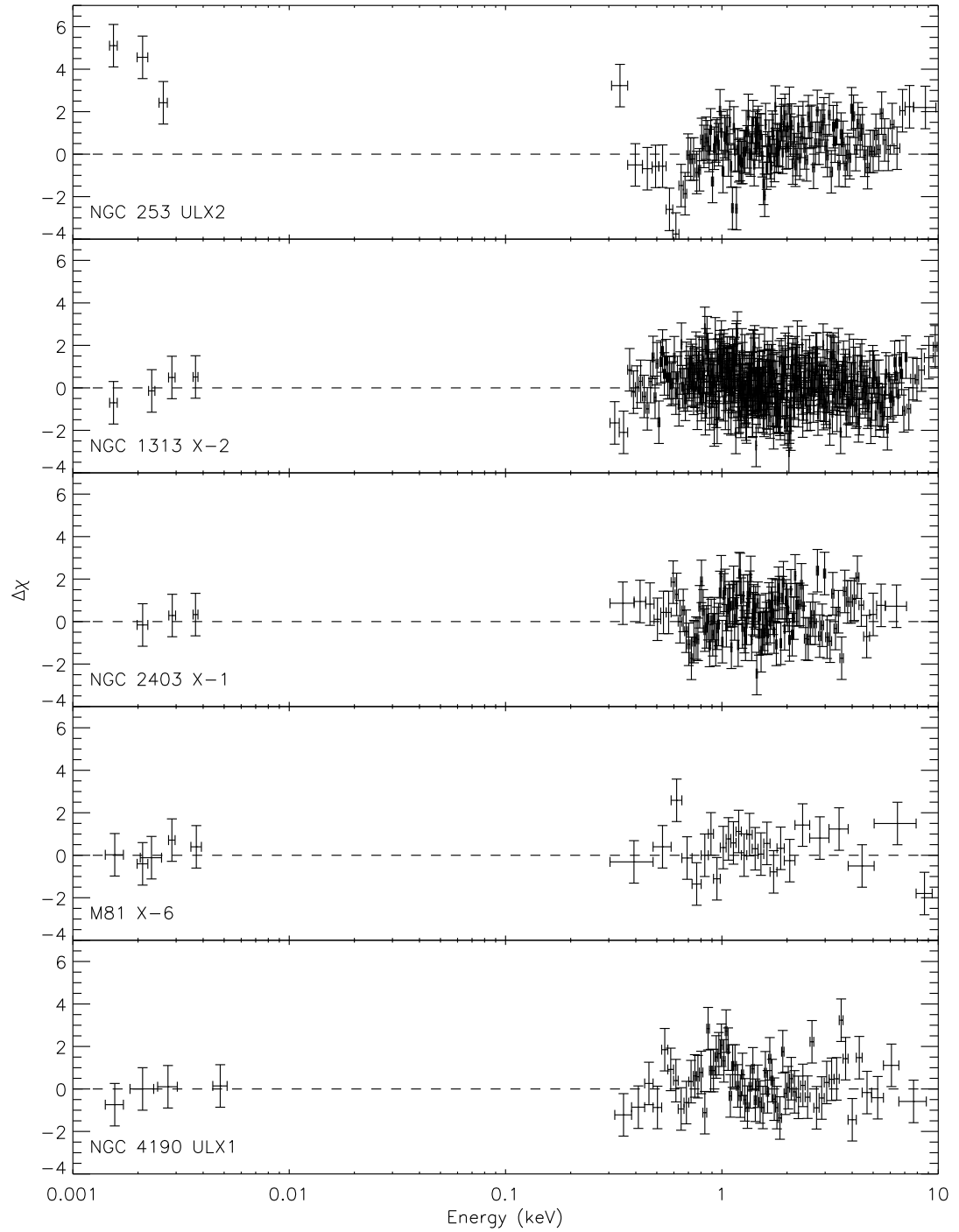
Figure 5.4: As Figure 5.3, but for the models with an outer disc radius of 10^6 r_g shown in Table 5.5.

counterparts in this sample; at a distance of 3.68 Mpc, NGC 253 ULX2 has a distance modulus of 27.8, thus the absolute magnitudes (Galactic-reddening-corrected absolute magnitudes of -6.1, -7.0 and -8.2 in the F475W, F606W and F814W bands respectively) and colours (F475W − F606W ≈ 0.9 and F475W − F814W ≈ 2.1; corrected for Galactic reddening only) of the counterpart may be suggestive of a stellar cluster in NGC 253. As the identity of the counterpart is uncertain, we do not consider NGC 253 ULX2 further.

Of the 4 other ULXs in the sample, 3 – NGC 1313 X-2, M81 X-6 and NGC 4190 ULX1 – had been observed to display a degree of inter-observational variability in X-ray flux; the X-ray spectra were flux-grouped, but with the lack of simultaneous *XMM-Newton* and *HST* observations, there is no way to determine which of the X-ray flux groups corresponds to the epoch of the optical observations. For NGC 1313 X-2 and NGC 4190 ULX1 we find statistically acceptable spectral fits at the 3σ level for both sets of flux grouped X-ray data, although the nominal best fits corresponded to the high flux and low flux X-ray spectra respectively. However, in the case of M81 X-6, no acceptable spectral fit was identified for the high flux X-ray data. For 2 sources – NGC 1313 X-2 and M81 X-6 – an irradiated, colour-temperature-corrected disc alone could not adequately fit the observed data; and, even in NGC 2403 X-1 and NGC 4190 ULX1, where a disc alone could not be rejected, the addition of a Comptonised component improved the fit statistic ($\Delta\chi^2 = 33.2$ and 60.1 for 3 degrees of freedom, between the best fitting disc and the equivalent model with the addition of a Compton corona). Further, neither of the characteristic black hole masses could be rejected in any of the ULXs, although a 10 $M_\odot$ black hole provided the preferred solution for NGC 1313 X-2 and NGC 4190 ULX1, and a 30 $M_\odot$ black hole for NGC 2403 X-1 and M81 X-6. To check whether larger black holes could also produce the observed broadband spectra, we attempted to fit the X-ray and optical data from NGC 1313 X-2 using the absorbed/reddened OPTXAGNIR model with a 100 and 1000 $M_\odot$ black hole. As these black hole masses would require the

ULX to be at a sub-Eddington luminosity, it is appropriate to use sub-Eddington BHB-like spectra, so all of the power produced within the coronal radius in the model was radiated as a power-law. These models were rejected at greater than 3σ significance, except for a combination of a 100 $M_\odot$ black hole and the low flux X-ray data. In this case, NGC 1313 X-2 would be at $\sim 0.2 L_{\rm Edd}$ with a power-law spectral index of $\Gamma \sim 2.2$, which is similar to the very high state in Galactic black holes (e.g. McClintock & Remillard 2006). However, the observed high energy curvature (Stobbart et al., 2006) and spectral progression with X-ray luminosity (Feng & Kaaret, 2007) are inconsistent with a sub-Eddington state identification in this source; also, the reprocessing fraction required to produce the optical spectrum ($f_{\rm out} \geq 5$ per cent) is a factor of $\gtrsim 10$ greater than would be expected for a sub-Eddington BHB (see below and Gierliński et al. 2009).

Of the two characteristic outer disc radii tested, neither can be ruled out based on the χ^2 statistic in any of the sample sources. But, it is evident from a comparison of Tables 5.4 and 5.5 that the 10^6 $r_{\rm g}$ outer disc radius offered at least a marginally improved fit in most of the models. However, given the relative amounts of optical and X-ray data points used in this analysis, the χ^2 statistic is heavily dominated by the X-ray spectrum; and, from an examination of the model residuals at optical wavelengths (Figures 5.3 and 5.4) it seems that a larger outer disc radius can better reproduce the observed spectral shape in most of the sources. Indeed, Gierliński et al. (2009) note that for the DISKIR model (which neglects the colour-temperature-correction) it is evident from the spectral shape that the irradiated fraction is the main parameter controlling the amount of optical flux, whilst the spectral slope is determined predominantly by the outer disc radius. An outer disc radius of 10^6 $r_{\rm g}$ for a $10 - 30$ $M_\odot$ black hole is equal to $\sim (1.5–4.5) \times 10^{12}$ cm, this is comparable to the ~ 14 $M_\odot$ (Greiner et al., 2001) mildly super-Eddington (Done et al., 2004) Galactic BHB – GRS 1915+105, which has an outer disc radius of $\sim 3 \times 10^{12}$ cm and may itself contain an irradiated disc (Rahoui et al., 2010).

Next, we consider the reprocessing fractions in the ULX sample. The best fitting irradiated, colour-temperature-corrected disc models indicate that reprocessing fractions of $\sim 10^{-3}$ are required in NGC 2403 X-1, M81 X-6 and NGC 4190 ULX1, and $\sim 3 \times 10^{-2}$ in NGC 1313 X-2; although models with a slightly larger black hole and a reprocessing fraction ~ 10 times lower cannot be rejected for NGC 1313 X-2. For the most part, these are a factor of ~ 10 lower than the reprocessing fractions claimed for ULXs using the DISKIR model, e.g. $f_{\text{out}} = 2.7^{+2.3}_{-1.0} \times 10^{-2}$ in Ho II X-1, Tao et al. 2012; $f_{\text{out}} \approx (3.0\text{--}4.6) \times 10^{-2}$ in NGC 5408 X-1, Grisé et al. 2012. However, both Ho II X-1 and NGC 5408 X-1 were classified with soft ultraluminous spectra in Chapter 4, which we suggested was associated with a strong, radiatively-driven wind. In which case, the increased reprocessing fraction may be in some way triggered by the wind; although, we caution that the DISKIR model (or indeed the OPTXAGNIR model) may not be adequate to estimate the reprocessing fraction in these ULXs, as the soft X-ray spectra do not appear to be disc-like. Instead, the inferred reprocessing fractions in the sample of broadened disc ULXs appear to be comparable with those seen in the Galactic BHB XTE J1817$-$330, where the DISKIR model indicates $f_{\text{out}} \sim 1 \times 10^{-3}$ (Gierliński et al., 2009). Here, to allow for a consistent comparison between our sample and a sub-Eddington Galactic BHB, we extend the analysis of Gierliński et al. (2009) and fit their spectrum 1 of XTE J1817$-$330 with the absorbed/reddened OPTXAGNIR model. The absorption, Eddington ratio, spin, coronal radius and outer disc radius were allowed to vary freely; all of the flux emitted within the coronal radius was approximated as a power-law with the spectral index set to the best fit value from Gierliński et al. (2009), $\Gamma = 2.34$; the black hole mass was fixed at 6 $M_{\odot}$, corresponding to the upper limit calculated by Sala et al. (2007); and, the distance was fixed to 8 kpc, which is consistent with the 1–10 kpc range estimated by Sala et al. (2007). We found an absorption column of $\sim 1.5 \times 10^{21}$ cm^{-2}, which is greater than the value from the DISKIR fits of Gierliński et al. (2009), but is close to the average galactic column in the direction of the source of 1.57×10^{21} cm^{-2}

(Dickey & Lockman, 1990). The other fitted model parameters were an Eddington ratio of ~ 0.3, a spin of ~ 0, and an outer disc radius of $\sim 1.3 \times 10^5$ r_{g}, which is similar to the value found by Gierliński et al. (2009) of $10^{4.5}$ r_{in}, assuming an inner disc radius of 6 r_{g}. Finally, we estimated an irradiated fraction of $f_{\mathrm{out}} \sim 3 \times 10^{-3}$ in XTE J1817−330; thus, confirming that it is of the same order of magnitude as the range seen in the ULX sample, even when the colour-temperature-correction is included.

Given the similarities between the reprocessing fractions in these ULXs and the sub-Eddington XTE J1817−330, then perhaps some of the ULXs may too be sub-Eddington. Indeed, the best fitting OPTXAGNIR models for NGC 2403 X-1 and M81 X-6 indicate that they have Eddington ratios of ~ 0.2–0.3. However, the cool, optically thick corona that are seemingly required by the data are unlike any known sub-Eddington state. The apparent discrepancy between the luminosity and the shape of the X-ray spectrum in these sources may imply that we are over-estimating the masses of the black holes. If we reject the statistically best fitting models with 30 $M_{\odot}$ black holes in NGC 2403 X-1 and M81 X-6 on these physical grounds, then the model parameters indicate that all of the ULXs in this sample may be powered by accretion on to ~ 10 $M_{\odot}$ sMBHs, with Eddington ratios of ~ 0.7–2. Then, we suggest that two opposing mechanisms determine the fraction of the emission reprocessed in the outer disc: firstly, ULX accretion discs may be convex in shape, Kaaret & Corbel (2009) argue that this geometry would reduce the reprocessing fraction due to self-shielding in the disc. However, as the Eddington limit is approached and exceeded, accretion discs are expected to drive a strong, outflowing wind (Poutanen et al., 2007); material in the wind will be optically thin far from the ULX, and may scatter radiation from the central accretion disc, some fraction of which can irradiate the outer disc, thus opposing the effect of self-shielding. Then, the reprocessing fractions in most of this ULX sample would suggest that the effects of these opposing influences must be similar in magnitude, whilst radiation scattered into lines-of-sight to the

disc may be the dominant process in NGC 1313 X-2. Furthermore, this scenario may be compatible with the larger reprocessing fractions reported for some soft ultraluminous ULXs (Grisé et al. 2012; Tao et al. 2012; albeit using the DISKIR model, with no colour-temperature-correction), if a larger wind results in more of the hard flux from close to the inner disc being scattered.

There are however a number of caveats to this work. Firstly, there are inevitably large uncertainties in the reprocessing fractions, as the *XMM-Newton* and *HST* observations are not simultaneous, and in the cases of M81 X-6 and NGC 4190 ULX1 the *HST* observations are themselves spread over time scales of $\sim$ months to a decade. Clearly, contemporaneous high quality X-ray and optical observations are required to better test the OPTXAGNIR model (and other models that span similar wavelength ranges) in ULXs. Furthermore, multiple epochs of multi-wavelength data spanning a range of X-ray fluxes would allow us to begin to better constrain some of the degeneracies in e.g. black hole mass inherent in the model. Also, it should be noted that the spectral model conserves the mass accretion rate in the disc. This assumption should not be valid in super critical accretion discs, where a significant degree of mass loss is expected to occur in a wind. We expect that this could reduce the global accretion rate required to produce the observed X-ray spectrum in the central disc, thus we may be underestimating the contribution of intrinsic disc emission from the outer disc to the observed spectrum, hence overestimating the required reprocessing fractions. Finally, we have been neglecting the contribution to the optical flux from the companion star. Given the similar colours of a blue star and emission from the accretion disc, it is difficult to disentangle these two contributions with the available data, although Gladstone et al. (2013) note that the optical counterparts to some ULXs are too bright to be powered by even the most luminous stars. Searches for associated X-ray and optical variability would be able to provide a test for reprocessed emission from the outer disc, but this is not currently possible using archival data.

5.7   Conclusions

This study demonstrates the importance of taking the colour-temperature-correction into account when estimating the contribution from the intrinsic disc emission to the optical and infrared flux in ULXs. We have modelled a small sample of ULXs that were identified as having disc-like X-ray spectra, using the new OPTXAGNIR spectral model, which accounts for: the colour-temperature-correction in the accretion disc; X-ray reprocessing in the outer disc; and a Compton corona covering the inner regions of the disc. Contrary to other studies which use the DISKIR model (which neglects the colour-temperature-correction), we find that large reprocessing fractions are not required in several ULXs with disc-like X-ray spectra, rather they are similar in this regard to thermal state Galactic BHBs, whilst one source – NGC 1313 X-2 – may have a slightly higher ~ 3 per cent reprocessing fraction. Despite the similar reprocessing fractions, the X-ray spectra arguably do not appear to be consistent with these ULXs being very sub-Eddington. Instead we suggest that the relative effects of two opposing mechanisms may influence the fraction of the bolometric luminosity reprocessed in the outer disc: it can be reduced by self-shielding in the accretion disc; and, material in a nascent super-Eddington disc wind may scatter radiation from above the plane of the disc, such that a fraction of it is reflected on to the outer regions of the accretion disc. This scenario may be consistent with the larger reprocessing fractions reported for wind-dominated soft ultraluminous ULXs.

Chapter 6

Conclusions

Throughout this thesis we have presented research that has attempted to progress our understanding in the field of ULX astronomy. In this chapter we briefly outline the key findings, and suggest a few potentially fruitful avenues for future progress.

6.1   The nature of the brightest ULXs

In Chapter 2 we looked at a sample of extreme luminosity ULXs; whilst we have argued that the majority of ULXs are probably stellar remnant black holes, many of the most luminous sources are difficult to explain, even by a combination of the largest MsBHs and super-Eddington accretion rates. Instead, these sources may indeed harbour IMBHs, so we attempted to test this hypothesis by examining their X-ray spectral and timing properties, and searching for potential optical counterparts in archival data. Of the 8 good extreme ULX candidates in the sample, seven were in spiral galaxies, several of which appeared to be closely related to regions of star formation, as is commonly seen for less luminous ULXs. The final source was a persistent HLX candidate in an S0 galaxy. However, the sample had X-ray spectra which were typically harder than is seen in fainter ULXs, and they were consistent with being variable. Indeed, these sources were consistent with being in the low/hard state, but with the black hole mass scaled up to the IMBH regime.

Although many of the extreme ULXs appeared to be sub-Eddington, in the one source with the best quality X-ray data - NGC 5907 ULX - we did find evidence for high energy spectral curvature. Such curvature is one of the key signatures of the ultraluminous state, so we returned to this source in Chapter 3, where we re-

examined it in more detail. Although NGC 5907 ULX peaked at a 0.3–10 keV luminosity of $\sim 6 \times 10^{40}$ erg s^{-1}, which is above the break in the HMXB XLF, its X-ray spectrum appeared to be dominated by a cool, optically thick corona which is suggestive of super-Eddington accretion. We speculated that the ~ 9 per cent fractional variability seen in this ULX could be imprinted by stochastic obscuration by clumpy material in an out-flowing wind, and that the lack of soft emission from a wind in the X-ray spectrum may be due to a combination of a low temperature in this component, and obscuration by the high column density in the direction of the source. In this scenario NGC 5907 ULX would not require an IMBH primary, rather it would most probably contain a MsBH.

In light of the evidence from NGC 5907 ULX, we caution that highly super-Eddington accretion onto large MsBHs cannot yet be completely ruled out in the rest of the extreme ULX sample presented in Chapter 2. However, previously progress in X-ray astronomy has frequently come as a result of improvements in instrumentation; and, future instrumentation will likely be able to discern the nature of these sources. Although it is still at the pre-selection stage, the *Advanced Telescope for High Energy Astrophysics+* (*ATHENA+*) is a likely candidate for the next major X-ray observatory. Proposals for *ATHENA+* include an effective photon collecting area of 2 m^2 at 1 keV, which is a large improvement over the mirrors on *XMM-Newton* ($\sim 3 \times 1400$ cm^2), which will make *ATHENA+* ideal for observing the faint X-ray spectra of extreme luminosity ULXs.

Current plans for the proposed mission include two focal plane instruments: the X-ray Integral Field Unit (X-IFU), which will use a microcalorimeter to offer imaging spectroscopy with excellent energy resolution (dE ~ 2.5 eV at 0.3–7 keV); and, the Wide Field Imager (WFI), which will provide sensitive energy and time resolved imaging spectroscopy capability over a large 40×40 arcminute field of view. The WFI has the highest quantum efficiency, making it the best choice for obtaining low resolu-

tion X-ray spectra of faint targets, so here we use the WFI on-axis response matrix[1] to simulate the X-ray spectrum from an extreme ULX in the hard ultraluminous state, to test whether it could be differentiated from a low/hard state IMBH. We use a spectral model of an absorbed MCD plus cool, optically thick Comptonisation (TBABS $\times$ (DISKBB + COMPTT) in XSPEC), with parameters: $N_{\mathrm{H}} = 3 \times 10^{21}$ cm^2, $kT_{\mathrm{in}} = 0.3$ keV, $T_0 = 0.3$ keV, $kT = 2$ keV and $\tau = 10$. The ratio of the normalisations of the 2 components was set by freezing all other components and fitting the model to a previously simulated absorbed low/hard state-like $\Gamma = 1.7$ power-law; these were then scaled such that the spectrum had a 0.3–10 keV flux of $\sim 3 \times 10^{-13}$ erg cm^{-2} s^{-1}. XSPEC was used to simulate a 100 ks observation of the model spectrum, which was then grouped to a minimum of 20 counts per bin using GRPPHA (although across much of the energy range the actual number of counts per bin was greater than this, as it was limited by the number of counts per channel), and fitted with phenomenological spectral models of a sub-Eddington state IMBH and a super-Eddington stellar remnant (TBABS $\times$ (DISKBB + POWERLAW); TBABS $\times$ (DISKBB + COMPTT); Figure 6.1). The fit statistics of the models were $\chi^2/\mathrm{dof} = 760.7/622$ and $644.6/620$ for the low/hard state IMBH and the ultraluminous state model respectively; thus, the low/hard state model would be rejected at greater than 3σ significance. To allow for a comparison with the capabilities of current instrumentation, we repeated the experiment using all of the *XMM-Newton* EPIC detector response matrices and ancillary response files from on-axis observations, finding that *XMM-Newton* was unable to differentiate between the models in a 100 ks observation ($\chi^2/\mathrm{dof} = 617.6/601$ and $608.3/599$ for the low/hard state and ultraluminous spectral models respectively). *ATHENA+* therefore offers the very real prospect of identifying whether these extreme ULXs are MSBHs in the ultraluminous state, or sub-Eddington IMBHs.

---

[1]`http://sci.esa.int/athena/43974-mission-tools/`
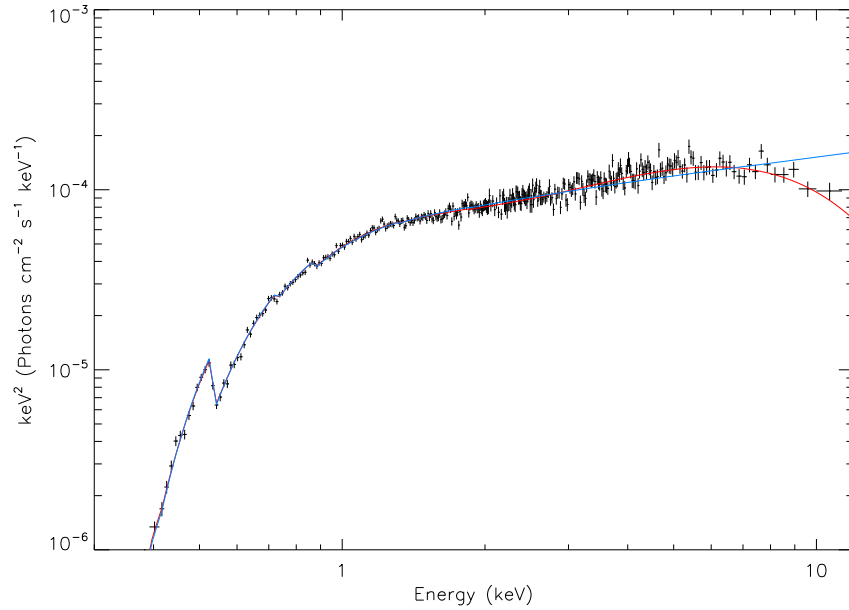
Figure 6.1: Simulated *ATHENA+* WFI spectrum for an observation of a source with a subtle ultraluminous state spectrum, which would be indistinguishable from a low/hard state IMBH in reasonable exposure times with *XMM-Newton*. The data are for a simulated 100 ks observation of a target with a 0.3–10 keV flux of $\sim 3 \times 10^{-13}$ erg cm^{-2} s^{-1}, and are binned to 10σ significance for clarity. Phenomenological models of an ultraluminous state spectrum (red line - TBABS $\times$ (DISKBB + COMPTT)) and a sub-Eddington IMBH (blue line - TBABS $\times$ (DISKBB + POWER-LAW)) are shown.

6.2   The X-ray spectral and timing properties of ULXs

In Chapter 4 we presented an X-ray spectral and timing study of a sample of ULXs with some of the best quality *XMM-Newton* data. Based on the ultraluminous state model of Gladstone et al. (2009), we suggested an empirical classification scheme for ULXs that separates them into three distinct classes based on their X-ray spectra: broadened discs, hard ultraluminous and soft ultraluminous. Broadened disc ULXs have singly peaked X-ray spectra, whilst hard and soft ultraluminous sources

have two component spectra, which peak in the hard and soft component respectively. At low X-ray luminosities ($\lesssim 3 \times 10^{39}$ erg s^{-1}) the ULX population is dominated by sources with broadened disc spectra, whilst hard and soft ultraluminous sources tend to be more luminous in X-rays, which is suggestive of a distinction between ~Eddington and super-Eddington accretion states. A few broadened discs were found to be more luminous than this, and these could be evidence for slightly larger black holes (i.e. MsBHs), or they possibly have misidentified hard ultraluminous spectra. We also examined the timing properties of the ULX sample, finding high levels of fractional variability in a number of sources, most of which had soft ultraluminous spectra, whilst only low levels of variability were seen in the hard ultraluminous sources. Furthermore, the variability in the ULXs was seen to peak at high energies, suggesting that it originates in the hard spectral component. Similar variability was also identified in a few of the broadened discs, which adds weight to the suggestion that the 'discs' may actually have subtle emerging hard/soft ultraluminous spectra.

We suggested that the properties of the sample ULXs were consistent with current models of super-Eddington accretion, with massive radiatively-driven winds. The wind forms a funnel-shape around the central regions of the accretion flow, and this introduces an angular-dependence into the observed properties. At inclinations close to face on, the spectrum is largely dominated by geometrically beamed emission from the central source, and the observer sees a hard ultraluminous source; whilst at higher inclinations, the balance of the two components shifts towards the soft wind emission, producing a soft ultraluminous spectrum. The observed variability can also be produced in this model if the edge of the wind is clumpy in nature. Then, in soft ultraluminous sources which are observed at inclinations close to the edge of the wind, the line-of-sight to the hard central emission can be stochastically obscured by the clumpy medium, which would imprint variability into the hard light curve. Additionally, transitions between the hard and soft ultraluminous regimes are

consistent with the the opening angle of the wind closing as the accretion rate rises, and vice-versa, shifting the observed spectrum and potentially the timing properties for a fixed observing angle.

As a consequence of the modified ultraluminous state model, we would predict the detection of wind absorption lines in the hard X-ray spectra of soft ultraluminous sources. Walton et al. (2013) used 500 ks of *Suzaku* data to test for narrow absorption features in Ho IX X-1, but ruled out any significant features down to an equivalent width of ~ 20 eV. However, in Chapter 4 we classify Ho IX X-1 as having a hard ultraluminous spectrum, so we may not expect to detect wind features. Here, we test whether *ATHENA+* would be capable of detecting such lines, if they were present in a soft ultraluminous ULX. As before, we produced a model ultraluminous state spectrum, using the same procedure as in Section 6.1. This time, we tuned the component normalisations using a power-law with $\Gamma = 2.7$, as is appropriate for a soft ultraluminous state source, and we normalised the model to a 0.3–10 keV flux of 5×10^{-12} erg cm^{-2} s^{-1}, which is comparable to the flux of Ho IX X-1 in three of the four observations examined in Chapter 4. We then added an absorption line to the spectrum using GAUSS in XSPEC, with centroid energy E = 6.4 keV, line width $\sigma = 10$ eV, and normalisation tuned such that the equivalent width of the line calculated using EQWIDTH was equal to ~ 20 eV. To detect narrow spectral features with *ATHENA+*, the X-IFU would be the instrument of choice due to its excellent energy resolution; so, we simulated a 100 ks *ATHENA+* X-IFU observation of the model spectrum, which we grouped to a minimum 20 counts per bin using GRPPHA. The simulated spectrum was then fitted in XSPEC using both an ultraluminous state spectrum alone (TBABS × (DISKBB + COMPTT)) and with the addition of a gaussian line (TBABS × (GAUSS + DISKBB + COMPTT); Figure 6.2). The addition of a gaussian absorption line improved the fit statistic by $\Delta\chi^2 = -238.8$ for 3 degrees of freedom, which indicates that *ATHENA+* will be capable of observing narrow wind absorption features that are currently undetectable, if present, even in the soft

ultraluminous ULXs. This would therefore provide unambiguous evidence of the presence of wind material in these ULXs.

As well as a super-Eddington wind, another key feature of the ultraluminous state model is the high energy curvature. Previously, this had only been identified using high quality *XMM-Newton* observations (e.g. Stobbart et al. 2006; Gladstone et al. 2009); however, close to the publication of this thesis, early results from *NuSTAR* were beginning to appear in the literature (Bachetti et al. 2013; Walton et al. 2013), and these constrained the X-ray spectra of ULXs up to ~ 30 keV for the first time. The *NuSTAR* observations confirm the presence of high energy curvature in NGC 1313 X-1, NGC 1313 X-2 and Circinus ULX5, and are inconsistent with current reflection models of ULX X-ray spectra, with emission from an optically thick corona being preferred by the data (Bachetti et al. 2013; Walton et al. 2013).

6.3 X-ray reprocessing in ULX optical counterparts

Chapter 5 detailed a combined X-ray and optical study of a small sample of ULXs, which were identified as having broadened disc X-ray spectra, and optical counterparts in the HLA data examined by Gladstone et al. (2013). We presented a new spectral model of an irradiated, colour-temperature-corrected accretion disc around a black hole, with a central Comptonising corona. The model indicates that ~ 0.1 per cent of the bolometric flux is reprocessed in the outer disc, which is similar to Galactic BHBs in the sub-Eddington high/soft state. However, the X-ray spectra of the ULXs are inconsistent with being in the high/soft state, rather we suggest that the reprocessing fractions are due to the opposing affects of self-shielding in a convex super-critical accretion disc, and irradiation of the outer disc by X-ray reflection in an optically thin medium above an accretion disc with a natal super-Eddington wind.
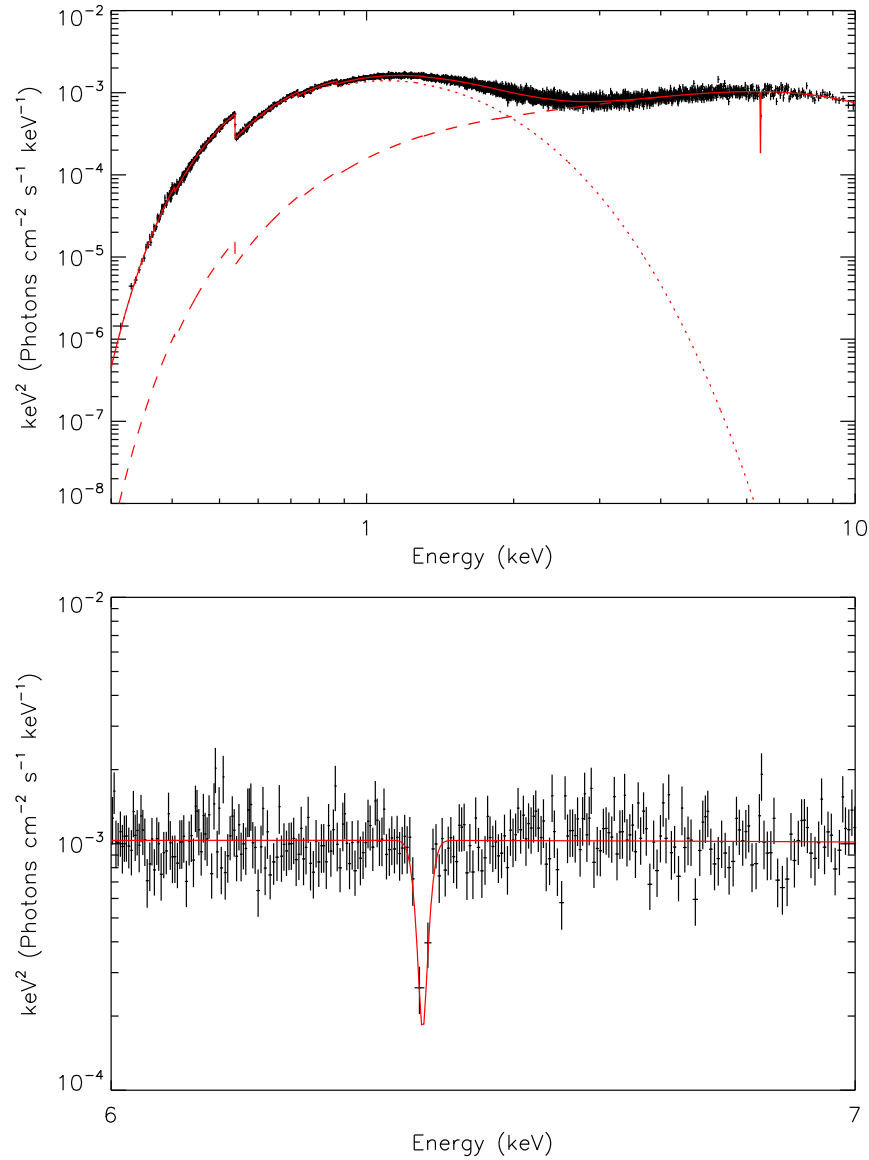
Figure 6.2: Simulated *ATHENA+* X-IFU spectrum from a 100 ks observation of a soft ultraluminous ULX, with a 0.3–10 keV flux of 5×10^{-12} erg cm^{-2} s^{-1}, and a narrow absorption line with an equivalent width of 20 eV. (*top*) The data are binned to 10σ significance for clarity. The red solid line shows the best fitting phenomenological model of a ultraluminous spectrum with a gaussian absorption line (TBABS $\times$ (GAUSS + DISKBB + COMPTT)), and the dotted and dashed lines show the MCD and Comptonising corona components respectively. (*bottom*) A zoomed in version of the spectrum, showing the region around the narrow absorption line.

Furthermore, this scenario may be consistent with the higher reprocessing fractions in the literature for a few ULXs with soft ultraluminous X-ray spectra.

However, the nature of ULX optical counterparts is still not certain; and one way to make progress is to carry out multi-epoch simultaneous X-ray and optical observations. Another tactic, which was used by Roberts et al. (2011) is to examine their optical spectra. Roberts et al. (2011) measured radial velocity shifts over time in the broad 4686 Å He II emission line in the counterparts to NGC 1313 X-2 and Ho IX X-1, with the intent of inferring mass functions and constraining the minimum black hole mass. Although they measured velocity shifts in the line, these were not sinusoidal, implying that the emission line may originate from X-ray reprocessing in a close to face-on accretion disc. The requirement for multiple epochs of spectroscopy can make such experiments rather time costly with the current generation of optical instrumentation, however once the 42 m *European Extremely Large Telescope* (*E-ELT*) is built, it will have to potential to vastly shorten the required integration times for optical observations. To demonstrate this, we here use the *E-ELT* spectroscopy mode exposure time calculator[2] to estimate the required exposure time to obtain an optical spectrum with a signal to noise of $\gtrsim$ 10 across the wavelengths of interest, with a spectral resolution of $\lambda/\mathrm{d}\lambda = 1000$. Exposure times were calculated without corrections for adaptive optics, for a seeing of 0.8 arcsecond and an airmass of 1.15, using a B0V stellar spectrum normalised to a V-band Vega magnitude of 24 as an approximation of a blue ULX counterpart. We estimate that it would require $\sim$ 10 minutes to obtain a signal to noise ratio of 10 across the $\sim$ 3200–4900 Å range, which covers the wavelength of the 4686 Å He II emission line. Therefore, the *E-ELT* will clearly be conducive to future attempts to measure velocity shifts, and to constrain mass functions in nearby ULXs.

The field of ULX astronomy has clearly come a long way since their discovery with *Einstein*. Much progress has been made using current observatories, including

---

[2]`http://www.eso.org/observing/etc/bin/gen/form?INS.MODE=swspectr+INS.NAME=E-ELT`

the contributions presented in this thesis, and from the designs for the following generation of X-ray and optical instrumentation, it is clear that there is much to be excited about in the future.

Appendix A

Appendix to Chapter 4: ULX X-ray spectral and timing results

Here we present the parameters resulting from the MCD plus power-law spectral model fits (Table A.1), and fractional variability observed in each observation (Table A.2).

Table A.1: Spectral parameters - TBABS × TBABS × (DISKBB + POWER-LAW)

Obs. ID[a]	$\chi^2/$dof[b]	$N_{\rm H}$[c]	$kT_{\rm in}$[d]	Γ[e]	$F_{\rm PL}/F_{\rm disc}$[f] (0.3–1 keV)	$L_{\rm X}$[g] (0.3–10 keV)	Spectral regime[h]
			NGC 55 ULX				
0028740201	928.9/881	0.49 ± 0.01	0.81 ± 0.02	$3.80^{+0.10}_{-0.09}$	14 ± 1	$3.4^{+0.1}_{-0.2}$	SUL
0028740101	690.2/669	$0.45^{+0.03}_{-0.02}$	0.87 ± 0.04	3.4 ± 0.2	9 ± 1	$3.9^{+0.7}_{-0.8}$	SUL
0655050101	1084.9/865	0.54 ± 0.01	0.67 ± 0.02	4.3 ± 0.08	28 ± 3	$1.49^{+0.04}_{-0.07}$	SUL

Here we report the model parameters, and the resulting spectral classification from fitting the ULX observations with a doubly-absorbed MCD plus power-law model. Errors and limits are shown at the 1σ level, and dashes indicate an unconstrained parameter. [a]*XMM-Newton* observation identifiers. [b]Statistical goodness of fit, in terms of of χ^2 and the number of degrees of freedom. [c]Extragalactic absorption column density ($\times 10^{22}$ cm^{-2}). [d]Inner disc temperature in keV. [e]Spectral index of the power-law component. [f]The ratio of the observed 0.3–1 keV component fluxes from the power-law and MCD. [g]0.3–10 keV deabsorbed luminosity ($\times 10^{39}$ erg s^{-1}), calculated from the absorbed MCD plus Comptonisation model. [h]The resulting spectral classification of the observation, these are either broadened disc (disc), hard ultraluminous (HUL) or soft ultraluminous (SUL). [i]An additional MEKAL component was included in the spectral model of NGC 253 ULX2 to model extended emission in the host galaxy; this had parameters fixed to the best fitting values from simultaneously fitting all observations with an appropriate model (TBABS × (MEKAL + TBABS × (DISKBB + COMPTT)), with a constant MEKAL component, but the parameters of the ULX model free to vary between observations. [j]The fit reported for observation 0145190101 of NGC 5907 ULX is a local minimum in χ^2 space, with χ^2/dof = 204.5/168. The global minimum occurs for a $2.1^{+0.2}_{-0.1}$ keV hot disc at χ^2/dof = 184.5/168, which would result in the source being classified as a broadened disc during this observation. However, the combination of a hot, low mass black hole and the extremely high luminosity of the source would require an unusually large Eddington ratio of ~ 100, which would seem rather unphysical. The very high line-of-sight absorption column of NGC 5907 ULX, likely due to its location in an edge on spiral galaxy, may suppress the soft excess, resulting in the ambiguity in spectral classification.

Table A.1: continued

Obs. ID[a]	χ^2/dof[b]	N_{H}[c]	kT_{in}[d]	Γ[e]	$F_{\mathrm{PL}}/F_{\mathrm{disc}}$[f] (0.3–1 keV)	L_{X}[g] (0.3–10 keV)	Spectral regime[h]
			M31 ULX1				
0600660201	1147.5/1042	0.07 ± 0.01	1.09 ± 0.01	2.7 ± 0.1	0.95 ± 0.08	$1.457^{+0.008}_{-0.007}$	disc
0600660301	940.7/1002	$0.080^{+0.017}_{-0.009}$	$1.025^{+0.014}_{-0.009}$	$2.79^{+0.17}_{-0.09}$	$1.26^{+0.08}_{-0.09}$	1.040 ± 0.005	disc
0600660401	995.7/977	$0.09^{+0.02}_{-0.01}$	$0.947^{+0.012}_{-0.008}$	$3.0^{+0.2}_{-0.1}$	$1.22^{+0.09}_{-0.12}$	$0.765^{+0.010}_{-0.006}$	disc
0600660501	948.8/900	$0.11^{+0.02}_{-0.01}$	0.86 ± 0.01	$3.0^{+0.2}_{-0.1}$	1.6 ± 0.1	$0.592^{+0.008}_{-0.005}$	disc
0600660601	871.0/857	$0.10^{+0.02}_{-0.01}$	0.80 ± 0.01	3.0 ± 0.1	$1.6^{+0.2}_{-0.1}$	$0.474^{+0.005}_{-0.003}$	disc
			NGC 253 XMM2				
0125960101	192.7/180	$0.08^{+0.31}_{-0.04}$	$1.11^{+0.34}_{-0.07}$	1 ± 3	< 0.8	$1.62^{+0.02}_{-0.03}$	disc
0110900101	47.9/44	< 0.06	$0.50^{+0.06}_{-0.05}$	$0.8^{+0.4}_{-0.9}$	$1.0^{+0.1}_{-0.2}$	$0.42^{+0.02}_{-0.03}$	disc/HUL
0152020101	532.6/541	$0.15^{+0.03}_{-0.02}$	$1.23^{+0.09}_{-0.07}$	$2.2^{+0.3}_{-0.2}$	$1.6^{+0.3}_{-0.2}$	1.60 ± 0.08	disc
0304850901	102.6/97	< 0.3	1.4 ± 0.1	3^{+1}_{-6}	< 2	$0.80^{+0.08}_{-0.05}$	disc
0304851001	115.5/110	0.08 ± 0.05	$1.1^{+0.4}_{-0.2}$	1.5 ± 0.4	< 2	$0.92^{+0.05}_{-0.04}$	disc
0304851201	197.6/190	$0.17^{+0.10}_{-0.08}$	$1.40^{+0.08}_{-0.07}$	$2.9^{+0.9}_{-1.3}$	$0.9^{+0.3}_{-0.5}$	$0.84^{+0.06}_{-0.02}$	disc
			NGC 253 ULX2[i]				
0125960101	597.9/581	$0.21^{+0.03}_{-0.02}$	1.52 ± 0.03	> 5	$0.06^{+0.07}_{-0.02}$	$2.54^{+0.07}_{-0.04}$	disc
0110900101	166.8/160	$0.28^{+0.04}_{-0.03}$	$1.64^{+0.07}_{-0.03}$	> 6	$0.15^{+0.09}_{-0.06}$	$3.11^{+0.33}_{-0.09}$	disc
0152020101	614.3/624	$0.33^{+0.08}_{-0.05}$	$1.69^{+0.05}_{-0.14}$	$2.2^{+0.8}_{-0.9}$	0.4 ± 0.2	$2.53^{+0.07}_{-0.11}$	disc
0304850901	179.4/176	$0.26^{+0.03}_{-0.02}$	1.59 ± 0.05	-	0.11 ± 0.07	2.1 ± 0.1	disc
0304851001	181.4/168	0.56 ± 0.05	$0.035^{+0.006}_{-0.007}$	$1.79^{+0.03}_{-0.05}$	3.1 ± 0.6	$2.02^{+0.15}_{-0.07}$	HUL
0304851201	319.6/287	$0.25^{+0.12}_{-0.04}$	1.52 ± 0.04	> 4	$0.2^{+0.3}_{-0.1}$	$2.01^{+0.22}_{-0.04}$	disc
0304851301	42.5/45	$0.29^{+0.06}_{-0.05}$	$1.4^{+0.2}_{-0.1}$	< 10	< 1	1.0 ± 0.3	disc

Table A.1: continued

Obs. ID[a]	χ^2/dof[b]	N_H[c]	kT_in[d]	Γ[e]	$F_\mathrm{PL}/F_\mathrm{disc}$[f] (0.3–1 keV)	L_X[g] (0.3–10 keV)	Spectral regime[h]
			M33 X-8				
0102640401	360.4/364	$0.16^{+0.05}_{-0.03}$	1.13 ± 0.08	$2.4^{+0.4}_{-0.2}$	2.0 ± 0.3	1.84 ± 0.01	disc
0102640101	1022.9/1035	$0.10^{+0.01}_{-0.02}$	$1.06^{+0.02}_{-0.04}$	$2.08^{+0.07}_{-0.12}$	1.2 ± 0.1	1.63 ± 0.03	disc
0102640701	360.3/350	0.16 ± 0.02	1.0 ± 0.2	$2.1^{+0.2}_{-0.1}$	5^{+1}_{-2}	1.79 ± 0.04	disc/HUL/SUL
0102641001	346.1/315	$0.17^{+0.04}_{-0.03}$	1.4 ± 0.1	$2.4^{+0.3}_{-0.2}$	$4.0^{+0.7}_{-0.6}$	$1.76^{+0.08}_{-0.04}$	disc
0102642001	689.0/698	0.11 ± 0.02	0.89 ± 0.05	$1.9^{+0.1}_{-0.2}$	$1.5^{+0.4}_{-0.5}$	1.96 ± 0.03	disc
0102642101	1078.7/1015	$0.08^{+0.02}_{-0.01}$	$1.01^{+0.04}_{-0.03}$	$1.91^{+0.11}_{-0.09}$	1.0 ± 0.1	1.86 ± 0.02	disc
0102642301	1060.9/1049	$0.14^{+0.02}_{-0.01}$	1.10 ± 0.03	$2.33^{+0.12}_{-0.09}$	$1.6^{+0.1}_{-0.2}$	1.96 ± 0.02	disc
0141980601	842.3/813	0.09 ± 0.02	$0.99^{+0.06}_{-0.04}$	$1.8^{+0.2}_{-0.1}$	1.1 ± 0.3	$1.73^{+0.05}_{-0.03}$	disc
0141980801	1163.8/1018	0.11 ± 0.01	$0.88^{+0.05}_{-0.04}$	$1.94^{+0.05}_{-0.06}$	3.0 ± 0.5	$1.74^{+0.04}_{-0.05}$	disc
0141980101	331.7/308	$0.14^{+0.04}_{-0.03}$	$0.97^{+0.12}_{-0.08}$	$2.1^{+0.3}_{-0.2}$	$2.1^{+0.4}_{-1.0}$	$1.76^{+0.03}_{-0.07}$	disc
0141980301	539.2/500	0.06 ± 0.02	$0.96^{+0.05}_{-0.03}$	$1.9^{+0.2}_{-0.1}$	$0.9^{+0.2}_{-0.3}$	$1.59^{+0.02}_{-0.01}$	disc
0650510101	1964.8/1658	$0.10^{+0.05}_{-0.08}$	$0.99^{+0.01}_{-0.02}$	$1.98^{+0.03}_{-0.05}$	1.18 ± 0.07	1.322 ± 0.006	disc
0650510201	2422.2/1967	0.090 ± 0.005	1.05 ± 0.01	2.06 ± 0.03	1.08 ± 0.05	$1.789^{+0.006}_{-0.005}$	disc
			NGC 1313 X-1				
0106860101	443.6/473	0.21 ± 0.02	0.26 ± 0.03	1.69 ± 0.05	1.8 ± 0.4	$7.6^{+0.3}_{-0.2}$	HUL
0150280301	271.3/254	$0.39^{+0.04}_{-0.03}$	2^{+2}_{-1}	$2.5^{+0.3}_{-0.2}$	> 20	$15.9^{+0.2}_{-0.3}$	SUL
0150280601	323.6/327	0.27 ± 0.03	$0.38^{+0.05}_{-0.06}$	$1.9^{+0.1}_{-0.2}$	$1.7^{+0.5}_{-0.6}$	$11.2^{+2.8}_{-0.5}$	HUL/SUL
0205230301	574.6/601	$0.44^{+0.03}_{-0.04}$	$0.08^{+0.01}_{-0.03}$	$2.35^{+0.03}_{-0.04}$	12^{+7}_{-9}	16 ± 1	SUL
0205230501	224.9/222	0.25 ± 0.03	$0.29^{+0.05}_{-0.04}$	$1.75^{+0.09}_{-0.10}$	1.5 ± 0.3	$9.6^{+0.2}_{-0.4}$	HUL
0205230601	219.8/218	0.27 ± 0.04	$0.23^{+0.04}_{-0.03}$	$1.72^{+0.07}_{-0.08}$	1.3 ± 0.3	$8.1^{+0.4}_{-0.2}$	HUL
0405090101	1657.9/1457	0.26 ± 0.01	$0.227^{+0.009}_{-0.008}$	1.68 ± 0.02	$1.33^{+0.07}_{-0.05}$	$6.92^{+0.07}_{-0.05}$	HUL

Table A.1: continued

Obs. ID[a]	χ^2/dof[b]	N_H[c]	kT_{in}[d]	Γ[e]	F_{PL}/F_{disc}[f] (0.3–1 keV)	L_X[g] (0.3–10 keV)	Spectral regime[h]
			NGC 1313 X-2				
0106860101	167.6/185	$0.39^{+0.05}_{-0.06}$	$2.0^{+0.9}_{-0.2}$	$3.2^{+0.3}_{-0.5}$	3 ± 1	$3.0^{+0.2}_{-0.1}$	disc
0150280301	412.2/423	0.22 ± 0.03	1.6 ± 0.3	1.7 ± 0.2	$2.8^{+0.7}_{-1.0}$	$8.6^{+0.2}_{-0.3}$	disc
0150280601	183.1/193	0.27 ± 0.04	$1.0^{+0.4}_{-0.3}$	$2.3^{+0.1}_{-0.2}$	11^{+6}_{-10}	$3.3^{+0.2}_{-0.3}$	disc/HUL
0205230301	546.4/580	$0.29^{+0.04}_{-0.03}$	$1.9^{+0.1}_{-0.2}$	$2.1^{+0.4}_{-0.2}$	$2.5^{+0.4}_{-0.3}$	9.9 ± 0.2	disc
0205230501	282.2/280	0.36 ± 0.04	$2.1^{+0.5}_{-0.3}$	3.0 ± 0.3	4 ± 1	3.0 ± 0.1	disc/SUL
0205230601	344.2/356	$0.30^{+0.12}_{-0.06}$	2.1 ± 0.1	$2.4^{+0.9}_{-0.5}$	2.1 ± 0.3	9.5 ± 0.3	disc
0301860101	735.1/732	$0.29^{+0.06}_{-0.03}$	$1.76^{+0.08}_{-0.06}$	$2.3^{+0.5}_{-0.2}$	1.6 ± 0.2	9.2 ± 0.5	disc
0405090101	1402.0/1484	$0.27^{+0.02}_{-0.01}$	$1.71^{+0.11}_{-0.08}$	$1.93^{+0.13}_{-0.07}$	2.9 ± 0.2	$8.7^{+0.2}_{-0.3}$	disc
			IC 342 X-1				
0093640901	145.3/163	$0.53^{+0.15}_{-0.09}$	$0.4^{+0.2}_{-0.1}$	$1.55^{+0.09}_{-0.11}$	4 ± 3	4.4 ± 0.5	disc/HUL
0206890201	482.0/486	$0.66^{+0.07}_{-0.06}$	$0.33^{+0.06}_{-0.05}$	1.66 ± 0.03	1.8 ± 0.4	$5.6^{+0.1}_{-0.2}$	HUL
			IC 342 X-2				
0093640901	48.9/49	$2.3^{+0.4}_{-0.2}$	2.1 ± 0.2	> -3	8^{+4}_{-5}	3.7 ± 0.2	disc/HUL/SUL
0206890201	344.7/389	$1.8^{+0.4}_{-0.1}$	$3.2^{+0.1}_{-0.3}$	8^{+2}_{-1}	3^{+2}_{-1}	3.73 ± 0.08	disc/SUL
			NGC 2403 X-1				
0164560901	344.6/333	$0.11^{+0.04}_{-0.05}$	$1.15^{+0.10}_{-0.09}$	$2.0^{+0.5}_{-0.3}$	< 1	$1.6^{+0.1}_{-0.2}$	disc
			Ho II X-1				
0112520601	637.9/684	0.11 ± 0.01	0.36 ± 0.02	2.38 ± 0.07	$3.3^{+1.1}_{-0.7}$	$10.4^{+0.2}_{-0.1}$	SUL
0200470101	1244.2/1118	$0.106^{+0.006}_{-0.005}$	0.34 ± 0.01	2.36 ± 0.03	$3.0^{+0.5}_{-0.2}$	10.13 ± 0.06	SUL
0561580401	846.6/753	0.098 ± 0.006	0.21 ± 0.01	2.46 ± 0.04	2.4 ± 0.3	$4.57^{+0.06}_{-0.07}$	SUL

Table A.1: continued

Obs. ID[a]	χ^2/dof[b]	N_H[c]	kT_in[d]	Γ[e]	$F_\mathrm{PL}/F_\mathrm{disc}$[f] (0.3–1 keV)	L_X[g] (0.3–10 keV)	Spectral regime[h]
			M81 X-6				
0111800101	1018.8/955	0.31 ± 0.03	1.42 ± 0.02	$2.8^{+0.3}_{-0.2}$	$1.7^{+0.2}_{-0.1}$	$7.1^{+0.2}_{-0.3}$	disc
0112521001	222.3/200	$0.33^{+0.14}_{-0.07}$	$1.9^{+0.2}_{-0.1}$	$2.6^{+1.0}_{-0.6}$	$2.2^{+0.7}_{-0.5}$	$7.7^{+0.3}_{-0.2}$	disc
0112521101	191.2/194	$0.20^{+0.10}_{-0.05}$	$1.4^{+0.4}_{-0.2}$	$1.6^{+1.4}_{-0.5}$	$1.1^{+0.5}_{-0.8}$	$7.5^{+0.3}_{-0.2}$	disc
0200980101	413.7/397	$0.17^{+0.03}_{-0.04}$	$1.5^{+0.3}_{-0.2}$	1.5 ± 0.3	$1.3^{+0.4}_{-0.5}$	$9.4^{+0.5}_{-0.4}$	disc
			Ho IX X-1				
0111800101	709.8/671	0.23 ± 0.02	$1.48^{+0.05}_{-0.06}$	2.2 ± 0.2	1.9 ± 0.1	24.5 ± 0.2	disc
0112521001	832.1/819	0.15 ± 0.01	$0.31^{+0.04}_{-0.03}$	$1.65^{+0.03}_{-0.04}$	4.1 ± 0.9	12.4 ± 0.2	HUL
0112521101	829.8/874	0.187 ± 0.006	< 0.01	1.83 ± 0.02	-	$13.8^{+0.4}_{-0.5}$	HUL
0200980101	1662.0/1617	$0.135^{+0.003}_{-0.006}$	0.28 ± 0.01	$1.45^{+0.01}_{-0.02}$	1.74 ± 0.09	$10.71^{+0.11}_{-0.07}$	HUL
			NGC 4190 ULX1				
0654650201	488.1/519	$0.15^{+0.07}_{-0.03}$	$1.38^{+0.07}_{-0.04}$	$2.4^{+0.6}_{-0.3}$	$1.1^{+0.3}_{-0.2}$	$4.82^{+0.11}_{-0.09}$	disc
0654650301	718.6/752	0.13 ± 0.02	$1.5^{+0.2}_{-0.1}$	$1.66^{+0.15}_{-0.09}$	2.1 ± 0.4	8.8 ± 0.1	disc
			NGC 4559 ULX2				
0152170501	439.5/465	0.18 ± 0.02	$0.17^{+0.02}_{-0.01}$	$2.18^{+0.04}_{-0.05}$	1.8 ± 0.3	$6.6^{+0.2}_{-0.4}$	SUL
			NGC 4736 ULX1				
0404980101	541.4/519	0.05 ± 0.02	$0.90^{+0.06}_{-0.05}$	2.2 ± 0.1	1.7 ± 0.3	1.93 ± 0.03	disc

Table A.1: continued

Obs. ID[a]	χ^2/dof[b]	N_{H}[c]	kT_{in}[d]	Γ[e]	$F_{\mathrm{PL}}/F_{\mathrm{disc}}$[f] (0.3–1 keV)	L_{X}[g] (0.3–10 keV)	Spectral regime[h]
			NGC 5204 X-1				
0142770101	411.5/465	0.049 ± 0.009	0.26 ± 0.02	1.85 ± 0.05	2.3 ± 0.4	$4.13^{+0.15}_{-0.09}$	HUL
0405690101	665.0/572	0.10 ± 0.01	0.37 ± 0.03	2.35 ± 0.08	4 ± 1	$7.8^{+0.2}_{-0.3}$	SUL
0405690201	782.0/738	$0.102^{+0.010}_{-0.009}$	$0.36^{+0.01}_{-0.02}$	$2.22^{+0.06}_{-0.07}$	2.2 ± 0.4	7.0 ± 0.1	SUL
0405690501	626.3/610	0.053 ± 0.008	0.31 ± 0.02	$1.83^{+0.06}_{-0.07}$	1.4 ± 0.2	$5.47^{+0.06}_{-0.11}$	HUL
			NGC 5408 X-1				
0112290601	297.8/317	0.02 ± 0.01	0.22 ± 0.01	2.5 ± 0.1	$0.6^{+0.2}_{-0.1}$	$7.6^{+0.4}_{-0.1}$	SUL
0112290701	106.1/138	0.05 ± 0.02	0.18 ± 0.02	2.7 ± 0.1	$1.2^{+0.3}_{-0.2}$	8.5 ± 0.6	SUL
0302900101	1166.3/930	$0.065^{+0.003}_{-0.004}$	$0.183^{+0.004}_{-0.003}$	$2.68^{+0.02}_{-0.03}$	$1.39^{+0.08}_{-0.05}$	$6.90^{+0.10}_{-0.07}$	SUL
0500750101	763.0/629	$0.077^{+0.006}_{-0.007}$	$0.179^{+0.007}_{-0.006}$	2.62 ± 0.04	1.5 ± 0.1	6.6 ± 0.2	SUL
0653380201	1448.3/1059	0.074 ± 0.004	$0.188^{+0.005}_{-0.004}$	2.55 ± 0.02	$1.54^{+0.09}_{-0.05}$	$7.03^{+0.05}_{-0.03}$	SUL
0653380301	1602.6/1126	$0.068^{+0.003}_{-0.004}$	0.194 ± 0.004	2.56 ± 0.02	$1.66^{+0.10}_{-0.06}$	$7.79^{+0.04}_{-0.11}$	SUL
0653380401	1222.5/1005	0.071 ± 0.004	$0.184^{+0.005}_{-0.004}$	$2.61^{+0.02}_{-0.03}$	$1.54^{+0.09}_{-0.05}$	$7.55^{+0.11}_{-0.06}$	SUL
0653380501	1246.3/1030	$0.061^{+0.004}_{-0.003}$	$0.194^{+0.004}_{-0.005}$	$2.47^{+0.03}_{-0.02}$	$1.26^{+0.07}_{-0.04}$	$7.43^{+0.07}_{-0.12}$	SUL
			NGC 5907 ULX				
0145190201	152.1/173	$0.93^{+0.06}_{-0.05}$	0.04 ± 0.02	1.72 ± 0.05	7 ± 6	46^{+1}_{-2}	HUL
0145190101[j]	204.5/168	$1.5^{+0.2}_{-0.3}$	$0.13^{+0.02}_{-0.01}$	$1.87^{+0.08}_{-0.10}$	$0.4^{+0.3}_{-0.2}$	$33.3^{+1.8}_{-0.6}$	HUL
0673920301	141.5/135	$0.87^{+0.08}_{-0.06}$	$0.050^{+0.009}_{-0.007}$	$1.41^{+0.06}_{-0.05}$	1.8 ± 0.7	16^{+2}_{-1}	HUL
			NGC 6946 X-1				
0200670101	35.8/26	$0.3^{+0.2}_{-0.1}$	$0.19^{+0.05}_{-0.04}$	$1.5^{+0.2}_{-0.4}$	$0.19^{+0.13}_{-0.07}$	15^{+10}_{-2}	HUL
0200670301	149.2/157	0.12 ± 0.04	$0.21^{+0.03}_{-0.02}$	$2.3^{+0.1}_{-0.2}$	1.0 ± 0.3	$8.6^{+0.6}_{-0.7}$	SUL
0200670401	60.3/54	< 0.1	0.24 ± 0.05	$1.9^{+0.3}_{-0.1}$	0.8 ± 0.3	$8.2^{+0.9}_{-0.7}$	HUL/SUL
0500730201	425.9/406	0.20 ± 0.03	0.18 ± 0.01	$2.26^{+0.08}_{-0.07}$	0.62 ± 0.07	$9.8^{+1.2}_{-0.6}$	SUL
0500730101	290.2/273	$0.07^{+0.03}_{-0.02}$	0.23 ± 0.02	$2.05^{+0.09}_{-0.08}$	0.8 ± 0.1	$7.9^{+0.2}_{-0.4}$	HUL/SUL

Table A.2: Fractional variability

Obs. ID[a]	F_{var}[b]			Obs. ID[a]	F_{var}[b]		
	0.3–10 keV	0.3–1 keV	1–10 keV		0.3–10 keV	0.3–1 keV	1–10 keV
NGC 55 ULX							
0028740201	16.2 ± 0.4	9.1 ± 0.7	24.0 ± 0.5	0028740101	19.1 ± 0.7	17 ± 1	20.6 ± 0.9
0655050101	8.6 ± 0.4	8.5 ± 0.6	8.6 ± 0.6				
M31 ULX1							
0600660201	1.2 ± 0.7	< 2	2.0 ± 0.7	0600660301	< 1	< 2	< 2
0600660401	< 2	< 3	< 3	0600660501	< 2	< 2	< 3
0600660601	< 5	4 ± 1	< 2				
NGC 253 XMM2							
0125960101	24 ± 2	-	26 ± 2	0110900101	< 10	-	-
0152020101	36.6 ± 0.9	25 ± 2	42 ± 1	0304850901	11 ± 4	-	< 10
0304851001	7 ± 4	-	12 ± 4	0304851201	< 6	-	< 7
NGC 253 ULX2							
0125960101	8 ± 1	-	9 ± 1	0110900101	5 ± 3	-	6 ± 3
0152020101	5 ± 1	-	5 ± 2	0304850901	7 ± 3	-	8 ± 3
0304851001	< 9	-	< 10	0304851201	< 10	-	< 5
0304851301	11 ± 4	-	13 ± 5				

[a] *XMM-Newton* observation identifiers. [b] Fractional variability in per cent, calculated from light curves in the appropriate energy band with 200s temporal binning. Dashes are shown for observations where fractional variability was not calculated in a particular energy band, as there were on average fewer than 20 counts per temporal bin. Errors and limits correspond to the 1σ uncertainty regions.

Table A.2: continued

Obs. ID[a]	F_{var}[b]			Obs. ID[a]	F_{var}[b]		
	0.3–10 keV	0.3–1 keV	1–10 keV		0.3–10 keV	0.3–1 keV	1–10 keV
			M33 X-8				
0102640401	< 3	< 9	< 3	0102640101	1.5 ± 0.7	< 4	< 3
0102640701	3 ± 2	5 ± 3	3 ± 2	0102641001	3 ± 2	9 ± 3	< 5
0102642001	< 2	< 6	< 3	0102642101	1.6 ± 0.9	< 7	2 ± 1
0102642301	1.6 ± 0.8	< 3	< 3	0141980601	< 2	< 4	< 2
0141980801	< 1	< 2	< 2	0141980101	< 4	7 ± 3	< 5
0141980301	< 2	< 5	< 4	0650510101	3.1 ± 0.3	4.5 ± 0.7	2.4 ± 0.5
0650510201	0.7 ± 0.5	1.3 ± 0.8	1.3 ± 0.4				
			NGC 1313 X-1				
0106860101	6 ± 1	6 ± 3	7 ± 2	0150280301	5 ± 2	12 ± 3	< 5
0150280601	< 5	< 6	4 ± 2	0205230301	5 ± 1	5 ± 3	6 ± 1
0205230501	< 7	-	< 9	0205230601	< 4	< 12	< 5
0405090101	2.6 ± 0.8	< 3	3.4 ± 0.9				
			NGC 1313 X-2				
0106860101	< 5	< 9	5 ± 4	0150280301	8 ± 1	< 7	8 ± 1
0150280601	4 ± 3	< 8	7 ± 3	0205230301	< 3	< 6	< 5
0205230501	< 7	< 8	< 5	0205230601	5 ± 2	6 ± 5	4 ± 2
0301860101	< 3	7 ± 3	< 3	0405090101	9.1 ± 0.4	< 8	10.7 ± 0.5
			IC 342 X-1				
0093640901	5 ± 3	-	6 ± 3	0206890201	< 6	-	3 ± 2
			IC 342 X-2				
0093640901	< 8	-	< 8	0206890201	5 ± 2	-	5 ± 2

Table A.2: continued

| Obs. ID[a] | F_{var}[b] | | | Obs. ID[a] | F_{var}[b] | | |
	0.3–10 keV	0.3–1 keV	1–10 keV		0.3–10 keV	0.3–1 keV	1–10 keV
			NGC 2403 X-1				
0164560901	< 6	-	< 10				
			Ho II X-1				
0112520601	< 3	3 ± 1	< 3	0200470101	2.0 ± 0.5	< 2	3.1 ± 0.7
0561580401	20.7 ± 0.5	20.0 ± 0.7	21.2 ± 0.8				
			M81 X-6				
0111800101	6.1 ± 0.7	8 ± 2	6.5 ± 0.9	0112521001	< 5	-	< 6
0112521101	7 ± 2	11 ± 7	< 8	0200980101	< 7	-	< 7
			Ho IX X-1				
0111800101	< 2	5 ± 3	< 4	0112521001	< 2	< 4	< 2
0112521101	< 2	< 3	< 4	0200980101	< 2	< 3	2 ± 1
			NGC 4190 ULX1				
0654650201	< 3	< 9	< 4	0654650301	< 2	< 4	< 3
			NGC 4559 ULX2				
0152170501	7 ± 2	9 ± 2	6 ± 3				
			NGC 4736 ULX1				
0404980101	16 ± 1	6 ± 3	22 ± 1				
			NGC 5204 X-1				
0142770101	4 ± 2	< 5	4 ± 3	0405690101	< 4	5 ± 2	3 ± 2
0405690201	3 ± 1	3 ± 2	< 10	0405690501	< 3	< 4	< 6

Table A.2: continued

Obs. ID[a]	F_{var}[b]			Obs. ID[a]	F_{var}[b]		
	0.3–10 keV	0.3–1 keV	1–10 keV		0.3–10 keV	0.3–1 keV	1–10 keV
NGC 5408 X-1							
0112290601	5 ± 1	3 ± 2	7 ± 3	0112290701	< 4	< 9	< 7
0302900101	9.8 ± 0.3	7.2 ± 0.5	15.4 ± 0.6	0500750101	14.9 ± 0.6	10.4 ± 0.8	23 ± 1
0653380201	6.3 ± 0.4	4.5 ± 0.6	9.4 ± 0.7	0653380301	7.1 ± 0.3	5.5 ± 0.5	10.2 ± 0.5
0653380401	8.6 ± 0.3	6.0 ± 0.5	13.2 ± 0.6	0653380501	8.2 ± 0.3	4.6 ± 0.6	13.4 ± 0.6
NGC 5907 ULX							
0145190201	8 ± 2	-	8 ± 2	0145190101	10 ± 2	-	10 ± 2
0673920301	9 ± 4	-	7 ± 5				
NGC 6946 X-1							
0200670101	10 ± 6	< 20	< 10	0200670301	14 ± 2	< 8	18 ± 3
0200670401	< 8	-	12 ± 6	0500730201	24 ± 1	13 ± 2	33 ± 1
0500730101	27 ± 1	15 ± 2	35 ± 2				

Bibliography

Abramowicz M. A., Czerny B., Lasota J. P., Szuszkiewicz E., 1988, ApJ, 332, 646

Anderson J., van der Marel R. P., 2010, ApJ, 710, 1032

Assef R. J., Kochanek C. S., Brodwin M., Cool R., Forman W., Gonzalez A. H., Hickox R. C., Jones C., Le Floc'h E., Moustakas J., Murray S. S., Stern D., 2010, ApJ, 713, 970

Bachetti M., et al., 2013, ApJ, 778, 163

Barthel P. D., 1989, ApJ, 336, 606

Bauer M., Pietsch W., Trinchieri G., Breitschwerdt D., Ehle M., Freyberg M. J., Read A. M., 2008, A&A, 489, 1029

Becker R. H., White R. L., Helfand D. J., 1995, ApJ, 450, 559

Begelman M. C., Volonteri M., Rees M. J., 2006, MNRAS, 370, 289

Belczynski K., Bulik T., Fryer C. L., Ruiter A., Valsecchi F., Vink J. S., Hurley J. R., 2010, ApJ, 714, 1217

Belczynski K., Taam R. E., 2008, ApJ, 685, 400

Belloni T., 2010, in Belloni T., ed., Lecture Notes in Physics, Vol. 794, The Jet Paradigm. Springer Berlin Heidelberg, pp 53–84

Bellovary J. M., Governato F., Quinn T. R., Wadsley J., Shen S., Volonteri M., 2010, ApJ, 721, L148

Berghea C. T., Dudik R. P., 2012, ApJ, 751, 104

Berghea C. T., Weaver K. A., Colbert E. J. M., Roberts T. P., 2008, ApJ, 687, 471

Blandford R. D., Rees M. J., 1974, MNRAS, 169, 395

Bromm V., Coppi P. S., Larson R. B., 2002, ApJ, 564, 23

Burrows D. N., et al., 2004, in Flanagan K. A., Siegmund O. H. W., eds, Society of Photo-Optical Instrumentation Engineers (SPIE) Conference Series Vol. 5165 of Society of Photo-Optical Instrumentation Engineers (SPIE) Conference Series, The Swift X-Ray Telescope. pp 201–216

Caballero-García M. D., Fabian A. C., 2010, MNRAS, 402, 2559

Caccianiga A., Severgnini P., Della Ceca R., Maccacaro T., Cocchia F., Barcons X., Carrera F. J., Matute I., McMahon R. G., Page M. J., Pietsch W., Sbarufatti B., Schwope A., Tedds J. A., Watson M. G., 2008, A&A, 477, 735

Carroll B. W., Ostlie D. A., 2003, An introduction to modern astrophysics. Pearson

Cash W., 1979, ApJ, 228, 939

Colbert E. J. M., Mushotzky R. F., 1999, ApJ, 519, 89

Colbert E. J. M., Ptak A. F., 2002, ApJS, 143, 25

Condon J. J., Cotton W. D., Greisen E. W., Yin Q. F., Perley R. A., Taylor G. B., Broderick J. J., 1998, AJ, 115, 1693

Corbel S., Tomsick J. A., Kaaret P., 2006, ApJ, 636, 971

Cseh D., et al., 2012, ApJ, 749, 17

Cseh D., Grisé F., Corbel S., Kaaret P., 2011, ApJ, 728, L5

Dalcanton J. J., et al., 2009, ApJS, 183, 67

Davis D. S., Mushotzky R. F., 2004, ApJ, 604, 653

de Vaucouleurs G., de Vaucouleurs A., Corwin Jr. H. G., Buta R. J., Paturel G., Fouque P., 1991, Third Reference Catalogue of Bright Galaxies, Vols 1–3. Springer-Verlag, Berlin, Heidelberg, New York, p. 7

Dewangan G. C., Griffiths R. E., Rao A. R., 2006, ApJ, 641, L125

Dewangan G. C., Miyaji T., Griffiths R. E., Lehmann I., 2004, ApJ, 608, L57

Dickey J. M., Lockman F. J., 1990, ARA&A, 28, 215

Dolan J. F., 1970, AJ, 75, 223

Done C., Davis S. W., Jin C., Blaes O., Ward M., 2012, MNRAS, 420, 1848

Done C., Gierliński M., 2003, MNRAS, 342, 1041

Done C., Gierliński M., Kubota A., 2007, A&A Rev., 15, 1

Done C., Kubota A., 2006, MNRAS, 371, 1216

Done C., Nayakshin S., 2001, MNRAS, 328, 616

Done C., Wardziński G., Gierliński M., 2004, MNRAS, 349, 393

Dotan C., Shaviv N. J., 2011, MNRAS, 413, 1623

Ebisuzaki T., et al., 2001, ApJ, 562, L19

Einstein A., 1916, Annalen der Physik, 354, 769

Eisenhauer F., et al., 2005, ApJ, 628, 246

Elvis M., Page C. G., Pounds K. A., Ricketts M. J., Turner M. J. L., 1975, Nature, 257, 656

Esin A. A., McClintock J. E., Narayan R., 1997, ApJ, 489, 865

Fabbiano G., 1989, ARA&A, 27, 87

Fabbiano G., Zezas A., Murray S. S., 2001, ApJ, 554, 1035

Farrell S., et al., 2012, ApJ, 747, L13

Farrell S. A., et al., 2011, AN, 332, 392

Farrell S. A., Webb N. A., Barret D., Godet O., Rodrigues J. M., 2009, Nature, 460, 73

Fender R., 2006, in Lewin W. H. G., van der Klis M., eds, Compact Stellar X-ray Sources. Cambridge Univ. Press, Cambridge, pp 381–419

Feng H., Kaaret P., 2006a, ApJ, 653, 536

Feng H., Kaaret P., 2006b, ApJ, 650, L75

Feng H., Kaaret P., 2007, ApJ, 668, 941

Feng H., Kaaret P., 2008, ApJ, 675, 1067

Feng H., Kaaret P., 2009, ApJ, 696, 1712

Feng H., Kaaret P., 2010, ApJ, 712, L169

Feng H., Soria R., 2011, New Astron. Rev., 55, 166

Forman W., Jones C., Cominsky L., Julien P., Murray S., Peters G., Tananbaum H., Giacconi R., 1978, ApJS, 38, 357

Fransson C., Lundqvist P., Chevalier R. A., 1996, ApJ, 461, 993

Fridriksson J. K., Homan J., Lewin W. H. G., Kong A. K. H., Pooley D., 2008, ApJS, 177, 465

Gao Y., Wang Q. D., Appleton P. N., Lucas R. A., 2003, ApJ, 596, L171

Gebhardt K., Rich R. M., Ho L. C., 2005, ApJ, 634, 1093

Georgantopoulos I., et al., 2013, A&A, 555, A43

Ghez A. M., et al., 2008, ApJ, 689, 1044

Giacconi R., et al., 1979, ApJ, 230, 540

Giacconi R., Gursky H., Kellogg E., Schreier E., Tananbaum H., 1971b, ApJ, 167, L67

Giacconi R., Gursky H., Paolini F. R., Rossi B. B., 1962, Physical Review Letters, 9, 439

Giacconi R., Kellogg E., Gorenstein P., Gursky H., Tananbaum H., 1971a, ApJ, 165, L27

Gierliński M., Done C., Page K., 2008, MNRAS, 388, 753

Gierliński M., Done C., Page K., 2009, MNRAS, 392, 1106

Gierliński M., Zdziarski A. A., 2005, MNRAS, 363, 1349

Gilfanov M., Grimm H.-J., Sunyaev R., 2004, Nuclear Physics B Proceedings Supplements, 132, 369

Gilli R., Comastri A., Hasinger G., 2007, A&A, 463, 79

Gladstone J. C., Copperwheat C., Heinke C. O., Roberts T. P., Cartwright T. F., Levan A. J., Goad M. R., 2013, ApJS, 206, 14

Gladstone J. C., Roberts T. P., 2009, MNRAS, 397, 124

Gladstone J. C., Roberts T. P., Done C., 2009, MNRAS, 397, 1836

Goad M. R., Roberts T. P., Knigge C., Lira P., 2002, MNRAS, 335, L67

Goad M. R., Roberts T. P., Reeves J. N., Uttley P., 2006, MNRAS, 365, 191

Godet O., Barret D., Webb N. A., Farrell S. A., Gehrels N., 2009, ApJ, 705, L109

Godet O., et al., 2012, ApJ, 752, 34

Gonçalves A. C., Soria R., 2006, MNRAS, 371, 673

Greiner J., Cuby J. G., McCaughrean M. J., 2001, Nature, 414, 522

Grimm H.-J., Gilfanov M., Sunyaev R., 2003, MNRAS, 339, 793

Grisé F., Kaaret P., Corbel S., Feng H., Cseh D., Tao L., 2012, ApJ, 745, 123

Grisé F., Kaaret P., Feng H., Kajava J. J. E., Farrell S. A., 2010, ApJ, 724, L148

Grisé F., Kaaret P., Pakull M. W., Motch C., 2011, ApJ, 734, 23

Grisé F., Pakull M. W., Soria R., Motch C., Smith I. A., Ryder S. D., Böttcher M., 2008, A&A, 486, 151

Gruendl R. A., Vogel S. N., Davis D. S., Mulchaey J. S., 1993, ApJ, 413, L81

Harrison F. A., et al., 2010, in Society of Photo-Optical Instrumentation Engineers (SPIE) Conference Series Vol. 7732 of Society of Photo-Optical Instrumentation Engineers (SPIE) Conference Series, The Nuclear Spectroscopic Telescope Array (NuSTAR)

Heger A., Fryer C. L., Woosley S. E., Langer N., Hartmann D. H., 2003, ApJ, 591, 288

Heil L. M., Vaughan S., Roberts T. P., 2009, MNRAS, 397, 1061

Henze M., Pietsch W., Haberl F., Greiner J., 2009, The Astronomer's Telegram, 2356, 1

Herrmann K. A., Ciardullo R., Feldmeier J. J., Vinciguerra M., 2008, ApJ, 683, 630

Hodge P. W., Kennicutt Jr. R. C., 1983, AJ, 88, 296

Holt S. S., 1993, A&AS, 97, 367

Holt S. S., Boldt E. A., Schwartz D. A., Serlemitsos P. J., Bleach R. D., 1971, ApJ, 166, L65

Hopman C., Portegies Zwart S. F., Alexander T., 2004, ApJ, 604, L101

Immler S., Lewin W. H. G., 2003, in K. Weiler ed., Supernovae and Gamma-Ray Bursters Vol. 598 of Lecture Notes in Physics, Berlin Springer Verlag, X-Ray Supernovae. pp 91–111

Impiombato D., Zampieri L., Falomo R., Grisé F., Soria R., 2011, AN, 332, 375

Irwin J. A., Bregman J. N., Athey A. E., 2004, ApJ, 601, L143

Islam R. R., Taylor J. E., Silk J., 2004, MNRAS, 354, 427

Isobe N., Kubota A., Sato H., Mizuno T., 2012, PASJ, 64, 119

Iwan D., Shafer R. A., Marshall F. E., Boldt E. A., Mushotzky R. F., Stottlemyer A., 1982, ApJ, 260, 111

Jacobs B. A., Rizzi L., Tully R. B., Shaya E. J., Makarov D. I., Makarova L., 2009, AJ, 138, 332

Jansen F., Lumb D., Altieri B., Clavel J., Ehle M., et al., 2001, A&A, 365, L1

Jenkins L. P., Roberts T. P., Ward M. J., Zezas A., 2004, MNRAS, 352, 1335

Jonker P. G., Torres M. A. P., Fabian A. C., Heida M., Miniutti G., Pooley D., 2010, MNRAS, 407, 645

Kaaret P., Alonso-Herrero A., Gallagher J. S., Fabbiano G., Zezas A., Rieke M. J., 2004, MNRAS, 348, L28

Kaaret P., Corbel S., 2009, ApJ, 697, 950

Kaaret P., Corbel S., Prestwich A. H., Zezas A., 2003, Science, 299, 365

Kaaret P., Feng H., 2007, ApJ, 669, 106

Kaaret P., Feng H., 2009, ApJ, 702, 1679

Kaaret P., Feng H., Gorski M., 2009, ApJ, 692, 653

Kaaret P., Prestwich A. H., Zezas A., Murray S. S., Kim D.-W., Kilgard R. E., Schlegel E. M., Ward M. J., 2001, MNRAS, 321, L29

Kaaret P., Simet M. G., Lang C. C., 2006, ApJ, 646, 174

Kajava J. J. E., Poutanen J., 2009, MNRAS, 398, 1450

Kajava J. J. E., Poutanen J., Farrell S. A., Grisé F., Kaaret P., 2012, MNRAS, 422, 990

Karachentsev I. D., et al., 2002, A&A, 385, 21

Karachentsev I. D., et al., 2003, A&A, 398, 467

Karachentsev I. D., Sharina M. E., Huchtmeier W. K., 2000, A&A, 362, 544

Kaur A., et al., 2012, A&A, 538, A49

Kawashima T., Ohsuga K., Mineshige S., Yoshida T., Heinzeller D., Matsumoto R., 2012, ApJ, 752, 18

Keller C. U., 1995, Experientia, 51, 710

Kerr R. P., 1963, Physical Review Letters, 11, 237

Kim D.-W., Fabbiano G., 2010, ApJ, 721, 1523

King A. R., 2004, MNRAS, 347, L18

King A. R., 2008, MNRAS, 385, L113

King A. R., 2009, MNRAS, 393, L41

King A. R., Dehnen W., 2005, MNRAS, 357, 275

King A. R., Kolb U., Burderi L., 1996, ApJ, 464, L127

King A. R., Pounds K. A., 2003, MNRAS, 345, 657

Komatsu E., et al., 2009, ApJS, 180, 330

Komossa S., 2012, Advances in Astronomy, 2012

Kong A. K. H., Yang Y. J., Yen T.-C., Feng H., Kaaret P., 2010, ApJ, 722, 1816

Kormendy J., Richstone D., 1995, ARA&A, 33, 581

Kubota A., Done C., Makishima K., 2002, MNRAS, 337, L11

Kuntz K. D., Gruendl R. A., Chu Y.-H., Chen C.-H. R., Still M., Mukai K., Mushotzky R. F., 2005, ApJ, 620, L31

Lang C. C., Kaaret P., Corbel S., Mercer A., 2007, ApJ, 666, 79

Lasota J.-P., Alexander T., Dubus G., Barret D., Farrell S. A., Gehrels N., Godet O., Webb N. A., 2011, ApJ, 735, 89

Lauberts A., 1982, ESO/Uppsala survey of the ESO(B) atlas. ESO, Garching

Liu J., Bregman J. N., McClintock J. E., 2009, ApJ, 690, L39

Liu J.-F., Bregman J., Miller J., Kaaret P., 2007, ApJ, 661, 165

Liu J.-F., Bregman J. N., 2005, ApJS, 157, 59

Liu J.-F., Bregman J. N., Seitzer P., 2002, ApJ, 580, L31

Liu J.-F., Bregman J. N., Seitzer P., 2004, ApJ, 602, 249

Madau P., Rees M. J., 2001, ApJ, 551, L27

Madhusudhan N., Justham S., Nelson L., Paxton B., Pfahl E., Podsiadlowski P., Rappaport S., 2006, ApJ, 640, 918

Madrid J. P., et al., 2010, ApJ, 722, 1707

Magorrian J., et al., 1998, AJ, 115, 2285

Makishima K., et al., 2000, ApJ, 535, 632

Mapelli M., Moore B., Giordano L., Mayer L., Colpi M., Ripamonti E., Callegari S., 2008, MNRAS, 383, 230

Mapelli M., Ripamonti E., Zampieri L., Colpi M., Bressan A., 2010, MNRAS, 408, 234

Massey P., DeGioia-Eastwood K., Waterhouse E., 2001, AJ, 121, 1050

Mateos S., Alonso-Herrero A., Carrera F. J., Blain A., Severgnini P., Caccianiga A., Ruiz A., 2013, MNRAS

Matsumoto H., Tsuru T. G., Koyama K., Awaki H., Canizares C. R., Kawai N., Matsushita S., Kawabe R., 2001, ApJ, 547, L25

McCammon D., Sanders W. T., 1990, ARA&A, 28, 657

McClintock J. E., Remillard R. A., 2006, in Lewin W. H. G., van der Klis M., eds, Compact Stellar X-ray Sources. Cambridge Univ. Press, Cambridge, pp 157–213

McHardy I. M., Koerding E., Knigge C., Uttley P., Fender R. P., 2006, Nature, 444, 730

Mendez M., van der Klis M., 1997, ApJ, 479, 926

Merloni A., Heinz S., di Matteo T., 2003, MNRAS, 345, 1057

Middleton M., Done C., Ward M., Gierliński M., Schurch N., 2009, MNRAS, 394, 250

Middleton M. J., Roberts T. P., Done C., Jackson F. E., 2011a, MNRAS, 411, 644

Middleton M. J., Sutton A. D., Roberts T. P., 2011b, MNRAS, 417, 464

Middleton M. J., Sutton A. D., Roberts T. P., Jackson F. E., Done C., 2012, MNRAS, 420, 2969

Middleton M. J., Walton D. J., Roberts T. P., Heil L., 2013, MNRAS, in press (arXiv:1309.3134

Miller J. M., Fabbiano G., Miller M. C., Fabian A. C., 2003, ApJ, 585, L37

Miller J. M., Fabian A. C., Miller M. C., 2004, ApJ, 607, 931

Miller N. A., Mushotzky R. F., Neff S. G., 2005, ApJ, 623, L109

Mineo S., Gilfanov M., Sunyaev R., 2012, MNRAS, 419, 2095

Mitsuda K., et al., 1984, PASJ, 36, 741

Mitsuda K., et al., 2007, PASJ, 59, 1

Miyawaki R., Makishima K., Yamada S., Gandhi P., Mizuno T., Kubota A., Tsuru T. G., Matsumoto H., 2009, PASJ, 61, 263

Moretti A., Campana S., Lazzati D., Tagliaferri G., 2003, ApJ, 588, 696

Moretti A., Vattakunnel S., Tozzi P., Salvaterra R., Severgnini P., Fugazza D., Haardt F., Gilli R., 2012, A&A, 548, A87

Mucciarelli P., Zampieri L., Falomo R., Turolla R., Treves A., 2005, ApJ, 633, L101

Mushotzky R. F., Cowie L. L., Barger A. J., Arnaud K. A., 2000, Nature, 404, 459

Oda M., Gorenstein P., Gursky H., Kellogg E., Schreier E., Tananbaum H., Giacconi R., 1971, ApJ, 166, L1

Ohsuga K., Mineshige S., 2011, ApJ, 736, 2

Okada K., Dotani T., Makishima K., Mitsuda K., Mihara T., 1998, PASJ, 50, 25

Orosz J. A., et al., 2007, Nature, 449, 872

Osterbrock D. E., 1977, ApJ, 215, 733

Pietsch W., et al., 2001, A&A, 365, L174

Pintore F., Zampieri L., 2012, MNRAS, 420, 1107

Pizzolato F., Wolter A., Trinchieri G., 2010, MNRAS, 406, 1116

Pooley D., et al., 2002, ApJ, 572, 932

Portegies Zwart S. F., Baumgardt H., Hut P., Makino J., McMillan S. L. W., 2004, Nature, 428, 724

Poutanen J., Fabrika S., Valeev A. F., Sholukhova O., Greiner J., 2013, MNRAS, 432, 506

Poutanen J., Krolik J. H., Ryde F., 1997, MNRAS, 292, L21

Poutanen J., Lipunova G., Fabrika S., Butkevich A. G., Abolmasov P., 2007, MNRAS, 377, 1187

Prestwich A. H., et al., 2007, ApJ, 669, L21

Rahoui F., Chaty S., Rodriguez J., Fuchs Y., Mirabel I. F., Pooley G. G., 2010, ApJ, 715, 1191

Rao F., Feng H., Kaaret P., 2010, ApJ, 722, 620

Rappaport S. A., Podsiadlowski P., Pfahl E., 2005, MNRAS, 356, 401

Rees M. J., 1984, ARA&A, 22, 471

Regan J. A., Haehnelt M. G., 2009, MNRAS, 396, 343

Remillard R. A., McClintock J. E., 2006, ARA&A, 44, 49

Roberts T. P., 2007, Ap&SS, 311, 203

Roberts T. P., Gladstone J. C., Goulding A. D., Swinbank A. M., Ward M. J., Goad M. R., Levan A. J., 2011, Astronomische Nachrichten, 332, 398

Roberts T. P., Kilgard R. E., Warwick R. S., Goad M. R., Ward M. J., 2006, MNRAS, 371, 1877

Roberts T. P., Levan A. J., Goad M. R., 2008, MNRAS, 387, 73

Roberts T. P., Warwick R. S., 2000, MNRAS, 315, 98

Roberts T. P., Warwick R. S., Ward M. J., Goad M. R., Jenkins L. P., 2005, MNRAS, 357, 1363

Roberts T. P., Warwick R. S., Ward M. J., Murray S. S., 2002, MNRAS, 337, 677

Rosado M., Ghosh K. K., Fuentes-Carrera I., 2008, AJ, 136, 212

Rowan-Robinson M., 1977, ApJ, 213, 635

Rozas M., Zurita A., Heller C. H., Beckman J. E., 1999, A&AS, 135, 145

Sala G., Greiner J., Ajello M., Bottacini E., Haberl F., 2007, A&A, 473, 561

Scheuer P. A. G., 1974, MNRAS, 166, 513

Schneider R., Ferrara A., Natarajan P., Omukai K., 2002, ApJ, 571, 30

Schödel R., et al., 2002, Nature, 419, 694

Schwarzschild K., 1916, Abh. Konigl. Preuss. Akad. Wissenschaften Jahre 1906,92, Berlin,1907, pp 189–196

Servillat M., Farrell S. A., Lin D., Godet O., Barret D., Webb N. A., 2011, ApJ, 743, 6

Seyfert C. K., 1943, ApJ, 97, 28

Shabala S. S., et al., 2012, MNRAS, 423, 59

Shakura N. I., Sunyaev R. A., 1973, A&A, 24, 337

Shanks T., Georgantopoulos I., Stewart G. C., Pounds K. A., Boyle B. J., Griffiths R. E., 1991, Nature, 353, 315

Silverman J. M., Filippenko A. V., 2008, ApJ, 678, L17

Sirianni M., et al., 2005, PASP, 117, 1049

Smith J. F., Courtier G. M., 1976, Royal Society of London Proceedings Series A, 350, 421

Soria R., Cropper M., Pakull M., Mushotzky R., Wu K., 2005, MNRAS, 356, 12

Soria R., Fender R. P., Hannikainen D. C., Read A. M., Stevens I. R., 2006, MNRAS, 368, 1527

Soria R., Hakala P. J., Hau G. K. T., Gladstone J. C., Kong A. K. H., 2012, MNRAS, 420, 3599

Soria R., Risaliti G., Elvis M., Fabbiano G., Bianchi S., Kuncic Z., 2009, ApJ, 695, 1614

Spitzer L., 2004, Physical Processes in the Interstellar Medium (3rd edition). Wiley-VCH Verlag GmbH & Co. KGaA, Weinheim

Staubert R., Maisack M., 1996, A&A, 305, L41

Stobbart A.-M., Roberts T. P., Wilms J., 2006, MNRAS, 368, 397

Strohmayer T. E., 2009, ApJ, 706, L210

Strohmayer T. E., Mushotzky R. F., 2003, ApJ, 586, L61

Strohmayer T. E., Mushotzky R. F., 2009, ApJ, 703, 1386

Strohmayer T. E., Mushotzky R. F., Winter L., Soria R., Uttley P., Cropper M., 2007, ApJ, 660, 580

Sunyaev R. A., Titarchuk L. G., 1980, A&A, 86, 121

Sunyaev R. A., Trümper J., 1979, Nature, 279, 506

Sutton A. D., Roberts T. P., Gladstone J. C., Farrell S. A., Reilly E., Goad M. R., Gehrels N., 2013, MNRAS, 434, 1702

Sutton A. D., Roberts T. P., Middleton M. J., 2013b, MNRAS, 435, 1758

Sutton A. D., Roberts T. P., Walton D. J., 2011, AN, 332, 362

Sutton A. D., Roberts T. P., Walton D. J., Gladstone J. C., Scott A. E., 2012, MNRAS, 423, 1154

Swartz D. A., Ghosh K. K., Tennant A. F., Wu K., 2004, ApJS, 154, 519

Swartz D. A., Soria R., Tennant A. F., Yukita M., 2011, ApJ, 741, 49

Swartz D. A., Tennant A. F., Soria R., 2009, ApJ, 703, 159

Tadhunter C., 2008, New Astronomy Reviews, 52, 227

Tadhunter C. N., Morganti R., Robinson A., Dickson R., Villar-Martin M., Fosbury R. A. E., 1998, MNRAS, 298, 1035

Takeuchi S., Ohsuga K., Mineshige S., 2013, PASJ, accepted (arXiv:1305.1023)

Tanaka Y., Inoue H., Holt S. S., 1994, PASJ, 46, L37

Tananbaum H., Gursky H., Kellogg E. M., Levinson R., Schreier E., Giacconi R., 1972, ApJ, 174, L143

Tao L., Feng H., Grisé F., Kaaret P., 2011, ApJ, 737, 81

Tao L., Kaaret P., Feng H., Grisé F., 2012, ApJ, 750, 110

Tikhonov N. A., Karachentsev I. D., 1998, A&AS, 128, 325

Torrejón J. M., Schulz N. S., Nowak M. A., Kallman T. R., 2010, ApJ, 715, 947

Tremaine S. D., Ostriker J. P., Spitzer Jr. L., 1975, ApJ, 196, 407

Trümper J., 1982, Advances in Space Research, 2, 241

Tully R. B., 1988, Nearby galaxies catalog. Cambridge Univ. Press, Cambridge

Tully R. B., Rizzi L., Shaya E. J., Courtois H. M., Makarov D. I., Jacobs B. A., 2009a, AJ, 138, 323

Tully R. B., Rizzi L., Shaya E. J., Courtois H. M., Makarov D. I., Jacobs B. A., 2009b, AJ, 138, 323

Ueda Y., Yamaoka K., Remillard R., 2009, ApJ, 695, 888

Vaughan S., Edelson R., Warwick R. S., Uttley P., 2003, MNRAS, 345, 1271

Veilleux S., 2003, in Collin S., Combes F., Shlosman I., eds, Active Galactic Nuclei: From Central Engine to Host Galaxy Vol. 290 of Astronomical Society of the Pacific Conference Series, The AGN Paradigm: Radio-Quiet Objects. p. 11

Vierdayanti K., Done C., Roberts T. P., Mineshige S., 2010, MNRAS, 403, 1206

Vierdayanti K., Mineshige S., Ebisawa K., Kawaguchi T., 2006, PASJ, 58, 915

Volonteri M., 2010, A&A Rev., 18, 279

Walton D. J., Gladstone J. C., Roberts T. P., Fabian A. C., Caballero-Garcia M. D., Done C., Middleton M. J., 2011a, MNRAS, 414, 1011

Walton D. J., Miller J. M., Harrison F. A., Fabian A. C., Roberts T. P., Middleton M. J., Reis R. C., 2013, ApJ, 773, L9

Walton D. J., Miller J. M., Reis R. C., Fabian A. C., 2012, MNRAS, 426, 473

Walton D. J., Roberts T. P., Mateos S., Heard V., 2011b, MNRAS, 416, 1844

Warwick R. S., Pye J. P., Fabian A. C., 1980, MNRAS, 190, 243

Watarai K.-y., Mizuno T., Mineshige S., 2001, ApJ, 549, L77

Watson M. G., et al., 2001, A&A, 365, L51

Watson M. G., et al., 2009, A&A, 493, 339

White N. E., Nagase F., Parmar A. N., 1995, X-ray Binaries, pp 1–57

Whitmore B. C., Zhang Q., Leitherer C., Fall S. M., Schweizer F., Miller B. W., 1999, AJ, 118, 1551

Wilkinson T., Uttley P., 2009, MNRAS, 397, 666

Wilms J., Allen A., McCray R., 2000, ApJ, 542, 914

Winter L. M., Mushotzky R. F., Reynolds C. S., 2006, ApJ, 649, 730

Wolter A., Gioia I. M., Henry J. P., Mullis C. R., 2005, A&A, 444, 165

Wolter A., Pizzolato F., Rota S., Mapelli M., Ripamonti E., 2011, AN, 332, 358

Wolter A., Trinchieri G., Colpi M., 2006, MNRAS, 373, 1627

Wood K. S., et al., 1984, ApJS, 56, 507

Yang L., Feng H., Kaaret P., 2011, ApJ, 733, 118

Yoshida T., Ebisawa K., Matsushita K., Tsujimoto M., Kawaguchi T., 2010, ApJ, 722, 760

Yu Q., Tremaine S., 2002, MNRAS, 335, 965

Zampieri L., Roberts T. P., 2009, MNRAS, 400, 677

Zdziarski A. A., Grove J. E., Poutanen J., Rao A. R., Vadawale S. V., 2001, ApJ, 554, L45

Zezas A., Fabbiano G., Rots A. H., Murray S. S., 2002, ApJ, 577, 710